SYNTHESIS OF PHOSPHONATE FUNCTIONALIZED SILICA NANOPARTICLES FOR PROTEIN IMMOBILIZATION, INTRACELLULAR PROTEIN DELIVERY AND CATALYTIC APPLICATIONS

Submitted in partial fulfilment of the requirements of the Degree of Doctor of Philosophy

By

Sai P. Maddala

School of Biological and Chemical Sciences

October 2014

Statement of Originality

I, Sai Prakash Maddala, confirm that the research included within this thesis is my own work or that where it has been carried out in collaboration with, or supported by others, that this is duly acknowledged below and my contribution indicated. Previously published material is also acknowledged below.

I attest that I have exercised reasonable care to ensure that the work is original, and does not to the best of my knowledge break any UK law, infringe any third party's copyright or other Intellectual Property Right, or contain any confidential material.

I accept that the College has the right to use plagiarism detection software to check the electronic version of the thesis.

I confirm that this thesis has not been previously submitted for the award of a degree by this or any other university.

Signature:

Date:

Abstract

Organosilica nanoparticles have attracted a lot of research interest in a variety of areas such as drug delivery and catalysis because of their properties which include high surface area as well as tunable particle and pore size. In particular, nanoparticles with large pore sizes are of great interest because of their potential to host large guest molecules such as proteins and as catalysts. The focus of the work in the thesis was to develop phosphonate functionalized organosilica nanoparticles for biomedical and catalytic applications. Raspberry textured phosphonatesilica nanoparticles denoted, RNPPME(2.5) (where the number in the brackets represents the moles of organophosphonate per gram), with large pore size (11–17 nm), uniform particle size (70 – 90 nm) and high surface area were produced through the use of template directed base catalysed synthesis, using tetraethylorthosilicate (TEOS) and dimethylphosphonatoethyltrimethoxysilane (DMPTMS) as the silica sources. The role of the reaction conditions such as temperature, surfactant concentration, pH, organosilane concentration and type were investigated and a mechanism for the raspberry nanoparticle formation was proposed. The particles were characterized using electron microscopy (SEM and TEM), Dynamic light scattering (DLS), silicon and phosphorus solid state NMR, and solution phase proton NMR of base digested particles, FT–IR, nitrogen adsorption porosimetry and thermal analysis (TGA).

The ability of the particles to host protein molecules of the model protein, bovine serum albumin (BSA) was investigated and the particle–protein composite was characterized using circular dichroism (CD). Raspberry textured nanoparticles were found to host large quantities (26 wt%) of protein. Studies on other (small pore (3 nm) phosphonate functionalized nanoparticles NP_PME(0.2) and NP_PME(1.0)) and (3 nm

pore) unfunctionalized mesoporous silica nanoparticles (MSN) revealed that phosphonate loading and the pore size influenced the protein uptake In addition to high protein uptake, the RNP_PME(2.5) particles also absorbed protein molecules rapidly (~ 20 minutes to maximum load). CD studies determined that the particle bound protein structure was not affected at physiological pH (7.40). The vast majority of the previously reported studies involving protein immobilization involved the use of bulk silica materials, which cannot be dispersed and hence those materials were unsuitable for *in vivo* protein delivery applications. The BSA@RNP_PME(2.5) particles showed good protein load and dispersion properties and hence are excellent protein delivery agents.

Dispersions of nanoparticle composite $BSA^{\#}$@RNP*_PME(2.5) (where $BSA^{\#}$ represents fluorescein isothiocyanate labelled BSA and RNP*_PME(2.5) represents rhodamine B isothiocyanate labelled RNP_PME(2.5)) was used to successfully deliver membrane impermeable protein BSA into HeLa cells. Intracellular protein delivery has attracted great interest due to its potential therapeutic applications and research tool value (e.g. for studying various cellular pathways). The toxicity of the guest free particles RNP*_PME(2.5) and the protein loaded particles $BSA^{\#}$@RNP*_PME(2.5) was studied using MTT (3-(4,5-dimethylthiazol-2-yl)-2,5-diphenyltetrazolium bromide) assay. The particles and the protein-particle composite were found to be non-toxic. The mechanism of the particle uptake by the cells was also studied. The unloaded (protein free) particles were found to be taken up by caveolar endocytosis pathway and the protein loaded particles were taken up by folic acid mediated pathway. The results indicated that the particles can successfully deliver membrane impermeable protein across the cell membrane. This result suggested that the particles can potentially be used for intracellular protein delivery applications.

Raspberry textured nanoparticles RNP_PME(2.5) were also used to host the enzyme lipase. It was demonstrated that immobilization increased the maximum velocity and Michaelis constant of the enzyme and also that the particles offered protection against the denaturing agent, urea. Finally, in a chemical catalysis application, the RNP_PME(2.5) particles were used to synthesize the platform chemical HMF, through Brönsted acid catalysed dehydration of fructose. High yields of HMF (87 %) were achieved when 10 wt% fructose was used. The particles demonstrated good recyclability and also the ability to convert up to 50 wt% fructose into HMF (80 % yield). The particles therefore acted as protective agents for enzymes and can therefore be used as enzyme immobilizing agents. Additionally, they also acted as excellent Brönsted acid catalysts.

Acknowledgements

I would like to thank my supervisor Prof A. C. Sullivan for providing me with the opportunity and funding to work on this PhD project. I thoroughly enjoyed working on project and I am very much grateful for the advice and guidance that I received for the entirety of my PhD. I would also like to thank my PhD panel members Dr. Abrahams and Dr. Zarbakhsh for providing me with valuable advice during the panel meetings. I would like to thank QMUL for providing me with a fee waiver.

I would like to thank my former group members, Patrick, Asma, Krystelle, and Sebastien for their help. I really enjoyed working with them in the lab. I would like to thank Siobhán for all the fun 'arguments' and for making sure that I had a regular supply of cake. I would like to thank Burcu, Roksana, Geoffrey, Harry, Kajally, Nicky, Fabrizio, Giorgio, Gabrielle, Freda, Mario, Paolo, Mark, Joey and Seble for all the good times during the last 4 years. I would like to thank Dolça and Jason for being such wonderful friends and for introducing me to some very interesting manga. I would like to thank Laura and Filippo for all the fun conversations.

I would like to thank the SBCS staff, Jalal, Jay, John, Janet, Greg, Harold, Ray, Agha, Andy, Raj and Ian for their help during my PhD. Special thanks to Jalal for 'lending' me the telephone charger. I would like to thank Diana for helping me with cell culture work, Ruth for providing access to the protein lab, Zofia for patiently training me to use the electron microscopes (SEM and TEM) and for all the academic support and Giulia for preparing HeLa cell TEM samples.

Finally, I would like to thank my family for their support and for always being there for me. I would especially like to thank Sudhamsh for being such a wonderful brother and

friend. I wouldn't have been able to enjoy these last 4 years, as much as I did, without his support.

Table of Contents

List of Abbreviations

AEPTMS: *N*–(2–aminoethylamino)ethylaminopropyltrimethoxysilane

ALTMS: Allyltrimethoxysilane

APTES: Aminopropyltriethoxysilane

BSA: Bovine Serum Albumin

CD: Circular Dichroism

CMSNs: Colloidal Mesoporous Silica Nanoparticles

CMC: Critical Micelle Concentration

CPMAS: Cross Polarized Magic Angle Spinning

CPP: Cell Penetrating Peptides (CPP)

CPTES: Cyanopropyltriethoxysilane

CTAB: Cetyltrimethylammonium Bromide

CTAT: Cetyltrimethylammonium Tosylate

DEP: Diethylphosphite

DEPTES: Diethylphosphonatoethyltriethoxysilane

DLS: Dynamic Light Scattering

DMP: Dimethylphosphite

DMPTMS: Dimethylphosphonatoethyltrimethoxysilane

DPMAS: Direct Polarization Magic Angle Spin

DTB: Di–t–butyl peroxide

FITC: Fluorecein isothiocyante

IR: Infrared Spectroscopy

LCP: Left Circular Polarized light

MSN: Mesoporous Silica Nanoparticles

NMR: Nuclear Magnetic Resonance

NP_PME: Nanoparticles_Phosphonate Monomethylester

NP_PEE: Nanoparticles_Phosphonate Monoethylester

OCMSN: Organic functionalized Colloidal Mesoporous Silica Nanoparticles

RITC: Rhodamine B isothiocyante

RCP: Right Circular Polarized light

RNP_PME: Raspberry textured Nanoparticles_Phosphonate Monomethylester

SDS–PAGE: Sodium Dodecyl Sulphate–Poly Acrylamide Gel Electrophoresis

SEM: Scanning Electron Microscope

SST: Surfactant–Silica Template

StEM: Standard error of mean

Std. Dev: Standard deviation

TEM: Transmission Electron Microscope

TEOS: Tetraethylorthosilicate

TMOS: Tetramethylorthosilicate

UDPTMS: Ureidopropyltrimethoxysilane

VTES: Vinyltriethoxysilane

VTMS: Vinyltrimethoxysilane

List of Schemes, Figures and Tables

Chapter 1

Figure 1.16: Variation in the uptake of nanoparticles by MCF–7 cells. Free dox = free doxorubicin; DMSNs1 = 3.2 nm pore sized particle; DMSNs2 = 6.4 nm pore sized particle and DMSNs3 = 12.6 nm. (A) Measurement of nanoparticle uptake by the cells (using Fluorescence–activated cell sorting (FACS)) and cell viability after doxorubicin treatment (using MTT assay).

Figure 1.17: (A) TEM image of COOH_MSNs; (B) Cell viability studies performed on CEM cells and Ramos cell line, showing strong reduction in viability of CEM cells

Figure 1.18: TEM image of poly–lactic acid coated mesoporous silica nanoparticle based sensor. The outer layer (11 nm) indicates the poly lactic acid layer.

Chapter 2

Chapter 3

Chapter 4

Figure 4.8: Time dependent uptake of RNP*_PME(2.5) nanoparticles by HeLa cells (Scale 20 µm). The red spots indicate the presence of Rhodamine B isothiocyanate functionalized nanoparticles RNP*_PME(2.5)

Figure 4.9 : Distribution of RNP*_PME(2.5) nanoparticles in HeLa cells at different exposure times (Scale bar 10 µm in all images); A) 1 hour; B) 2 hours; C) 4 hours and D) 6 hours

Figure 4.10: TEM images of HeLa cells 6 hours after RNP*_PME(2.5) particle uptake. A) HeLa cell (Scale 5 µm); B) Particles in cytoplasm (black arrows) (Scale 500 nm); C) Particles within vesicles (black arrow) (Scale 500 nm) (Inset 2X magnification of the region containing the particles, indicated by black arrows); D) Caveolae on the cell surface (black arrow) (Scale 500 nm) (Inset 2X magnification of the region containing the particles, indicated by black arrows); E) Nucleus (Scale 500 nm)

Figure 4.11: BSA$^{\#}$@ RNP*_PME(2.5) uptake versus time (n = 20 ± SEM)

Figure 4.12: Time dependent uptake of BSA$^{\#}$@RNP*_PME(2.5)nanoparticles by HeLa cells (Scale 20 µm). The red spots indicate the presence of Rhodamine B isothiocyanate functionalized nanoparticles RNP*_PME(2.5) and the presence of protein molecules was determined by identifying fluorescein isothiocyanate functionalized BSA, green spots.

Figure 4.13 : Distribution of BSA$^{\#}$@RNP*_PME(2.5)nanoparticles in HeLa cells at different exposure times; A) 1 hour(Scale bar 5 µm); B) 2 hours (Scale bar 7 µm); C) 4 hours (Scale bar 10 µm) and D) 6 hours (Scale bar 5 µm)

Figure 4.14: TEM images A) HeLa cell (Scale 5000 nm); B) Protein loaded nanoparticle BSA$^{\#}$@ RNP*_PME(2.5)localisation (black arrows) within the cytoplasm (Scale 1000 nm) (Inset 2X magnification of the region containing the particles, indicated by black arrows); C) Localization of nanoparticles within mitochondria (Scale 500 nm); D) Nucleus , note that particles were not observed (Scale 1000 nm) (Inset 2X magnification of the region containing the particles, indicated by black arrows); E) Particles within endosomes (indicated by black arrows) (Scale 1000 nm) (Inset 2X magnification of the region containing the particles, indicated by black arrows)

Figure 4.15: BSA$^{\#}$@ RNP*_PME(2.5) Particle uptake versus protein load. (n = 20 ± SEM.)

Figure 4.16: Effect of protein load in BSA$^{\#}$@ RNP*_PME(2.5) particles on particle uptake (Scale bar 20 µm). The red spots indicate the presence of Rhodamine B isothiocyanate functionalized nanoparticles RNP*_PME(2.5) and the presence of protein molecules was determined by identifying fluorescein isothiocyanate functionalized BSA, green spots.

Figure 4.17: Distribution of BSA$^{\#}$@RNP*_PME(2.5)nanoparticles in HeLa cells at different protein load; A) 111.1 mg/g (Scale bar 5 µm); B) 166.7 mg/g (Scale bar 5 µm); C) 223.0 mg/g (Scale bar 10 µm)

Figure 4.18: Effect of RNP*_PME(2.5) particle numbers on incubation in particle free media (n = 20 ± SEM)

Figure 4.19: Effect of incubation in particle free media on RNP*_PME(2.5) particle loaded cells (Scale 20 µm). The red spots indicate the presence of Rhodamine B isothiocyanate functionalized nanoparticles RNP*_PME(2.5).

Figure 4.20: Distribution of RNP*_PME(2.5)nanoparticles in HeLa cells at different incubation times in particle free media; A) 0 hours (Scale bar 10 µm); B) 1.5 hours (Scale bar 10 µm); C) 2.5 hours (Scale bar 10 µm) and D) 3 hours (Scale bar 10 µm)

Figure 4.21: TEM images of RNP*_PME(2.5) particle loaded cells after 3 hours of incubation in cell free media. A) Complete HeLa cell (Scale 5000 nm); B) Localization of the particles in cytoplasm (Scale 500 nm) (Inset 2X magnification of the region containing the particles, indicated by black arrows); C) Particle exocytosis (indicated by black arrows) (Scale 200 nm)

Figure 4.22: Effect of BSA#@RNP*_PME(2.5) particle numbers on incubation in cell free media (n = 20 ± SEM)

Figure 4.23: Effect of incubation in cell free media on BSA$^{\#}$@RNP*_PME(2.5) particle loaded cells (Scale 20 µm). The red spots indicate the presence of Rhodamine B isothiocyanate functionalized nanoparticles RNP*_PME(2.5) and the presence of protein molecules was determined by identifying fluorescein isothiocyanate functionalized BSA, green spots.

Figure 4.24: Distribution of BSA$^{\#}$@RNP*_PME(2.5) nanoparticles in HeLa cells at different incubation times in particle free media; A) 0 hours (Scale bar 5 µm); B) 1.5

hours (Scale bar 10 µm); C) 2.5 hours (Scale bar 10 µm) and D) 3 hours (Scale bar 10 µm)

Figure 4.25: TEM images of BSA$^{\#}$@RNP*_PME(2.5) particle loaded cells after 3 hours of incubation in cell free media. A) Complete HeLa cell (Scale 5000 nm); B) Localization of the particles in cytoplasm (Scale 1000 nm) (Inset 2X magnification of the region containing the particles, indicated by black arrows); C) Nucleus, note the absence of particles (Scale 1000 nm)

Figure 4.26: Receptor mediated uptake of RNP*_PME(2.5) particles (n = 20 ± SEM.). Statistical significance was measured at p-value of 0.01 using Wilcoxon ranked sum test. Statistical significance was determined by comparing against the uptake when surface receptors were not blocked (Sample: None). Statistical significance is denoted by ** and non-significant results by *.

Figure 4.27: Confocal microscope images depicting the effects of blocking surface receptors on RNP*_PME(2.5) particle uptake. (Scale 20 µm). The red spots indicate the presence of Rhodamine B isothiocyanate functionalized nanoparticles RNP*_PME(2.5).

Figure 4.28: Distribution of RNP*_PME(2.5)nanoparticles in HeLa cells in presence of various cell surface receptor inhibitors; A) No inhibitor (Scale bar 10 µm); B) Clathrin (Sucrose) (Scale bar 10 µm); C) Folate receptor (Folic acid) (Scale bar 10 µm) and D) Caveolae (Nystatin) (Scale bar 10 µm)

Figure 4.29: Receptor mediated uptake of BSA$^{\#}$@ RNP*_PME(2.5) particles (n = 20 ± Rel. std. dev.) Statistical significance was measured at p-value of 0.01 using Wilcoxon ranked sum test. Statistically significance was determined by comparing against the uptake when surface receptors were not blocked (Sample: None). Statistical significance is denoted by ** and non-significant results by *

Figure 4.30: Confocal microscope images depicting the effects of blocking surface receptors on RNP*_PME(2.5) particle uptake. (Scale 20 µm). The red spots indicate the presence of Rhodamine B isothiocyanate functionalized nanoparticles RNP*_PME(2.5) and the presence of protein molecules was determined by identifying fluorescein isothiocyanate functionalized BSA, green spots.

Figure 4.31: Distribution of BSA$^{\#}$@RNP*_PME(2.5) nanoparticles in HeLa cells at in presence of various cell surface receptor inhibitors; A) No inhibitor (Scale bar 10 µm);

B) Clathrin (Sucrose) (Scale bar 10 µm); C) Folate receptor (Folic acid) (Scale bar 10 µm) and D) Caveolae (Nystatin) (Scale bar 10 µm)

Table 4.1: Morphological properties of RNP_PME(2.5)

Chapter 5

Chapter 1

Chapter 1: Silica Nanoparticles:Development and Applications

1.1 Silica Nanoparticles

In the early 20th century Paul Ehrlich coined the term "Magic Bullet" to describe chemical agents that would selectively target disease causing pathogens and leave the host unharmed.[1] The discovery of the therapeutic potential of nanoparticles in medicine aligns well with Ehrlich's vision of targeted drugs. Several reviews described the properties of an ideal drug delivery system and as collated from these reports an ideal drug delivery platform would have a number of properties including for example a) small size (below 200 nm) , stable , biocompatible composition and excellent dispersion properties that would allow the particles to remain dispersed in the blood stream; b) ability to host a variety of guest molecules like drugs, proteins; DNA etc.; c) zero premature release; d) the ability to accommodate different functionalities that would allow it to target specific receptors and finally, e) controlled release at the target site.[2] Colloidal mesoporous silica nanoparticles (CMSNs) stand out as potential drug delivery candidates because of their properties such as high surface area, large pore volume, uniform and tunable pore size, facile functionalization and the ability to accommodate multiple functional groups. Because of these properties they have attracted a lot of research interest in fields such as biomedical research (including drug delivery, biomarkers and biological sensors) and catalysis. These applications and relevant literature are covered in section 1.3.

CMSNs are typically synthesized using base catalysed sol-gel processing. The general procedure utilizes alkoxysilane precursors (such as TEOS (tetraethylorthosilicate), TMOS (tetramethylorthosilicate) and VTMS (vinyltrimethoxysilane)) dissolved in a solvent and to this mixture base is added to initiate

base catalysed hydrolysis and condensation of the alkoxysilanes. The mechanism of the hydrolysis and condensation is shown below (Schemes 1.1 and 1.2):

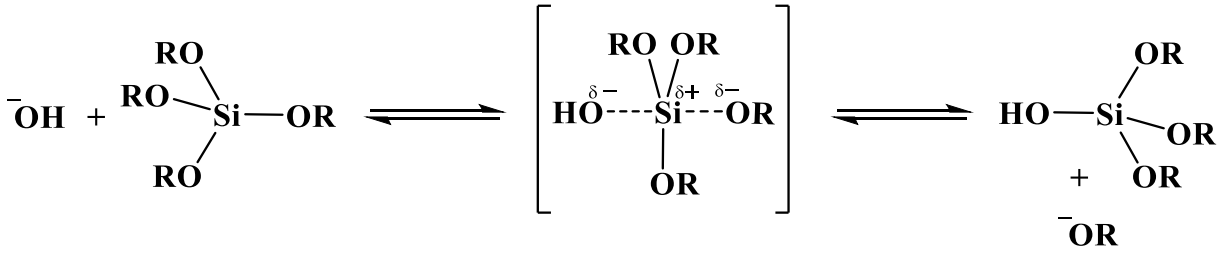

Scheme 1.1: Base catalysed hydrolysis[3]

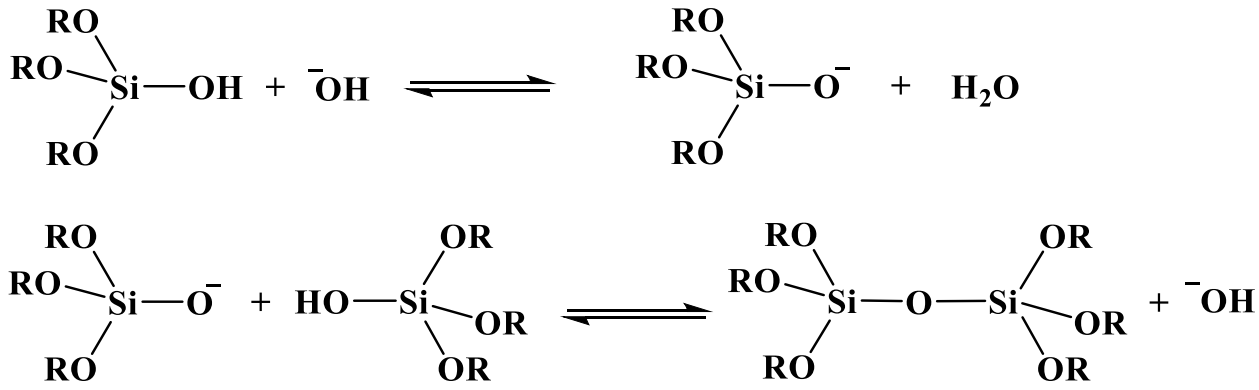

Scheme 1.2: Base catalysed condensation[3]

Hydrolysis (Scheme 1.1) involves nucleophilic attack at the silicon atom resulting in the formation of silanol. Condensation (Scheme 1.2) is a polymerization reaction to form siloxane bonds with the liberation of either alcohol or water. The consequence of these reactions is the formation of a new phase known as a sol. Commonly used alkoxysilanes such TEOS, TMOS and VTMS are not soluble in water and either need a mutual solvent such as alcohol or a surfactant to disperse them. The first demonstration of silica nanoparticle synthesis was performed by Stöber *et al*. in 1968.[4]

1.1.1 Stöber Process

The very first demonstration of silica nanoparticle synthesis was carried out by Stöber *et al*. in 1968 (Figure 1.1). This method involved base (ammonia) catalysed hydrolysis and condensation of the silica precursor, TEOS, in ethanol to form spherical silica particles in the nanometer and micrometer range.[4] Further refinements such as the use of non-ionic surfactants as well as controlling the precursor and base concentrations lead to improvements in the monodispersity and sphericity of the particles and some of these examples are shown in Figures 1.2 and 1.3. This facile synthesis of nanoparticles lends itself to industrial production.

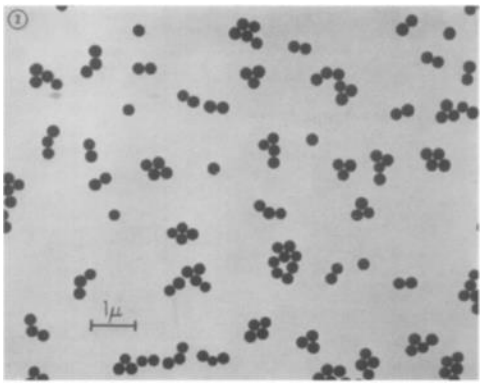

Figure 1.1: Silica particles (Scale 1 μm) synthesized by method of Stöber *et al.* [4]

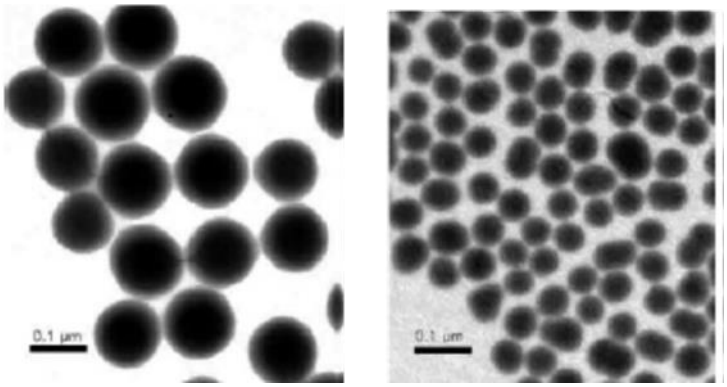

Figure 1.2: Effect of water concentration (10M LHS and 20M RHS) on the particle size (reaction carried out in ethanol) (scale 0.1 μm) [6]

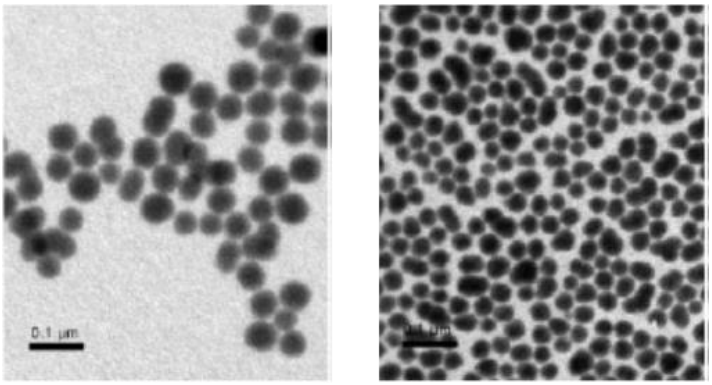

Figure 1.3: Effect of base (ammonia) concentration (2M LHS and 1.75 M RHS) on the particle size (reaction carried out in methanol) (scale 0.1 μm) [6]

The mechanism of particle formation was reported by Van Blaadren *et al*. and proceeded through two steps where the first step involved the formation of "seed particles" or pre-polymers by the base catalysed hydrolysis and condensation of the alkoxysilane. These seed particles then aggregated and underwent interparticle condensation to form nanoparticles (Scheme 1.3). Control of the particle morphology was achieved by carefully controlling the number of seed particles and their subsequent aggregation.[5] This can be achieved by controlling various reaction parameters like temperature, base concentration, polarity of the solvent[6] and the type of the silane precursor[7] used in the particle synthesis.

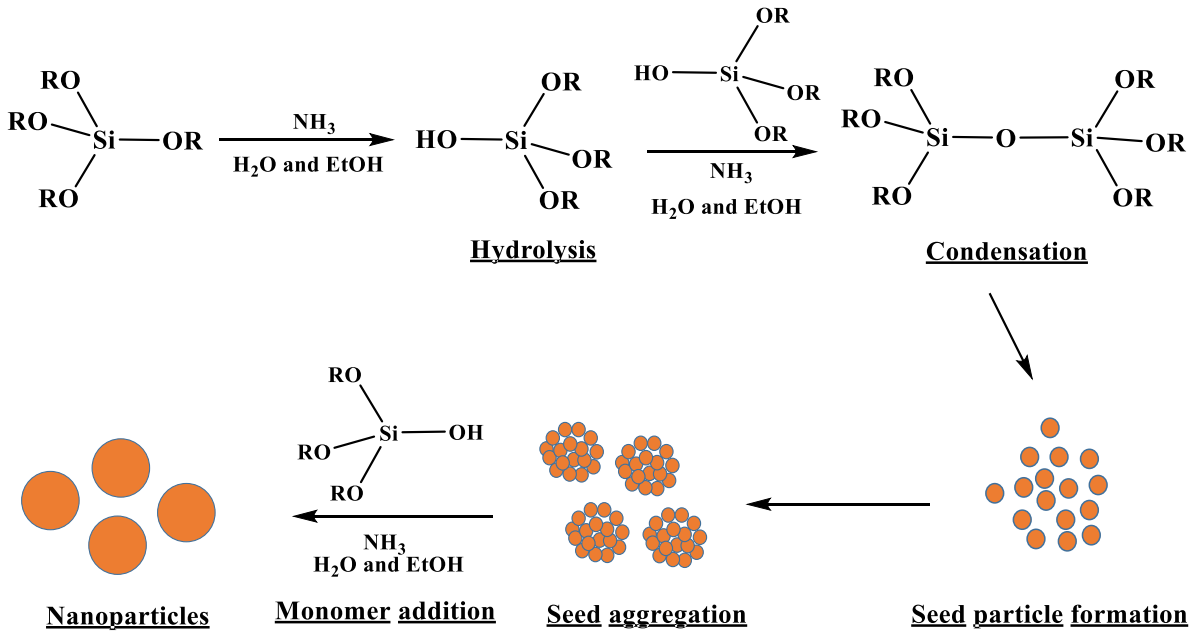

Scheme 1.3: Mechanism of Stöber particle formation

Many modifications to the Stöber method have been reported.[8] An important example involved the use of basic amino acids. Amino acids are the building blocks of proteins and basic amino acids such as lysine and arginine have been demonstrated as efficient catalysts for the synthesis of silica nanoparticles. In addition to their role as bases the amino acids also acted as capping agents limiting particle growth and aggregation and played a structure directing role in assisting the particles to arrange in a uniform lattice (Figure 1.4).[9] This strategy has been demonstrated to be scalable.

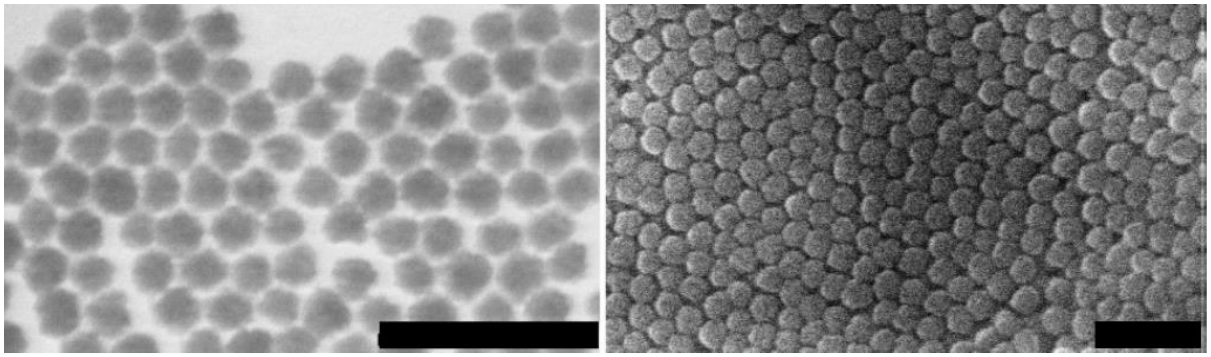

Figure 1.4: Silica nanoparticles synthesized using arginine as catalyst (TEM LHS and SEM RHS) (bar = 100 nm)[9]

The main drawback of the Stöber process is that the particles produced are non-porous and have low surface area. Due to the absence of a template the seed particles show non-directional aggregation.[10] Following the aggregation of the seed particles further particle growth takes place through monomer addition, this prevents the formation of pores. This limits the ability of Stöber particles to host guest molecules or perform drug delivery applications. However, they have been used as sensors and cell markers.[11]

1.1.2 Colloidal Mesoporous Silica Nanoparticles

Kresge *et al*. developed the mesoporous silica MCM-41 in 1992 using base catalysed hydrolysis-condensation on the alkoxysilane TEOS and using CTAB (cetyltrimethyl ammonium bromide) as the surfactant template. This method resulted in the production of mesoporous silica material with ordered mesopore arrangement (pore size 3 nm).[12] This method later formed the basis for the production of CMSNs. Much of the initial focus was aimed at using these materials for catalysis applications. Between 1999 and 2001 several papers were published exploring the possible use of these materials for controlled release of biomedically relevant molecules (such as proteins and drugs).[13,14] These materials offered several advantages over conventional drug delivery systems as outlined below:

1. **Ordered pore network**: Homogenous pore network to facilitate the control of drug upload and release.

2. **Large pore volume and surface area**: This helps host a large quantity of biologically relevant molecules.

3. **Free silanol groups on the surface**: The surface silanols can be used to functionalize the surface with organic molecules to better control the interactions with the guest molecules.[15]

The challenge, however, was the control of particle morphology. Initial synthetic procedures for MCM-41 and similar silicas such as SBA-15 and MCM-48 resulted in the formation of particles with irregular particle size, hence their application as potential drug delivery agents was severely limited despite their excellent controlled release properties. This problem was solved in the early 2000s when several groups independently synthesized silica nanoparticles using soft template approaches. In addition to the pore size and surface area, the nanoparticles have additional advantages such as fast mass transport, effective adhesion of substrates and good dispersability in solutions.[16] The particle synthesis was the result of specific interactions between the surfactant, alkoxysilane precursor, base and co-solvent. The following sections discuss some of the key strategies used in controlling the particle morphology.

1.1.2.1 Role of surfactant templates

The interactions between silica and the surfactant head groups play a major role in determining the final pore morphology of the particles. Cationic surfactants such as quaternary ammonium surfactants are commonly used in the synthesis of CMSNs. Particle synthesis is typically carried out under basic conditions, resulting in the formation of negatively charged silica back bone (isoelectric point at pH ≈ 2). The negatively charged silica interacts with cationic surfactant through S^+I^- interactions (where S represents the surfactant and I the inorganic species) (Scheme 1.4). Non-ionic surfactants such as block co-polymers are sometimes used in the synthesis of mesoporous silica nanoparticles. In this case the inorganic silica species interact with the surfactant through hydrogen bonding (S^0I^0 interaction). [17]

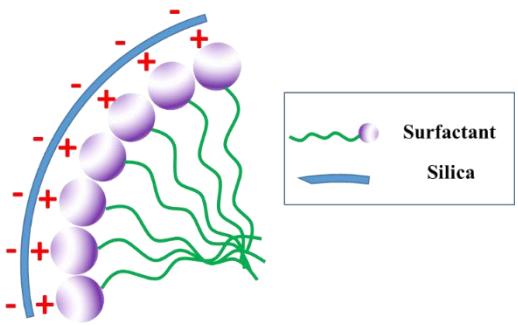

Scheme 1.4: Interactions between positively charged surfactants and negatively charged silica S^+I^- (under basic conditions)

The early reports on silica nanoparticles used the cationic surfactant CTAB. Mann *et al*. in 2001 used base catalysed synthesis to prepare silica nanoparticles. CTAB was used as the surfactant. The particle morphology was controlled by dilution using a large amount of water followed by neutralization by adding HCl. The particle morphology varied depending on the acid quenching time. When the particles were quenched after 60 seconds, the particle size was 23 ± 4 nm with a pore size of 6.64 nm. Quenching after 220 seconds of reaction resulted in the formation of larger particles (100 ± 26 nm) with slightly smaller pores (4.64 nm) see (Figure 1.5).[18] Cai *et al*. in the same year reported a low surfactant strategy for the synthesis of silica nanoparticles and variations of this method are widely used to produce CMSNs. In addition morphology control of silica nanoparticles was achieved simply by changing the base from ammonia to sodium hydroxide (Figure 1.6).[19]

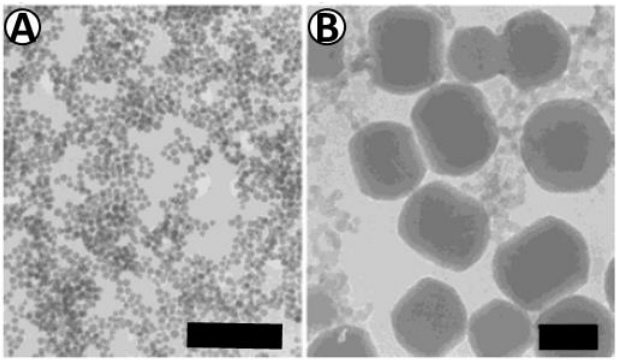

Figure 1.5: CMSNs synthesized by quenching the reaction after A) 60s and B) 220s (Scale bar 100 nm).[18]

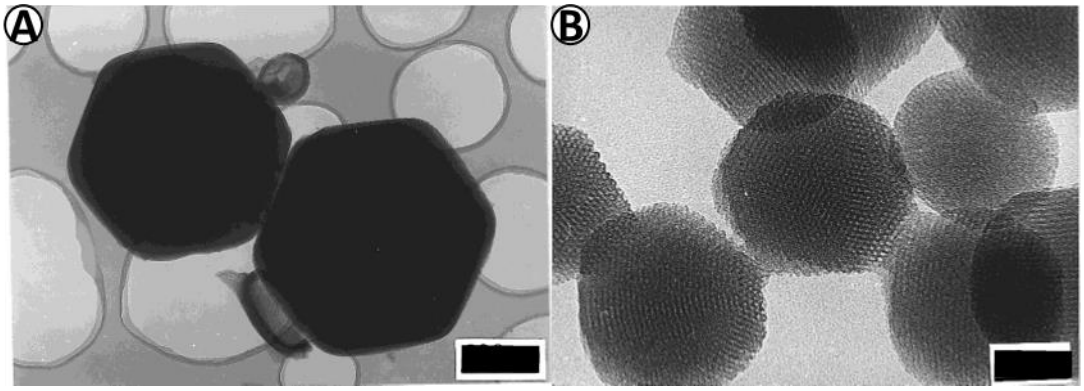

Figure 1.6: Particles synthesized using A) ammonia as catalyst (Scale 500 nm) B) NaOH as catalyst (Scale 50 nm).[19]

Template directed synthesis of silica nanoparticles involves the use of a surfactant template to guide the particle growth. Surfactants play a dual role in this process. First, the surfactants help evenly disperse the alkoxysilane precursor in water by forming an oil in water emulsion. The second role of the surfactants is to act as templates to guide the formation of the nanoparticles. The mechanism behind the silica nanoparticle formation was determined by Cai *et al.*[19] and Nooney *et al.*[10] The mechanism for the particle formation was determined from silica nanoparticles synthesized using the cationic surfactant CTAB as template. CTAB micelles undergo three phase transitions as the surfactant concentration is increased. First, the critical micelle concentration (CMC) of CTAB is 1 mM[20a], which increases to 24 mM under basic conditions (pH ~ 12.5)[20b] and CTAB forms spherical micelles that are about 3 nm in diameter. Then as the concentration is increased it undergoes a second critical micelle concentration (CMC_2) at 0.3 M at

neutral pH wherein the micelles now assume a rod shape with similar pore diameter. Further increase in the concentration leads to the formation of hexagonal liquid crystals at 1.1 M at neutral pH.[20c,21] Colloidal mesoporous silica nanoparticles with ordered mesopore structure have the same pore diameter as the diameter of CTAB rod shaped micelles (CMC_2), however, the concentration of CTAB typically used in this type of silica nanoparticle formation is at least two orders of magnitude lower (~ 1.7 mM) than the concentration needed for spherical micelle to rod micelle transition. This suggests that the structure directing effect of the surfactant phase is probably due to a transient surfactant-silica template (which we will subsequently refer to as SST). Thus an SST phase (rather than pure surfactant micelles) formed after interaction between the surfactant and silica oligomers is likely to be structure directing. Under the reaction conditions (pH > 11) the silica oligomers attain a negative charge due to the deprotonation of the silanol groups.[22] These oligomers would interact with the positively charged surfactant through very strong multidentate linkages (Scheme 1.5). Frasch *et al.* demonstrated that the silica oligomers are formed prior to the formation of the silica-surfactant template (SST).[23] This is the first step in the formation of CMSNs (Scheme 1.5).

The second step is seed particle growth and aggregation. In this step, the particle growth takes place by the same two mechanisms that influence the particle growth in Stöber silica nanoparticles. Seed particle growth takes place through slow addition of the silane monomers to the silica-surfactant composite. Aggregation of these seed particles leads to the final nanoparticle.[24] The evidence for this comes from the work of Cai *et al.*[19] and Nooney *et al.*[10] Cai *et al.* grew nanoparticles at very low concentration of TEOS and the resultant particles had an urchin like structure, indicating the formation, aggregation and precipitation of rod shaped micelles. However, instead of the random aggregation of

the silica seed particles of the Stöber synthesis, the aggregation of the particles was directed along the crystal planes. This resulted in the formation of mesoporous silica nanoparticles.[10,19] (Scheme 1.5).

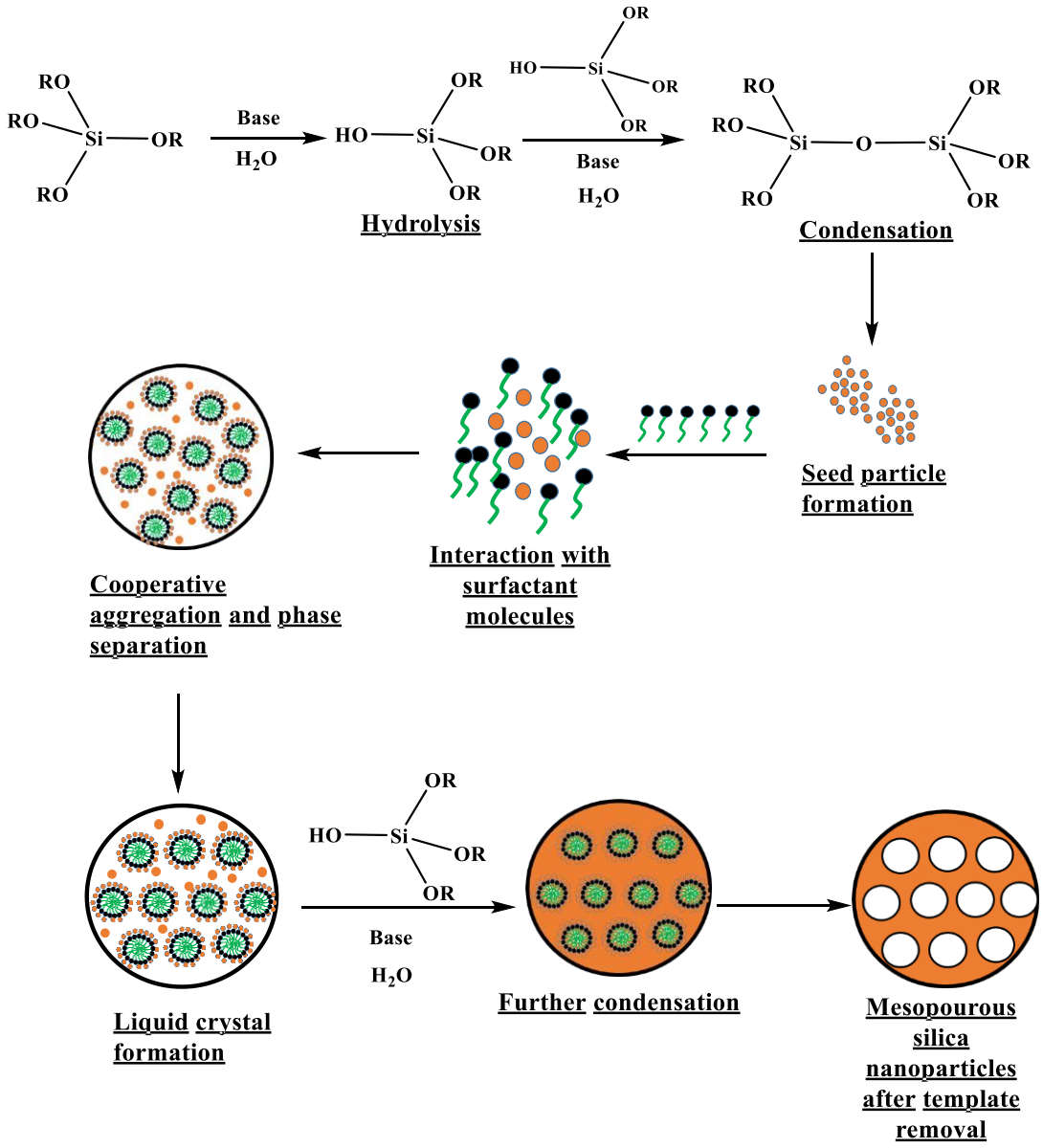

Scheme 1.5: Mechanism of CMSN formation

Surfactant charge has a great effect on the silica nanoparticle formation and neutral surfactants like n-dodecylamine and block co-polymers like pluronic P-123 and F-127 do not form charged species in solution and they interact with the silica species through hydrogen bonds (S^0I^0). Block co-polymers have been used in the production of large pore mesoporous silica materials such as SBA-15. However, controlling the particle

size was very difficult under the acidic conditions needed to prepare these materials probably because siloxane chain growth is favoured under acidic conditions and small particle formation is favoured under basic conditions.[16b]. Zhang *et al.* used block co-polymer Pluronic P123 to prepare mesoporous silica which was a mixture of amorphous silica and ordered mesoporous particles with relatively uniform particle size of around 300 nm. (Figure 1.7).[25]

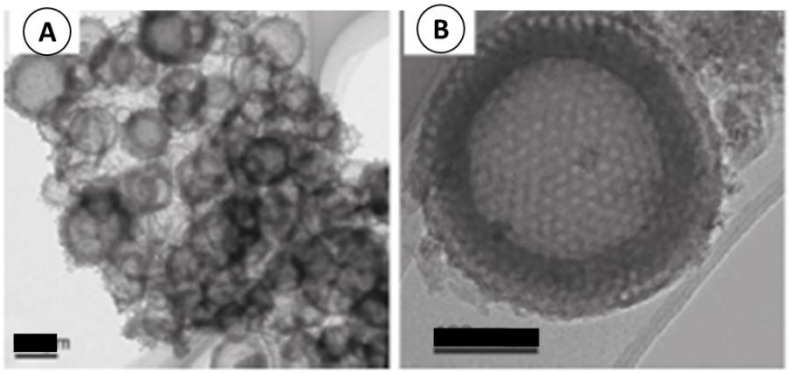

Figure 1.7: Mesoporous silica nanoparticles synthesized using pluronic P123 as surfactant at different magnifications.[25]

The use of surfactant template offers other advantages, for example, if the micelle size can be increased then the resultant pore size can be increased as well. This can be achieved by using pore enlargement agents and mixed micelles. Pore size enlargement is very important as this will help accommodate large, medically relevant molecules such as proteins and DNA. Lin *et al*. first demonstrated this using mesitylene as the pore enlargement agent. Particles with 6 nm ordered pores were obtained and these materials were used to encapsulate and deliver the membrane impermeable protein cytochrome C into HeLa cells.[26] Kao *et al*. used alkane/ethanol mixtures to expand the pore size of mesoporous silica nanoparticles. Under these conditions the pore diameter of the silica nanoparticles increased from 2.5 nm (no alkane) to 5.6 nm when dodecane was used as the pore enlargement agent. In this mechanism of particle formation the pore enlargement agent, a hydrophobic molecule, resides within and thus enlarges the surfactant micelles.

[27] This strategy, however had a major drawback, the particle size uniformity was severely affected by this process. For example the particle size reported by Lin *et al.* was between 300-600 nm[26] and this wide range in particle size makes these materials unsuitable for drug delivery applications.

Several other groups reported on an alternative strategy to increase the pore size of the silica nanoparticles. In this process, mixed micelles containing two different surfactants were used to increase the pore size and limit the particle growth. One of the earliest reports by Gao *et al*. used mixed micelles of mesitylene, non-ionic surfactant F-127 and fluorinated surfactant FC-4 as pore enlargement and particle growth limiting agents. In the proposed mechanism the silica species interacts with the block co-polymer surfactant under mildly acidic conditions and is converted into a partially ordered mesophase with face centred cubic symmetry. The fluorocarbon surfactant FC-4 interacts with the silica-surfactant mesophase and limits the particle growth. The reaction was carried out under mildly acidic conditions which facilitated slow hydrolysis and condensation of silica precursor TEOS and assisted in co-assembling silica oligomers and surfactant molecules. The resultant silica nanoparticles had an average pore size of 20 nm.[28] In a related type of study He *et al*. used dodecanethiol as a co-template to enlarge the pore size of silica nanoparticles to 16 ± 8 nm when coupled with high stirring rate (2600 rpm) nm.[29]

While surfactant templates have a profound effect on generation of nanoparticle morphology, the post synthesis method for removal of template is critical for ensuring retention of critical properties. The most common method used in removing surfactants from mesoporous silica nanoparticles is calcination,[30] however calcination caused interparticle siloxane bond formation between the surface silanol groups and caused irreversible aggregation between the particles and thus affected the particle

dispersability.[33] Therefore solution based methods are preferred. The most common solution based method is the overnight reflux of particles suspended in acidic methanol or ethanol.[31] Bein *et al*. developed different methods for removing surfactants from CMSNs. For example, ammonium nitrate/ethanol solution proved effective for rapid removal of surfactants.[32] Another strategy involved, treating the nanoparticles for about 3 hours in hydrogen peroxide to oxidize the surfactant templates. This process however lacks specificity and is incompatible with organosilanes, since the organic groups may also be oxidised by hydrogen peroxide.[33] Urata *et al*. developed a dialysis strategy to remove surfactants from CMSNs that are smaller than 30 nm, as these particles cannot be centrifuged. Dialysis was demonstrated to protect the particle morphology, while completely removing the surfactant.[34]

1.1.2.2 Role of Co-Solvent

Co-solvents such as ethanol are used in the synthesis of mesoporous silica nanoparticles to evenly disperse the alkoxysilane precursors. However, the presence of co-solvents has a strong influence on the formation of silica nanoparticles. Polar protic solvents, with intermediate dielectric constant, such as small chain alcohols, are solubilized near the interface of the SST and water,[35] thus reducing the interactions between the silica oligomers and the surfactant head groups. Small chain alcohols also influence the hydrolysis and condensation of the silane monomers under basic conditions by hydrogen bonding with the hydroxyl groups.[36]

1.1.2.2.1 Ethanol

Ethanol is the most common co-solvent used in the synthesis of CMSNs. It was demonstrated by Grün *et al*. that the presence of ethanol resulted in the formation of spherical particles.[37] Spherical particles are of great biomedical significance (section 1.3).

The presence of ethanol had a strong influence on the final morphology of the silica nanoparticles. Nooney *et al*. observed that use of ethanol resulted in a reduction of 0.5 nm in the pore diameter. They reasoned that this was due to the reduction in the template size by 0.4 nm, due to the influence of ethanol.[10] In addition to this, the presence of ethanol also lowers the hydrolysis rate and condensation of the silane precursors.[38] Higher concentrations of alcohol resulted in a disordered pore structure in CMSNs and increased the particle size. All these factors defined conditions for the formation of monodisperse CMSNs and resulted in the formation of spherical particles.[39]

1.1.2.2.2 Ethylene glycol

Ethylene glycol was also reported as a co-solvent and strongly interacted with the CTAB thereby limiting the interactions between silica oligomers and the surfactant. This helped achieve a monodisperse particle size distribution (Figure 8).[40]

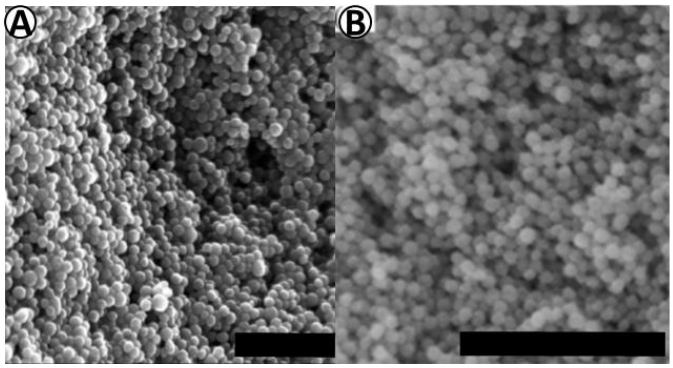

Figure 1.8: Nanoparticles synthesized using A) ethylene glycol (Scale 1000 nm)[40] B) Formaldehyde (Scale 500 nm)[41] as co-solvents.

1.1.2.2.3 Formaldehyde:

Formaldehyde polymerizes under the particle synthesis reaction conditions to form a polymer layer (of paraformaldehyde) around the silica nanoparticles. This strategy was used by Gu *et al*. to limit the growth of the silica nanoparticles to 30 nm. The authors

observed that increasing the formaldehyde concentration led to an increase in the pore volume, however it had no effect on the pore diameter or the particle size (Figure 1.8).[41]

1.1.2.2.4 Ethers:

Chen *et al*. studied the effects of two ethers, diethyl ether and 2-ethoxyethanol on the morphology of silica nanoparticles. 2-Ethoxyethanol (bp 135°C), produced particles with 3 nm pore channels. The authors observed that an increase in concentration of 2-ethoxyethanol lead to an increase in the particle size.[42] This observation was similar to that observed by Tan *et al*.[43] The results also indicated that the behaviour of 2-ethoxyethanol in water was similar to that of methanol, in that increasing concentration resulted in an increase in the particle size.

In the same study, the effect of diethyl ether (bp 34.6 °C) on the particle morphology was studied. Diethyl ether has very low solubility in water. It was therefore expected to reside deep in the core of the surfactant template.[42] However, due to its low boiling point it vaporized during the course of the nanoparticle formation and this resulted in the formation of particles with a thin outer shell and empty core, nanocapsule morphology.[42]

1.1.2.3 Role of Base

Silica nanoparticle formation is strongly influenced by the catalyst used in the reaction. Cai *et al*. demonstrated that final particle morphology is strongly influenced by the base used.[19] They found that the use of strong bases such as sodium hydroxide lead to the formation of small particles (100 nm diameter), while the use of a weak base such as ammonia lead to the formation of large particles. In order to explain these results the

authors suggested that the particle size was dependent on the length of the silica-surfactant composite micelles. The silica oligomers interact with the micelles in two ways, under the basic reaction conditions the silanol groups dissociate to form negatively charged Si-O^- groups that interact with the positively charged surfactant. In addition to the hydrophilic silanol groups, the oligomers contain hydrophobic siloxane linkages. The results from the experiment showed a strong increase in the particle size when sodium hydroxide was replaced with ammonia as the catalyst. It was suggested that the length of the silica-surfactant micelle was dependent on the interactions between the oligomers and the hydrophobic region of the surfactant. Weak bases like ammonia promoted these interactions while strong bases disrupted them, thus resulting in particles of smaller size.[19]

The interactions between the surfactants and the base have been used to achieve some interesting morphological changes, as demonstrated by Zhang *et al*. They used two surfactants; a surfactant with a hard head group –bromide ion, cetyltrimethylammonium bromide and a surfactant with a soft head group – tosylate ion, cetyltrimethylammonium tosylate. The reactions were carried out under two reaction conditions, low base (pH 7.2 to 7.4) and high base (pH 10). All the particles synthesized at pH 10 had wormhole pore structure (wormhole pore structure consists of irregular but interconnected pores) and smaller particle size, irrespective of the surfactant used. However, the particles synthesized at low base conditions resulted in a diversity of particle morphologies, depending on the surfactant and the organic amine used. When the particles were synthesized using CTAB as template and triethanolamine as the base, the particles with raspberry texture were observed. However, when cetyltrimethylammonium tosylate (CTAT) was used as the template, the particles formed with stellate morphology. The pore size of the particles varied from 54 nm (trimethylamine) to 16 nm (triethanolamine) and 17 nm (2-amino-2-(hydroxymethyl)propane-1,3-diol). The authors suggested that the

morphology changes were due to the interactions between the counterions and surfactants; bromide ions strongly dissociate from the CTAB while tosylate ions dissociate to a smaller extent, thus there is increased competition between the surfactant and silica oligomers. This could explain the differences in morphology for different surfactants (Figure 1.9).[44]

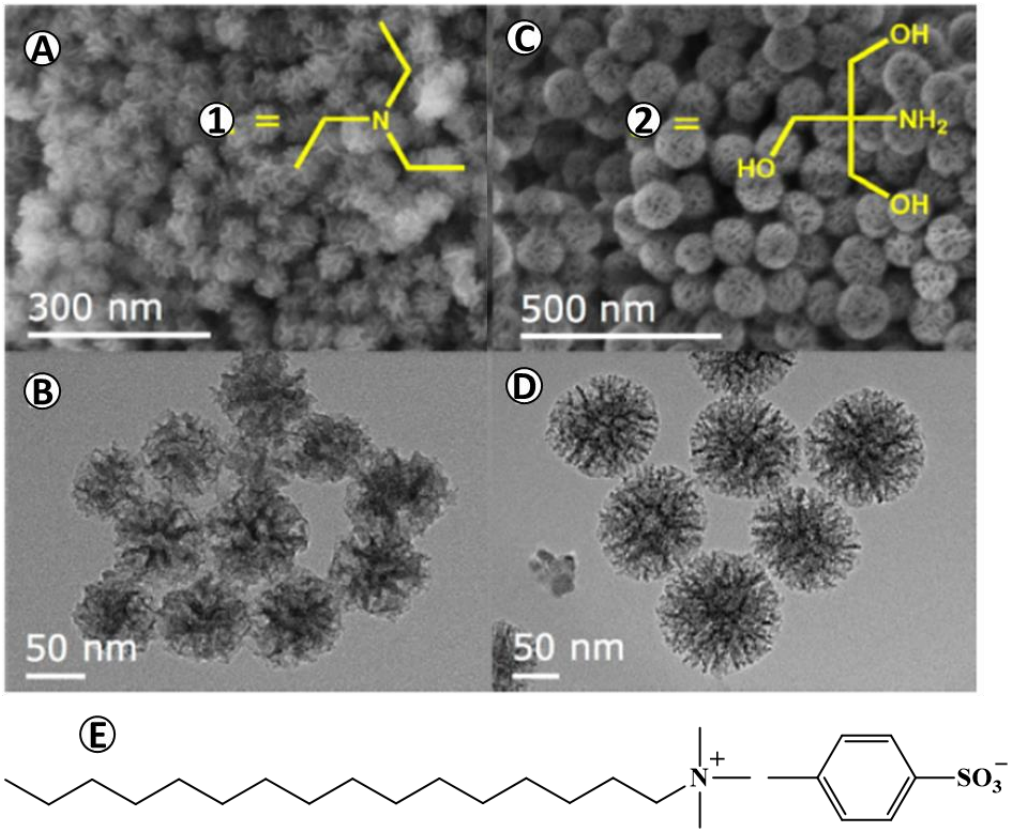

Figure 1.9: Particles formed by different amine catalysts (A and B triethylamine) (C and D 2-amino-2-(hydroxymethyl)propane-1,3-diol) at different magnifications[44] and using CTAT (E) as surfactant template.

Bein *et al*. developed a novel method to synthesize CMSNs, where triethanolamine was used as both catalyst and particle size control agent. Interactions between triethanolamine and alkoxysilanes were exploited to control the particle morphology. Triethanolamine when heated with alkoxysilanes resulted in formation of silatranes. These silantranes slowly dissociated in water to produce silica oligomers. The

oligomers condensed around the micelles to form silica nanoparticles. Using this process, mesoporous silica nanoparticles with uniform pore and particle size were produced.[32] Similarly Okuyama *et al*. used the basic amino acid lysine as the catalyst and particle size control agent. Lysine acquired a positive charge under basic conditions and interacted with the negatively charged silane monomers to restrict their growth. The mechanism used by the basic amino acid to control the particle size is similar to the one described earlier in section 1.1.1.[45]

1.2 Organosilica nanoparticles

Despite their interesting morphological properties such as monodisperse particle size, tunable pore size, high surface area and pore volume, the applications of silica nanoparticles would be greatly limited without organic functionalization. Organic functional groups aid dispersion and promote particle stability and are crucial for various applications of these particles[46] (see section 1.3). Organo-functionalization of silica nanoparticles can be achieved by grafting or co-condensation methods.

1.2.1 Grafting:

Grafting involves treatment of CMSNs with organoalkoxysilanes or organotrichlorosilanes in a non-polar anhydrous solvent. This is to ensure the functionalization of the particles and prevent condensation between the organoalkoxysilanes which is difficult to control. Grafting is not the favoured method for synthesizing organosilica nanoparticles because it results in inhomogeneous distribution of the organic groups on the particle surface. This is because the external surface and the outer pore walls of the CMSNs have greater kinetic accessibility compared to the inner surfaces.[43]

Several groups have developed strategies to improve the functionalization efficiency of grafting. Tsai *et al*. synthesized mercaptopropyl functionalized silica nanoparticles by grafting the mercaptopropyl silane onto as synthesized CMSNs with surfactant in their pores.[48] The presence of the surfactant in the pores restricts the access of the organosilane and helps limit the organic group functionalization to the surface. Other groups such as Yang *et al*. partially cleaved the surfactant pluronic P123 to expose the micropores and functionalize them.[49]

Despite these results grafting is severely restrictive in terms of the number of groups that can be attached to CMSNs. For example, the presence of organic groups at the pore entrances limits the diffusion of the additional organosilanes.[50] Therefore the co-condensation strategy is favoured to synthesize organically functionalized CMSNs (OCMSNs) with uniform distribution of organic groups.

1.2.2 Co-condensation

Bein *et al*. developed a novel strategy to selectively functionalize the outer and inner surfaces of the CMSNs by carefully timing the addition of organosilane 3-aminopropyltriethoxysilane (APTES) and TEOS mixtures. The reaction was carried out under basic conditions with triethanolamine as the base and cetyltrimethylammonium chloride (CTAC) as the surfactant. At the start of the reaction only TEOS was used as the silica source. TEOS and APTES mixtures were then carefully added after 5, 10 and 30 minute time intervals to functionalize the core, middle and the outer surface of the nanoparticles. (Figure 1.10)[51]

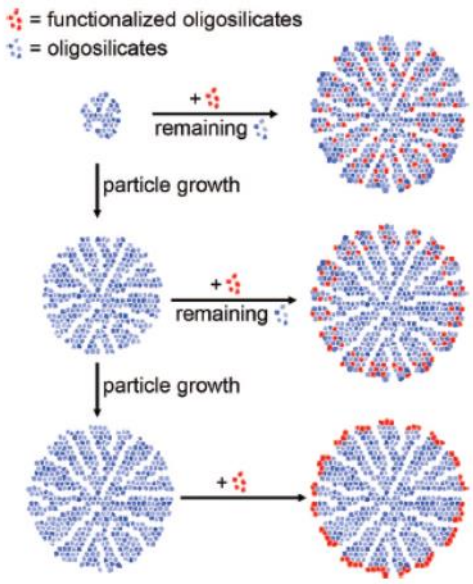

Figure 1.10: Selective functionalization strategy based on addition of organosilane at different time points (Figure from ref. 51).

The presence of the amine groups on the particles was confirmed by FTIR. The location of the amine was determined by measuring the zetapotential of the particles. The zeta potential of the unfunctionalized CMSs and particle functionalized after 5 minutes (APCMS 7) had similar zetapotential. However, the particles functionalized after 30 minutes (APCMS 9) showed a positive surface charge, indicating surface functionalization by the amines. Additional confirmation of the location of the amines was obtained by complexing iridium to the amine groups and determining its location by Z-scanning using scanning transmission electron microscopy (STEM). The STEM results showed that the amines in the sample examined after 30 minutes were almost completely located on the outer surface, while the sample examined after 10 minutes (APCMS 8) had amines located on the inner surface (Figure 11).[51]

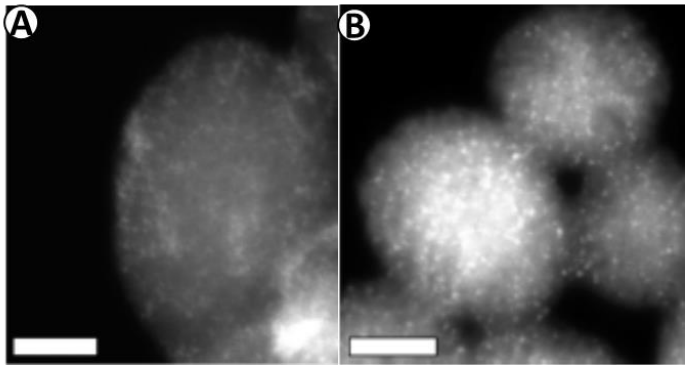

Figure 1.11: STEM images of iridium immobilized particles A) represents APCMS-9 (30 min); B) represents APCMS-8 (10 min).[51]

They extended this strategy to achieve functionalization of the inner and outer surfaces of the nanoparticles by adding different silanes at different times during the reaction. [52] A similar strategy was adopted by Zink *et al*. to attach phosphonate groups on the surface of silica nanoparticles.[53]

1.2.3 Morphology control of OCMSNs:

The studies performed by Bein *et al*. were carried out in the presence of a very small amount of organosilane (~2 mol %). At that quantity, the organosilane has very little influence on the particle morphology. However, for catalytic and drug delivery applications large quantities of organosilanes are required (> 10 mol %). At large concentrations, the interactions between the organosilanes and the monomers start to have a strong effect on the particle formation.[47] Lin *et al*. demonstrated that the surfactant organosilica interactions depended on the polarity of the organic groups. Non-polar organic groups helped stabilize the SST, while polar organic groups destabilized the SST. Stabilization of the template involved favourable interactions between the siloxane backbone and the hydrophobic surfactant tail. This resulted in an increase in the SST size and resulted in the formation of long cylindrical surfactant silica composite. The presence of non-polar groups thus resulted in the formation of rod particles. Polar molecules on the

other hand did not favourably interact with the hydrocarbon tail of the surfactants. Thus, the SST growth was limited and short spherical surfactant silica composites were produced.[54] In their study Lin *et al*. demonstrated that particles produced using hydrophilic groups such as *N*-(2-aminoethylamino)ethylaminopropyltrimethoxysilane (AEPTMS) and ureidopropyltrimethoxysilane (UDPTMS) resulted in the formation of spherical particles and when silanes with non-polar groups such as cyanopropyltriethoxysilane (CPTES) or allyltrimethoxysilane (ALTMS) were used, the resulting particles had rod shape (Figures 1.12 and 1.13). The authors also demonstrated that increasing the concentration of hydrophilic silane (AEPTMS) resulted in rod to sphere transition in nanoparticle shape.[54]

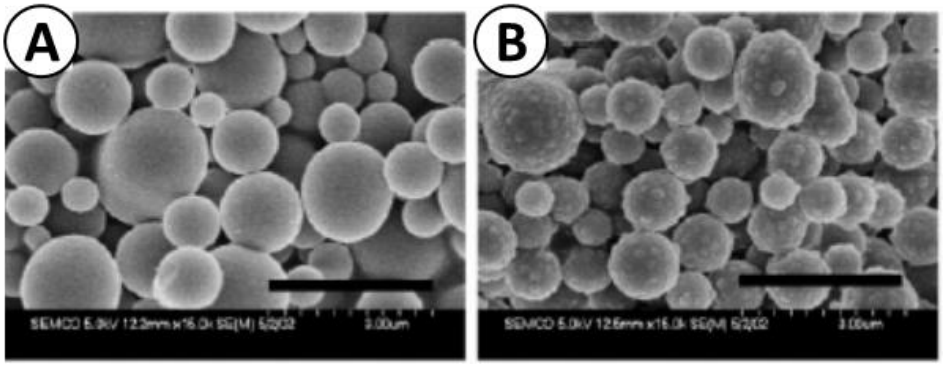

Figure 1.12: Organosilica particle synthesis using polar organic groups A) AEPTMS and B) UDPTMS (Scale 3000 nm).[54]

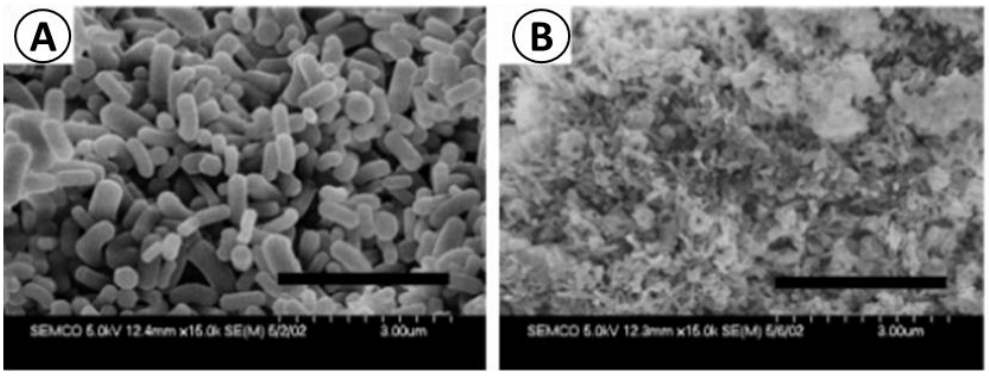

Figure 1.13: Organosilica particle synthesis using non-polar organic groups A) CPTES and B) ALTMS (Scale 3000 nm).[54]

In addition to this, when mixtures of hydrophilic and hydrophobic groups were used, then the final particle morphology of the particles was determined by the silane that apparently had the stronger structure directing effect. When, AEPTMS was mixed with CPTES, the resulting particles all had spherical particle morphology. Varying the ratios of the organosilanes did not have an effect on the shape of the particles, indicating that AEPTMS had the stronger structure directing effect of the two. The porosity of the particles, however was affected. Particles made from non-polar silanes had a regular honeycomb pore structure.[55] An increase in the concentration of the polar groups resulted in the formation of the particles with greater distortion in pore structure.

1.3 Applications of CMSNs

Mesoporous silica nanoparticles have numerous applications ranging from drug delivery to catalysis. The following section describes some of the recent applications of these materials. Scheme 1.6 illustrates the timeline of the development of biomedical applications of silica nanoparticles.

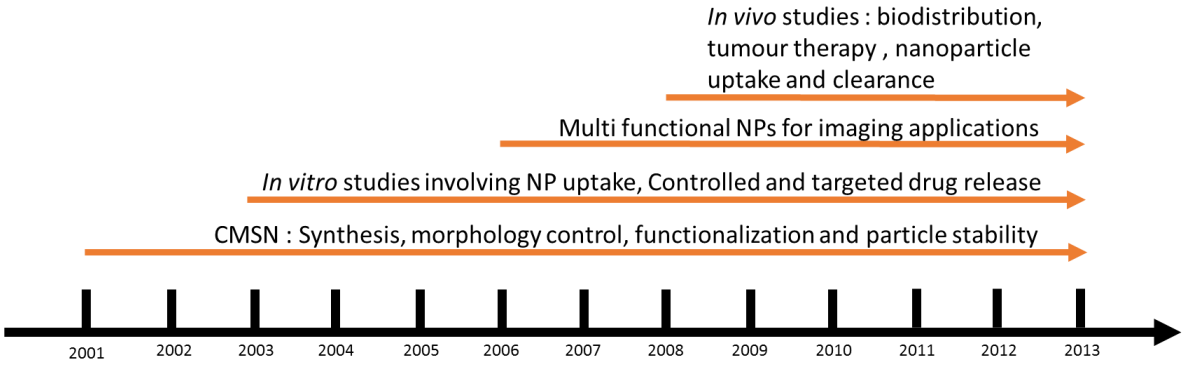

Scheme 1.6: Schematic representation of development of CMSNs for biomedical applications (adapted from ref 56)

1.3.1 Drug delivery

Until the early 2000s much of the focus involving systems for controlled delivery of drug molecules was focussed on polymers. These systems however, have many disadvantages. Most polymeric nanoparticles involved in controlled release applications, use hydrolysis induced erosion of the polymeric structure, and this could lead to premature release of the guest molecules.[52] Polyesters such as PLGA (poly lactic co-glycolic acid) are widely used for drug delivery applications.[56b] Nano/microparticles made from these polymers release acid molecules upon degradation, which can denature the protein molecules.[56c] In contrast, silica nanoparticles represent a robust drug delivery system. CMSNs, have a biocompatible silica framework.[52] The silica framework is stable under physiological conditions and does not have an antigenic effect. The particle properties such as particle size, pore size, pore volume and surface functionality can be optimised for different drug delivery applications.

Section 1.1.2 listed a few properties of silica materials that make them excellent materials for drug delivery applications. The following section discusses some of the properties of drug delivery platforms and how the properties of CMSNs can be modified to improve their properties as drug delivery systems.

1. **Stable and bio compatible framework**: Silica nanoparticles have a biocompatible framework.[56a] The main challenge involved in the use of CMSNs for *in vivo* drug delivery applications is their poor dispersibility and stability in biological media. Bein *et al*. demonstrated that silica nanoparticles dispersed in SBF (simulated body fluid) undergo morphological changes.[57] Lin *et al*. developed dual functionalized mesoporous silica nanoparticles with hydrophobic groups (methyl from trimethyl chlorosilane (TMS) or trifluoropropyl from 3,3,3-trifluoropropyldimethylchlorosilane (TFS)) and hydrophilic groups (poly

ethyleneglycol (PEG) from PEG-silane) as surface modifiers to improve the long term dispersion stability of the nanoparticles. The attachment of hydrophilic silane helped improve the dispersion stability of the particles and the presence of the hydrophobic silane reduced the silica dissolution.[58] Dispersions of the dual functionalized nanoparticles were stable in PBS (phosphate buffer saline), SBF (simulated body fluid) and DMEM (Dulbecco's Modified Eagle Medium) for 15 days (Figure 1.14).

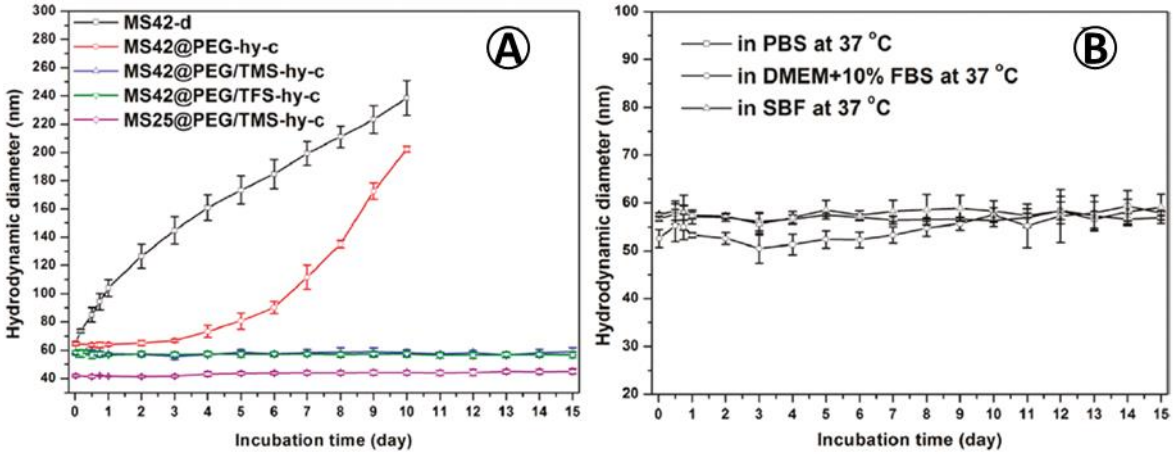

Figure 1.14: Hydrodynamic radius versus time in A)PBS and B) Various media (sample MS25@PEG/TMS-hy-c), of surface functionalized nanoparticles (*hy* stands for hydrothermal treatment).[58]

2. **Drug uptake**: Commonly used drug delivery systems such as polymers typically have low surface areas and this limits their ability to take up large quantities of drug molecules.[59] Liu *et al*. recently developed a mesoporous silica nanosphere based drug delivery system, whose surface area can be varied by varying the ratio of surfactants (FC4 and Pluronic F127) used in the synthesis. FC4 is a fluorocarbon surfactant and is known to form vesicles, while pluronic F127 is a block co-polymer surfactant, consisting of polyethylene glycol and polypropylene glycol. They demonstrated that the particle surface area had a high impact on the uptake of the hydrophobic drug ibuprofen. Drug loads up to 448 mg g^{-1} were

achieved and the particles were shown to release the drug for 24 hours under physiological conditions.[60] The process of loading drugs in polymers often requires the use of organic solvents.[59] This limits the application of polymer particles solely for the delivery of small organic molecules. Biomolecules such as proteins and DNA undergo denaturation in presence of organic solvents. CMSNs can take up molecules from both aqueous and organic solvents and therefore represent a robust drug delivery platform.

3. **Controlled drug release**: Drug release from many polymers (such as polylactic glycolic acid (PLGA)) has typically involved erosion of the polymer matrix and this causes difficulties in controlling the rate of drug release and also in premature release of the drug molecules.[59] The rate at which the guest molecules are released from CMSNs depends on the pore size of the nanoparticles. By adjusting the pore size of the nanoparticles the rate of drug delivery can be altered.[61] Gao *et al*. synthesized mesoporous silica nanoparticles with varying pore size (3.6, 7.2 and 12.6 nm) (Figure 1.15) and used these nanoparticles to deliver doxorubicin, a hydrophobic anticancer drug, to MCF-7 breast cancer cells. The study showed that the large pore particles (12.6 nm) demonstrated enhanced cell uptake (Figure 1.16a) and higher cell mortality compared to small pore nanoparticles or treatment with free doxorubicin (Figure 1.16).[62] The authors suggested that the higher rate of cancer cell mortality was due to increased particle uptake and higher rate of drug delivery by large pore size particles (Scheme 1.7). In addition to controlling drug release by tuning the pore sizes of the particles, drug release can be controlled by using a variety of methods such as use of rotaxane nanovalves[63], or nanoparticle [64] and enzyme responsive caps.[65]

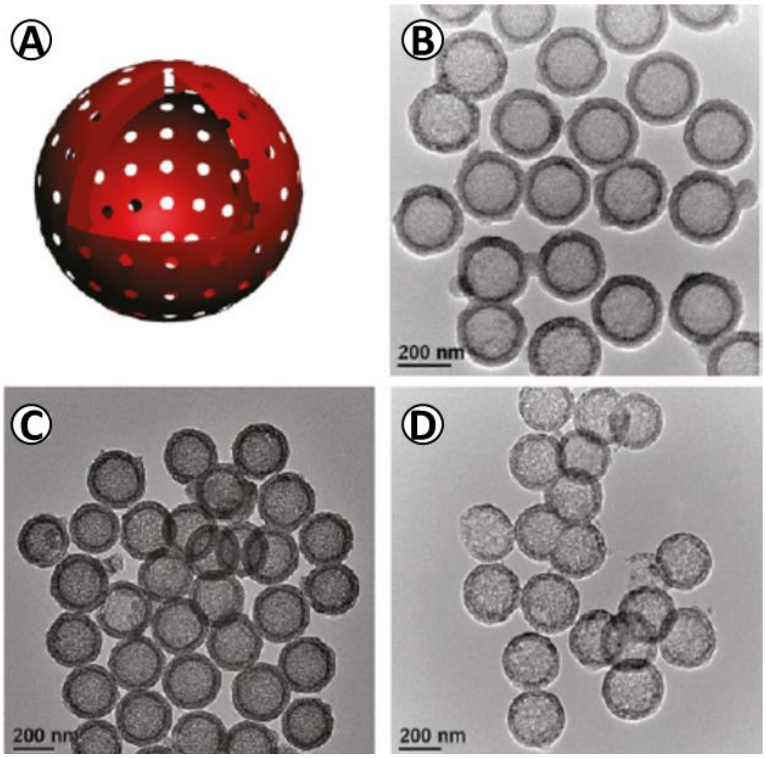

Figure 1.15: Mesoporous silica nanoparticles with different pore sizes (A) Schematic representation of particle morphology (B) Particles with 3.2 nm pores (HMSN-1) (C) Particles with 6.4 nm pores (HMSN-2) (D) Particles with 12.6 nm pores (HMSN-3) (Scale 200 nm).[62]

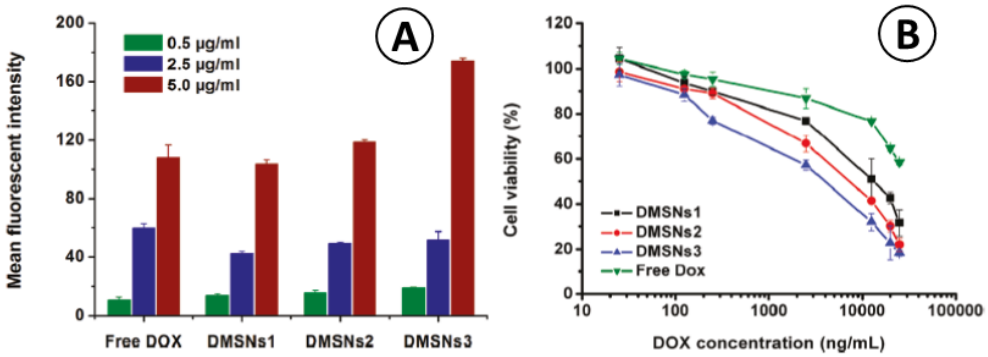

Figure 1.16: Variation in the uptake of nanoparticles by MCF-7 cells. Free dox = free doxorubicin; DMSNs1 = 3.2 nm pore sized particle; DMSNs2 = 6.4 nm pore sized particle and DMSNs3 = 12.6 nm. (A) Measurement of nanoparticle uptake by the cells (using Fluorescence-activated cell sorting (FACS)) and cell viability after doxorubicin treatment (using MTT assay).[62]

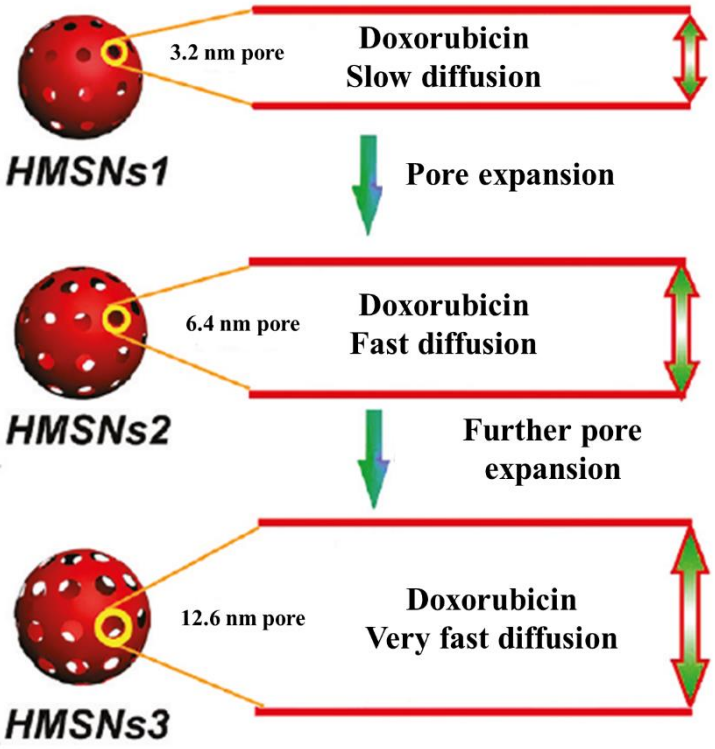

Scheme 1.7: Effect of pore size on the delivery of doxorubicin (Scheme modified from ref 62).

4. **Targeted drug release**: The surface of the silica nanoparticles can be modified by reacting the surface silanols with a variety of organosilanes. This helps in changing the surface properties of the mesoporous nanoparticles. It can be used to attach groups to achieve targeted delivery to cancer cells. He *et al*. synthesized carboxylic acid functionalized mesoporous silica nanoparticles (COOH_MSNs) (Figure 1.17) to carry the anti-cancer drug doxorubicin to the leukaemia cell line, CEM (Scheme 1.8). In order to specifically target the cancer cells an aptamer *Sgc8c*, that binds to the protein tyrosine kinase 7 (*PTK7)* which is highly expressed in CEM cells,[66a] was attached to the particle surface by the EDC/NH_2 coupling method. (Note: aptamers are oligonucleotide or small peptide molecules that bind to specific target molecules on the cell surface and *Sgc8c* is a DNA aptamer). This study demonstrated that the nanoparticles specifically inhibited the

growth of the CEM cell line, while another cell line, Ramos, for which the aptamer has no affinity, was not inhibited.[66b]

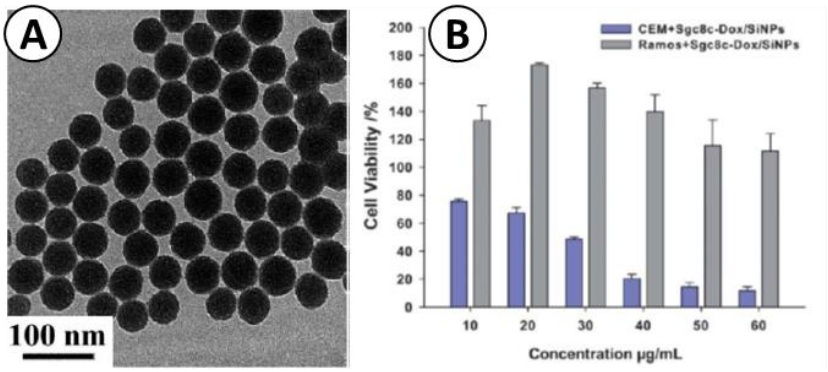

Figure 1.17: (A) TEM image of COOH_MSNs; (B) Cell viability studies performed on CEM cells and Ramos cell line, showing strong reduction in viability of CEM cells.[66a]

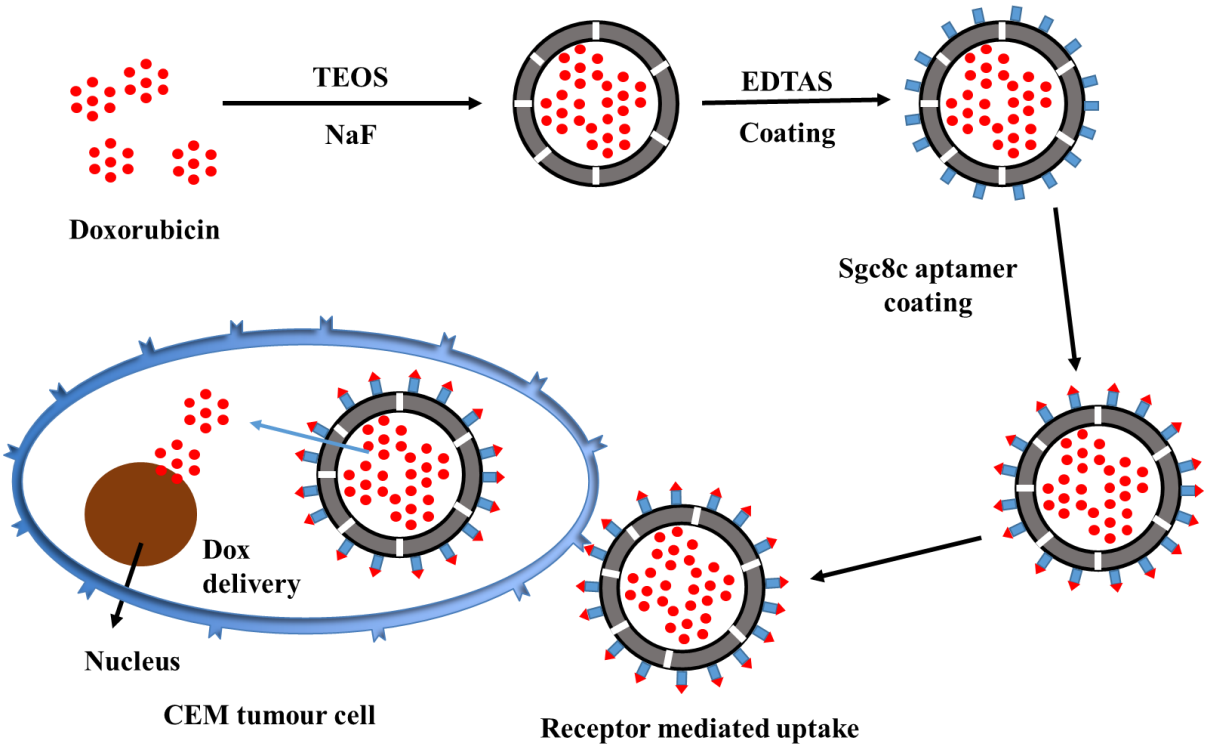

Scheme 1.8: Synthesis and targeted delivery of *Sgc8c* tagged particles.[66a]

1.3.2 Biosensors and biomarkers:

In addition to the applications in the area of drug delivery, mesoporous silica nanoparticles can be used for detection of small molecules and also for tracking cells.

Detection of analytes such as hydrogen peroxide often involve the use of enzymes.[67] However, enzymes are prone to denaturation and this limits their applications.[52] Mesoporous silica nanoparticles have a stable framework that is stable in presence of aqueous and organic solvents and it is therefore advantageous to use them.[52] Additionally, the particles have a large surface area and pore size which can be used to immobilize large quantities of sensing molecules, improving the sensitivity of the system. Mesoporous silica materials are optically transparent and this enables detection of analytes through the layers of material.[52]

Lin *et al*. synthesised *o*-phthalic hemithioacetal functionalized mesoporous silica material as a detector for primary amines. In order to improve the selectivity of the system, various organic groups such as propyl, phenyl and pentafluorophenyl were introduced. In this way selectivity was achieved for dopamine, which has aromatic groups, over glycosamine which does not. Through this work a viable strategy was demonstrated for improving the selectivity of mesoporous silicas through non covalent interactions.[68] A method to improve the selectivity of the system was demonstrated by installing gate keeper molecules at the pore openings. Polylactic acid was used as the gatekeeper (Figure 1.18). The aim of the study was to selectively identify the neurotransmitter dopamine in the presence of glutamic acid or tyrosine. The study was carried out under physiological conditions (pH 7.4). Under these conditions, the material has a negative surface charge due to the polylactic acid groups (pI < 3.0). Tyrosine and glutamic acid have isoelectric points below 7.4 and are therefore negatively charged under the experimental conditions. Thus the particles did not take up these compounds. However, dopamine which has an isolectric point of 9.7, acquires a positive charge a pH 7.4 and is taken up by the particles and is selectively detected (Scheme 1.9).[69] Yu *et al.* recently improved the specificity of this system by using *o*-pthalic hemithioacetal

modified cyclodextrin instead of polylactic acid. Cyclodextrin has a hydrophobic cavity and a hydrophilic rim. This system enabled the group to selectively identify dopamine with a detection limit of 50 nM in presence of physiological fluids.[68]

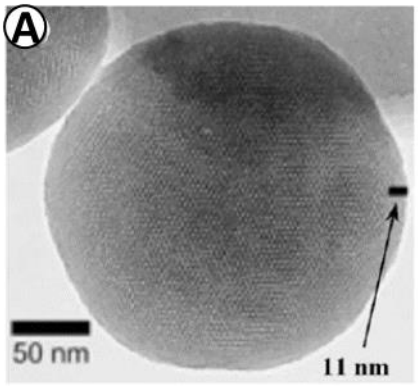

Figure 18: TEM image of poly-lactic acid coated mesoporous silica nanoparticle based sensor. The outer layer (11 nm) indicates the poly lactic acid layer.[68]

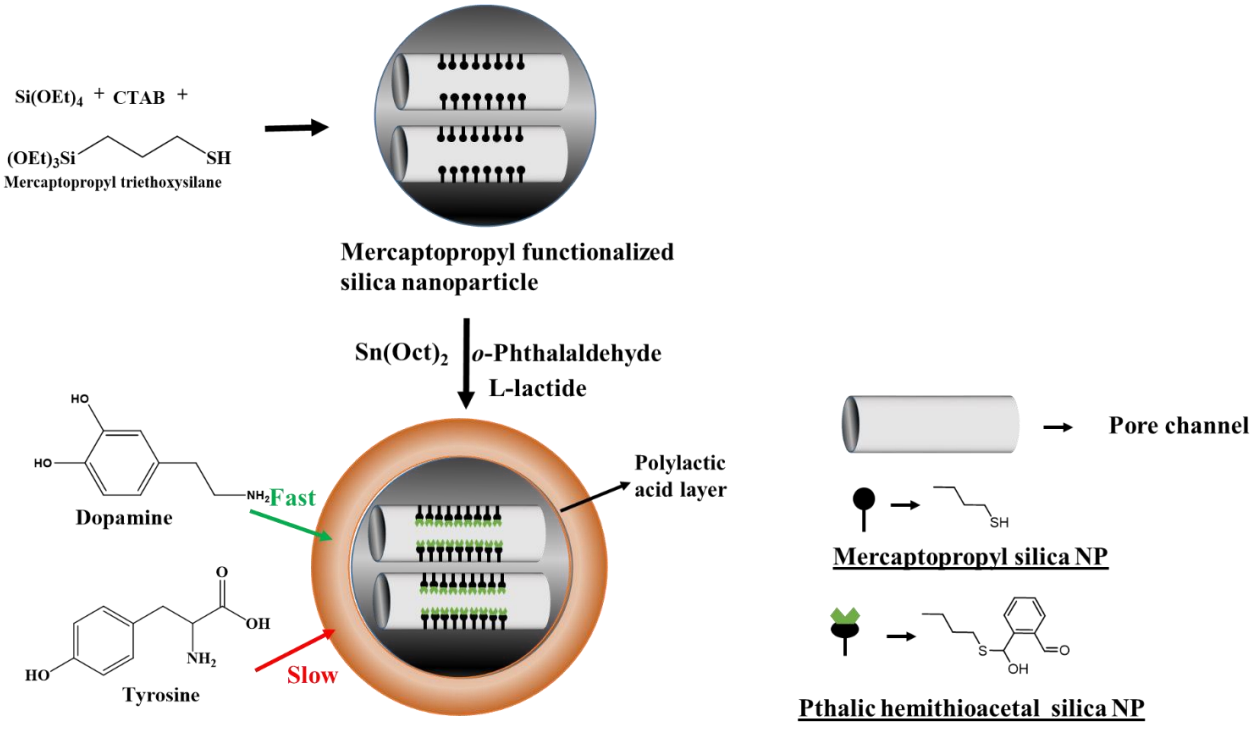

Scheme 1.9a: Synthesis of dopamine sensor based on poly-lactic acid functionalized mesoporous silica nanoparticles (RNH_2 is dopamine).(Adapted from ref 68).

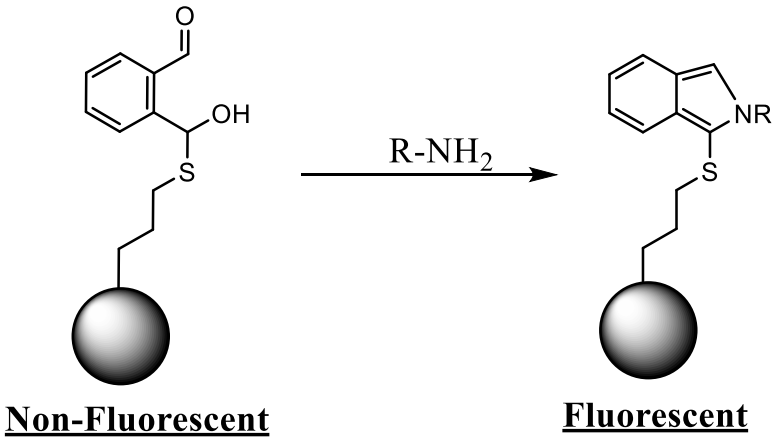

Scheme 1.9b: Mode of action of dopamine sensor

The principle of attaching functional groups that respond to specific stimuli can be extended to applications such as tracking specific cell organelles. Han *et al*. developed a dye based detection system that is sensitive to pH changes. Mesoporous silica nanoparticles with the dyes fluorescein and rhodamine 6G-lactam attached to their surface were synthesised. The dyes exhibited an increase in fluorescence intensity as a function of pH. Rhodamine 6G-lactam exhibited this under acidic conditions and fluorescein under basic conditions. By controlling the ratio of these dyes, the authors prepared a material that showed increased fluorescence intensity in the pH range of 3.5 to 6.0, which is the pH range of the lysosomes. Cell studies revealed that the particles were readily internalized and accumulated in the lysosomes. When the lysosome pH was increased using bafilomycin A1, an ATP–H1 inhibitor, the fluorescence of the Rhodamine 6G-lactam was reduced.[71]

1.3.3 Catalysis:

Organosilica nanoparticles can function as excellent catalysts in part because of their high surface area and porosity. In addition to these properties however, the particles can be functionalized by a variety of organic groups to improve the selectivity

and range of catalytic applications. Lin *et al*. provided one of the first examples of silica nanoparticles as catalysts with the catalyst 3-[2-(2-aminoethylamino)ethylamino]propyl (AEP) functionalized nanoparticles for nitradiol condensation (Scheme 1.10).[60] The selectivity of the reaction was improved by attaching hydrophobic groups such as ureidopropyl (UDP), allyl (AL) or mercaptopropyl (MP) groups. [72]

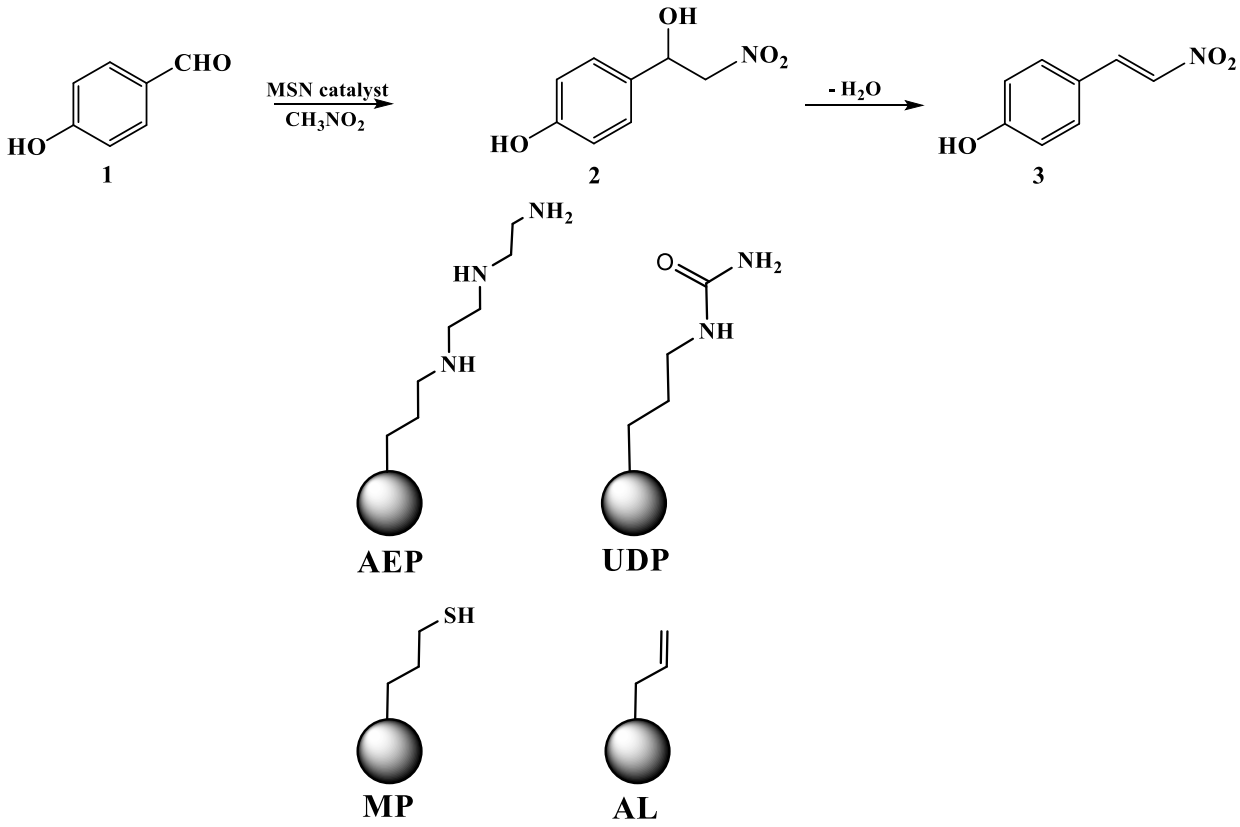

Scheme 1.10: Nitradiol condensation by AEP functionalized silica nanoparticles.(Adapted from ref 71)

Similarly, alkylpyridinium group functionalized nanoparticles were used as highly efficient catalysts in several nucleophilic substitution reactions such as Baylis-Hillman, acylation, and silylation.[73] Mesoporous silica nanoparticles were also used to entrap metal nanoparticles such as magnetite and gold nanoparticles. Ge *et al*. developed a mesoporous silica nanoparticle system to immobilize gold and magnetite nanoparticles. Gold nanoparticles catalysed the hydrogenation of 4-nitrophenol by sodium borohydride

and magnetite nanoparticles helped separate the particles. The role of the porous silica matrix is to protect the metal and metal oxide nanoparticles and the pores in the silica matrix promote efficient catalysis.[74]

The particles can also be used to immobilize large quantities of enzymes such as lipase[75], lactase[76], and chymotrypsin.[77] The studies showed that immobilization of the protein on these particles helped improve their stability against pH and temperature inactivation.[76, 77]

1.4 Characterization of CMSNs

In this section the analytical tools used for the characterisation of the materials, chemistry and biology described in this thesis are briefly described.

1.4.1 Molecular spectroscopy:

Molecular spectroscopy is based on the adsorption of energy by molecules and examining the response of the molecules to that adsorption of energy. Depending on the nature of the absorption energy this can result in specific changes in the molecule from the ground state E_1 to an excited state E_2. The difference in energy between these states $E_2 - E_1 = \Delta E$. In infrared spectroscopy these energies correspond to two different vibrational states; in UV-Vis spectroscopy they correspond to two different electronic states and in NMR (nuclear magnetic resonance) spectroscopy they correspond to two different nuclear spin states.[78]

Spectrometers are used to measure the absorption of electromagnetic radiation by the molecules. The simplest setup of a spectrometer consists of a radiation source, a sample chamber, an amplifier and a detector (Scheme 1.11). The frequency of the radiation is continuously varied and the changes in the intensity of the radiation as it

passes through the sample is measured. The relation between frequency and absorption is plotted and this is known as the spectrum. The interpretation of the spectrum provides structural information.[78]

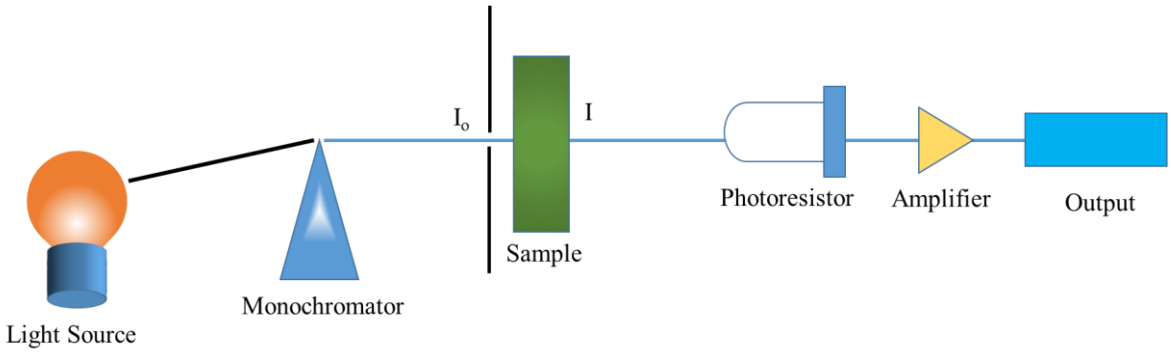

Scheme 1.11: Basic spectrophotometer design.

1.4.1.1 Infrared spectroscopy:

Infrared radiation has wavelengths between 10^{-4} to 10^{-6} m. The part of the spectrum that lies between 2.5×10^{-6} to 16×10^{-6} m is most used for structural determination. The most commonly used unit in IR is wave number (cm^{-1}). The region between 2.5×10^{-6} to 16×10^{-6} m corresponds to wave numbers 4000 to 600 cm^{-1}. When a molecule absorbs a photon from the infrared region, it excites the molecule from its ground vibrational state to a higher vibrational state. The vibrations include stretching and bending modes.[78] IR vibrational regions for organic groups are given in Scheme 1.12. In addition to this, silica nanoparticles exhibit a characteristic peak between 900 – 1200 cm^{-1} corresponding to silicon-oxygen stretching.[79] Infrared spectroscopy can therefore be used for the identification of various organic groups on silica nanoparticles.[80] In this work IR was used for compound characterisation. For example it was used to confirm the removal of the CTAB, which was determined by the disappearance of the characteristic ammonium peak at 2900 cm^{-1}.[33] In addition to this IR was also used to confirm the presence of protein adsorption on silica nanoparticles. This was determined by the presence of amide I and amide II peaks at 1400 and 1600 cm^{-1} respectively.

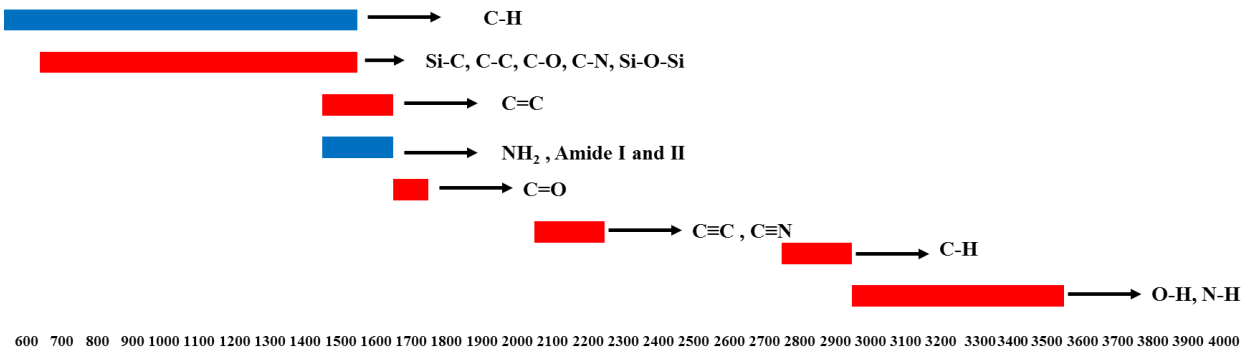

Scheme 1.12: IR frequencies of various organic groups. (Adapted from ref 81)

1.4.1.2 UV-Vis spectroscopy:

When white light is passed through a sample it absorbs a characteristic portion of the light and the transmitted light assumes the colour complementary to the wavelengths absorbed. In UV-Vis spectroscopy, light between the wavelengths of 200 to 800 nm is used. The energy of the radiation in the visible region (800 to 400 nm) ranges from 150 to 300 kJ/mol, while the energy of the UV radiation (400 to 200 nm) ranges from 300 to 600 kJ/mol. When molecules are irradiated with this radiation they undergo a change in their electronic structure. This occurs because absorption of energy by a ground state molecular orbital electron promotes it to a higher energy molecular orbital. Molecules absorb radiation that has the energy to match a possible electronic transfer within the molecule. A UV-Vis spectrophotometer records the wavelengths at which the absorption occurs. The absorbance by the sample is proportional to the number of molecules present. Therefore, UV-Vis spectroscopy can be used to calculate the concentration of various organic molecules that absorb within this region.[82] In this work it was primarily used to measure the protein uptake by silica nanoparticles.

1.4.1.3 Solid State NMR

Subatomic particles such as protons, neutrons and electrons can be imagined as spinning on an axis. The spin of these particles exists in two states $^1/_2$ or - $^1/_2$ In the nuclei the spins of the nucleons are paired with each other. Therefore when even numbers of protons and neutrons are present the overall nuclear spin I is zero. When and the number of neutrons plus the number of protons is odd then the nuclei have an overall half integer spin ($^1/_2$, $^3/_2$, $^5/_2$) etc. and when odd number protons and odd number neutrons are present, it results in integer spin (1, 2, 3 etc.). A spinning charged particle produces a magnetic field. Nuclei possessing an overall spin have $2I+1$ orientations. In the absence of a magnetic field the magnetic nuclei have random orientation. However, in the presence of a magnetic field, the nuclei orient either parallel or anti-parallel to the magnetic field. The nuclei that are oriented parallel to the magnetic field have a slightly lower energy than the nuclei that have an anti-parallel orientation. Therefore, the nuclei with parallel orientation have a slightly greater number. When the oriented nuclei are irradiated with electromagnetic radiation of specific frequency, energy absorption occurs and the "spin-flips". The magnetic nuclei are then said to be in resonance with the applied radiation. The energies of the radiation applied to the magnetized samples is quite small (about 2.4×10^{-5} kJ/mol), and corresponds to the radio frequency.[83, 84]

The magnetic field experienced by the nucleus depends on the location of the nucleus within the molecule. This is because, every nucleus is surrounded by electrons and the electrons shield the nuclei from the magnetic field, thus the spatial proximity of two nuclei changes their interactions with the external magnetic field, the interactions are also dependent on the orientation of the molecules. Thus, NMR provides a "map" of the nuclei of interest.[83] When NMR is carried out on a liquid where the molecules undergo Brownian motion, this averages out anisotropic interactions.[85] However, NMR carried

out on solids display very broad peaks due to these anisotropic interactions. The anisotropic interactions can be suppressed by spinning the solid sample oriented at 54.74°, also known as "magic angle". Thus, it is possible to obtain NMR spectra of solid samples.[86]

In this work we used solid state ^{29}Si and ^{31}P NMR to determine the organic group loading and surface coverage of organic molecules. ^{29}Si is the only naturally occurring magnetic isotope of silicon.[86] It has a natural abundance of 4.7%, a spin of $^1/_2$ and a magnetic moment of -0.5548 (Nm/T). Inorganic silica species show peaks (Quadrafunctional $Si(OR)_4$, Q sites) between -110 and -90 ppm, while organosilica species show peaks (Trifunctional $RSi(OR)_3$, T) between -68 and – 58 ppm.[88] The resonances of the silicon atoms bonded to organic groups may be split due to coupling with protons but this is prevented by performing decoupling.[87,89] For quantitative analysis DPMAS (Direct Polarization Magic Angle Spin) spectra were acquired.[88] Phosphorus NMR was also obtained to demonstrate the presence of phosphorus in the particles. ^{31}P has a low gyromagnetic ratio (108.291), compared to ^{1}H (267.513), which results in a smaller signal. In order to enhance the signal CPMAS (Cross Polarized Magic Angle Spin) was performed. In this process the signal is enhanced by magnetization transfer from protons. Use of CPMAS, however can result in different signals no longer having quantitative intensity relationships.[90]

1.4.1.4 Circular Dichroism

Samples containing chiral chromophore molecules absorb either right polarized light (RCP) or left polarized light (LCP). Circular dichroism (CD) is the difference in the absorbance of the (LCP) light and absorbance of (RCP). Far-UV circular dichroism

corresponds to the peptide bond absorption and it provides useful information about the secondary structure of proteins. The secondary structure of proteins consists of three conformations; α-helix, β-sheet and open chain. When a protein is denatured, its α-helices are converted into β-sheet and open chain structures. CD provides an estimate of these conformations.[91]

The CD spectrometer consists of a light source which produces unpolarised light. The unpolarised light is converted into linear polarized light by a monochromator. The linear polarized light is converted into circular polarized light by a photoelastic modulator (PEM). CD spectra of the sample is obtained because there is some switching of the polarization of the light incident on the sample. Circular dichroism is measured by calculating the difference in absorption of LCP or RCP (Scheme 7).[92] In this work circular dichroism was used to determine whether denaturing of BSA had occurred following adsorption to phosphonate silica nanoparticles.

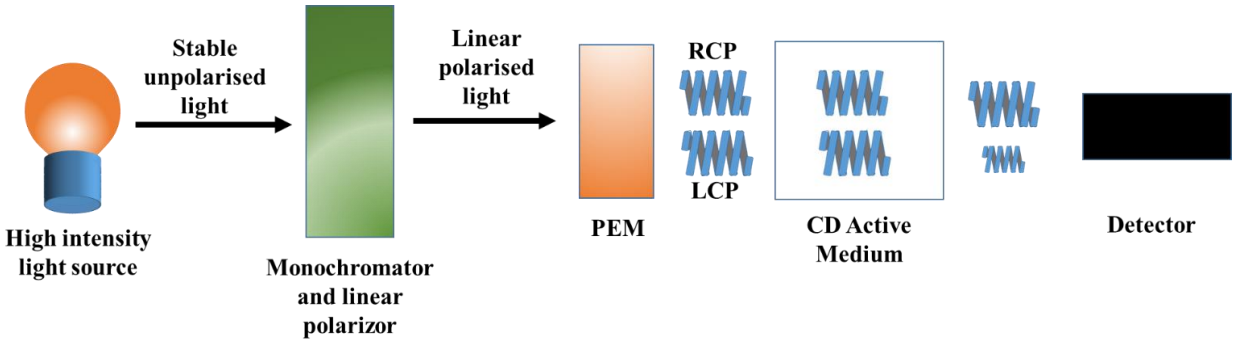

Scheme 1.13: Schematic representation of circular dichroism

1.4.2 Thermogravimetric Analysis

Thermogravimetric analysis (TGA) is a technique that measures the sample weight loss or gain as a function of the temperature. It provides information about the

various organic groups present in a sample. Weight loss or gain can occur due to decomposition, oxidation, reduction, dehydration or vaporization of the sample. TGA consists of a sample pan loaded onto a precision balance. This setup is placed in a furnace and the temperature of the sample is raised at a controlled rate. The balance records the changes in the sample mass as a function of temperature. The sample environment can be changed by changing the sample purge gas.[93] In this work TGA was used to assess stability of phosphonate functionalized nanoparticles.

1.4.3 Electron Microscopy

The general principle of microscopy involves magnification of small objects by using lenses. In an electron microscope, electrons are used instead of light waves and the electrons are focussed onto the surface of an object by using magnetic lenses. There are two main methods of electron microscopy

1. Scanning Electron Microscope (SEM)
2. Transmission Electron Microscope (TEM)

1.4.3.1 Scanning Electron Microscope (SEM)

The SEM is an excellent tool for imaging nanoparticle surfaces. The SEM consists of an electron source, which is usually a tungsten filament. The electrons produced from the source are focussed on the sample through the condenser, which controls the size of the beam and the objective lens, which focuses the beam. When the electrons strike the surface of the sample, they collide with the atoms on the surface and produce secondary electrons. These are low energy electrons and they are passed through a detector, the detector has a positive potential and it therefore attracts the secondary electrons. The data from these electrons is then passed to a scan generator, which produces the final image (Scheme 1.14). SEM produces images that have light and dark regions and it is therefore

useful in studying the topology of the sample. SEM needs conductive samples, non-conductive samples like silica nanoparticles are usually coated with gold before imaging them.[94] In this work SEM was used to measure the particle size, to study the elemental composition using EDX (energy dispersive X-ray spectroscopy) and to study the particle morphology.

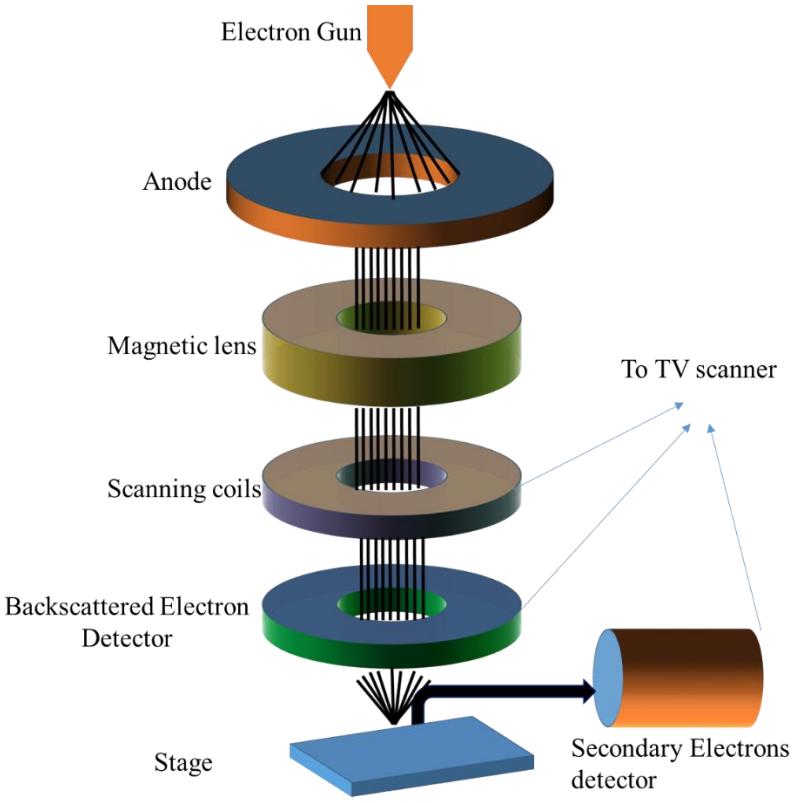

Scheme 1.14: Scanning Electron Microscope (Adapted from ref 94)

1.4.3.2 Transmission electron Microscope (TEM)

In a TEM the electrons pass through the sample. It is therefore useful for imaging the internal features of the particles such as pore channels. The sample to be used for imaging is deposited on a thin electron grid, which is either made of copper or electron transparent plastic. The sample thickness must be less than 500 nm to image the sample. The electron beams pass through the sample. The electrons that strike the specimen are scattered, while the unscattered electrons pass through the sample and hit a phosphor screen, which results in image production (Scheme 1.15).[95] In this study TEM was used

to study the particle morphology and also to study the uptake of nanoparticles by HeLa cells.

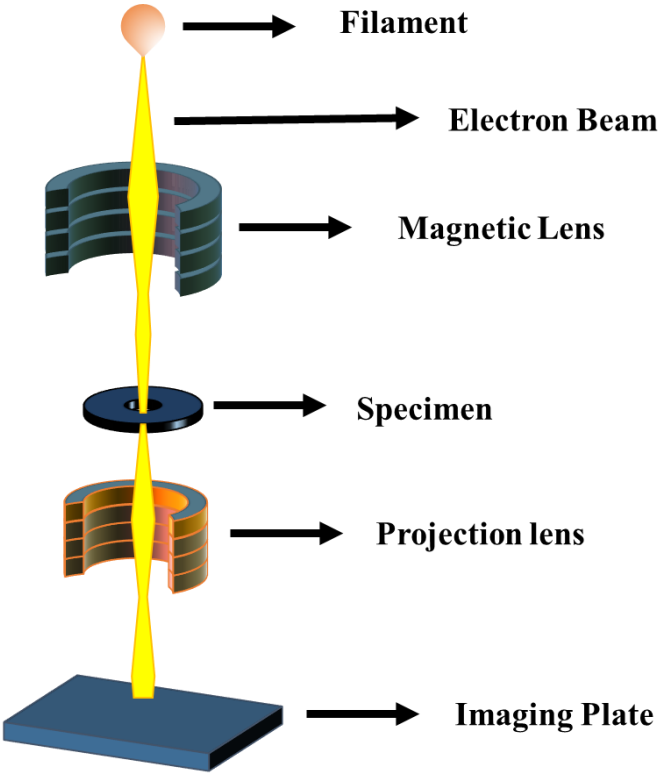

Scheme 1.15: Transmission Electron Microscope (Adapted from ref 95)

1.4.4 Dynamic Light Scattering (DLS)

Dynamic light scattering is used for measuring the particle size of nanoparticles dispersed in a solvent. DLS determines the hydrodynamic radius of the particles. The value of the hydrodynamic radius depends on the solvent used. For example, the ionic strength of the media affects the hydrodynamic radii of the particles. DLS can also be used to monitor the stability of the particles in the dispersion media.[56] The general principle of DLS is as follows. Dispersed nanoparticles scatter light. This results in the formation of a speckle pattern. A speckle pattern consists of bright and dark spots. The bright spots are the regions where the light undergoes constructive interference and the dark spots are regions where light undergoes destructive interference. A DLS instrument

contains a device known as photon correlator, which measures the changes in this pattern. The parameter Γ, is measured during the experiment according to the following formula.

$$\Gamma = Dq^2$$

D = translational diffusion coefficient

$$q = (4\pi n)\lambda_o \sin\left(\frac{\theta}{2}\right)$$-----Equation 2

Where n = refractive index of the medium

λ_o = Wavelength of the laser

θ = scattering angle

Different measurements of Γ are performed at different scattering angles and the final particle size (hydrodynamic radius) R_H is calculated (Equation 3)[96] In this study DLS was used to determine the hydrodynamic radius of the particles and to determine the stability of particle dispersions.

$$R_H = kT^2q^2/3\pi\eta D$$-----Equation 3

Where η = viscosity of the medium and T = temperature.

1.4.5 Porosimetry

Nitrogen adsorption porosimetry is used to measure the surface area and pore size of nanoparticles. The sample is degassed under vacuum to remove any surface contamination and exposed to nitrogen at cryogenic temperatures. In practice the sample is inserted into liquid nitrogen and known aliquots of nitrogen are introduced. The quantity adsorbed and equilibrium pressure is measured. Desorption of the adsorbed

nitrogen gas is then measured in similar sequential steps. The result gives nitrogen adsorption-desorption isotherms for the material. The data from the isotherm can be used to measure the surface area according to BET theory and pore size using BJH theory.[97]

1.4.5.1 Surface area:

BET theory was proposed by Braunner, Emmett and Teller to determine the surface areas of solids. The surface area measurements are performed between relative pressures of 0.05 and 0.3. First, the volume of the monolayer of the gas adsorbed on the particle surface is determined using the equation 4.[98]

$$\frac{1}{v(p_o - p)} = \frac{1}{v_m c} + \frac{(c-1)p}{v_m c p_o}$$-----Equation 4

Where v = volume adsorbed

v_m = volume of monolayer

p = equilibrium pressure above the sample after adsorption

p_o = saturation pressure

c = constant related to enthalpy of adsorption

The specific surface area of the sample is determined using Equation 5

$$S_{BET} = v_m n_a a_m / m v_l$$---Equation 5

n_a = Avogadro's constant

a_m = cross sectional area occupied by nitrogen molecule (0.162 nm^2)

v_l = molar volume of nitrogen (22414 cm^3)

m = mass of the sample.[98]

1.4.5.2 BJH pore size

Depending on the pore size, pores are classified into

1. Micropore : Pore size less than 2 nm
2. Mesopores : Pore size between 2 to 50 nm.
3. Macropores : Pore size greater than 50 nm.[99]

The pore radius is determined from the Kelvin equation (Equation 6). The BJH model assumes that the pores have a cylindrical shape.

$$\ln\left(\frac{p}{p_o}\right) = \left(-\frac{2\gamma V_L}{rRT}\right) cos\theta$$

p = equilibrium vapour pressure

p_o = saturation pressure

γ = surface tension of the liquid

R = gas constant

r = pore radius

θ = contact angle

V_L = molar volume of the liquid.[100]

1.5 Aims of work in this Thesis

Reports in the literature discussed above on OCMSNs pointed to the advantages in terms of dispersability and drug vehicle efficiency that organofunctionalisation could confer of these systems. However there remained great scope for improvement of these

properties as well as a need for better particle size uniformity and access to larger pore particles. As mentioned earlier, nanoparticles for drug delivery applications should possess five characteristics. a) small size (below 200 nm), stable, biocompatible composition and excellent dispersion properties that would allow the particles to remain dispersed in the blood stream; b) ability to host a variety of guest molecules like drugs, proteins; DNA etc.; c) zero premature release; d) the ability to accommodate different functionalities that would allow it to target specific receptors and finally, e) controlled release at the target site. The Sullivan group had developed considerable expertise with bulk phosphonate silica systems[101, 102] and a few reports on phosphonate silica nanoparticles had appeared in the literature.[103] The phosphonate group is a biocompatible entity and we set out to explore the possibility of developing large pore phosphonatesilica nanoparticles drug delivery systems for large biomolecule immobilisation and delivery, which would potentially meet the above requirements.

Considering previous reported work it was decided that a base catalysed low surfactant route would be used to synthesize nanoparticles of suitable dimensions (sub 200 nm diameter) and large pore size. The study would entail determining the influence of various reaction conditions such as the effects of base, surfactant, co-solvent concentration on the particle morphology. These results would be used elucidate the mechanism of the particle formation.

A particular objective was to develop nanoparticles with capacity to act as vehicles for large biomolecules like proteins since earlier reported variants were restricted to smaller drug molecules owing to smaller pore sizes. To suitably challenge the ability of the particles to adsorb protein molecules, bovine serum albumin (BSA, mol wt. 66kD) would be used as the model protein. The properties of the protein-particle composites, such as protein load, dispersion stability, hydrodynamic radius, variation of particle

morphology and secondary structure of the adsorbed proteins would be studied. Also, the stability of the protein-particle composites would be studied to determine its usefulness as a drug delivery platform.

With drug delivery vehicle applications in mind the study would also include cell work to establish potential cell internalisation and effects on cell viability. Studies would involve determining the cytotoxicity of the particles, understanding the rate of particle uptake and the mechanism of the particle uptake.

The scope of the protein-particle composites to act as enzyme immobilizing agents would be studied. For this application, an industrially relevant enzyme, lipase would be used. The study would involve determining the enzyme kinetics and studying the ability of the particles to protect the immobilized enzyme from denaturation. Finally, the bulk phosphonatsilica system is also well known in the area of heterogeneous catalysis and it was of interest to explore potential of the nanoparticle format in this context as well with a selection of test reactions.

1.6. References

1. F. Winau, O. Westphal and R. Winau, *Microbes Infect.*, 2004, **6**, 786.

2. a)N. Desai, *AAPS J.*, 2012, **14**, 282. b) W. X. Mai and H. Meng, *Integr. Biol.*, 2013, **5**, 19-28.

3. J. Brinker and G. W.Sherer, " Sol gel Science", Elsevier, California, 1989, Ch. 3, pp. 97-228.

4. W. Stober, A. Fink and E. Bohn, *J. Colloid Interface Sci.*, 1968, **26**, 62–69.

5. A. Van Blaadren, J. Van Geest and A. Vrij, , *J. Colloid Interface Sci*., 1992, **154**, 481-501.

6. J. W. Kim, L. U. Kim and C. K. Kim, *Biomacromolecules*, 2007, **8**, 215-222.

7. H. Yamada, C. Urata, H. Ujiie, Y. Yamauchi and K. Kuroda, *Nanoscale*, 2013, 5, 6145-6153.

8. A) H. Liu, H. Li, Z. Ding, A. Fu, H. wang, P. Guo, J. Yu, Cunguo W., Xiu S. Zhao, *J. Clust. Sci*., 2012, **23**, 273- 285. B) T. Gholami, M. S.-Niasari, M. Bazarganipour, E. Noori, *Superlattice. Microst.*, 2013, **61**, 33- 41.

9. K. D. Hartlen, A. P. T. Athanasopoulos, and V. Kitaev, *Langmuir*, 2008**, 24**, 1714-1720

10. R. I. Nooney, D. Thirunavukkarasu, Y. Chen, R. Josephs and A. E. Ostafin, *Chem. Mater.*, 2002, **14**, 4721-4728.

11. B. G. Trewyn, S. Giri, I. I. Slowing and V. S.-Y. Lin, *Chem. Commun*., 2007, 3236–3245.

12. C.T. Kserge, M. E. Leonowicz, W. J. Roth, J. C. Vartuli, J. S. Beck, *Nature*, 1992, **359**, 710-712.

13. Y.-J. Han, G. D. Stucky and A. Butler, *J. Am. Chem. Soc.*, 1999**, 121**, 9897-9898.

14. M. Vallet-Regi, A. Rámila, R. P. del Real, and J. Pérez-Pariente, *Chem. Mater*.,2001,**13**, 308–311.

15. M. Vallet-Regi, F. Balas, and D. Arcos, *Angew. Chem. Int. Ed*., 2007, **46**, 7548 – 7558.

16. a) K. C.-W. Wu and Y. Yamauchi, *J. Mater. Chem*., 2012, **22**, 1251-1256. b) A. C. Pierre, *Introduction to Sol-Gel processing*, Kulwer academic publishing, Boston, pp 66-67.

17. F. Hoffmann, M. Cornelius, J. Morell, and M. Fröba, *Angew. Chem. Int. Ed*. 2006, **45**, 3216 – 3251.

18. C. E. Fowler, D. Khushalani, B. Lebeau, and S. Mann, *Adv. Mater.*, 2001, **13**, 649-652.

19. Q. Cai, Z.-S. Luo, W.-Q. Pang, Y.-W. Fan, X.-H. Chen, and F.-Z. Cui, *Chem. Mater.*, 2001**, 13**, 258-263.

20. a)S. Choudhary, R. Roy Yadav, A. N. Maitra, P. C. Jain, *Colloids Surf. A: Physiochem. Eng. Aspects,* 1994, **82**, 49 -58. b) S. Javadian, V. Ruhi, A. Heydari, A. Asadzadeh Shahir, A. Yousefi and J. Akbari, *Ind. Eng. Chem. Res*., 2013, **52**, 4517−4526. c) H. Topallar and B. Karadag, *J. Surfactants Deterg.*, 1998, **1**, 49-51.

21. Q. Huo, D. I. Margolese, U. Ciesla, D. G. Demuth, P. Feng, T. E. Gier, P. Sieger, A. Firouzi, B. F. Chmelka, F. Schuth, G. D. Stucky, *Chem. Mater.*, 1994, **6**, 1176-1191.

22. S. H. Behrens and D. G. Grier, *J. Chem. Phys.*, 2001, **115,** 6716-6721.

23. J. Frasch, B. Lebeau, M. Soulard, J. Patarin, R. Zana, *Langmuir*, 2000, **16**, 9049- 9057.

24. S. Sadasivan, C. E. Fowler, D. Khushalani, and S. Mann, *Angew. Chem. Int. Ed*., 2002, **41**, 2151-2153.

25. A. Zhang, Y. Zhang, N. Xing, K. Hou, and X. Guo, *Chem. Mater*. 2009, **21**, 4122–4126.

26. I. I. Slowing, B. G. Trewyn, and V. S.-Y. Lin, *J. Am. Chem. Soc***.,** 2007, **129**, 8845-8849.

27. K.-C. Kao, C.-Y. Mou, *Micropor. Mesopor. Mater.*, 2013, **169**, 7 – 15.

28. F. Gao, P. Botella, A. Corma, J. Blesa, and L. Dong, *J. Phys. Chem. B*, 2009**,** **113**, 1796–1804.

29. X. Du and J. He, *Chem. Eur. J*., 2011, **17**, 8165 – 8174.

30. K. Suzuki, K. Ikari and H. Imai, *J. Am. Chem. Soc.*, 2004**, 126**, 462–463.

31. X. Li, X. Du and J. He, *Langmuir*, 2010, **26**, 13528–13534.

32. K. Möller, J. Kobler and T. Bein, *Adv. Funct. Mater.*, 2007, **17**, 605–612.

33. J. Kecht and T. Bein, *Micropor. Mesopor. Mater.*, 2008, **116**, 123-130.

34. C. Urata, Y. Aoyama, A. Tonegawa, Y. Yamauchi and K. Kuroda, *Chem. Commun*., 2009, 5094–5096.

35. Q. He, X. Cui, F. Cui, L. Guo and J. Shi, *Micropor. Mesopor. Mater.*, 2009, **117**, 609-616.

36. A. Firouzi, D. Kumar, L. M. Bull, T. Besier, P. Sieger, Q. Huo, S. A. Walker, J. A. Zasadzinski, C. Glinka, J. Nicol, D. Margolese, G. D. Stucky, B. F. Chmelka, *Science*, 1995, **267**, 1138.

37. M. Grün, K. K. Unger, A. Matsumoto K. Tsutsumi, *Microporous Mesoporous Mater*. **1999**, *27*, 207.

38. W. Zhang, T. R. Pauly, T. J. Pinnavaia, *Chem. Mater*., 1997, **9**, 2491.

39. M. T. Anderson, J. E. Martin, J. G. Odinek, and P. P. Newcomer, *Chem. Mater.* **1998,** *10*, 311-321.

40. J. Gu, W. Fan, A. Shimojima, and T. Okubo, *Small*, 2007, **3**, 1740 – 1744.

41. L. Gu , A. Zhang , K. Hou, C. Dai , S. Zhang , M. Liu , C. Song, X. Guo, *Micropor. Mesopor. Mater*., 2012, **152** ,9–15.

42. H. Chen, J. He, H. Tang and C. Yan, *Chem. Mater.* 2008**, 20**, 5894–5900.

43. S. Tan, Q. Wu, J. Wang, Y. Wang, X. Liu, K. Sui, X. Deng, H. Wang, M. Wu, *Micropor. Mesopor. Mater*., 2011, **142**, 601–608.

44. K. Zhang, L.-L. Xu, J.-G. Jiang, N. Calin, K.-F. Lam, S.-J. Zhang, H.-H. Wu, G.-D. Wu, B. Albela, L. Bonneviot, and P. Wu, *J. Am. Chem. Soc*. , 2013, **135**, 2427−2430.

45. A. B. D. Nandiyanto, S.-G. Kim, F. Iskandar and K. Okuyama, *Micropor. Mesopor. Mater*., 2009, **120** , 447–453.

46. R. P. Bagwe, L. R. Hilliard, and W. Tan, *Langmuir*, 2006, **22** , 4357–4362.

47. B. G. Trewyn, I. I. Slowing, S. Giri, H.-T. Chen and V. S.-Y. Lin, *Acc. Chem. Res.*, 2007**, 40**, 846–853.

48. C.-P. Tsai, C.-Y. Chen, Y. Hung, F.-H. Chang and C.-Y. Mou, *J. Mater. Chem*., 2009, **19**, 5737–5743.

49. C.-Min Yang, H.-A. Lin, B. Zibrowius, B. Spliethoff, F. Schüth, S.-C. Liou, M.-W. Chu and C.-Hs. Chen, *Chem. Mater.* , 2007**, 19**, 3205-3211.

50. F. de Juan and E. Ruiz-Hitzky, *Adv. Mater*. 2000, **12**, 430-432.

51. J. Kecht, A. Schlossbauer and T. Bein, *Chem. Mater.*, 2008**, 20**, 7207–7214.

52. V. Cauda, A. Schlossbauer, J. Kecht, A. Zürner and T. Bein, *J. Am. Chem. Soc*., 2009, **131**, 11361- 11370.

53. J. Lu, M. Liong, J.I. Zink and F. Tamanoi, *Small*, 2007, **3**, 1341 – 1346.

54. S. Huh, J. W. Wiench, J.-C. Yoo, M. Pruski, and V. S.-Y. Lin, *Chem. Mater.*, 2003**, 15**, 4247-4256.

55. S. Huh, J. W. Wiench, B. G. Trewyn, S. Song, M. Pruski and V. S.-Y.Lin, *Chem. Commun.* , 2003, 2364–2365.

56. a)Y.-Shen Lin, K. R. Hurley, and C. L. Haynes, *J. Phys. Chem. Lett*. 2012, **3**, 364−374.b) R. C. Mundragi, V. R. Babu, V. Rangaswamy, P. Patel, T. M. Aminabhavi, *J. Control.* Release, 2008, **125**, 193-209.c)A. S. Determan, J. H. Wilson, M. J. Kipper, M. J. Wannemuehler, B. Narasimhan, *Biomaterials*, 2006, **27**, 3312-3320.

57. V. Cauda, A. Schlossbauer, T. Bein, *Micropor. Mesopor. Mater*.,2010, **132**, 60 – 71.

58. Y.-Shen Lin, N. Abadeer, K. R. Hurley, and C. L. Haynes, *J. Am. Chem. Soc*. 2011, **133**, 20444–20457.

59. B. G. Trewyn, S. Giri, I. I. Slowing and V. S.-Y. Lin, *Chem. Commun*., 2007, 3236–3245.

60. J. Liu, S. B. Hartono, Y. G. Jin, Z. Li, G. Q. (Max) Lu and S. Z. Qiao, *J. Mater. Chem*., 2010, **20**, 4595–4601.

61. Q. He and J. Shi, *J. Mater. Chem*., 2011, **21**, 5845- 5855.

62. Y. Gao,Y. Chen, X. Ji, X. He, Q. Yin, Z. Zhang, J. Shi, and Y. Li, *ACS Nano*, 2011. 5, 9788 – 9798..

63. T. Chen, N. Yang and J.Fu, *Chem. Commun.*, 2013, **49**, 6555 – 6557.

64. J. L. Vivero-Escoto, I. I. Slowing, C.-Wen Wu, and V. S.-Y. Lin, *J. Am. Chem. Soc*. 2009, **131**, 3462–3463.

65. A. Schlossbauer, J. Kecht, and T. Bein, *Angew. Chem*. 2009, **121**, 3138 –3141.

66. a) Y.-F. Huang,D. Shangguan, H. Liu, J. A. Phillips, X. Zhang, Y. Chen and W. Tan, *Chem. Bio. Chem*, 2009, **10**, 862 – 868 b) X. He, L. Hai, J. Su, K. Wang and X. Wu, Nanoscale, 2011, 3, 2936–2942.

67. F. Wen, Y. Dong, L. Feng, S. Wang, S. Zhang and X. Zhang, *Anal. Chem*., 2011, **83**, 1193–1196.

68. D. R. Radu, C.-Y. Lai, J. W. Wiench, M. Pruski and V. S. Y. Lin, *J. Am. Chem. Soc*., 2004, **126**, 1640–1641.

69. V. S. Y. Lin, C.-Y. Lai, J. Huang, S. A. Song and S. Xhu, *J. Am. Chem. Soc*., 2001, **123**, 11510–11511.

70. C. Yu, M. Luo, F. Zeng, F. Zheng and S. Wu, *Chem. Commun.*, 2011, **47**, 9086–9088.

71. S. Wu, Z. Li, J. Han and S. Han, *Chem. Commun*., 2011, **47**, 11276–11278.

72. S. Huh, H.-T. Chen, J. W. Wiench, M. Pruski, and V. S.-Y. Lin, *J. Am. Chem. Soc*., 2004, **126**, 1010-1011.

73. H.-T. Chen, S. Huh, J. W. Wiench, M. Pruski, and V. S.-Y. Lin, *J. Am. Chem. Soc*., 2005, **127**, 13305-13311.

74. J. Ge, Q. Zhang, T. Zhang, and Y. Yin, *Angew. Chem*., 2008, **120**, 9056 –9060.

75. Q.-G. Xiao , X. Tao , H.-K. Zoub, J.-Feng Chen, *Chem. Eng. J*., 2008, **137**, 38–44.

76. F. Wang, C. Guo , L.-R. Yang, C.-Z. Liu, *Bioresource Technol.*, 2010, **101**, 8931‑8935.

77. T. G. Terentyeva, A. Matras, W. V. Rossom, J. P. Hill, Q. Ji and K. Ariga, *J. Mater. Chem. B*, 2013, **1**, 3248–3256.

78. F. A. Carey, *Organic Chemistry*, McGraw-Hill, 1987, pp 474-504.

79. K. A. Pettigrew, Q. Liu, P. P. Power, and S. M. Kauzlarich, *Chem. Mater.*, **2003,** *15*, 4005-4011.

80. H. Xu, F. Yan, E. E. Monson, R. Kopelman, *J. Biomed. Mater. Res. A*, 2003, **66A**, 870-879.

81. http://www2.chemistry.msu.edu/faculty/reusch/VirtTxtJml/Spectrpy/InfraRed/infrared.htm (accessed 06/04/14).

82. http://www2.chemistry.msu.edu/faculty/reusch/VirtTxtJml/Spectrpy/UV-Vis/spectrum.htm#uv4 (accessed 06/04/14)

83. http://teaching.shu.ac.uk/hwb/chemistry/tutorials/molspec/nmr1.htm. (accessed 11/02/14)

84. J. McCurry, *Organic chemistry*, Brooks / Cole, Belmont, 8th edition, 2008 pp 456- 500.

85. H. Günther, *NMR Spectroscopy: Basic Principles, Concepts and Applications in Chemistry*, Wiley- VCH, 3rd Edition, 2013,pp 557.

86. http://mutuslab.cs.uwindsor.ca/schurko/ssnmr/ssnmr_schurko.pdf (accessed 11/02/14)

87. F. Uhlig, and H. C. Marsmann, "29 Si NMR Some Practical Aspects", *Gelest Catalog*, Gelest Inc., 2009, 208 – 222.

88. J. L. Rapp, Y. Huang, M. Natella, Y. Cai, V. S.-Y. Lin and M. Pruski, *Solid State Nucl. Mag.*, 2009, **35**, 82 – 86.

89. J. Blümel, *J. Am. Chem. Soc.*, 1995, **117**, 2112- 2113.

90. R. Lungwitz, T. Linder, J. Sundermeyer, I. Tkatchenko and S. Spange, *Chem. Commun*., 2010, **46**, 5903–5905.

91. S. M. Kelly and N. C. Price, *Curr. Protein Pept. Sc.*, 2000, **1**, 349-384.

92. http://www.photophysics.com/tutorials/circular-dichroism-cd-spectroscopy/4-cd-spectrometer-operating-principles (Accessed 06/02/2014).

93. http://www.perkinelmer.co.uk/CMSResources/Images/44-74556GDE_TGABeginnersGuide.pdf (accessed 11/02/14)

94. http://www.purdue.edu/rem/rs/sem.htm (accessed 11/02/14)

95. http://micron.ucr.edu/public/manuals/Tem-intro.pdf (accessed (11/02/14)

96. http://www3.nd.edu/~rroeder/ame60647/slides/dls.pdf (accessed 11/02/14)

97. http://cma.tcd.ie/misc/Surface_area_and_porosity.pdf (accessed 06/04/14)

98. S. Brunauer, P. H. Emmett and E. Teller, *J. Am. Chem. Soc.*, 1938, **60**, 309-319.

99. http://www.micromeritics.com/repository/files/gas_adsorption_theory_poster.pdf (Accessed 06/04/14)

100. E. P. Barrett, L. G. Joyner, P. P. Halenda, *J. Am. Chem. Soc.*, 1951, **73** , 373–380.

101. M. Sebah, S. P. Maddala, P. Haycock, A. Sullivan, H. Toms, J. Wilson, *J. Mol. Catal. A* , 2013, **374- 375**, 59- 65.

102. A. Aliev, D. L. Ou, B. Ormsby and A. C. Sullivan, *J. Mater. Chem* , 2000, **10**, 2758-2764.

103. Y. Gang Jin, S. Z. Qiao, Z. P. Xu, J. C. Diniz da Costa and G. Q. Lu, *J. Phys. Chem. C*, 2009, **113**, 3157–3163.

Chapter 2

Chapter 2: Phosphonate functionalized silica nanoparticles

Some of the results from this chapter have been published in: Sai Prakash Maddala , Diana Velluto, Zofia Luklinska and Alice C. Sullivan, "Large Pore Raspberry Textured Phosphonate@Silica Nanoparticles for Protein Immobilization" *J. Mater. Chem. B,* 2014**, 2,** 903–914.

2.1 Summary

In this chapter work leading to the synthesis of new large pore (11 to 18 nm) raspberry textured organosilica nanoparticles is discussed. The particles were functionalized using the organosilane $(MeO)_3SiCH_2CH_2PO(OMe)_2$, (dimethylphosphonatoethyltrimethoxysilane, DMPTMS). The particle synthesis was performed under base catalysed–low surfactant conditions. Raspberry textured silica nanoparticle formation took place under specific reaction conditions including temperature, pH, co-solvent (ethanol) concentration and DMPTMS concentration. The effect of these components on the particle morphology was studied. The particles were characterized by scanning and transmission electron microscopy (SEM and TEM), dynamic light scattering (DLS), zeta potential, ^{29}Si and ^{31}P solid state MAS NMR, thermogravimetric analysis (TGA) and infrared spectroscopy (IR). The results and discussion are presented in separate sections.

2.2 Background

Large pore silica nanoparticles (pore size > 5 nm) were demonstrated to have great potential for immobilization of large biomolecules such as proteins[1] and DNA.[2, 3] However, almost all the major studies involving the synthesis of large pore silica nanoparticles to date have involved unfunctionalized silica nanoparticles. Furthermore, the applications of these particles are restricted due to the absence of organosilane

functionalization. Some of the previously published papers reported on grafting of organosilane groups after the particle synthesis.[2,3] This method however, resulted in uneven distribution of the organic groups on the silica surface (for reasons outlined in Chapter 1). In order to improve the organic group distribution on the particle surface and thereby improve its interactions with biomolecules, particle synthesis by co-condensation was shown to be a better approach.[4]

In this chapter a study leading to large pore organosilica nanoparticles through co-condensation of the silane precursors TEOS and DMPTMS under a base catalysed – low surfactant process is described. The organosilane acted both as a surface modifier and structure directing agent.[5] The final particle morphology was found to have resulted from a specific combination of reaction conditions. The organophosphonate functional group was chosen in part due to its excellent biocompatibility.[6a] It had been used by others as a precursor (diethylphosphonatoethyl triethoxysilane, DEPTES) for silica materials for various applications such as proton conducting[6b], metal immobilization[6c] applications. Phosphonates have also been used to surface modify silica nanoparticles to improve their dispersion stability.[6c,6d] The group is an excellent hydrogen bond acceptor and this would in principle allow it to interact with a wide range of biomolecules.[7]

2.3 Experimental

2.3.1 Materials

Cetyltrimethylammonium bromide (CTAB, 95%), dimethylphosphite (DMP, 98%), diethylphosphite (DEP, 98%) vinyltrimethoxysilane (VTMS, 98%), vinyltriethoxysilane (VTES, 98%) and di-t-butyl peroxide (DTB, 98%) were purchased from Sigma Aldrich and used as received. TEOS was purchased from Sigma Aldrich, distilled and dried over 3Å molecular sieves. DEPTES was prepared as previously described.[8] NaOH pellets, ethanol and HCl (35% w/w) was purchased from VWR and used without further

purification. The particle synthesis was carried out in deionized water dispensed from an 18 mΩ Millipore system supplied by Elba UK.

Code-names given to phosphonate silica nanoparticles synthesized in this work and explanations of these names are listed below.

CP_PME(1.6)	Colloidal (silica) particles functionalized with phosphonate monoester, ~$CH_2CH_2P(OMe)OH$ loading at 1.6 $mmolg^{-1}$.
RNP_PME(2.5)	Raspberry textured nanoparticles functionalized with phosphonate monoester ~$CH_2CH_2P(OMe)OH$ loading at 2.5 $mmolg^{-1}$.
NP_PME(1.0)	Phosphonate monoester ~$CH_2CH_2P(OMe)OH$ functionalized nanoparticles loading at 1.0 $mmolg^{-1}$.
NP_PME(0.2)	Phosphonate monoester ~$CH_2CH_2P(OMe)OH$ functionalized nanoparticles loading at 0.2 $mmolg^{-1}$.
NP_PEE(2.1)	Phosphonate monoethylester ~$CH_2CH_2P(OEt)OH$ functionalized nanoparticles loading at 2.1 $mmolg^{-1}$

2.3.2 Synthesis of DMPTMS

A 500 mL round bottom flask was charged with a 25 mm stirrer bar and kept under nitrogen atmosphere. To this flask DMP (53.9 g, 0.49 mol) and DTB (7.30 g, 0.05 mol) were added under N_2 atmosphere. The flask was heated to 130 °C while stirring constantly at 600 rpm. Once the temperature stabilized the addition funnel was charged with VTMS (59.2 g, 0.40 mol), which was added dropwise into the reaction vessel for the next three hours. After further 2 hours, 1 mL of DTB was added dropwise and the reaction was monitored for the next 12 hours using ^1H NMR by periodically taking samples. The reaction was stopped after the complete disappearance of vinyl peaks. At the end of the reaction the crude was distilled to remove unreacted DMP and DTB. The colourless liquid obtained after distillation was further distilled under vacuum to give pure DMPTMS (60%, b. p. 130-140 °C/10 mm Hg).

^{1}H NMR (400 MHz, $CDCl_3$, δ) 0.77–0.86 (2H, bm, C*H*$_2$Si), 1.69-1.75 (2H, bm, C*H*$_2$P), 3.50 (9H, s, Si*OCH*$_3$), 3.66 (6H, d, P*OCH*$_3$, $^{3}J_{P,H}$= 8 Hz).

^{31}P NMR (161.9 MHz, $CDCl_3$, δ) 35.6

2.3.3 Synthesis of CP_PME(1.6)

The molar ratio of reagents used in this formulation (**Formulation 1**) with respect to TEOS was: CTAB(0.19): TEOS(1.00): (DMPTMS(0.61): NaOH(0.52): EtOH(7.74): Water(1961). A 250 mL round bottom flask was charged with a 12 mm stirrer bar and 100 mL of deionized water. To this CTAB (0.2 g, 0.55 mmol) and 2M NaOH (0.73 mL, 1.46 mmol) were added and the flask was stirred at 1100 rpm. When CTAB completely dissolved, the resultant clear solution was heated to 80 °C while maintaining the stirring rate. Meanwhile TEOS (0.59 g, 2.83 mmol) and DMPTMS (0.45 g, 1.74 mmol) were weighed in a vial and dissolved in ethanol (1.01 g, 21.9 mmol). This solution was added dropwise to the round bottom flask containing the micellar solution (once the temperature stabilized) using a syringe while stirring continuously. Following the addition of the silane precursors the reaction mixture first turned cloudy and after around 10 to 15 minutes a white precipitate started to settle at the bottom of the flask. The reaction was carried out overnight. The white solid was then filtered, washed with ethanol and dried. A 100 mL round bottom flask was charged with a stirrer bar, the dried powder (0.35 g) from the first step and 2 g of ammonium nitrate. To this mixture 50 mL of ethanol was added and the mixture was heated under reflux to 90 °C under constant stirring overnight. The reaction mixture was then cooled and the particles were filtered by Buchner filtration and washed with water and ethanol and dried (0.25 g, 38.9%). IR spectroscopy was

performed on the dried powder to determine the complete removal of the surfactant. Details of the characterization are provided in section 2.3.6.

2.3.4 Variations of reaction parameters on the particle morphology:

In order to study the effects of the temperature and reagents on the particle morphology, the reaction temperature and the mole ratio of the reagents used in **Formulation 1** as described in the above procedure was varied as tabulated for each parameter changed below. Results are given and discussed in sections 2.4 and 2.5.

Sample Name	Temperature	CTAB:TEOS mole ratio	Ethanol:TEOS mole ratio	NaOH:TEOS mole ratio
CP_PME(1.6)[a]	**80°C**	**0.19**	**7.74**	**0.52**
CP_PME(1.6)_60	60°C			
CP_PME(1.6)_40	40°C			
CP_PME(1.6)_20	20°C			
CP_PME(1.6)_0.00CTAB		0.00		
CP_PME(1.6)_0.05CTAB		0.05		
CP_PME(1.6)_0.10CTAB		0.10		
CP_PME(1.6)_0.00EtOH			0.00	
CP_PME(1.6)_2.12EtOH			2.12	
CP_PME(1.6)_11.0EtOH			11.0	
CP_PME(1.6)_0.00NaOH				0.00
CP_PME(1.6)_0.17NaOH				0.17
RNP_PME(2.5)				0.34

[a] These conditions apply except where indicated.

Raspberry textured nanoparticles (RNP_PME(2.5)) were obtained when the NaOH mole ratio was reduced to 0.34. The formulation used to prepare RNP_PME(2.5) was denoted

as **Formulation 2**: CTAB(0.19): TEOS(1.0): (DMPTMS(0.61): NaOH(0.34): EtOH(7.74): Water(1961).

2.3.5 Variation of Formulation 2

Formulation 2 was further varied in terms of temperature and mole ratio of reagents other than base as tabulated below. Results are given and discussed in sections 2.4 and 2.5.

Sample Name	Temperature	CTAB:TEOS mole ratio	Ethanol:TEOS mole ratio	DMPTMS:TEOS mole ratio
RNP_PME(2.5)[a]	**80**°C	**0.19**	**7.74**	**0.34**
RNP_PME(2.5)_60	60°C			
RNP_PME(2.5)_40	40°C			
RNP_PME(2.5)_20	20°C			
RNP_PME(2.5)_0.00CTAB		0.00		
RNP_PME(2.5)_0.05CTAB		0.05		
RNP_PME(2.5)_0.10CTAB		0.10		
RNP_PME(2.5)_0.00EtOH			0.00	
RNP_PME(2.5)_2.12EtOH			2.12	
RNP_PME(2.5)_11.0EtOH			11.0	
NP_PME(0.0)				0.00
NP_PME(0.2)				0.10
NP_PME(1.0)				0.20

[a] These conditions apply except where indicated.

DMPTMS in **Formulation 2** was replaced with DEPTES and the reaction was carried out under the conditions described in the preparation of RNP_PME(2.5) to produce NP_PEE(2.1).

2.3.6 Characterization:

Solid state spectra were obtained using a Bruker AMX 600MHz instrument: ^{29}Si HPDec MAS, frequency 119.2 MHz, spinning speed 12 kHz; 1 minute recycle delay, with 2 μs ~ 45° pulse; ^{31}P CPMAS; frequency 242.9 MHz, spinning speed 12 kHz, 1 ms contact

time, 1.5 s delay, 90° pulse for 2.0 μs. IR spectra were recorded on a Bruker-FTIR spectrophotometer with an ATR accessory containing ZnSe crystal. 16 scans between 600 -4000 cm^{-1} were performed for each sample. The hydrodynamic radius, R_H of the particles was measured on a Malvern Zetasizer Nano ZS instrument equipped with a 633 nm laser. For analysis 1 mg/mL particle dispersion in a glass cuvette was prepared by sonication for (15 min) in PBS (10 mM) with pH adjusted to 4.73 or 7.4 using 1 M HCl and 2 M NaOH a 5 mm ultrasonic probe was used for sonication of the sample. Stock dispersions of the particles were prepared by dispersing 20 mg of particles in 10 mL of PBS and the height of liquid was kept constant at 80 mm, the inner radius of the tube was 15 mm. Sonication was carried out at 65% amplitude. TEM (Transmission Electron Microscope) images were obtained using a JEM JEOL 2010 TEM operating at 200 kV. Samples were prepared by dipping carbon coated TEM grids (Agar Scientific) into the particle dispersions. SEM (Scanning Electron Microscope) images were obtained from gold coated samples, using an FEI 100 instrument (Oxford Instruments) operating at 20 kV; spot size of 10 nm was used for the analysis. The surface area of the particles was measured at 77 K using a Quantachrome NOVA 1200e nitrogen adsorption porosimeter. The surface area was obtained using the Brunauer-Emmett-Teller (BET) method and the pore size distribution and pore volume were obtained using the Barrett-Joyner-Halenda (BJH) method. TGA (thermogravimetric analysis) was performed on TA Instruments Q500 thermogravimetric analyser; the measurement was performed under a flow of air (60 mL/min) between room temperature and 750 °C at scan rate 10 °C/min.

2.4. Results

2.4.1 DMPTMS synthesis

DMPTMS was synthesized by a free radical addition reaction in the manner previously described for DEPTES.[8] Di-tertbutylperoxide (DTB) was used as the initiator.

DTB undergoes homolysis above 120 °C.[9] The resulting free radicals help initiate the reaction. The reaction was followed by observing the consumption of VTMS using proton NMR. The product was isolated by distillation under reduced pressure. The reaction scheme is as follows (Scheme 2.1):

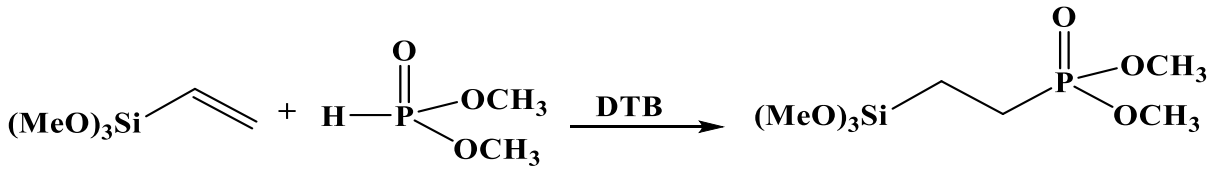

Scheme 2.1: DMPTMS synthesis

2.4.2 Nanoparticle Synthesis

The aim of the study was to synthesize large pore phosphonatesilica nanoparticles for drug delivery applications. The particle synthesis was carried out at low surfactant concentrations, using a method that was previously reported to synthesize pure silica nanoparticles.[10] TEOS and DMPTMS were used as silica and organic modifier sources, CTAB was used as the surfactant template, NaOH (2M) as the base and ethanol as the co-solvent. The initial ratio of the reagents with respect to TEOS was CTAB(0.19): TEOS(1.00): (DMPTMS(0.61): NaOH(0.52): EtOH(7.74): Water(1961). This formulation was denoted as **Formulation 1**.

Particle synthesis took place through the base catalysed hydrolysis and co-condensation of the silane monomers (TEOS and DMPTMS) while CTAB acted as a template to guide the particle formation. Under the basic conditions of the reaction the phosphonate diester component ~$PO(OMe)_2$ was partially hydrolysed to the monoester form ~PO(OMe)(ONa) and converted to the monoacid form ~PO(OMe)(OH) after surfactant removal (Scheme 2.2).

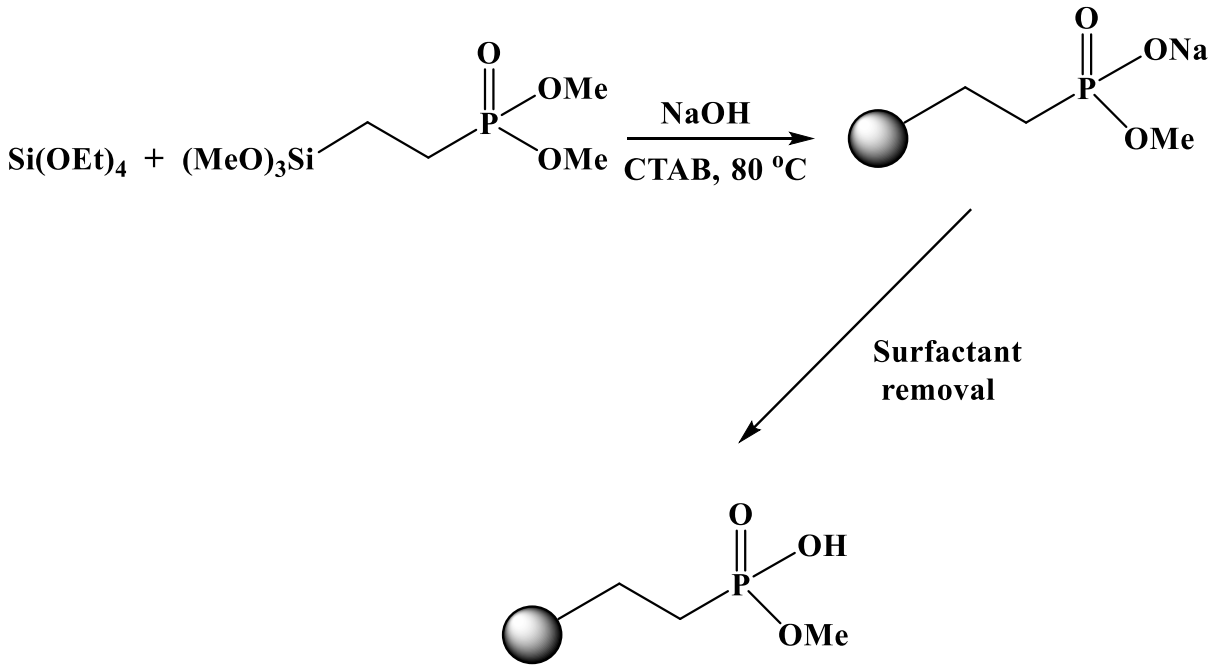

Scheme 2.2: Phosphonate monoester (PME) functionalized silica particle synthesis

The surfactant was removed by refluxing the particles in ethanolic ammonium nitrate solution.[11] The removal of the surfactant was confirmed by the disappearance of the characteristic ammonium ion peak.[12] The composition of the particles and the presence of phosphorus was verified by ^{1}H and ^{31}P NMR after dissolving a small amount (10 mg) of the surfactant-free particles in NaOD/D_2O solution (See appendix 1 for spectra). The total loading of phosphonate was determined by ^{29}Si solid state NMR using fractional signal intensity (see below) and the particles were denoted as CP_PME(1.6) (with 1.6 mmol/g phosphonate loading) (Figure 2.1).

2.4.3 ^{29}Si and ^{31}P solid state NMR for CP_PME(1.6)

The phosphonate loading and the surface coverage was determined by ^{29}Si MAS NMR. The spectrum revealed T^2, T^3, Q^2 and Q^3 peaks (Figure 3) with terms T and Q as defined in Chapter 1.[5] The surface coverage of the particle was determined using the formula $\mathbf{((T^2+ T^3)/(Q^2 +Q^3+ T^2+ T^3))}$.[5] The surface coverage was used to calculate the number of phosphonate groups per nm^2 of the particle surface. The ^{31}P CPMAS NMR of

the particles revealed that the particles had the monoester group (Figure 2.1).[13] A summary of the NMR data for CP_PME(1.6) is given in Table 2.1.

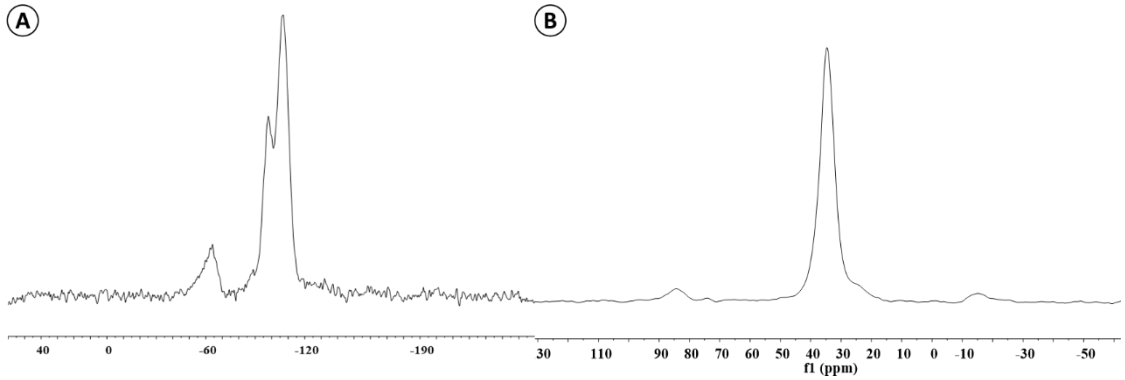

Figure 2.1: CP_PME(1.6) A) ^{29}Si MAS NMR B) ^{31}P CP-MAS NMR.

Table 2.1: Solid state ^{29}Si and ^{31}P NMR results of CP_PME(1.6) with deconvolution.

Property	**CP_PME(1.6)**
P : Si ratio[1]	0.12
δ_{29Si} T^2, T^3, Q^3, Q^4 ((%) T^2, T^3, Q^3, Q^4)	-58.4,-63.8,-97.8,-107.0 (4, 8, 39, 49)
% Condensation in T, Q sites	88,89
(%)T of surface coverage*	23
δ_{31P}	34.5
Number of Phosphonate groups/nm^2	0.29

* $(T^2+ T^3/ Q^2 +Q^3+ T^2+ T^3)^5$

2.4.4 CP_PME(1.6) Morphology

SEM and TEM analysis of the particles revealed that CP_PME(1.6) had nearly spherical shape and demonstrated a polydisperse particle size distribution (between 170 and 330 nm). The TEM image of the particles (Figure 2.2) also showed that some of the particles were fused together. The particles had a rough surface and were otherwise featureless. The surface analysis of the particles was performed using nitrogen adsorption

porosimetry (Figure 2.3). The particles had a high surface area of 765 m^2/g but were essentially non-porous. A summary of the particle morphology is given in Table 2.2.

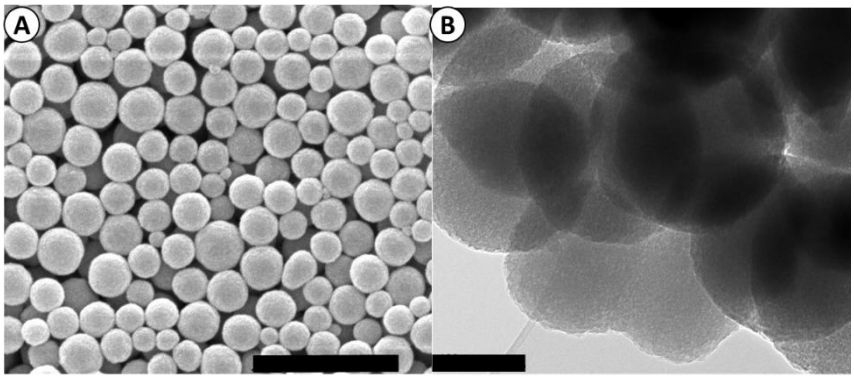

Figure 2.2: A) SEM (Scale 1000 nm) and B) TEM (Scale 100 nm) images of CP_PME(1.6).

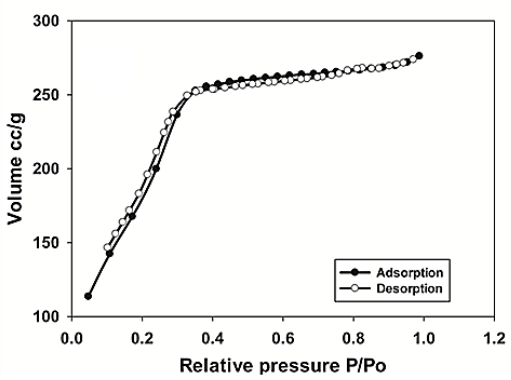

Figure 2.3: Nitrogen adsorption-desorption isotherm of CP_PME(1.6)

Table 2.2: Morphological properties of CP_PME(1.6)

Property	**CP_PME(1.6)**
Particle shape	Spherical
Particle size distribution	170 – 330 nm
Surface area	765 m^2/g
Pore volume	0.05l mL/g
Pore size	microporous (< 2 nm)

In order to fine-tune the particle morphology, specifically to identify conditions to increase porosity and decrease particle size distribution, the effect of each component in the formulation was studied. The reaction parameters were varied as follows:

1. Effect of temperature
2. Effect of surfactant
3. Effect of ethanol
4. Effect of NaOH

2.4.5 Effect of temperature

Reduction in temperature had a significant effect on the particle morphology wherein the average particle size increased while the particle surface became smoother (Figure 2.4). When the particle synthesis was attempted at 20 °C only fused particles were obtained. A summary of the particle morphology observed is given in Table 2.3

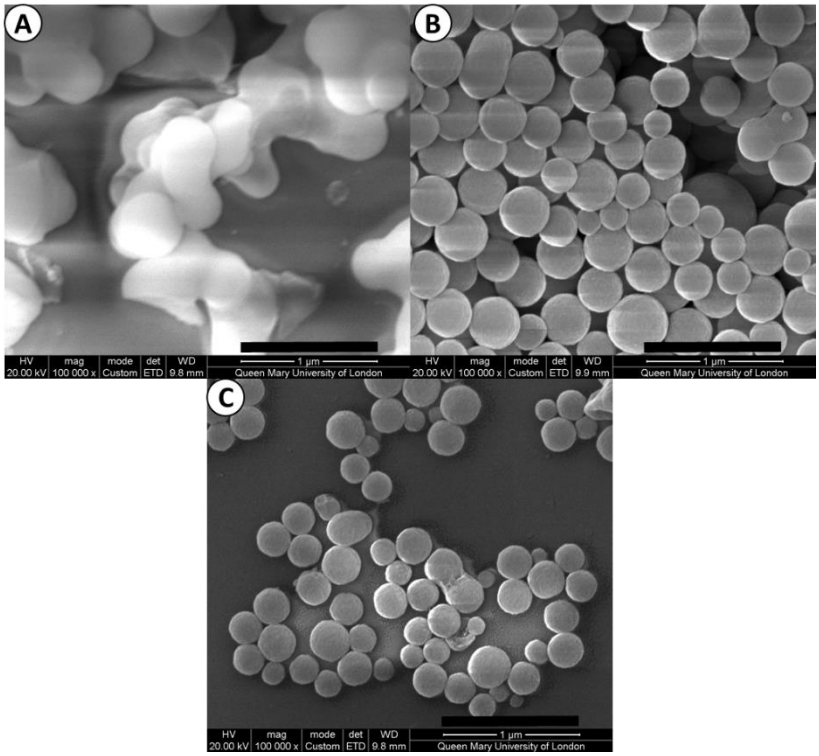

Figure 2.4: SEM after changing temperature with Formulation 1 to A) 20 B) 40 C) 60 °C (Scale 1000 nm)

Table 2.3: Summary of morphological properties after changing temperature in Formulation 1

Sample	**Morphology**
CP_PME(1.6)*	**Spherical particles**
CP_PME(1.6)_60	Spherical particles
CP_PME(1.6)_40	Large spherical particles
CP_PME(1.6)_20	Fused particles

*Temperature of synthesis 80 °C

2.4.6 Effect of CTAB

The presence of the surfactant was found to be essential for particle synthesis. When the particle synthesis was carried out in the absence of surfactant, particle formation was not observed. When the mole ratio CTAB: TEOS was increased to 0.05:1.00, amorphous silica and a few particles in sub-micron size range were observed

(Figure 2.5). Further increase in the surfactant concentration (mole ratio CTAB: TEOS 0.10: 1.00) resulted in a greater proportion of particles relative to amorphous silica and also a reduction in particle size. A summary of the particle properties is given in Table 2.4.

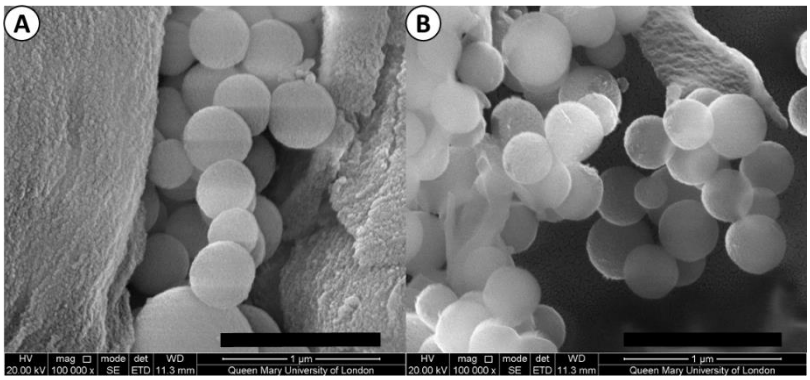

Figure 2.5: SEM after changing surfactant mole ratio in Formulation 1 to A) 0.05; B) 0.1 (Scale 1000 nm)

Table 2.4: Summary of morphological properties after changing surfactant mole ratio in Formulation 1

Sample	**Morphology**
CP_PME(1.6)*	**Spherical particles**
CP_PME(1.6)_0.00CTAB	No particles observed
CP_PME(1.6)_0.05CTAB	Mostly amorphous silica and a few large particles
CP_PME(1.6)_0.1CTAB	Mostly large particles and some amorphous silica

* CTAB mole ratio 0.19

2.4.7 Effect of ethanol

Ethanol was used as a co-solvent in this reaction. Variation in ethanol concentration resulted in changes in the particle size. When the particle synthesis was carried out in the absence of ethanol, the resultant particles showed monodisperse particle size distribution (Figure 2.6). Ethanol, however had no effect on porosity as the above

system was non-porous. Increase in ethanol concentration resulted in an increase in the polydispersity of the particles. Particles produced at ethanol: TEOS mole ratio of 11 had a size distribution of 50 to 200 nm (Figure 2.6). A summary of the particle properties is given in Table 2.5.

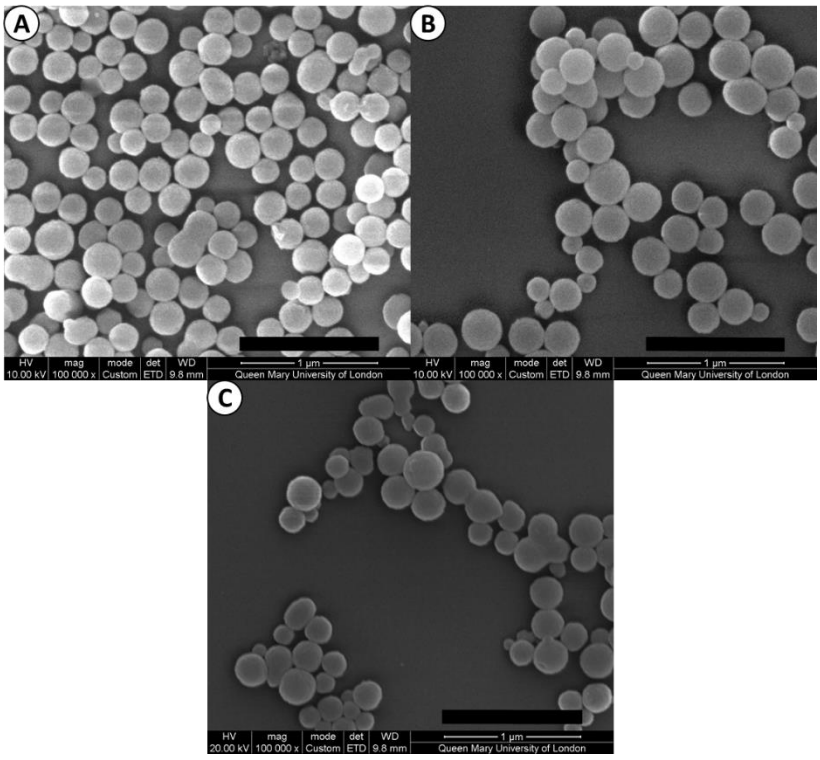

Figure 2.6: SEM after changing ethanol mole ratio in Formulation 1 to A) 0; B) 2.12; C) 11 (Scale 1000 nm)

Table 2.5: Summary of morphological properties after changing ethanol mole ratio in Formulation 1

Sample	**Morphology**
CP_PME(1.6)*	**Spherical particles**
CP_PME(1.6)_0.00EtOH	Monodisperse spherical particles
CP_PME(1.6)_2.12EtOH	Spherical particles
CP_PME(1.6)_11.0EtOH	Polydisperse spherical particles

*EtOH mole ratio 7.74

2.4.8 Effect of base

The hydrolysis and condensation of the silane precursors is catalysed by base. In the absence of the base, particle formation wasn't observed. When NaOH: TEOS mole ratio was increased to 0.17 (Figure 2.7), aggregates of 10 nm particles were observed. Further increase to 0.34 lead to the formation of raspberry textured particles. These particles (denoted RNP_PME(2.5)) showed an extremely monodisperse particle size distribution (70 to 90 nm). SEM analysis revealed that the particles were composed of aggregated smaller 5 to 10 nm particles. A summary of the particle properties is given in Table 2.6.

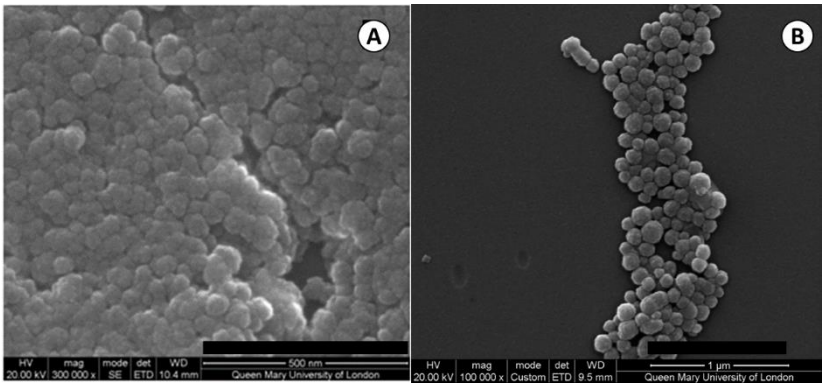

Figure 2.7: SEM after changing base mole ratio in Formulation 1 to A) 0.17 (Scale 500 nm); B) 0.34 (Scale 1000 nm)

Table 2.6: Summary of morphological properties after changing ethanol mole ratio in Formulation 1

Sample	**Morphology**
CP_PME(1.6)*	**Spherical particles**
CP_PME(1.6)_0.00NaOH	No particle formation
CP_PME(1.6)_0.17NaOH	Fused 10 nm particles
RNP_PME(2.5)**	Raspberry textured monodisperse particles

mole ratio of base *0.52 **0.34

2.4.9 RNP_PME(2.5)

The formulation used to produce RNP_PME(2.5) nanoparticles was CTAB(0.19): TEOS(1.00): DMPTMS(0.61): NaOH(0.34): EtOH(7.74)Water(1961) and it was denoted **Formulation 2**. ^{29}Si NMR RNP_PME(2.5) (Figure 2.8) showed degree of phosphonate loading (2.5 mmol/g) compared to CP_PME(1.6). Deconvolution of the spectrum revealed that while the overall degree of condensation was similar to CP_PME(1.6) (Table 2.7), the surface coverage of RNP_PME(2.5) was greater. Further confirmation of the presence of the organic groups was obtained by thermogravimetric analysis (TGA). The particles showed > 2% weight loss below 150 °C, which corresponded to surface adsorbed water molecules, a 16% weight loss was observed between 175 and 375 °C that corresponded to the loss of organic groups. The weight loss above 375 °C corresponded to the loss of phosphonate groups from the particles (Figure 2.9).[14]

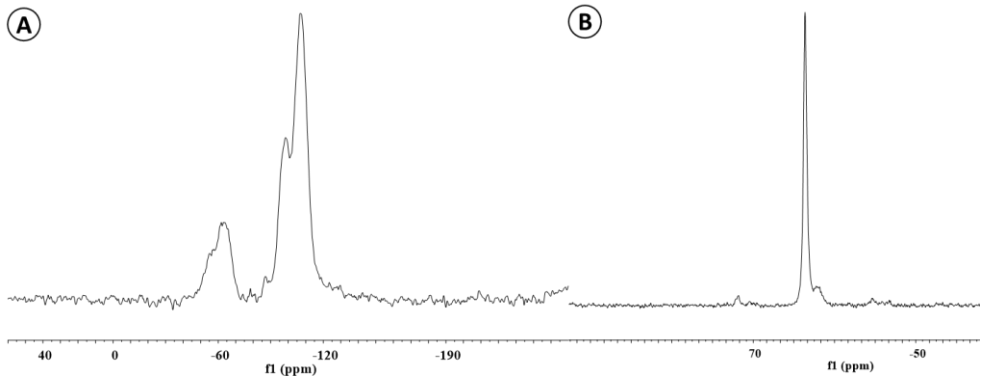

Figure 2.8: RNP_PME(2.5) A) ^{29}Si MAS NMR B) ^{31}P CP-MAS NMR.

Table 2.7: Solid state ^{29}Si and ^{31}P NMR results of RNP_PME(2.5) with deconvolution

Property	**RNP_PME(2.5)**
P : Si ratio	0.22
δ_{29Si} T^2, T^3, Q^3, Q^4	-55.3,-63.9,-98.6,-106.9
((%) T^2, T^3, Q^3, Q^4)	(8, 14, 24, 54)
% Condensation in T, Q sites	88,92
(%)T of surface coverage*	48
δ_{31P}	35.6
Number of phosphnate groups per nm^2	0.94

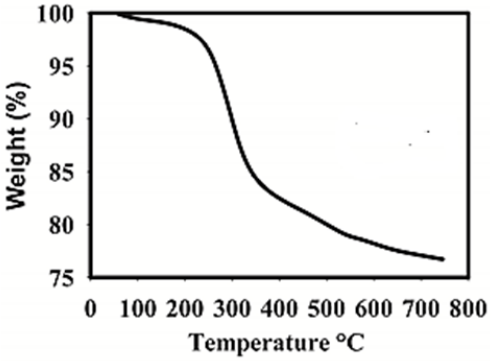

Figure 2.9: TGA of RNP_PME(2.5)

The nitrogen adsorption isotherm of the particles (Figure 2.10) revealed that the surface area of the particles (772 m^2/g) (Table 2.8) was about the same as for CP_PME(1.6) (765 m^2/g). However, the mesopore surface area of the RNP_PME(2.5) (472 m^2/g) was a lot higher than that of CP_PME(1.6) (126 m^2/g). The RNP_PME(2.5) particles also displayed porosity and had an average pore size of 11.1 nm and a pore volume of 0.576 mL/g (Table 2.8 and Figure 2.10 inset). However the textural properties of the particles was found to vary between samples. The surface area varied between 584 to 772 m^2/g, with an average surface area of 672.5 ± 81.1 m^2/g (no. of batches = 6). The pore size varied between 11.1 to 17.6 nm with an average pore size of 13.9 ± 3 nm (no. of batches = 6) and the pore volume varied between 0.54 and 0.82 mL/g with an average

pore volume of 0.71 ± 0.17 mL/g (n = 6). All the samples, however displayed similar shaped adsorption isotherms.

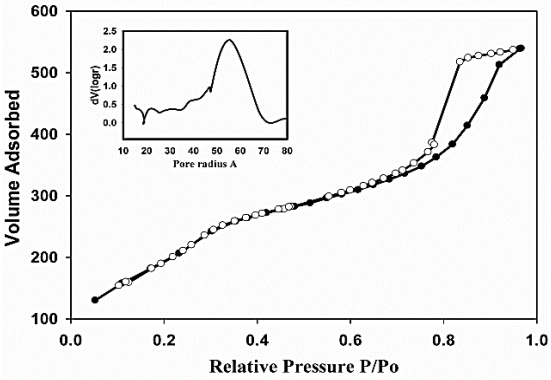

Figure 2.10: RNP_PME(2.5) N_2 sorption isotherm (inset pore radius distribution)

Table 2.8: Morphological properties of RNP_PME(2.5)

Property	**RNP_PME(2.5)**
Particle shape	Spherical
Particle size distribution	70- 90 nm
Surface area	772 m^2/g
Pore volume	0.576 mL/g
Pore size	11.1 nm
Hydrodynamic radius	165 (±1.0)

The particles showed excellent dispersion properties being easily dispersed in water and also in PBS (Phosphate buffered saline). The hydrodynamic radius R_H, was 164.86 (± 1.19) and 161.18 (± 5.11) nm at pH 4.73 and 7.40, respectively in PBS (Figure 2.11). The measurement was performed on 1 mg/mL particle dispersion. This particle size was as expected larger than the size observed using SEM and TEM (Figure 2.12) (Table 2.8). The particles showed good dispersion stability with dispersions remaining

stable for up to 3 months when dispersed in water. A Zeta potential of – 28 mV was measured for the particles RNP_PME(2.5) dispersed in water (2 mg/mL).

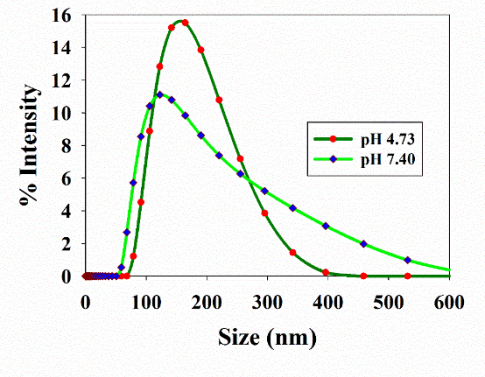

Figure 2.11: Hydrodynamic radius of particles at pH 4.73 and pH 7.40

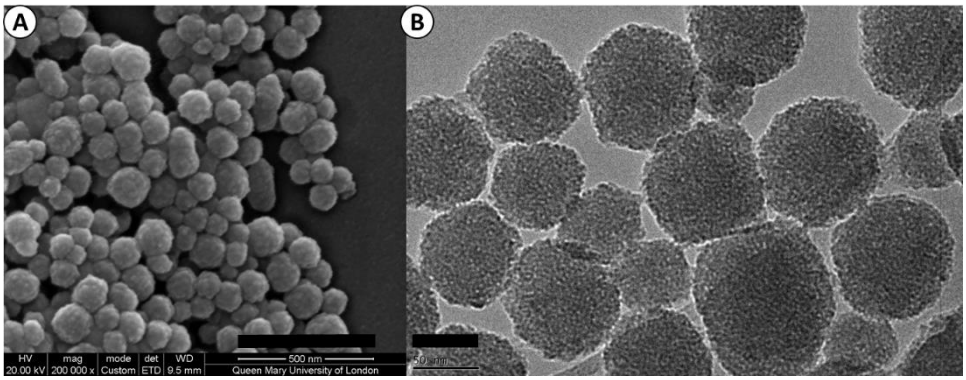

Figure 2.12**:** RNP_PME(2.5) particles A) SEM (Scale 500 nm); B) TEM (Scale 50 nm)

2.4.10 Variations in Formulation 2

The variations in parameters such as temperature, CTAB concentration and ethanol concentration in Formulation 2 showed in the main the same trends as the variations studied in Formulation 1. The trends are illustrated below using SEM images for samples from each set of reaction conditions.

2.4.11 Effect of temperature

Variation of temperature resulted in significant changes in the particle morphology. When the particle synthesis was carried out at 20 °C (Figure 2.13 A), only

fused particles were obtained. Increase in temperature resulted in the formation of distinct particles. Raspberry texture was observed from 60 °C onwards up to 80 °C (Figure 2.13 C).

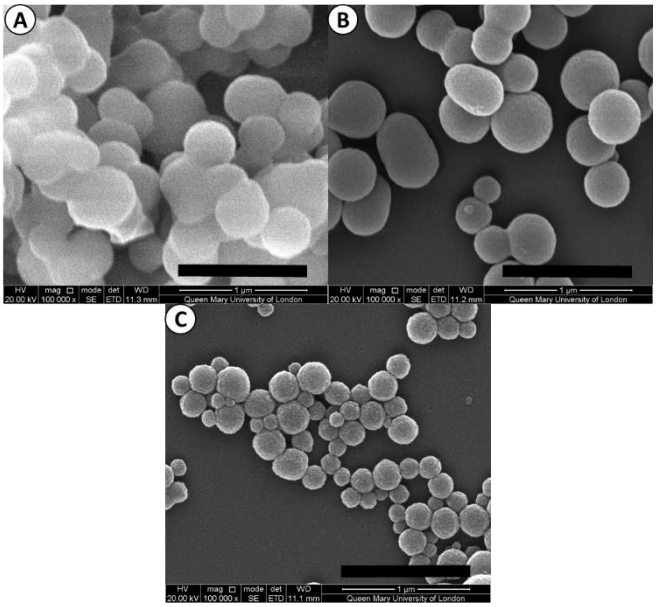

Figure 2.13: Effect of temperature on Formulation 2 A) 20 °C; B) 40 °C; C) 60 °C. (Scale 1000 nm)

2.4.12 Effect of CTAB

Reduction in CTAB concentration resulted in polydisperse, fused particles in micron size range (Figure 2.14 A). When synthesis was carried out in the absence of CTAB, particle formation was not observed. Gradual increase in CTAB concentration resulted in the formation of more discrete particles (Figure 2.14 B).

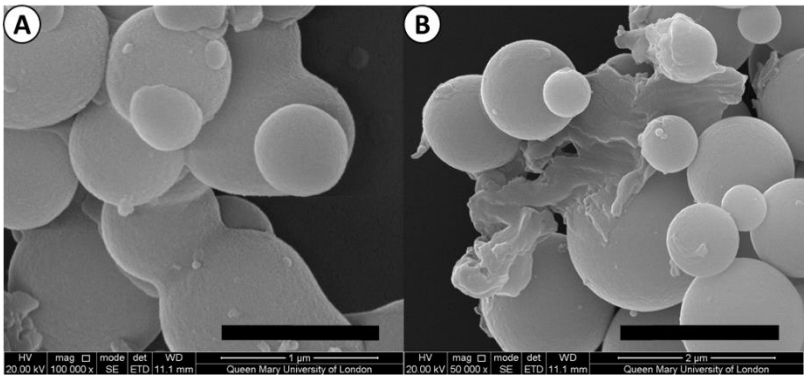

Figure 2.14: Effect of variation of CTAB mole ratio on Formulation 2 A) 0.05 (scale 1000 nm) B) 0.10. (Scale 2000 nm)

2.4.13 Effect of ethanol

Variation in ethanol concentration resulted in changes in the particle size, however the raspberry particle texture was not affected. When the synthesis was carried out in the absence of ethanol polydisperse particles were observed (Figure 2.15 A). Addition of a small quantity of ethanol (mole ratio silane to ethanol 1: 2.12) resulted in larger but more monodisperse particles (Figure 2.15 B). Further increase resulted in RNP_PME(2.5) particles (mole ratio 1: 7.78). Further increase resulted in polydisperse particles (mole ratio 1: 11)

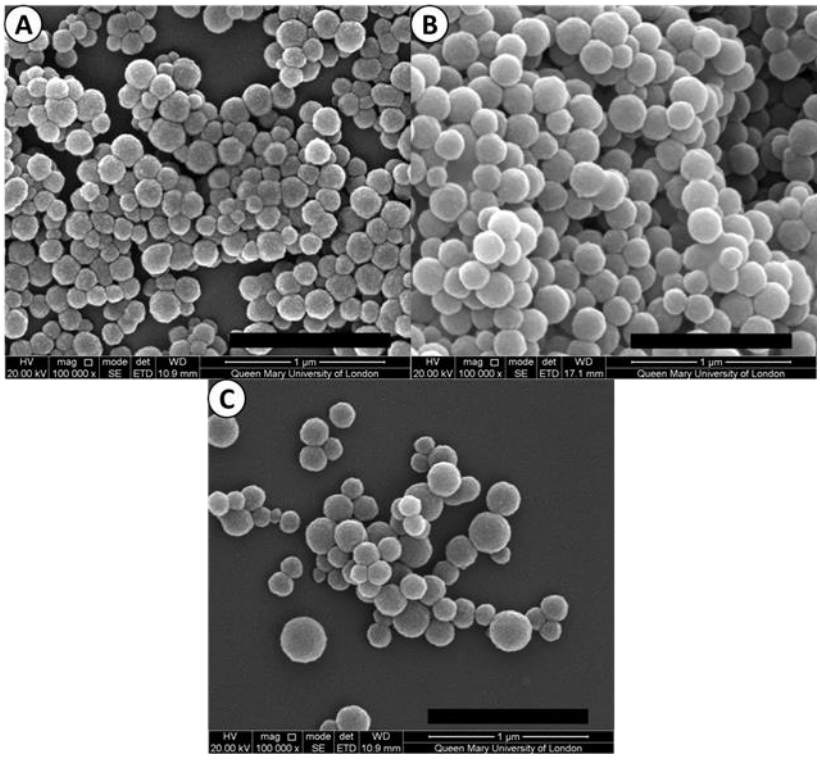

Figure 2.15: Effect of ethanol on Formulation 2 A) mole ratio 0; B) mole ratio 2.12 C) mole ratio 11.0 (Scale 1000 nm)

2.4.14 Effect of DMPTMS on particle morphology in Formulation 2

In order to fully understand the role of DMPTMS as a structure directing agent, the ratio of DMPTMS: TEOS in Formulation 2 was varied, while keeping the overall silane concentration constant. When DMPTMS was not used, discrete particle formation

was not observed. Instead the particles had fused morphology (Figure 2.16). When the mole ratio of was increased to 0.1 leading to material (NP_PME(0.2)) monodisperse spherical particles (65 to 70 nm diameter) (Figure 2.17) were obtained. Further increase in the ratio to 0.2 lead to a slight increase in the particle size (75 to 80 nm) (Figure 2.18).

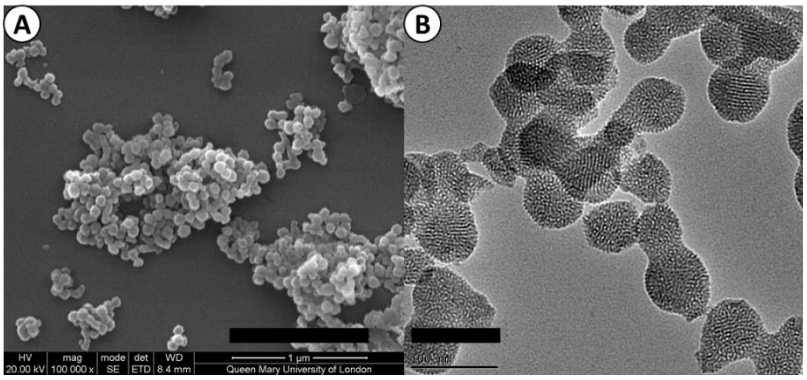

Figure 2.16: DMPTMS: TEOS mole ratio of 0 A); (SEM Scale 1000 nm) B) (TEM Scale 100 nm)

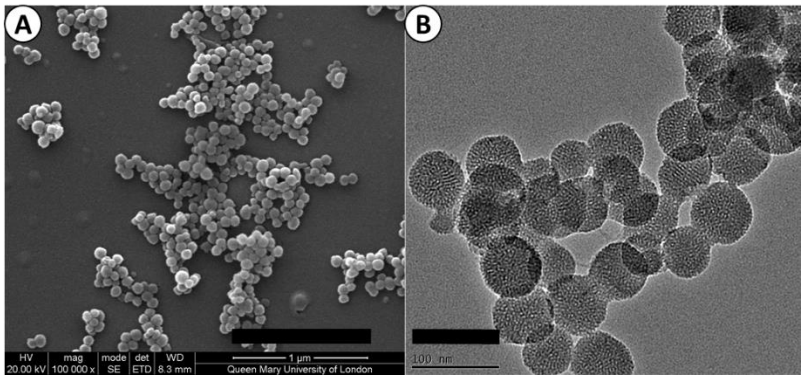

Figure 2.17: DMPTMS: TEOS mole ratio of 0.1(NP_PME(0.2)) A);SEM (Scale 1000 nm) B) TEM (Scale 100 nm)

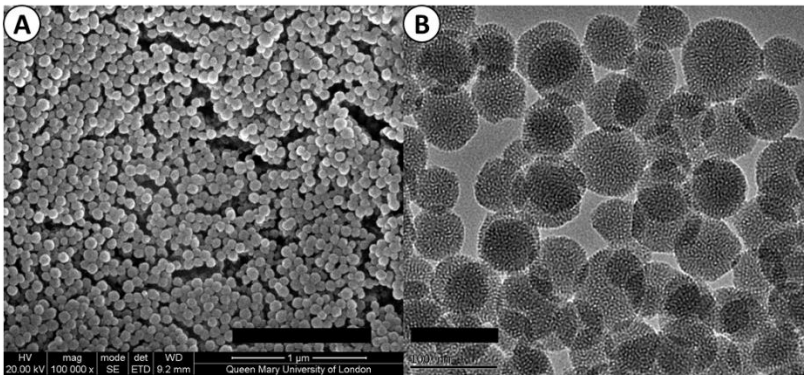

Figure 2.18: DMPTMS: TEOS mole ratio of 0.2 (NP_PME(1.0)) A)SEM (Scale 1000 nm) B)TEM (Scale 100 nm)

^{29}Si NMR revealed that both NP_PME(0.2) and NP_PME(1.0) particles showed only T^2 environments(Figures 2.19 and 2.20). The surface coverage of the particles was 4% and 21% respectively (Table 2.9). The hydrodynamic radii of these particles were larger than those of RNP_PME(2.5) (Table 2.10) suggesting that the particles aggregated. The stability of the particle dispersion decreased with the decrease in the phosphonate loading. Nitrogen adsorption isotherms of NP_PME(0.2) and NP_PME(1.0) revealed that both particles had similar surface areas and pore sizes, while the pore volume decreased slightly with the increase in phosphonate loading (Table 2.10).

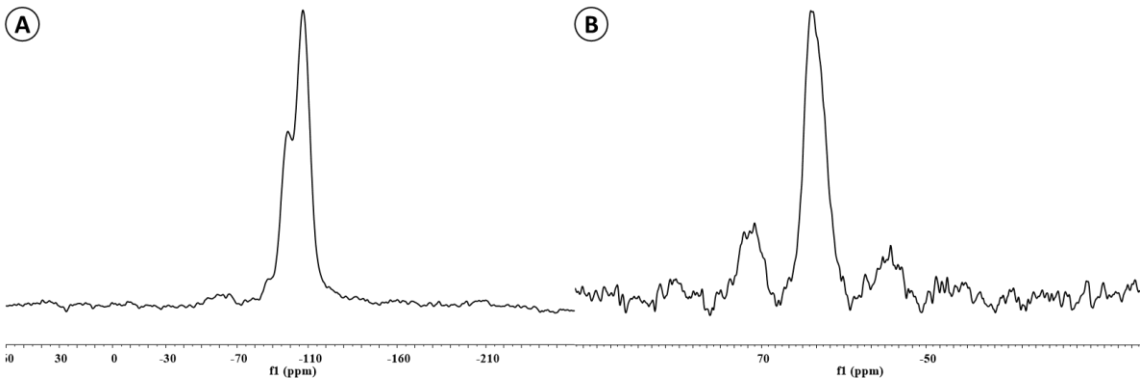

Figure 2.19: NP_PME(0.2) A) ^{29}Si MAS NMR B) ^{31}P CP-MAS NMR.

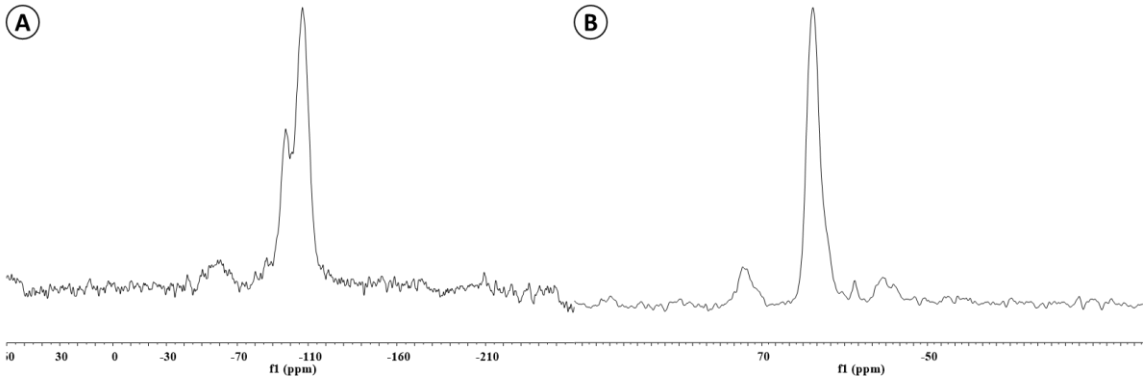

Figure 2.20: NP_PME(1.0) A) ^{29}Si MAS NMR B) ^{31}P CP-MAS NMR.

Table 2.9: Solid state ^{29}Si and ^{31}P NMR results of NP_PME(0.2) and NP_PME(1.0) with deconvolution

Property	**NP_PME(0.2)**	**NP_PME(1.0)**
P : Si ratio	0.01	0.07
δ_{29Si} T^2, T^3, Q^3, Q^4 (($\%$) T^2, Q^3, Q^4)	-59.9(T^2),-98.8,-107.2 (1, 28, 71)	-58.7(T^2),-97.3,-106.7 (7, 25, 68)
% Condensation in T, Q sites	66, 93	66, 93
(%)T of surface coverage*	4	22
δ_{31P}	34.1	32.9
Number of phosphonate groups per nm^2	0.006	0.18

Table 2.10: Morphological properties of NP_PME(0.2) and NP_PME(1.0)

Property	**NP_PME(0.2)**	**NP_PME(1.0)**
Particle shape	Spherical	Spherical
Particle size distribution	65 - 70 nm	75 -80 nm
Surface area	766 m^2/g	742 m^2/g
Pore volume	0.411 mL/g	0.356 mL/g
Pore size	2.9 nm	2.9 nm
Hydrodynamic radius, R_H	278	192±33.0

2.4.15 Effect of DEPTES on particle morphology in Formulation 2

In order to further understand the effects of DMPTMS on the particle formation, it was replaced with the ethoxysilane DEPTES in Formulation 2 for particle synthesis. Fused particle clusters were produced by this method and the particles were denoted NP_PEE(2.1). ^{29}Si NMR (Figure 2.21a) showed that the organic group loading (2.1 mmol/g) was similar to that of RNP_PME(2.5) particles (Table 2.11). The particles had a uniform particle size of ~ 60 nm. However, the particles were fused together and could not therefore be dispersed (Figure 2.22). Nitrogen adsorption isotherms revealed that the surface area of the particles decreased to 599 m^2/g and the mesopore surface area of the particles was only 173 m^2/g (Figure 2.22) (Table 2.12).

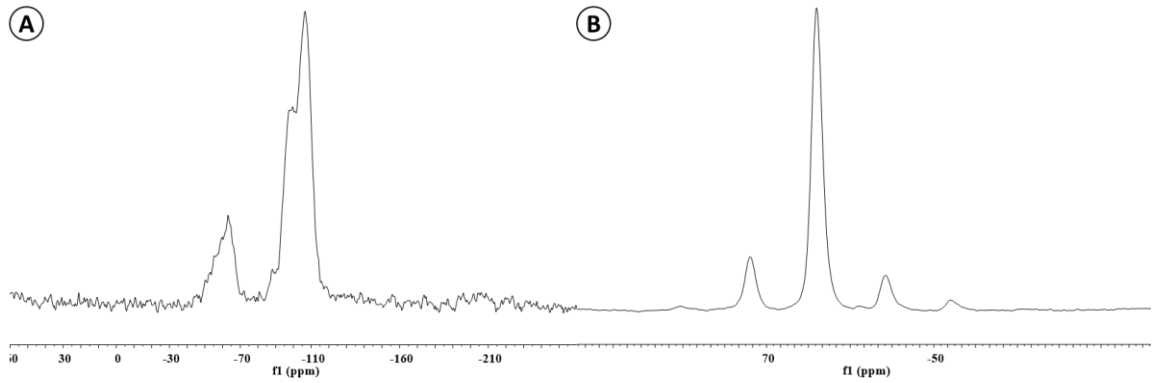

Figure 2.21: NP_PEE(2.1) a) ^{29}Si MAS NMR b) ^{31}P CP-MAS NMR

Table 2.11: Solid state ^{29}Si and ^{31}P NMR results of NP_PEE(2.1) with deconvolution

Property	**NP_PEE(2.1)**
P : Si ratio	0.18
δ_{29Si} T^2, T^3, Q^3, Q^4 ((%) T^2, T^3, Q^3, Q^4)	-57.3,-63.6,-98.2,-106.6 (8, 10, 31, 51)
% Condensation in T, Q sites	84, 91
(%)T of surface coverage*	37
δ_{31P}	34.1
Number of phosphonate groups per nm^2	0.78

Table 2.12: Morphological properties of NP_PEE(2.1)

Property	**NP_PEE(2.1)**
Particle shape	Fused spherical particles
Particle size	~ 60 nm
Surface area	599 m^2/g
Pore volume	0.400 mL/g
Pore size	Microporous (< 2 nm)
Hydrodynamic radius	Not dispersible

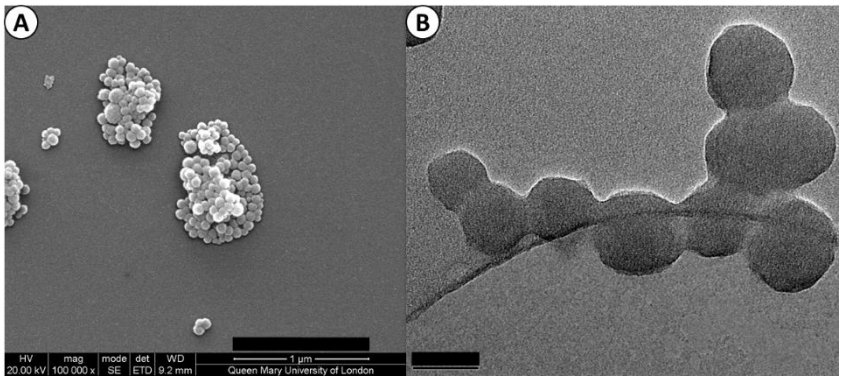

Figure 2.22 NP_PEE(2.1) A) SEM (Scale 1000 nm); B) TEM (Scale 50 nm)

2.5 Discussion

2.5.1 Variation of Reaction parameters

CP_PME(1.6) particles were produced by adapting a previously published report.[22] The particles displayed high surface area (765 m^2/g) and good organic group loading of 1.6 mmol/g. However, they lacked the porosity that is essential for protein immobilization applications.[1] In order to optimise the particle properties, the role of each component in the reaction was analysed. The components analysed were: 1) Temperature; 2) Ethanol mole ratio; 3) Surfactant (CTAB) mole ratio; 4) Base mole ratio

The particle size was strongly influenced by temperature. Previous studies on the role of temperature in Stöber silica nanoparticle synthesis showed that the particle size decreased with an increase in temperature.[15] This is due to an increase in the hydrolysis and condensation of the silane monomers which leads to increased seed nuclei formation and smaller particle size. This was precisely what was observed when the temperature was varied from 20 to 80 °C. Higher temperature lead to a reduction in the particle size and relatively improved the particle monodispersity (Figure 2.4 and Table 2.3).

Ethanol was used as the co-solvent in the particle synthesis to assist the even distribution of the silane monomers. Previous studies have shown that its use resulted in the production of spherical particles.[16] In the current study it was observed that low concentration of ethanol had a favourable influence on the particle size distribution, resulting in monodisperse particles (mole ratio ethanol:TEOS of 2) (Figure 2.6 and Table 2.5). Possible reasons for this are that ethanol reduces the rates of hydrolysis and condensation of the silane monomers[17] and also causes the surfactant micelles to assemble slowly. Consequently monodisperse particles are produced. However, higher concentration of ethanol (mole ratio ethanol: TEOS of 11) resulted in the formation of highly polydisperse spheres (Figure 2.6 and Table 2.5). This result could be attributed to a strong reduction in the co-hydrolysis and co-condensation of the silane precursors and also a disruption of the micellar structure.

Surfactants play a crucial role in the formation of silica nanoparticles. Particle formation did not take place when the particle synthesis was carried out in the absence of CTAB. The crucial step in surfactant assisted formation of silica nanoparticles is the formation of silica-surfactant seed template through the association of silica oligomer and surfactant molecules. The seed particles thus formed aggregate and grow via monomer addition.[18,19] Therefore in the absence of surfactant, particle formation was not observed.

Gradual increase in the surfactant concentration (CTAB: TEOS mole ratio of 0.05) resulted in the formation of bulk silica and a few sub-micron spheres. Further increase (mole ratio of 0.10) resulted in an increase in the number of particles. (Figure 2.5 and Table 2.4).

The presence of base had the strongest effect on the particle morphology. The primary role of base was that of a catalyst for the silane hydrolysis and condensation reactions. Not surprisingly, particle formation did not take place in the absence of base. A small increase in the concentration of base (NaOH:TEOS mole ratio of 0.17 (Figure 2.7) resulted in the formation of 10 nm fused particle aggregates. These particles could not be dispersed. Further increase (mole ratio of 0.34 (Figure 2.7)) resulted in the formation of highly monodisperse nanoparticles (70 – 90 nm). The rates of hydrolysis and condensation are strongly dependent on the pH. Under basic conditions the rate of hydrolysis increased with increase in pH, while the rate of condensation decreased.[20] This was reflected by the fact that CP_PME(1.6) particles (mole ratio of 0.52) had a large particle size and a relatively smooth surface compared to RNP_PME(2.5) particles.

2.5.2 Role of DMPTMS

Lin *et al*. demonstrated that the organosilanes act as structure directing agents by modifying the surfactant-silica interactions.[5] DMPTMS was found to be crucial to particle formation in Formulation 2. Fused, irregularly shaped particles were obtained in the absence of DMPTMS (Figure 2.16). Increase in DMPTMS concentration (DMPTMS:TEOS mole ratios 0.1 and 0.2) resulted in spherical particles (Figures 2.17 and 2.18). In addition to acting as a structure directing agent, DMPTMS apparently had a second role (as illustrated in Scheme 2.2). DMPTMS reacted with NaOH forming the monoester P(O)OMe(O^-), and thus reduced the concentration of the base in solution. The effect of this was seen as the concentration of DMPTMS in the reaction mixture was

increased from NP_PME(0.2) , NP_PME(1.0) to RNP_PME(2.5) while the NaOH : DMPTMS mole ratio decreased from 2.5, 1.3 to 0.56 respectively. This reduction in the concentration of available base resulted in a reduction in the reaction pH as the reaction progressed, which influenced the hydrolysis and condensation rates of the silane monomers and consequently the particle morphology of the formed products. The RNP_PME(2.5) particles showed the best particle properties such as average pore size (11.1 nm) and pore volume (0.576 mL/g). Nitrogen adsorption porosimetry of the particles illustrated this wherein the isotherm showed hysteresis at higher relative pressure (> 0.8), suggesting the presence of large amounts of textural porosity. In the case of the raspberry textured particles this porosity was most likely due to the pores located between the interstices of the fused 5 to 10 nm seed particles. Batch to batch variations in the textural properties of the RNP_PME material was observed with average surface area of 672.5 ± 81.1 m^2/g (n = 6) and average pore size of 13.9 ± 3 nm (n = 6) over six separate batch syntheses. These differences may reflect sensitivity to some variation in stirring rates and the rates of precursor addition.

As stated above, the nanoparticle porosity is due to the consequence of the unique nanoparticle texture. Two recent publications[23,24] reported similarly large pore sizes arising from unfunctionalized silica nanoparticles or microparticles with raspberry texture. Neither reports involved the use of strong bases such as NaOH but instead small quantites of organic amines triethanolamine[23] and triethylamine[24] were used and the pH of the reaction was close to neutral. The reaction conditions would have promoted silane condensation at a rate which could have resulted in the formation of the raspberry texture. In contrast the present work illustrated how the organosilane played the role of the structure directing agent and pH quencher (due to monophosphosphoate formation during the reaction).

Phosphonate functionalization also improved the dispersion properties of the nanoparticles. Organosilica nanoparticles with very low or no silane content, NP_PME(0.2) and MSN respectively showed poor or no dispersion stability. Increasing organosilane loading (RNP_PME(2.5)) resulted in excellent particle dispersion stability. The phosphonate group is extremely hydrophilic and a strong hydrogen bond acceptor.[7] The strong negative zeta potential -28 mV, of the RNP_PME(2.5) particles dispersed at pH 7 was the result of the dissociation of the phosphonate monosodium salt. These two factors could have resulted in an increase in the dispersion stability.

In order to further investigate the role of organosilane in influencing the particle morphology, DMPTMS was replaced with DEPTES. In this case only fused particles were obtained (Figure 2.22). This could be accounted for by the fact that the ethoxysilanes are known to have lower rates of hydrolysis and condensation compared to methoxysilanes.[21]

2.6 Conclusion

Phosphonate monoester functionalized silica nanoparticle synthesis was performed using the organosilane (dimethylphosphonatoethyltrimethoxysilane, DMPTMS $(MeO)_3SiCH_2CH_2PO(OMe)_2$,) and TEOS as alkoxysilane precursors. The particle synthesis was carried out using CTAB as surfactant. Ethanol was used as the co-solvent and sodium hydroxide was used as the base to catalyse the nanoparticle formation.

Preliminary reaction (Formulation 1) resulted in particles (CP_PME(1.6)) with good phosphonate loading of 1.6 mmol/g. However, the particles lacked porosity and were polydisperse. Reaction parameters (temperature, base concentration, ethanol concentration and surfactant concentration) were varied. From these experiments it was

determined that while temperature and ethanol concentration influenced the particle shape and size distribution, surfactant and base influenced the particle formation.

Variation of base concentration resulted in the formation of large pore (13.9 ± 3.0 nm, n = 6) raspberry textured phosphonate functionalized silica nanoparticles (RNP_PME(2.5) (Formulation 2). The particle formed by the aggregation of small (5 to 10 nm) seed particles. The particles displayed a monodisperse particle size distribution (70 – 90 nm) and high surface area (672.5 ± 81.1 m^2/g, n = 6) and high pore volume (0.71 ± 0.12 mL/g, n = 6). The porosity of these particles most likely arises due to the presence of textural pores in the interstices formed between the aggregated seed particles.

Previous studies aimed at increasing the pore size used pore enlargement agents such as mesitylene[1] or through the use of a dual surfactant system containing fluorinated surfactant, FC-4 and CTAB.[2,3] The use of mesitylene resulted in the formation of irregular and polydisperse particles. Fluorinated surfactants are highly expensive and the resultant nanoparticles contained a mixture of porous and non-porous silica nanoparticles. Hydrothermal treatment was required to remove the non-porous silica particles.[2] The strategy used in the synthesis of RNP_PME(2.5) involved the use of a low-surfactant system and did not involve any additional tough or damaging processing steps. The raspberry textured nanoparticles (RNP_PME(2.5)) represented a significant improvement in organosilica nanoparticle synthesis.

The influence of the organosilane on the particle morphology was studied by varying the concentration of DMPTMS in the reaction (while keeping the total silane concentration constant). In the absence of DMPTMS, irregular silica aggregates were formed. Addition of DMPTMS lead to the formation of small pore (2.96 nm) and

monodisperse particles (NP_PME(0.2) and NP_PME(1.0). When DMPTMS was replaced by DEPTES, fused silica nanoparticles (NP_PEE(2.1)) were formed.

The organosilane loading on the particles also represented another major improvement. Increasing the concentration of organosilane often resulted in a reduction in the pore size and pore volume.[5,14] In some cases the particle size also increased.[14] In this study, high phosphonate loading resulted not only an increase in the pore size, but it also increased the pore volume. The particle size showed only a slight increase. Finally, RNP_PME(2.5) nanoparticles showed excellent dispersion stability. Therefore, these particles are well suited for various biomedical applications.

2.7 References

1. I. I. Slowing, B. G. Trewyn and V. S. Y. Lin, *J. Am. Chem. Soc*., 2007, **129**, 8845-8849.

2. F. Gao, P. Botella, A. Corma, J. Blesa and L. Dong, *J. Phys. Chem. B*, 2009, **113**, 1796-1804.

3. S. B. Hartono, W. Gu, F. Kleitz, J. Liu, L. He, A. P. J. Middelberg, C. Yu, G. Q. M. Lu and S. Z. Qiao, *ACS Nano*, 2012, **6**, 2104-2117.

4. B. G. Trewyn, I. I. Slowing, S. Giri, H.-T. Chen and V. S.-Y. Lin, *Acc. Chem. Res.*, 2007**, 40**, 846–853.

5. S. Huh, J. W. Wiench, J. C. Yoo, M. Pruski, and V. S. Y. Lin, *Chem. Mater*., 2003, **15**, 4247-4256.

6. a)J. Tan, R. A. Gemeinhart, M. Ma and W. M. Saltzman, *Biomaterials*, 2005, **26**, 3663-3671. b) L. Y. Yuan, Y. L. Liu, W. Q. Shi, Y. L. Lv, J. H. Lan, Y. L. Zhao

and Z. F. Chai, *Dalton Trans*., 2011, **40**, 7446–7453.c) R. P. Bagwe, L. R. Hilliard and W. Tan, *Langmuir*, 2006, **22**, 4357–4362.

7. P. Van Nieuwenhuyse, V. Bounor-Legaré, F. Boisson, P. Cassagnau and A. Michel, *J. Non-Cryst. Solids*, 2008, **354**, 1654-1663.

8. A. Aliev, D. L. Ou, B. Ormsby and A. C. Sullivan, *J. Mater. Chem*., 2000, **10**, 2758-2764.

9. http://cost.ensic.univ-lorraine.fr/cost/index.php?id=375 (accessed 06/04/2014)

10. J. Lu, M. Liong, J. I. Zink and F. Tamanoi, *Small*, 2007, **3**, 1341-1346.

11. J. Kecht, A. Schlossbauer and T. Bein, *Chem. Mater*., 2008, **20**, 7207-7214.

12. J. Kecht and T. Bein, *Micropor. Mesopor. Mater.*, 2008, **116**, 123-130.

13. M. Sebah, S. P. Maddala, P. Haycock, A. Sullivan, H. Toms, J. Wilson, *J. Mol. Catal. A: Chemical*, 2013, **374-375**, 59 -65.

14. Y. Gang Jin, S. Z. Qiao, Z. P. Xu, J. C. Diniz da Costa and G. Q. Lu, *J. Phys. Chem. C*, 2009, **113**, 3157-3163.

15. G.H. Bogush, M.A. Tracy and C.F. Zukoski IV, *J. Non-Cryst. Solids*, 1988, **104,** 95 -106.

16. M. Grün, K. K. Unger, A. Matsumoto, K. Tsutsumi, *Microporous Mesoporous Mater.* **1999**, *27*, 207.

17. W. Zhang, T. R. Pauly, T. J. Pinnavaia, *Chem. Mater*., 1997, **9**, 2491.

18. Q. Cai, Z. S. Luo, W. Q. Pang, Y. W. Fan, X. H Chen and X.-F. Z. Cui, *Chem. Mater*., 2001, **13**, 258-263.

19. R. I. Nooney, D. Thirunavukkarasu, Y. Chen, R. Josephs and A. E. Ostafin, *Chem. Mater*., 2002, **14**, 4721-4728.

20. H.-P. Lin and C.-Y. Mou, *Acc. Chem. Res.*, 2002, **35, 11**, 927–935.

21. B. Arkles, J. R. Steinmetz, J. Zazyczny and P. Mehta, *Silanes and other coupling agents*; ed. K. L. Mittal, VSP, Netherlands, 1992, pp 91-104.

22. J. Lu, M. Liong, J.I. Zink and F. Tamanoi, *Small*, 2007, **3**, 1341 – 1346.

23. K. Zhang, L.-L. Xu, J.-G. Jiang, N. Calin, K.-F. Lam, S.-J. Zhang, H.-H. Wu, G.-D. Wu, B. Albela, L. Bonneviot, and P. Wu, *J. Am. Chem. Soc*. , 2013, **135**, 2427−2430.

24. Y. Wang, J. He, J. Chen, L. Ren, B. Jiang and J. Zhao, *ACS Appl. Mater. Interfaces*, 2012, **4**, 2735−2742.

Chapter 3

Chapter 3: Phosphonate functionalized organosilica nanoparticles for immobilization of the model protein, BSA (Bovine Serum Albumin)

Some of the results from this chapter have been published in: Sai Prakash Maddala , Diana Velluto, Zofia Luklinska and Alice C. Sullivan, "Large Pore Raspberry Textured Phosphonate@Silica Nanoparticles for Protein Immobilization" *J. Mater. Chem. B*, 2014**, 2,** 903–914.

3.1 Summary

In this chapter, the application of large pore (11.1 nm) raspberry textured phosphonate monoester nanoparticles (RNP_PME(2.5)) as a host for proteins is reported. Protein immobilization studies were performed using Bovine Serum Albumin (BSA) on small pore (3 nm) particles (MSN, NP_PME(0.2) and NP_PME(1.0)) and on large pore (11.1 nm) particles (RNP_PME(2.5)). The protein uptake by the particles was measured using UV-Vis spectroscopy. The protein-particle composites were characterized using IR, SDS-PAGE, electron microscopy (SEM and TEM), DLS and circular dichroism (CD). The RNP_PME(2.5) gave the highest protein loading 266 mg/g and also showed stable dispersion properties. CD studies showed no distortion in the structure of the BSA immobilized on RNP_PME(2.5) at physiological pH (7.40). The results and discussion are presented in separate sections.

3.2 Background

Intracellular delivery of protein molecules has attracted a considerable amount of research interest due to potential therapeutic and research applications.[1] For example, various enzymes such as lysine oxidase[2] and arginine deiminase[3] inhibit the growth of tumours by degrading the amino acids. Therapeutic enzymes are also used to treat inflammatory diseases, antibacterial and antiviral diseases.[4] Peptides such as endostatin (mol. wt 20 kD) are currently in clinical trials for cancer treatment.[5] Intracellular delivery

of antibodies such as monoclonal antibodies to shutdown various cellular processes has great potential in the area of cancer treatment and can potentially be used in the development of personalized medicine.[6,7] Protein molecules such as antibodies are vitally important to study various cellular pathways.[8] Improved understanding of various cellular pathways can help in finding new drug targets.[9]

Protein molecules, however, cannot be delivered intracellularly. Medicinally relevant peptides and proteins display low stability under physiological conditions.[4] *In vitro* administration of protein molecules is achieved using techniques such as microinjection or electroporation. However, these techniques are highly invasive and damage the cell membrane.[4,10,11] *In vitro* and *in vivo* delivery of proteins was also achieved using liposomes.[12] Liposomes are non-toxic and can carry large quantities of the protein molecules.[13] However, the drug molecules loaded into liposomes displayed delayed adsorption, restricted biodistribution, decreased volume of drug clearance and retarded drug metabolism.[14] Other commonly used techniques involved the use of cell penetrating peptides. TAT-peptide and Herpes Simplex Virus VP22 protein demonstrated high efficiency in intracellular delivery of protein molecules.[4] TAT peptide is an 86-mer trans-acting transcriptional activator from HIV-1, when conjugated with proteins through genetic engineering.[15] These methods were used to deliver protein molecules of various sizes (15 to 115 kD) to a wide range of cells.[4,15-17] Despite these advantages, synthesis of TAT and VP22 conjugated proteins are highly expensive[4] and action non-specific.[18] Other methods of delivery included using carbon-nanotube composites, however these protein-nanotube composites did not show any endosomal escape[19], which can result in the degradation of the proteins.[20]

Several groups devised a variety to strategies for protein entrapment. The most commonly used method involved growing a silica shell around the protein molecules

using reverse emulsion synthesis.[21] The particles thus obtained had good protein loading and were used for biosensing applications. [21,22] However, the method lends itself only to small scale synthesis as it required large quantities of surfactants and organic solvents.[21,22] In addition to this, leaching of encapsulated protein was observed in a few cases.[21] Mesoporous silica nanomaterials have attracted a great deal of interest due to their biocompatiblilty[23] and properties such as high surface area and tunable pore size.[24] Bulk silica materials such as SBA-15 have been used to immobilize the proteins.[25] Immobilization of enzymes in the silica pores was found to preserve the enzyme activity.[26] Difficulty in controlling the particle morphology of these materials renders them unsuitable for intracellular delivery.[27] Mesoporous silica nanoparticles can be used to overcome these problems, however most reports of MSNs involved the synthesis of small pore (3 to 4 nm) nanoparticles. While this pore size is suitable for the immobilization and delivery of small molecules, it is not suitable for large biomolecules such as proteins.[28] This is due to the pore size exclusion effect, which limits the adsorption and retention of biomolecules that are larger than the pore size.[29] Some recent studies involved the synthesis of large pore silica nanoparticles using pore enlargement agent resulting in a modest increase in the pore size from 3 nm to 6 nm, which is suitable for smaller proteins such as cytochrome c.[30,31a] However, the pore size reported has been shown to be unsuitable for larger proteins like BSA.[31b] In addition, the particle morphology was greatly altered and the particle size increased to 300 to 600 nm range[30] by the synthesis, further limiting the application of these particles for drug delivery. Recently, large pore (20 nm pore size) nanoparticles were synthesized using fluorocarbon surfactants.[32] As stated in the previous chapter, the fluorocarbon surfactants are expensive and the synthesis involved hydrothermal treatment to remove amorphous silica.

In this chapter, the details of studies that determined the capacity of the phosphonate functionalized nanoparticles (described in Chapter 2) for protein (BSA) immobilisation are presented and discussed. The protein uptake was measured using UV-Vis spectroscopy. Both concentration and time dependent uptake of the protein was studied. RNP_PME(2.5) particles were shown to have excellent protein immobilization properties. The final protein uptake was found to depend on the particle morphology and also phosphonate loading. Dispersion properties of the protein-particle composites were measured using DLS (Dynamic Light Scattering). The effect of the particles on the protein structure was studied using circular dichroism (CD).

3.3 Experimental

3.3.1 Materials

RNP_PME(2.5), NP_PME(0.2) and NP_PME(1.0) were synthesized using the methods described in the previous chapter. MSN was synthesized using a previously published method[33] (See appendix 2 for characterization details). BSA and PBS (Phosphate Buffered Saline) tablets were purchased from Sigma Aldrich and used without any further purification. PBS (10 mM) solution was prepared by dissolving one PBS tablet in 200 mL of deionized water. NaOH pellets, ethanol and HCl (35% w/w) was purchased from VWR and used without further purification. The particle synthesis was carried out in deionized water dispensed from an 18 mΩ Millipore system supplied by Elba UK.

3.3.2 Characterization

IR spectra were recorded on a Bruker-FTIR spectrophotometer with an ATR accessory containing a ZnSe crystal. 16 scans between 600- 4000 cm^{-1} were performed

for each sample. UV measurements were performed on a Perkin Elmer UV spectrophotometer, containing a Deuterium lamp source for the UV region and Tungsten lamp source for the visible region. Gel electrophoresis was carried out on a Novex 4-20% Tris-Glycine gradient gel from Life Technologies. The hydrodynamic radius, R of the particles was measured on a Malvern Zetasizer Nano ZS instrument equipped with a 633 nm laser. For analysis, a 1 mg/mL particle dispersion in a glass cuvette was prepared by sonication for (15 min) in PBS (10 mM) with pH adjusted to 4.73 or 7.4 using 1 M HCl and 2 M NaOH a 5 mm ultrasonic probe was used for sonication of the sample. Stock dispersions of the particles were prepared by dispersing 20 mg of particles in 10 mL of PBS and the height of liquid was kept constant at 80 mm, the inner radius of the tube was 15 mm. Sonication was carried out at 65% amplitude. TEM (Transmission Electron Microscope) images were obtained using a JEM JEOL 2010 TEM operating at 200 kV. Samples were prepared by dipping carbon coated TEM grids (Agar Scientific) into the particle dispersions. SEM (Scanning Electron Microscope) images were obtained from gold coated samples, using an FEI 100 instrument (Oxford Instruments) operating at 20 kV; spot size of 10 nm was used for the analysis. CD (Circular Dichroism) measurements were performed on 300 µL samples in 1mm path length cuvettes using an Applied Photophysics Chirascan CD Spectrometer, equipped with a 150 W air cooled Xe arc lamp.

3.3.3 Adsorption of BSA

The pH of PBS solution (10 mM) was adjusted to 4.73 using 1 M HCl solution. 2 mg/mL dispersions of the nanoparticles (RNP_PME(2.5), NP_PME(0.2), NP_PME(1.0), MSN and CP_PME(1.6)) were prepared by sonicating the particles (20 mg) in PBS (pH 4.73, 10 mL) using an ultrasonic probe for 45 minutes. The sonicator amplitude was set to 65% and pulse time of 45 seconds was used for sonication. After sonication the

dispersion was allowed to cool down to room temperature. Particle dispersions (1 mL) were then added to different concentrations (from 0.06 to 2 mg/mL) of BSA solutions (1 mL), gently mixed and allowed to stand for 45 minutes (at 20 °C). After 45 minutes, the dispersions were centrifuged at 14,000 rpm for 10 minutes and the supernatant was collected. BSA concentration in the supernatant was determined by measuring its absorbance at 280 nm in a UV-Vis spectrophotometer.

3.3.4 Time dependent BSA adsorption

Nanoparticle dispersions were prepared as described above. The dispersions (1 mL) were then added to 2 mg/mL BSA solutions (1 mL), gently mixed and allowed to stand (at 20 °C). At different time intervals, the samples were centrifuged at 14000 rpm for 10 minutes. The BSA concentration in the supernatant was determined by measuring the absorbance of the supernatant at 280 nm in a UV-Vis spectrophotometer.

3.3.5 BSA@RNP_PME(2.5) composite stability study

RNP_PME(2.5) dispersions in PBS(pH 4.73) were prepared as described above. To 1 mL samples of this dispersion equivolumes of BSA solutions (0.4 mg/mL and 0.6 mg/mL) were added and incubated at 20 °C for 30 minutes. After 30 minutes the pH of the solutions was raised to 7.4 by adding 0.1 M NaOH solution. The dispersions were then transferred to an incubator at 37 °C and shaken at 300 rpm. Over the next 24 hour period 200 µL aliquots of the dispersion was collected and centrifuged at 13000 rpm for 10 minutes. The protein concentration in the supernatant was determined by Bradford assay.[34] The protein concentration determined at 0 hour (first sample) was used as the reference and this value was used to determine any increase in the concentration of BSA in the supernatant (indication of BSA release).

3.3.6 SDS-PAGE

SDS-PAGE (Sodium Dodecyl Sulphate-Poly Acrylamide Gel Electrophoresis) was performed on BSA and BSA loaded particle dispersions. BSA was loaded onto the particles in PBS buffer as described in the previous sections. Equivolumes of particle dispersion (1 mg/mL) and BSA solution (0.27 mg/mL for RNP_PME(2.5), 0.17 mg/mL for NP_PME(1.0) and 0.15 mg/mL for NP_PME(0.2)) were mixed at 20 °C and allowed to stand for 45 minutes. The concentration of BSA solutions used to load different types of particles reflect the loading capacities determined from the corresponding adsorption study. 20 µL aliquots of these dispersions were mixed with similar volume of SDS loading buffer in a 1 mL centrifuge tube. This mixture was then heated to 95 °C for 10 minutes to denature the proteins. After 10 minutes the tube was cooled to room temperature and centrifuged to remove any suspended solids. 15 µL aliquot of the supernatant was then transferred to the polyacrylamide gradient gel and the electrophoresis was performed at 180 V during 60 min.

3.3.7 Circular Dichroism

Circular dichroism (CD) was performed on BSA and BSA loaded particle dispersions (BSA@RNP_PME(2.5), BSA@NP_PME(0.2) and BSA@NP_PME(1.0)). BSA was loaded onto the particles in PBS buffer as described in the previous sections. Equivolumes of particle dispersion (1 mg/mL) and BSA solution (0.27 mg/mL for RNP_PME(2.5), 0.17 mg/mL for NP_PME(1.0) and 0.15 mg/mL for NP_PME(0.2)) were mixed at 20 °C and allowed to stand for 45 minutes. The concentration of BSA solutions used to load different types of particles reflect the loading capacities determined from the corresponding adsorption study. CD scans were performed between the wavelengths 200 to 260 nm. A total of 5 scans were performed at scan rate 10 nm/min

and data interval 0.5 nm. The sample volume was 300 µL. Measurements at pH 7.4 were performed by adjusting the pH of the dispersion using 0.1 M NaOH. The spectra thus obtained were then processed by averaging and subtracting the background. Savitsky-Golay algorithm, window size of 3 was used to smooth the spectra. The spectra were zeroed at 255 nm.

3.4 Results

3.4.1 BSA Adsorption study

Adsorption studies were performed to determine the capacity of the particles to immobilise BSA. Nanoparticle dispersions (2 mg/mL) were treated with various BSA concentrations ranging from 0.06 to 2 mg/mL. The study was carried out at pH 4.73, the isoelectric point of BSA, to promote high BSA uptake.[35] The amount of BSA taken up by the particles was determined by measuring the absorbance of the supernatant at 280 nm. Typical concentration dependent UV spectra from which the data were extracted are shown in Appendix 2. All the particles showed the same protein uptake profile up to concentration of 0.2 mg/mL (Figure 3.1). RNP_PME(2.5) particles took up 266 ± 0.84 mg/g. All other particles used in the study adsorbed significantly smaller quantities of BSA (Table 3.1 and Figure 3.1). Hard sphere particles CP_PME(1.6) adsorbed a negligible amount of protein (~ 1 mg/g).

Table 3.1: BSA load of BSA@phosphonatesilica materials at pH 4.73

Sample Name	Pore size (nm)	BSA load (mg/g)	K_d(mL/mg)
BSA@RNP_PME(2.5)	11.1	266(±0.842)	0.35
BSA@NP_PME(1.0)	2.96	180(±2.19)	0.22
BSA@NP_PME(0.2)	2.96	152(±9.50)	0.19
BSA@MSN	3	142(±9.28)	0.16
BSA@CP_PME(1.6)	Microporous	~1	

BSA load n = 3 ±std

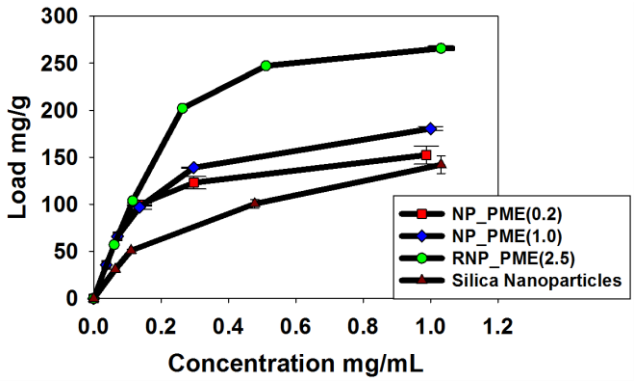

Figure 3.1: Concentration dependent BSA uptake (n = 3)

3.4.2 Time dependent BSA adsorption and dispersion stability

Time dependent BSA adsorption studies were performed on the same batch nanoparticles. The results showed that irrespective of the particle morphology, all the particles reached their maximum loading within 20 minutes of exposure to protein solutions. This suggests that the unlike the total protein uptake, organic functionalization and particle morphology had little impact on the rate of protein uptake (Figure 3.2).

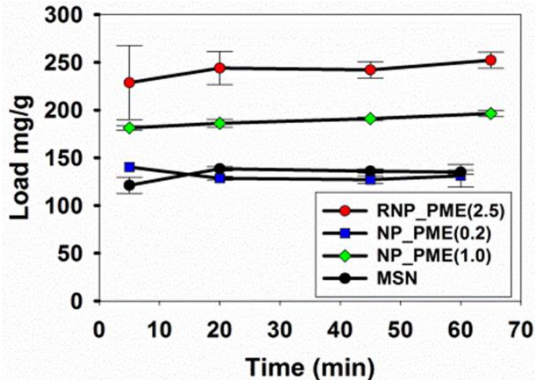

Figure 3.2: Time dependent BSA adsorption profiles (n = 3)

The stability of the BSA@RNP_PME(2.5) composite was measured under physiological conditions (pH 7.4 and 37 °C) for 24 hours. The protein release from the particles was measured by Bradford assay.[34] The study was performed at two different protein loadings (17 and 22 wt%). Protein release from the BSA@RNP_PME(2.5) was not observed even after 24 hours. Thus, BSA@RNP_PME(2.5) represented a stable composite.

3.4.3 SDS-PAGE and IR spectroscopy

Evidence for the presence of BSA on the nanoparticles was obtained using SDS-PAGE (Figure 3.3) and IR spectroscopy (Figure 3.4). SDS-PAGE is an excellent technique for separating macromolecules by weight. Separation of the macromolecules takes place under the influence of an electric field and is hence termed electrophoresis. The principle behind this method is as follows; sodium dodecylsulphate (SDS) is an anionic surfactant (Figure 3.3b) and is a well-known protein denaturant. SDS also has a negative charge at a wide pH range. Polypeptide chains bind to SDS in proportion to mass and this results in a negatively charged protein-surfactant complex. When the protein-surfactant complex is placed under an electric field it moves towards the anode. The charge/mass ratio is nearly the same for all polypeptides, therefore the separation of the polypeptides takes place based on the mass of the polypeptide. The polyacrylamide gel traps the proteins within its matrix and retards the motion of the proteins. Higher the concentration of polyacrylamide, the denser the gel and greater the retardation.[36] For this experiment 4 to 20% polyacrylamide gradient gel was used. At higher concentration (between 12 to 20%) the gel is densely packed and retards the motion of large proteins.

The sample preparation involved treating the protein samples with SDS-PAGE loading buffer. The buffer consisted of 1% SDS, mercaptoethanol, 10% glycerol, 10 mM Tris-Cl, pH 6.8, 1 mM ethylenediamine tetraacetic acid (EDTA), 2-mercaptoethanol and bromophenol blue, which served as tracking agent. 2-mercaptoethanol was the reducing agent and it was responsible for breaking the disulphide bridges and denaturing the protein molecules.[37] The gel was stained with coomassie blue. Bands were observed at 66 kDa and no other bands were observed. This suggested that the particles did not cleave the protein (Figure 3.3).

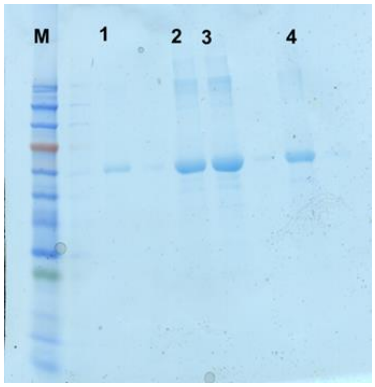

Figure 3.3: Gel Electrophoresis of BSA from LHS Marker (M), 1 BSA, 2 BSA@NP_PME(0.2); 3 BSA@NP_PME(1.0); 4 BSA@RNP_PME(2.5)

Further evidence demonstrating BSA immobilization on the nanoparticles was obtained from IR spectroscopy. IR spectroscopy was performed on lyophilized BSA@RNP_PME(2.5) particles. The spectrum showed two prominent peaks at 1649 and 1543 cm^{-1} corresponding to C=O and C-N stretching and NH bending in Amide I and Amide II groups (Figure 3.4).[38]

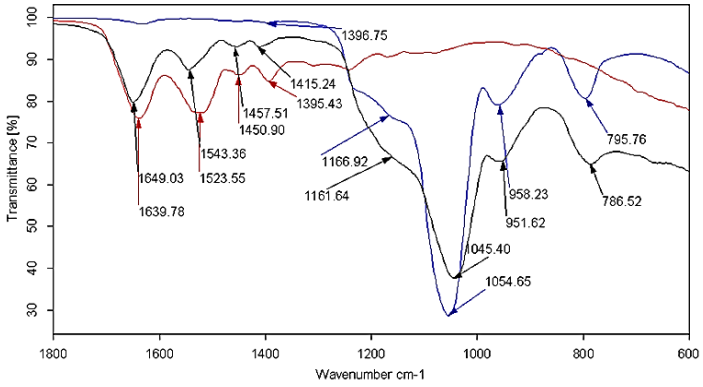

Figure 3.4: of BSA (red) RNP_PME(2.5) (blue) and BSA@RNP_PME(2.5) (black)

3.4.4 Particle dispersion properties and morphology

The protein-particle dispersion properties were studied using dynamic light scattering (DLS). This was done to assess the dispersion stability of the particles. As prepared nanoparticle-protein composites were used for this measurement. The measurements were performed at pH 4.73 and pH 7.40. BSA@RNP_PME(2.5) was the most stable composite. DLS measurements showed that the hydrodynamic radius of the

particles (R_H) did not change greatly from the parent to the BSA loaded material (Figure 3.5) thus suggesting that the composite represented discrete protein-particle composite. The particle size measurement was performed over a 2 hour period and during this time the particle size remained the same, indicating the stability of the composite. Other particle systems including BSA@NP_PME(1.0) and BSA@NP_PME(0.2) exhibited much poorer levels of stability and showed aggregation, as indicated by increased hydrodynamic radii (Table 1.2). The BSA@MSN composite could not be dispersed and was not used in further analysis.

Table 3.2: Hydrodynamic radius of BSA loaded particle composites

Sample Name	R_H pH 4.73	R_H pH 7.40
BSA@RNP_PME(2.5)	172.76(±2.01)	167.97(±0.90)
BSA@NP_PME(1.0)	484(±113)	217 (±3.0)
BSA@NP_PME(0.2)	5470	2750

n = 6 ±std for BSA@RNP_PME(2.5) measured over a 2 hour period; n = 3 ±std for BSA@NP_PME(1.0) measured during 30 minute period and n = 1 for BSA@NP_PME(0.2) at 25 minutes.

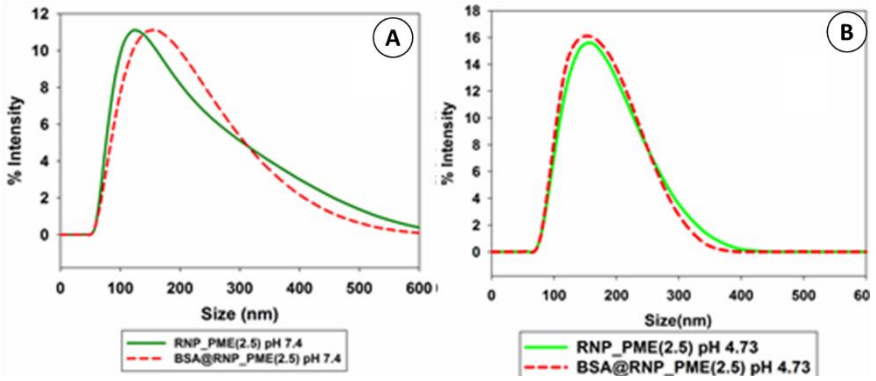

Figure 3.5: Hydrodynamic radius distribution of RNP_PME(2.5) and BSA@RNP_PME(2.5) particles at pH 7.4 and pH 4.73.

To further explore the effects of protein uptake on the particle morphology, electron microscopy analysis of the protein-particle composites was performed. SEM and TEM analysis of the BSA@RNP_PME(2.5) particles showed that the particles did not

undergo any size change upon protein adsorption (Figure 3.6 compared to Figure 2.12). This observation was in line with the results obtained from DLS experiments (Figure 3.5). SEM analysis of the BSA@NP_PME(0.2) and BSA@NP_PME(1.0) particles showed thatwhile the particle size or shape did not change, the protein loaded particles (Figures 3.6 and 3.7) showed a reduction the surface roughness compared to the parent particles (Chapter 2 Figures, 2.12 (RNP_PME(2.5); 2.16 (NP_PME(0.2), 2.17 (NP_PME(1.0))).

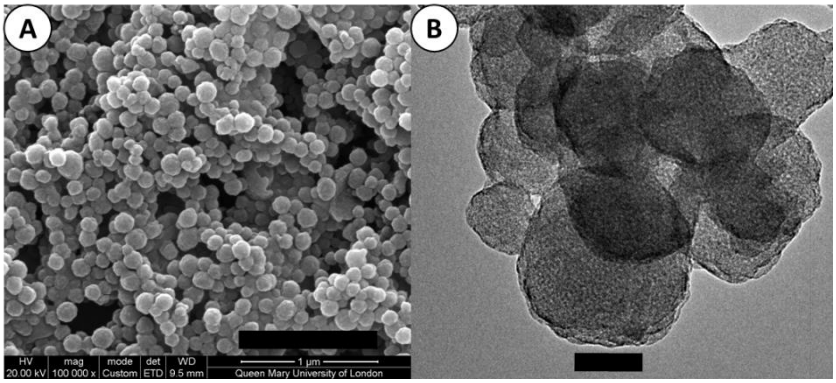

Figure 3.6: BSA@RNP_PME(2.5) particles A) SEM image(scale 1000 nm) B) TEM image (Scale 50 nm)

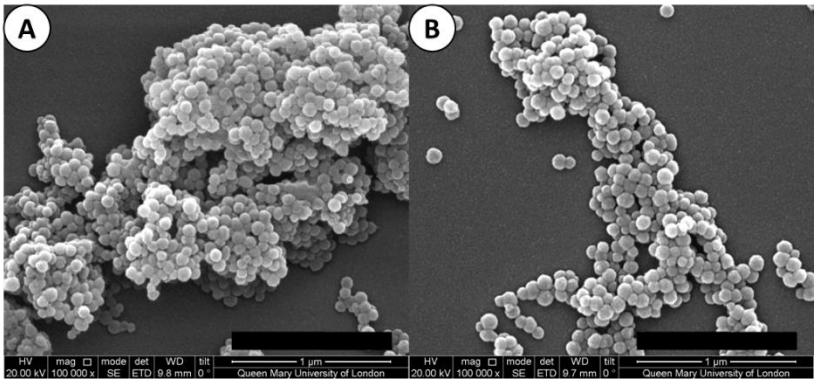

Figure 3.7: SEM of A) BSA@NP_PME(0.2) and B) BSA@NP_PME(1.0) (Scale bar 1000 nm)

3.4.5 Circular Dichroism

CD spectra of the protein loaded particles were measured to determine the effect of the particles on the protein structure. The spectra were collected between 200 to 260 nm. The spectra obtained at pH 4.73 revealed that BSA adsorbed on all three types of

particles showed a strong distortion in the protein structure. When the pH of the dispersions was raised to 7.40 by adding 0.1 M NaOH, the protein structure in BSA@RNP_PME(2.5) was fully restored, while in the other two particle systems complete restoration was not observed. (Figure 3.8)

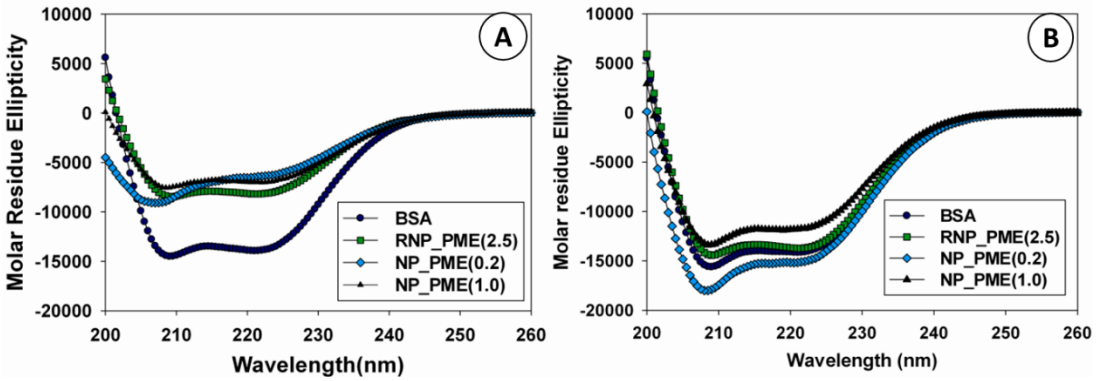

Figure 3.8: Circular dichroism spectra of protein loaded particles A) pH 4.73 and B) pH 7.40

3.5 Discussion

In Chapter 1 the characteristics of an ideal drug delivery system were discussed. They were 1) biocompatible material; 2) large quantity of drug uptake; 3) zero-premature release; 4) targeted delivery; 5) controlled release at the target site.[39] In Chapter 2, the synthesis of silica nanoparticles with phosphonate functionality was discussed. Phosphonate functionality was chosen to functionalize the particles due to its excellent biocompatibility.[40] The focus of this chapter is on the properties 2) and 3) mentioned above. As stated in the introduction, there is an urgent need to develop novel protein delivery systems that can adsorb and deliver large quantities of proteins across the cell membrane. The RNP_PME(2.5) nanoparticles have a pore size of 11.1 nm, which is suitable for the immobilization of a large number of protein molecules. In order to suitably challenge this system, bovine serum albumin (BSA) was chosen as the model protein. BSA has a molecular weight of 66 kD and has the molecular dimensions of 5 x 7 x 7 nm^3 (from the Protein Data Bank).[41]

Non-covalent immobilization of proteins predominantly involves three interactions; electrostatic, hydrogen bond and hydrophobic interactions.[42] Electrostatic forces strongly interfere with protein adsorption on surfaces. To minimize these effects and to optimise the protein uptake, the adsorption was carried out at the isolectric point (pH 4.73 for BSA).[35,43] All particles showed Langmuir type adsorption profiles (Figure 3.1 and Appendix 2 for Langmuir plots). The results from the adsorption study showed that the raspberry textured nanoparticles had very high protein uptake (266 ± 0.84 mg/g) which is higher than the reports on large pore bulk silica materials such as SBA-15 and hollow silica.[35,43-46]

3.5.1 BSA adsorption

As stated earlier, all nanoparticles reached their maximum protein load within a short time (20 minutes) (Figure 3.2) after exposure to protein solution. This result was a significant improvement over the bulk silica materials, which have been reported to take a few hours to reach their maximum loading.[35,43-46] The rapid uptake in all nanoparticles suggested that the morphological differences such as pore size (11.1 nm for RNP_PME(2.5) and ~3 nm for all other nanoparticles), surface area (772 m^2/g for RNP_PME(2.5) and 890 m^2/g for MSNs) or chemical differences such as phosphonate load (0.0 mmol/g for MSNs to 2.5 mmol/g for RNP_PME(2.5)) had little influence on the rate of protein uptake among these porous nanoparticles. These factors did however influence the final protein load on the particles.

While the particle morphology or composition had little influence on the rate of the protein uptake, these had considerable impact on the total protein uptake by the particles. Nanoparticles with low or no phosphonate loading (NP_PME(0.2) and MSNs respectively) did not show any statistically significant differences in the protein uptake

(*p=0.05*) (final protein load 152 (± 9.50) and 142 (± 9.28) mg/g respectively) (Figure 3.1). In comparison, a 5-fold increase in the phosphonate functionalization (NP_PME(1.0)) resulted in an 18 % increase in the BSA uptake despite no significant morphological differences (compared to NP_PME(0.2)). A further 2.5 fold increase in the phosphonate functionalization (RNP_PME(2.5)) resulted in a 74% increase in the protein loading (Table 3.1). The increase in the phosphonate load on the particles also resulted in an increase in the pore size from 3 nm to 11.1 nm. However, it must be noted that the microporous CP_PME(1.6) despite relatively high phosphonate loading adsorbed only 1 mg/g, indicating that accessible porosity is vital for protein uptake. It was therefore identified that a combination of high degree of porosity and phosphonate functionality was needed for high protein uptake. The BSA@RNP_PME(2.5) composites exhibited excellent stability. Protein release was not observed at pH 4.73 or at pH 7.40 at 37 °C suggesting that the protein was strongly bound to the particle surface. The phosphonate group is a strong hydrogen bond acceptor[41] and it is likely that the proteins were held on the particle surface through strong hydrogen bond interactions between the phosphonate group and the silane. The role of phosphonate was in protein binding was further established by measuring the distribution co-efficients (K_d) of the mesoporous nanoparticles. High K_d value corresponds to high binding affinity[47], the K_d values showed the following trend RNP_PME(2.5)> NP_PME(1.0)>NP_PME(0.2)>MSN, indicating a strong link between phosphonate load and protein binding (Table 3.1).

3.5.2 Dispersion properties

The presence of phosphonate on the particle surface also contributed to the stability of the particle dispersions. Based on DLS measurements the order of the stability of particle dispersion is BSA@RNP_PME(2.5)>> BSA@NP_PME(1.0)>

BSA@NP_PME(0.2)>>> BSA@MSN (Table 3.2 and Figure 3.5). It must also be noted that the protein-particle composites underwent irreversible aggregation when separated from the dispersion by centrifugation and could not be redispersed.

3.5.3 Protein structure

The presence of the protein on the particles was confirmed by IR and gel electrophoresis. Gel electrophoresis confirmed that the protein molecules did not undergo any degradation after immobilization on the particle surface (Figures 3.3 and 3.4). However, structural information could not be obtained from these results. Protein molecules are prone to denaturation and ideal protein delivery candidates should preserve the protein structure. In order to determine changes to protein structure post-immobilization, circular dichroism (CD) spectra of the protein particle composites were obtained. It should be noted that previous studies involving bulk mesoporous silica materials as BSA hosts did not present any protein structural information. The CD spectrum of BSA consists of α-helix signals including π-π* at 208 nm and n-π* at 222 nm.[48] Protein denaturation results in an attenuation of these CD signals.[42] CD therefore represented an excellent method to study protein structure changes. CD spectra obtained at pH 4.73 showed significant differences between the free and immobilized protein (on all three particles), whereby the strong attenuation of the CD signal suggested that the protein underwent significant denaturation on adsorption at this pH (Figure 3.8).[49] When the pH was raised to physiological 7.40, the protein structure of BSA@RNP_PME(2.5) was fully restored, while only partial restoration was observed in the case of NP_PME(1.0) and NP_PME(0.2) (Figure 3.8). The porosity of the particles could have played a significant role in driving the restoration of the protein structure. At pH 7.40, BSA molecules would have obtained a significant negative charge and this charge build-

up within the constrained environment in the pores of the raspberry textured particles would have resulted in a greater degree of restoration of the protein structure than for the smaller pore particles, which would have predominantly surface adsorbed protein.[50]

3.6 Conclusion

As described in the previous section an ideal drug delivery agent should be able to take up large quantities of protein molecules and prevent their premature release (zero premature release). The results presented above conclusively demonstrate that RNP_PME(2.5) nanoparticles are excellent candidates for protein uptake and delivery applications. BSA was chosen as the model protein for the study. The pore size of RNP_PME(2.5) nanoparticles was 11.1 nm, which was large enough to accommodate BSA molecules. In order to establish the factors affecting protein uptake by the nanoparticles a variety of studies were performed. The protein uptake by the particles was determined by UV-Vis spectroscopy. The presence of the protein on the particles was studied using IR and SDS-PAGE. The effect of the protein on the dispersion properties was studied using DLS. Electron microscopy (SEM and TEM) was used to study the morphological changes in the particle-protein composites. Finally, CD was used to monitor the changes in the protein structure, following particle uptake.

The rate of protein uptake by the particles was studied by treating the particles with protein solutons at pH 4.73. All the particles, irrespective of their pore size and composition, reached the maximum loading in less than 20 minutes. The results suggested that the particle morphology and pore size had no effect on the rate of protein uptake. Previous experiments involving BSA uptake by mesoporous bulk silica materials required at least a few hours of exposure to reach maximum loading. The particles presented here

therefore represent a major improvement in the development of substrates for protein immobilization.

RNP_PME(2.5) particles were found to be an excellent system for protein immobilization. Adsorption studies showed that the particles adsorbed 266 ± 0.84 mg/g protein, which was significantly higher than all the other types of particles. Based on the adsorption study the order of protein uptake was, BSA@RNP_PME(2.5) >> BSA@NP_PME(1.0) > BSA@NP_PME(0.2) ≈ BSA@MSN. This result suggested that the protein uptake was influenced by a combination of the phosphonate loading and pore size of the particles. The final protein load of the BSA@RNP_PME(2.5) particles was comparable to that obtained using large pore mesoporous silica materials. The BSA@RNP_PME(2.5) composite also displayed excellent stability, protein desorption was not observed under *in vitro* conditions. The material thus demonstrated the "no premature release" and the high protein load properties needed by a drug delivery system.

BSA@RNP_PME(2.5) particles displayed good dispersion stability compared to the other protein-particle systems. The order of dispersion stability was BSA@RNP_PME(2.5)>> BSA@NP_PME(1.0)> BSA@NP_PME(0.2)>>> BSA@MSN. However, none of the protein-particle systems could be redispersed after precipitation by centrifugation.

Finally the effect on the protein structure was determined by SDS-PAGE and circular dichroism. SDS-PAGE results showed that the protein molecules did not undergo cleavage after immobilization. The effect of the particles on the protein structure was studied using circular dichroism. CD studies revealed that the adsorbed proteins underwent significant denaturation when adsorbed at pH 4.73. However, when the pH of the media was increased to 7.40 the protein underwent either partial (NP_PME(0.2) and

NP_PME(1.0)) or complete (RNP_PME(2.5)) restoration of the native protein structure. The constrained environment within the pores of RNP_PME(2.5) particles is proposed to be responsible for the restoration of the protein structure. The results presented in this chapter demonstrate that the RNP_PME(2.5) nanoparticles possess properties that make them excellent protein immobilization agents. The next chapter discusses the results involving the study of the intracellular delivery of BSA.

3.7 References

1. J. Du, J. Jin, M. Yan and Y. Lu, *Curr. Drug Metab.*, 2012, **13**, 82-92.
2. H. Kusakabe, K. Kodama, A. Kuninaka, H. Yoshino, H. Misono and K. Soda, *J. Biol. Chem*., 1980, **255**, 976-981.
3. H. Takaku, S. Misawa, H. Hayashi and K. Miyazaki, *Jpn. J. Cancer Res*., 1993, **84**, 1195-1200.
4. V.Torchillin, *Drug Discov. Today*, 2008, **5**, e95-e103.
5. W. D. Figg, E. A. Kruger, D. K. Price, S. Kim and W. D. Dahut, *Invest. New Drugs*, 2012, **20**, 183–194.
6. R. H. Weisbart , J. F. Gera, G. Chan, J. E. Hansen, E. Li, C. Cloninger, A. J. Levine and Robert N. Nishimura, *Mol. Cancer Ther.*, 2012; **11**, 2169-2173.
7. C. T. Chu, J. J. Jacoby and R. S. Herbst, *Oncology*, 2010, **24**, 1226-1228.
8. L. N. Patel. J. N. Zaro and W. C. Shen, *Pharm. Res*, 2007, **24**, 1977-1988.
9. J. D. Benson, Y.-N. P. Chen, S. A. Cornell-Kennon, M. Dorsch, S. Kim, *Nature*, 2006, **441**, 451-456.
10. L. Hasadsri, J. Kreuter, H. Hattori, T. Iwasaki and J. M. George, *J. Biol. Chem*., 2009, **284**, 6972-6981.
11. R. Chakrabarti, D. E. Wylie and S. M. Schuster, *J. Biol. Chem*., 1989, **264**, 15494-15500.

12. V. P. Torchillin, *Nat. Rev. Drug Discov*., 2005, **4**, 145–160.

13. J. Swaminathan, C. Ehrhardt, *Expert Opin. Drig Deliv.*, 2012, **9**, 1489-1503.

14. T. M. Allen, C. B. Hansen and D. E. Lopez De Menezes, *Adv. Drug Deliv. Rev*., 1995, **16**, 267–284.

15. B. Gupta, T. S. Levchenko, V. P. Torchillin, *Adv. Drug Deliv. Rev.*, 2005, **57**, 637-651.

16. A. Vocero-Akbani, N. A. Lissy and S. F. Dowdy, *Methods Enzymol*., 2001, **322**, 508–521.

17. M. Becker- Hapak, S. S. McAllister and S. F. Dowdy *Methods*, 2001, **24**, 247–256.

18. U. Niesner, C. Halin, L. Lozzi, M. Günthert, P. Neri, H. Wunderli-Allenspach, L. Zardi and D. Neri, *Bioconjug. Chem*., 2002, **13**, 729–736.

19. N. W. S. Kam and H. Dai, *J. Am. Chem. Soc.*, 2005, **127**, 6021–6026.

20. T.E. Tjelle, A. Brech, L.K. Juvet, G. Griffiths and T. Berg, *J. Cell, Sci,*1996, **109**, 2905-2914.

21. H. H. Yang, S. Q. Zhang, X. L.Chen, Z. X. Zhuang, J. G. Xu, and X. R. Wang, *Anal. Chem*., 2004, **76**, 1316-1321.

22. X. Yang, Z. Cai, Z. Ye, S. Chen, Y. Yang, H. Wang, Y. Liu, and A. Cao, *Nanoscale*, 2012, **4**, 414-416.

23. V. Cauda, A. Schlossbauer, J. Kecht, A. Zürner and T. Bein, *J. Am. Chem. Soc*., 2009, **131**, 11361- 11370.

24. J. Gu, K. Huang, X. Zhu, Y. Li, J. Wei, W. Zhao, C. Liu and J. Shi, *J. Colloid Interface Sci.*, 2013, **407**, 236-242.

25. H. H. P. Yiu, P. A. Wright, *J. Mater. Chem.* 2005, **15**, 3690-3700.

26. S. Gao, Y. Wang, X. Dao, G. Luo, Y. Dai, *Bioresource Technol.*, 2010, **101**, 3830-3837.

27. S.-H. Wu , Y. Hung and C.-Y. Mou, *Chem. Commun.*,2011, **47**, 9972-9985.

28. I. I. Slowing, J. L. Vivero-Escoto, B. G. Trewyn and V. S. Y. Lin**,** *J. Mater. Chem.***,** 2010, **20**, 7924-7937.

29. J. F. Diaz and K. J. Balkus Jr., *J. Mol. Catal. B: Enzym.*, 1996, **2**, 115-126.

30. I. I. Slowing, B. G. Trewyn and V. S. Y. Lin, *J. Am. Chem. Soc***.,** 2007, **129**, 8845-8849.

31. a) K.-C. Kao, C.-Y. Mou, *Micropor. Mesopor. Mater.*, 2013, **169**, 7 – 15.b) H. P. Humphrey, C. H. Yiu, N. P. Botting and P. A. Wright, *Phys. Chem. Chem. Phys*., 2001, **3**, 2983-2985.

32. F. Gao, P. Botella, A. Corma, J. Blesa, and L. Dong, *J. Phys. Chem. B,* 2009**,** **113**, 1796–1804.

33. C.-Yu Lai , B. G. Trewyn , D. M. Jeftinija , K. Jeftinija , S. Xu , S. Jeftinija and V. S.-Y. Lin, *J. Am. Chem. Soc.*, 2003, **125**, 4451–4459.

34. M. M. Bradford, *Anal. Biochem.*, 1976, **72** , 1 -2, 248- 254.

35. S. B. Hartono, S. Z. Qiao, K. Jack , B. P. Ladewig, Z. Hao and G. Q. (Max) Lu, *Langmuir*, 2009, **25**, 6413-6424.

36. http://www.ruf.rice.edu/~bioslabs/studies/sds-page/gellab2.html (accessed 06/05/14)

37. http://www.ruf.rice.edu/~bioslabs/studies/sds-page/denature.html (accessed 06/05/14)

38. L. P. DeFlores, Z. Ganim, R. A. Nicodemus and A. Tokmakoff, *J. Am. Chem. Soc.,* 2009, **131**, 3385-3391.

39. W. X. Mai and H. Meng, *Integr. Biol.*, 2013, **5**, 19-28.

40. J. Tan, R. A. Gemeinhart, M. Ma and W. M. Saltzman, *Biomaterials*, 2005, **26**, 3663-3671.

41. H. M. Berman, J. Westbrook, Z. Feng, G. Gilliland, T. N. Bhat, H. Weissig, I. N. Shindyalov and P. E. Bourne, *Nucl. Acids Res.* 2000, **28**, 235-242.

42. V. Silin, H. Weetall and D. J. Vanderah *J. Colloid Interface Sci.,* 1997, **185**, 94-103.

43. Y. Chen, Y. J. Wang, L. M. Yang and G. S. Luo, *AIChe. J.*, 2008**, 54**, 298-309.

44. L. Zhu, X. Liu, T. Chen, Z. Xu, W. Yan and V. Zhang , *Appl. Surf. Sci*., 2012**, 258**, 7126-7134.

45. A. Katiyar, L. Ji, P. G. Smirniotis and N. G. Pinto, *Micropor. Mesopor. Mater.*, 2005**, 80**, 311-320.

46. C. Wu, Y. Zhang, X. Ke, Y. Xie, H. Zhu, R. Crawford, Y. Xiao, *J. Biomed. Mater. Res. A*, 2010, **95A**, 2, 476- 485.

47. K. Z. Hossain and L. Mercier, *Adv. Mater.*, 2002, **14**, 1053-1056.

48. C. H. Yu, A. Al-Saadi, S. J. Shih, L. Qiu, K. Y. Tam and S. C. Tsang, *J. Phys. Chem. C,* 2009, **113**, 537–543.

49. L. Whitmore and B. A. Wallace, *Biopolymers,* 2007, **89**, 392-400.

50. R. Ravindra, S. Zhao, H. Gies, and R. Winter, *J. Am. Chem. Soc.,* 2004, **126**, 12224-12225.

Chapter 4

Chapter 4: RNP_PME(2.5) nanoparticles for intracellular protein delivery

The effect of nanoparticles on cell viability results (Figure 4.5) from this chapter have been published in: Sai Prakash Maddala, Diana Velluto, Zofia Luklinska and Alice C. Sullivan, "Large Pore Raspberry Textured Phosphonate@Silica Nanoparticles for Protein Immobilization" *J. Mater. Chem. B*, 2014**, 2,** 903–914.

4.1 Summary

Protein (FITC_BSA, Fluorecein isothiocyante (FITC) labelled BSA) (hereafter $BSA^{\#}$) uptake and intracellular delivery using $BSA^{\#}$@RNP_PME(2.5) nanoparticles was achieved. HeLa cells were used as the model system. Both protein loaded and unloaded nanoparticles were rapidly taken up by HeLa cells. Nanoparticle uptake and localization within the cells was studied using confocal microscopy and transmission electron microscopy. Protein free Rhodamine B isothiocyante (RITC) labelled RNP_PME(2.5), RITC@RNP_PME(2.5) (hereafter RNP*_PME(2.5)) particles were taken up by caveolar receptor mediated uptake, while $BSA^{\#}$@RNP*_PME(2.5) particles were taken up by folic acid receptor mediated uptake. Folic acid receptors are over expressed on many types of cancers and $BSA^{\#}$@RNP*_PME(2.5) nanoparticles have great potential for cancer cell targeting applications.

4.2 Background

Proteins and nucleic acids are integral components of the cells. Proteins drive essential cell functions such as gene regulation, DNA replication and enzyme catalysis.[1] Many diseases such as cardiovascular disease, cancer, arthritis arise due to the presence of defective proteins, which in turn arise from defective genes.[2] Molecular evaluation of various diseases routinely involves the detection of defective genes and proteins.[3] For example, p53 is a protein involved in the regulation of cell cycle and plays an important

role in inducing apoptosis or cell death upon detecting defective genes and is therefore vital in preventing the occurrence of cancer. However, as much as 60% of the cancers have a defective *TP53* gene (gene associated with p53 protein).[4] Thus large biomolecules are not only important for disease detection and diagnosis, they are also important clinical targets and can also be used as therapeutic agents.[2] The focus of this chapter is on the latter, specifically involving the immobilization and delivery of proteins.

Protein delivery presents an attractive option for treating various disorders such as cancer, neurological diseases such as Alzheimer's, heart disease and vaccine development.[5] During the last two decades, extensive research has been focussed on the development of monoclonal antibodies that can target and shut down specific cell pathways. Drugs based on these antibodies are currently on the market. However, there are many challenges involved in efficient delivery of these proteins. The most formidable challenge arises from the exclusion of large molecules (> 1000 Da) by the cell membrane.[5] Some of the negatively charged proteins are prevented from entering the cells due to charge repulsion.[2] For therapeutic purposes, it is important to develop pathways that can help the proteins retain their structure and function.

The primary means of delivering proteins involves the use of small cell penetrating peptides (CPP). There are three different types of CPPs. The most commonly used CPPs are polycationic and contain large numbers of arginine and lysine residues.[6] The widely used TAT peptide (trans-activating transcriptional activator) is an example of this kind of CPPs. Other types of CPPs contain alternating polar charged and non-polar residues or a sequence of hydrophobic residues. CPPs have been shown to be highly versatile and have been used to deliver proteins with sizes between 15 to 115 kDa. TAT conjugated antibodies have been evaluated at preclinical stage and have shown good results. However, there are two major challenges involved in the use of CPPs. First the

TAT peptide must be conjugated to the protein. In order to achieve this, the protein must be modified chemically to conjugate it to the CPPs. Second, many of the TAT conjugated proteins have been shown to remain entrapped in the endosomes.[7] Other methods of protein delivery include electroporation,[8] where small pores are introduced in the cell membrane through the application of electric current in order to facilitate protein uptake and cell membrane permeabilization through the use of detergents or pore forming bacterial toxins.[9] Neither of these methods lend themselves to clinical protein delivery applications and have been shown to irreparably damage the cell membrane.[8] Various pathways that a protein carrier might take are illustrated in Scheme 1.

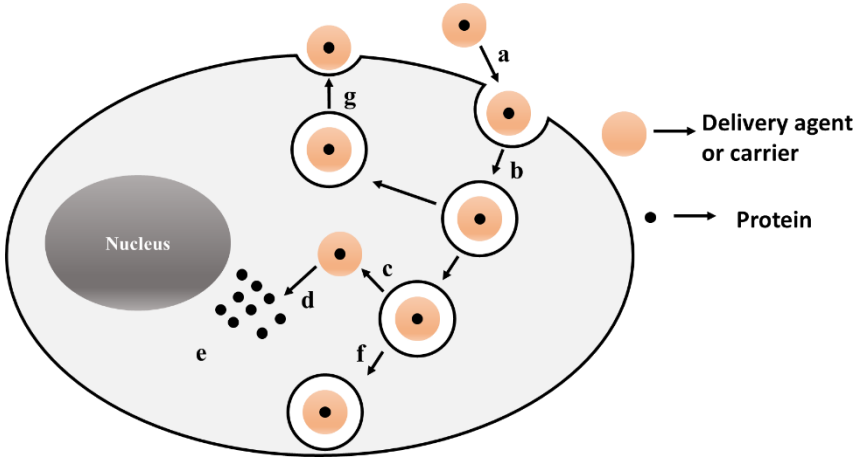

Scheme 1: Various pathways a protein carrier might follow upon cell entry a) protein carrier uptake, b) encapsulation in early endosome, c) endosomal escape and carrier release, d) controlled release of encapsulated protein, e) protein action inside the cell, f) transfer to endosomes and digestion, g) exocytosis of the carrier.

Nanoparticle based delivery agents offer an attractive option for protein delivery. They have been used to address the three main challenges involved in protein delivery, 1) cell uptake; 2) endosomal escape; 3) controlled delivery. Additionally, the particles have been functionalized with specific ligands to achieve targeted delivery. Protein loading in nanoparticle carriers was achieved either by direct conjugation, physical adsorption or encapsulation as discussed below.

Direct conjugation has been performed between proteins and PEG (polyethylene glycol) derived polymers. Several FDA (Food and Drug Administration) approved PEG-protein conjugates have been approved for clinical use.[10] The main advantage of PEGylation was to increase the circulation times of these proteins. Polyethyleneimine (PEI) protein conjugates have attracted much attention due to their superior cell uptake properties. PEI is a cationic polymer. It can be conjugated to the acid groups on the protein surface through DCC coupling. Several proteins such as ribonuclease (RNase), enhanced green fluorescent protein or IgG antibody for example, have been conjugated to PEI without any loss in function and were successfully internalized into the cells.[11] An important therapeutic application of the system involved the delivery of the denatured tumour suppressor protein p53 into sarcoma derived Saos-2 cells. The denatured protein underwent reassembly under the reducing conditions of the cytosol and induced apoptosis in the cancer cells.[12] Lackey *et al.* developed a delivery system for anti-CD3 antibody using poly(propylacrylic acid) (PPAAc) as the conjugating polymer. PPAAc is a pH sensitive polymer, which has been shown to destabilize the endosomes. PPAAc conjugated anti-CD3 antibody was observed through confocal microscopy to have escaped the endosomes and was successfully delivered into the cytosol.[13] In all the above studies conjugation of the protein molecules to polymers helped in cell uptake and endosomal escape of the protein. This was due to the properties of the individual polymers that were used for conjugation. However, the method has a few drawbacks. Polymer conjugation to the protein surface was achieved through DCC coupling. The method requires the availability of free amine or carboxylic acid groups on the surface. These surface groups play an important role in stabilizing the protein structure. Excessive conjugation would therefore disrupt the delicate tertiary structures of the proteins, which

could result in loss of function.[2] The method is therefore not entirely suitable for drug delivery applications.

Polymeric micelles and liposomes have been widely used to entrap and deliver protein molecules. The method can be used to entrap large quantities of protein molecules and release at the target site in a controlled way. Encapsulation of the protein prevents the need for chemical conjugation, thus preventing unnecessary structural changes.[2] The method, therefore has an advantage over direct conjugation. Polymeric micelles consist of AB or ABA type block co-polymers (where A is a hydrophilic polymer such as PEG and B is a hydrophobic polymer such as polypropylene glycol). Lee *et al.* used cationic block co-polymer PEG-pAsp(DET) micelles to encapsulate membrane impermeable protein, cytochrome c. The micelles underwent dissociation at pH 5.5 (pH of the endosomes). The micelles were used to escape the endosomes and efficiently deliver protein molecules into the cytosol.[14] Other groups used poly(L-lysine)-poly(ethylene glycol)-folate (PLL-PEG-FOL) co-polymers to encapsulate and deliver FITC-BSA into folate receptor expressing, KB cells.[15] Poly(γ-glutamic acid) modified with amino acid derivatives, L-phenylalanine ethylester and L-tryptophan methylester groups was used to encapsulate ovalbumin and recombinant HIV-1 gp120 and was injected into mice. The protein encapsulated micellar system elicited immune responses in mice, demonstrating the possibility of using this system for vaccine development.[16] Many phospholipids and lipids self-assemble to form bilayered vesicles, known as liposomes. Liposomes have been used to encapsulate a variety of molecules for drug delivery applications. Liposomes are highly versatile and were used to encapsulate and deliver a variety of protein molecules into the cells. Liposomes also display endosomal escape making them more suitable for intracellular protein delivery.[17] Liposomes derived from *N*-[1-(2,3-dioleyloxy)propyl]-*N, N, N*-trimethylammonium chloride (DOTMA) were used to

encapsulate T7X556, a mammalian transcriptional regulator and a glucocorticoid receptor derivative. The encapsulated protein was successfully delivered to nucleus.[18] Other groups reported the encapsulation of β-galactosidase, caspase-3, caspase-8 and gramzyme B in liposomes synthesized from trifluoroacetylated lipopolyamine and dioleoyl phosphatidylethanolamine (DOPE).[19] The protein expression was observed following uptake in a variety of cell types. The latter three proteins induced apoptosis. Other proteins such as anti-α-tubulin IgG and therapeutic membrane proteins, pro-apoptotic BAK and voltage-dependent anionic channel proteins were also encapsulated and delivered into cells.[20] The above examples illustrate the versatility of the encapsulation approach. However, the delivery vehicles used have numerous drawbacks. Polymeric micelles, for example, are difficult to synthesize. Additionally, the micelles have been demonstrated to have chronic cytotoxity to the liver.[21] Liposomes on the other hand are highly expensive, displayed premature drug release and have been shown to have very low shelf life. Thus, the applications of these vehicles are limited.[22]

Finally, protein molecules can be attached to various polymers through electrostatic or van der Waals interactions.[2] Physical interactions between the protein molecules and the polymers can be fine-tuned to change the delivery profile of the adsorbed polymer. Cationic polymers such as polyethyleneimine, polylysine and polyarginine have been used to deliver a variety of proteins across the cell membrane. These polymers were chosen due to their ability to penetrate the cell membrane and display endosomal escape.[22] However, polymers have low surface area and therefore only have a limited capability to carry protein molecules across the cell membrane.

Inorganic nanoparticles such as mesoporous silica nanoparticles (MSNs) have been be used to overcome the limitations described above. Mesoporous silica nanoparticles have unique features such as high surface area, high pore volume and

tunable pore size.[23] The particle surface chemistry can be altered by attaching various organosilanes. The particle properties can thus be fine-tuned to enable endosomal escape.[24] This highlights the suitability of these nanoparticles for protein delivery. However, only a few reports exist that describe protein uptake and delivery by MSNs.[29] The main challenge here involves the production of MSNs with large pores. Pore sizes greater than 10 nm are required for protein delivery, as they promote efficient protein encapsulation. MSNs typically have pore sizes in the range of 2 to 4 nm, many protein molecules have dimensions larger than those pore sizes, and as a result little or no protein adsorption was observed due to pore size exclusion effect.[25] A few studies describing the use of small pore MSNs as potential vaccine delivery agents have been reported.[26] An alternative encapsulation method has been published, which involved reverse micellar encapsulation of the protein molecules. While the method resulted in high weight percent of protein adsorption, the protein molecules were not accessible, hence these protein encapsulate particles could not be used for drug delivery applications.[27,28] Lin *et al.* developed large pore MSN synthesis using pore enlargement agents. Pore size of 5.4 nm was observed using this method. However, severe distortion in the particle shape was also observed, which could potentially limit the biomedical applications of these particles.[29] Large pore silicas such as SBA-15 have been used to encapsulate large quantities of proteins mainly for catalytic applications. The studies using these systems revealed that the immobilized proteins had superior stability to temperature and denaturing agents compared to native proteins.[30,31] This example highlights the potential of large pore silica nanoparticles for protein delivery applications. The following chapter discusses this application using RNP_PME(2.5) nanoparticles to deliver bovine serum albumin (BSA) across the cell membrane of HeLa cells.

4.3 Experimental

4.3.1 Materials

RNP_PME(2.5) was synthesized using the methods described in the previous chapter. BSA and PBS (Phosphate Buffered Saline) tablets were purchased from Sigma Aldrich and used without any further purification. PBS (10 mM) solution was prepared by dissolving one PBS tablet in 200 mL of deionized water. NaOH pellets, ethanol and HCl (35% w/w) was purchased from VWR and used without further purification. The particle synthesis was carried out in deionized water dispensed from an 18 mΩ Millipore system supplied by Elba UK.

4.3.2 Characterization

IR spectra were recorded on a Bruker-FTIR spectrophotometer with an ATR accessory containing a ZnSe crystal. 16 scans between 600 and 4000 cm^{-1} were performed for each sample. UV measurements were performed on a Perkin Elmer UV spectrophotometer, containing a Deuterium lamp source for the UV region and Tungsten lamp source for the visible region. The hydrodynamic radius, R_H of the particles was measured on a Malvern Zetasizer Nano ZS instrument equipped with a 633 nm laser. For analysis a 1 mg/mL particle dispersion in a glass cuvette was prepared by sonication for (15 min) in PBS (10 mM) with pH adjusted to 4.73 or 7.4 using 1 M HCl and 2 M NaOH a 5 mm ultrasonic probe was used for sonication of the sample. Stock dispersions of the particles were prepared by dispersing 20 mg of particles in 10 mL of PBS and the height of liquid was kept constant at 80 mm, the inner radius of the tube was 15 mm. Sonication was carried out at 65% amplitude. TEM (Transmission Electron Microscope) images were obtained using a JEM JEOL 2010 TEM operating at 200 kV. Samples were prepared by dipping carbon coated TEM grids (Agar Scientific) into the particle dispersions. SEM

(Scanning Electron Microscope) images were obtained from gold coated samples, using an FEI 100 instrument (Oxford Instruments) operating at 20 kV; spot size of 10 nm was used for the analysis. CD (Circular Dichroism) measurements were performed on 300 µL samples in 1mm path length cuvettes using an Applied Photophysics Chirascan CD Spectrometer, equipped with a 150 W air cooled Xe arc lamp. FLUOstar OPTIMA optical plate reader was used to analyze HeLa cell cultures following MTT assay. Cells were imaged by Leica TCS SP5 confocal microscope.

4.3.3 Synthesis of FITC labelled BSA or BSA#

FITC labelled BSA was synthesized as follows. BSA (20 mg) was dissolved in carbonate buffer, pH 9.2 (10 mL). FITC (1 mg) was dissolved in 1 mL of carbonate buffer. The BSA solution was placed in a temperature controlled shaker at 25 °C and was shaken gently at 150 rpm and was allowed to equilibrate for 30 minutes. After equilibration, the FITC solution was added in aliquots of 50 µL, while gently shaking the reaction flask. The flask then shaken in the dark for 4 hours. After 4 hours, the reaction mixture was transferred to a dialysis tube and dialyzed against water for 48 hours (3 washes), in the dark to prevent quenching of fluorescein. After 48 hours, the contents of the dialysis bag were lyophilized. The yellow-orange solid obtained was used for further experiments.

4.3.4 Synthesis of Rhodamine B labelled RNP_PME(2.5) or RNP*_PME(2.5)

To Rhodamine B isothiocyante solution (0.2 mg/mL, 10 mL) in absolute ethanol, aminopropyltriethoxysilane, APTES, ($3.3x10^{-6}$ mol) was added and stirred for 5 hours. The resultant solution was then stored at -25 °C. Prior to use, the dye mixture was allowed to stand in the dark, until it reached room temperature. Rhodamine B labelled RNP_PME(2.5) was syntesized by treating RNP_PME(2.5) (73.9 mg) with the above dye solution. Following the reaction, the particles were separated by centrifugation and the

supernatant was discarded. The particles were then passed through repeated centrifugation and suspension cycles until the supernatant was clear of any dye. The pink coloured particles were then dried under high vacuum at 60 °C for 10 hours. The particles thus obtained were designated RNP*_PME(2.5)

4.3.5 Adsorption of BSA

The pH of PBS solution (10 mM) was adjusted to 4.73 using 1 M HCl solution. 2 mg/mL dispersions of the nanoparticles (RNP*_PME(2.5), were prepared by sonicating the particles (20 mg) in PBS (pH 4.73, 10 mL) using an ultrasonic probe for 45 minutes. The sonicator amplitude was set to 65% and pulse time of 45 seconds was used for sonication. After sonication the dispersion was allowed to cool down to room temperature. Particle dispersions (1 mL) were then added to different concentrations (from 0.06 to 2 mg/mL) of BSA solutions (1 mL), gently mixed and allowed to stand for 45 minutes (at 20 °C). After 45 minutes, the dispersions were centrifuged at 14,000 rpm for 10 minutes and the supernatant was collected. BSA concentration in the supernatant was determined by Bradford assay (Calibration curve provided in Appendix 4) .[32]

4.3.6 Synthesis of BSA#@RNP*_PME(2.5)

The general protocol for BSA#@RNP*_PME(2.5) synthesis was as follows. RNP*_PME(2.5) (2 mg/mL) dispersions in PBS (pH 4.73) were prepared by ultrasonicating the particles in the buffer. Protein solutions were prepared at the same pH (as described above). Different concentrations ranging from 0.247 to 0.574 mg/mL were prepared and mixed with equivolumes of particle dispersions. Adsorption studies revealed that complete protein uptake took place at these concentrations.

4.3.7 Cellular uptake: General protocol

HeLa cells, a cervical cancer cell line, were chosen as the model system to study the nanoparticle uptake. The cells were seeded on coverslips in 12 well plates with a density of 10^5 cells/mL in 2 mL of Dulbecco's modified eagle medium. The cells were incubated for 24 hours at 37 °C under 5% CO_2 and after the 24 hours confluent cell growth was observed. The cell culture media was then removed and 0.9 mL of fresh media and 0.1 mL of particle dispersions (e.g.1 mg/mL RNP*_PME(2.5)) in PBS at pH 7.4 were added and incubated for different time periods between 1 to 6 hours. The cell media was then removed and thoroughly washed with PBS to remove any loosely adsorbed particles. The cells were fixed using paraformaldehyde (4 wt%) and stained with mounting media containing DAPI. The particle uptake was studied using a Leica TCS SP5 confocal microscope.

4.3.8 Cellular uptake: Time dependent uptake

The cells were cultured according to the procedure described above. Following the addition of nanoparticles, RNP*_PME(2.5) (1 mg/mL) or $BSA^{\#}$@RNP*_PME(2.5) (1 mg/mL with $BSA^{\#}$ load 223 mg/g), the cells were incubated for different time periods between 1 to 6 hours. The particles were fixed and stained as described above. The experiment was performed in duplicate.

4.3.9 Cellular uptake: Protein load dependent uptake

The procedure described above was followed to prepare the cell culture. Following this, different protein loaded particles, 111.1, 166 and 223 mg/g $BSA^{\#}$ load were incubated with the cells for 6 hours. Following this, the cells were fixed and stained as described above. The experiment was performed in duplicate.

4.3.10 Cellular uptake: Prolonged incubation

Protein loaded BSA#@RNP*_PME(2.5) (1 mg/mL and BSA# load 223 mg/g) and protein free RNP*_PME(2.5) (1 mg/mL) particles were used for this experiment. HeLa cells were incubated with the particles as described above for 6 hours. After 6 hours the media was removed and cells were washed twice with PBS and fresh media was added. The cells were the incubated again for different time periods, 1.5 hours, 2.5 hours and 3 hours. The cells were fixed and stained as above. The experiment was performed in duplicate.

4.3.11 Cellular uptake: Mechanism of uptake

In order to determine the mechanism of uptake, the cells were pre-treated with various receptor blocking reagents as described in the literature.[24,33] The general procedure is as follows; the confluent cells were treated with the receptor blocking agents (450 mM sucrose for clathrin, 5 μg/mL Nystatin for caveolar and 10 mM folic acid for folate receptor blocking). All blocking reagents were dispersed in DMEM media for 30 minutes. After treatment for 30 minutes the cells were washed thrice with PBS to remove traces of the reagents and fresh media (0.9 mL) with nanoparticles (0.1 mL, 1 mg/mL) were added and incubated for 6 hours. Following this, the cells were stained and fixed as described above.

4.3.12 HeLa cell sample preparation for TEM analysis

Cell culture and incubation with nanoparticles (both protein loaded (223 mg/g) and protein free nanoparticles) were performed as described above. Samples were prepared for TEM analysis based on a previously published method.[34] After incubating the particles for the required time period, the cells were treated with 4 wt% gluteraldehyde

in 0.125 M PBS for 2 hours. After 2 hours, the cells were suspended in 0.125 M PBS and washed twice. The cells were then transferred to fresh PBS (0.125 M) and stored at 4 °C, overnight. The cells were then treated with 1% osmium tetroxide and incubated at room temperature for 1 hour. The cells were then washed twice with distilled water. Following the washes, the cells were suspended in 30% industrial methylated spirt (IMS) for 15 minutes. The cells were then isolated by centrifugation and the suspended in 50% IMS for 15 minutes and centrifuged again. The cells were then suspended in 70% IMS for 15 minutes and centrifuged. The cells were then suspended in 90% IMS for 15 minutes and centrifuged. The cells were then suspended in 100% IMS for 20 minutes and centrifuged. The last step was repeated twice. The cells were next dispersed in propylene oxide for 5 minutes and centrifuged. The step was repeated twice. Finally, the particles obtained after this final step were transferred to 50 wt% araldite and the resin was allowed to set and the set resin was added to specially designed moulds. Once the resin settled, the araldite stubs (thickness 50 nm) were sectioned using a diamond knife. The newly cut sections were placed on copper TEM grids for characterization.

4.3.13 Cell viability study

HeLa cells were seeded in 24 well plates with a density of 10^5 cells/mL in 1 mL of Dulbecco's modified eagle medium and incubated at 37 °C under 5% CO_2. The media was then removed and fresh media containing different particle concentrations ranging from 0 (control) to 0.2 mg/ mL, was added to the wells and incubated for 24 hours. For the protein loaded samples, the nanoparticle concentration was fixed at 1 mg/mL and the protein load was varied between 47 to 223 mg/g. $BSA^{\#}$ cytotoxicity was also analysed, protein weight between 0 (control) to 50 µg was used for analysis. The study was done in triplicate. After incubation the cell culture medium was removed and the cells were

washed with PBS. The cells were then incubated for 2 hours with 0.5 mL of 5 mg/mL MTT solution, prepared by dissolving MTT tetrazolium salt in PBS. After 2 hours the MTT solution was discarded and 0.3 mL of isopropanol was added to the wells and thoroughly mixed to dissolve the formazan crystals. 0.1 mL of this solution was then transferred into 96 well plates and the optical density (OD) at 570 nm was measured using a microplate reader.[35] Cell viability was calculated by measuring the ratio of the mean OD at each particle concentration to that of the control (no particles). The values are given in % survival ± % RSD (relative standard deviation).

4.4 Results

4.4.1 Nanoparticle characterization

RNP*_PME(2.5) nanoparticles were synthesized as described in Chapter 1 and labelled as described in section 4.3.4. The label free particles had an average size of 80 nm (size distribution between 60 to 90 nm) (Figure 4.1). Following synthesis, the particles were modified with Rhodamine B silane reagent prepared by reacting Rhodamine B isothiocyanate (RITC) with 3-aminopropyl triethoxysilane (Scheme 2). The particles had high surface area of 641.8 m^2/g, the pore size of the particles was 11.6 nm and the pore volume was 0.821 mL/g. (Figure 4.2 and Table 4.1).

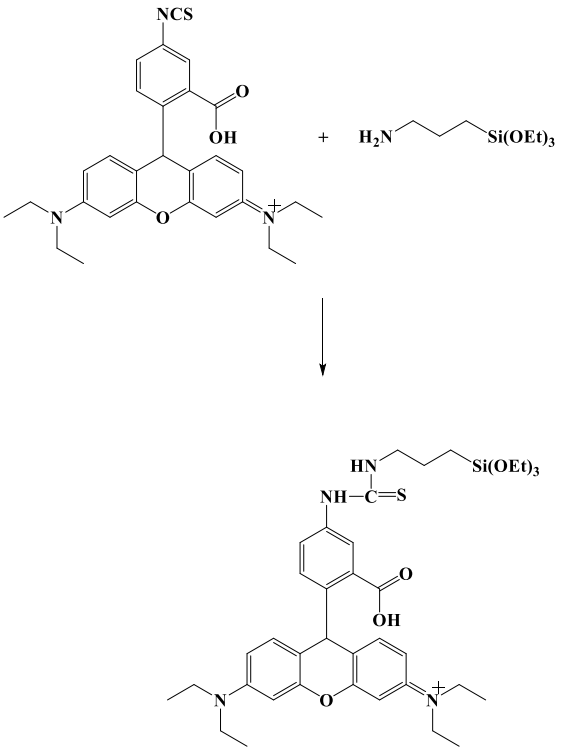

Scheme 2: Rhodamine B silane synthesis

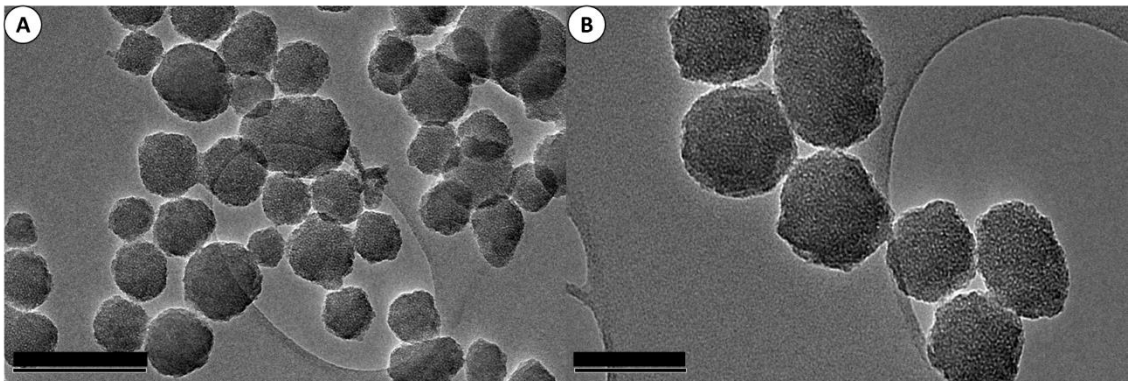

Figure 4.1: TEM images of RNP*_PME(2.5) (Scale A) 200 nm ; B) 100 nm)

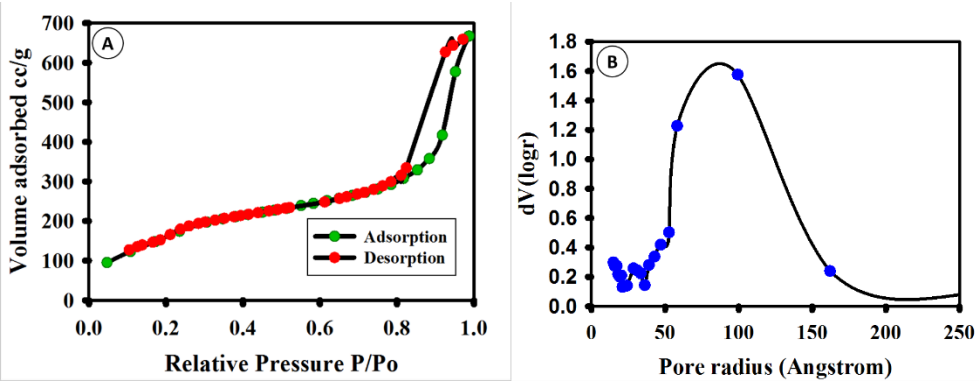

Figure 4.2: Nitrogen sorption porosimetry of RNP_PME(2.5) A) Sorption isotherm; B) BJH pore size distribution

Table 4.1: Morphological properties of RNP_PME(2.5)

No.	Property	RNP_PME(2.5)
1	Particle shape	Spherical
2	Particle size distribution	60-90 nm
3	Surface area	641.8 m^2/g
4	Pore volume	0.821 mL/g
5	Pore size	11.64 nm

4.4.2 BSA# adsorption on RNP*_PME(2.5)

BSA# was synthesized by reacting FITC to BSA under basic conditions, and characterized by UV-Vis spectroscopy to confirm the presence of fluorescein (Appendix 4). Adsorption of BSA# to RNP*_PME(2.5) was performed at the isoelectric point of BSA (pH 4.73, PBS) and the total maximum load of BSA# adsorbed onto the RNP*_PME(2.5) particles was determined (Figure 4.3). The maximum protein load was 240.13 ± 5.62 mg/g.

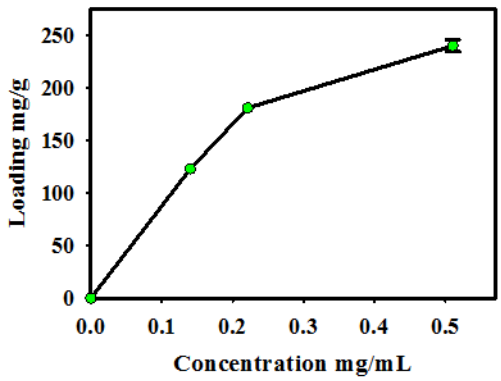

Figure 4.3: Adsorption of BSA# to RNP*_PME(2.5) particles (n = 2 ± Std. dev.)

4.4.3 Properties of the BSA# adsorbed nanoparticles BSA#@ RNP*_PME(2.5):

Following the adsorption study, the suitability of the particles for cell studies was determined by measuring the dispersion properties and by determining the effect of adsorption on the secondary structure of the protein (determined using CD). The dispersion properties of the particles were measured in Dulbecco's Modified Eagle Medium (DMEM) media (at physiological pH, 7.4). The RNP*_PME(2.5) particles showed an increase in the hydrodynamic radius, compared to the dispersion in PBS. This was probably due to aggregation of the nanoparticles due to the high ionic strength of the media (Figure 4.4) (compared to PBS Figure 3.5). The protein loaded particles, BSA#@ RNP*_PME(2.5) however, did not show any aggregation. It is possible that some of the BSA# was present on the particle surface and acted as a stabilizing agent.

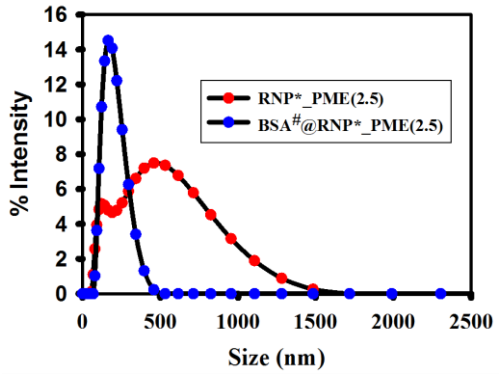

Figure 4.4: DLS data of the BSA loaded and unloaded particles in DMEM media.

Analysis of the effect of immobilization on the protein structure was performed by Circular Dichroism (CD), the analysis was performed in PBS at physiological pH 7.40. CD analysis revealed that immobilization and FITC functionalization did not affect the protein structure (Figure 4.5).

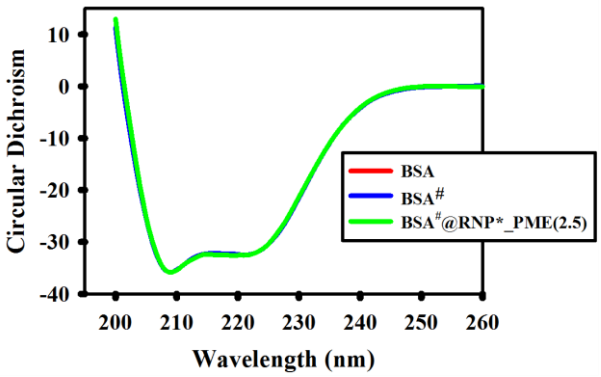

Figure 4.5: Circular Dichroism spectra of BSA, BSA$^{\#}$ and BSA$^{\#}$@ RNP*_PME(2.5)

4.4.4 Cell Viability studies

HeLa cells were chosen as the model system to study nanoparticle uptake. Protein free nanoparticles were tested for concentration dependent toxicity (RNP*_PME(2.5) concentration ranging from 0.025 to 0.2 mg/mL in cell culture media) (Figure 4.6). BSA$^{\#}$ loaded nanoparticles BSA$^{\#}$@ RNP*_PME(2.5) were tested for the effect of varying protein concentration on the cell cytotoxicity (BSA$^{\#}$@ RNP*_PME(2.5) concentration was kept constant at 0.1 mg/mL so maximum BSA dose concentrations were 0.07-0.42 µM) (Figure 4.7). In both cases no toxicity was observed. BSA$^{\#}$ cytotoxicity was also tested and no cytotoxicity towards HeLa cells was observed upon exposure to 50 µg/mL or 0.75 µM of the protein.

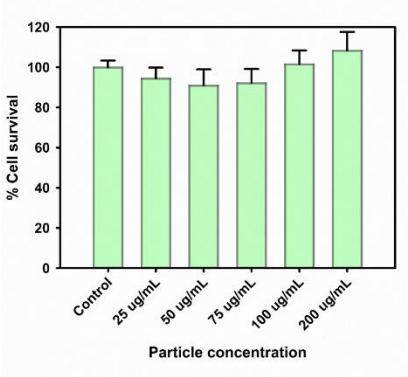

Figure 4.5: Effect of RNP*_PME(2.5) particle concentration on HeLa cell survival. (n = 3 ± Std. dev.)

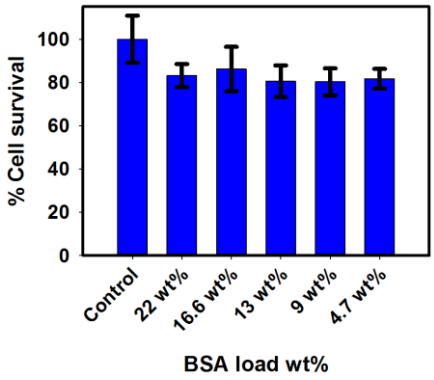

Figure 4.6: Effect of BSA$^{\#}$ load in nanoparticles BSA$^{\#}$@ RNP*_PME(2.5) on cell survival (n = 3 ± Std. dev.)

4.4.5 Time dependent uptake of RNP*_PME(2.5)

Nanoparticle uptake by HeLa cells was studied using the Spots package in Imaris software. RNP*_PME(2.5) nanoparticles were rapidly taken up by the cells. About 63% of the total particle uptake was measured within the first hour. A slight increase in the particle uptake was observed during the next hour and the value remained constant for the next two hours followed by a further increase after 6 hours, this was however not statistically significant at $p = 0.01$ (Figure 4.7 and 4.8). The Spots package was used to prepare 3D representations of the particle distribution in the cells (Figure 4.9). It must be mentioned that the particles localized over the nucleus were found to be either above or below the plane of the nucleus and were absent in the confocal image sections that

contained the nucleus. The confocal images from Figure 4.8 and 3D representations from Figure 4.9 show that the particles were initially distributed around the cells in aggregates (at the 1 hour time point), further increase in time resulted in an even distribution of the particles within the cells. TEM analysis was performed on the cell after 6 hours of exposure to the particles. Many of the particles were located in the cytoplasm (Figure 4.10 B), some of the particles were observed in vesicles (Figure 4.10 C) and particle uptake by caveolae (Figure 4.10 D) was also observed. No particles were detected in the nucleus (Figure 4.10 E)

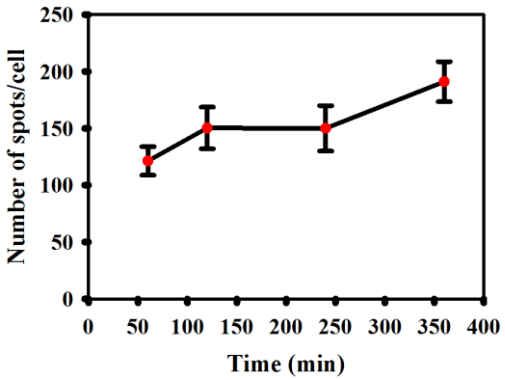

Figure 4.7: RNP*_PME(2.5) nanoparticle uptake versus time (n = 20 ± SEM (standard error of mean))

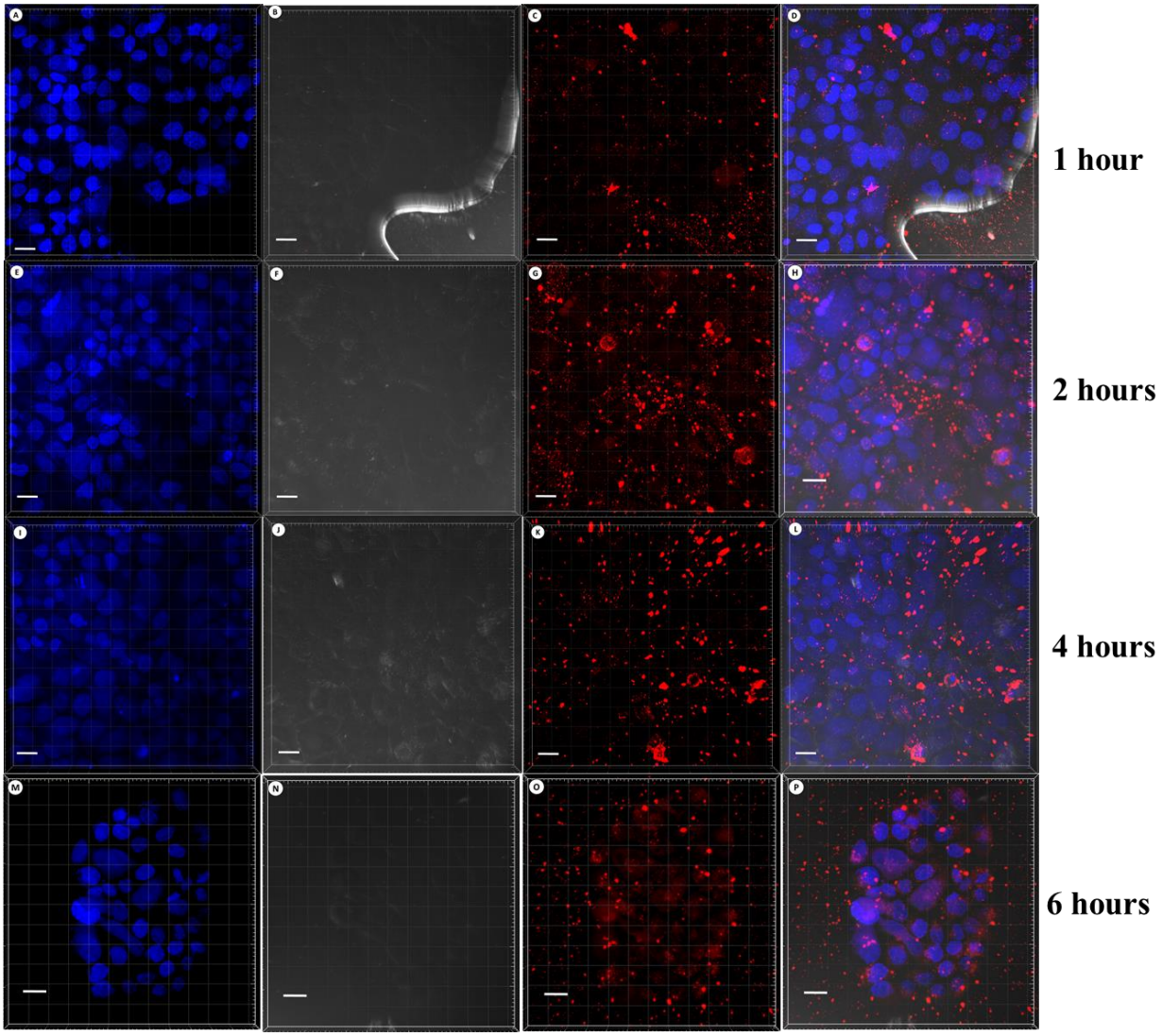

Figure 4.8: Time dependent uptake of RNP*_PME(2.5) nanoparticles by HeLa cells (Scale 20 µm). The red spots indicate the presence of Rhodamine B isothiocyanate functionalized nanoparticles RNP*_PME(2.5)

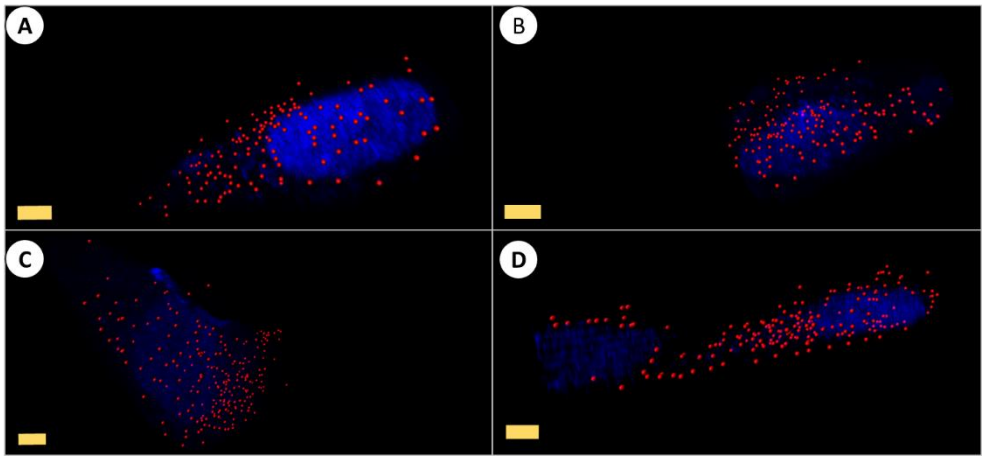

Figure 4.9 : Distribution of RNP*_PME(2.5) nanoparticles in HeLa cells at different exposure times (Scale bar 10 µm in all images); A) 1 hour; B) 2 hours; C) 4 hours and D) 6 hours

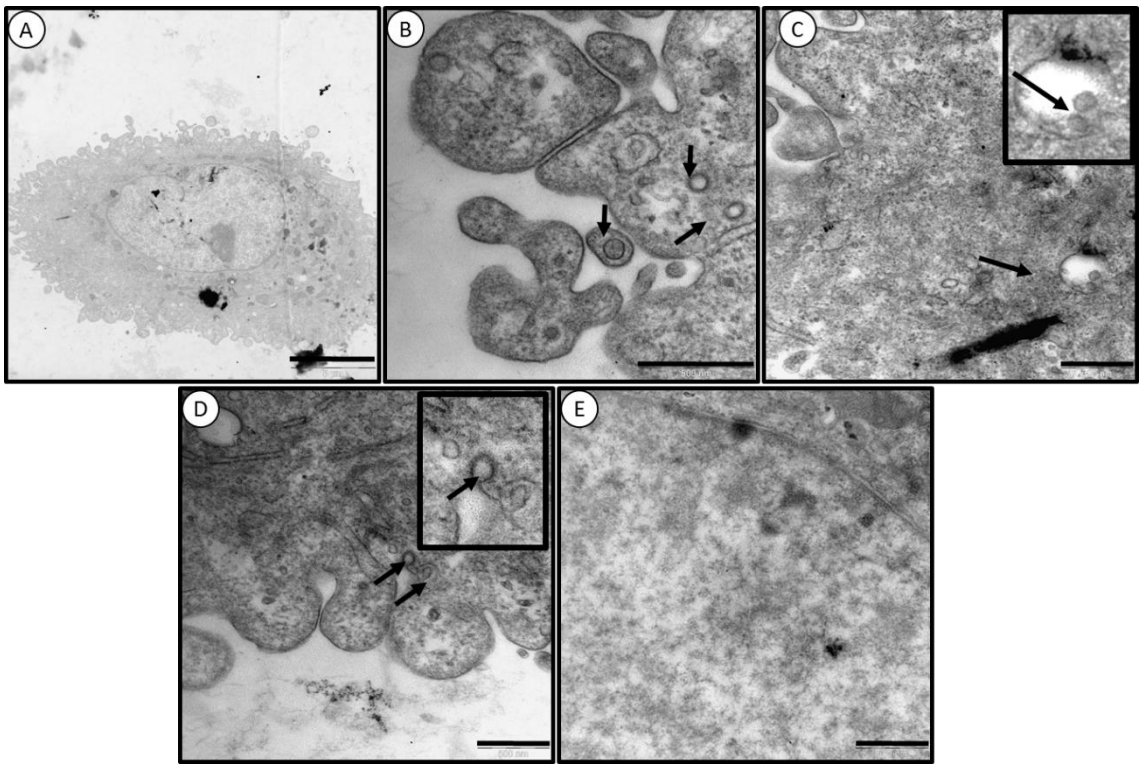

Figure 4.10: TEM images of HeLa cells 6 hours after RNP*_PME(2.5) particle uptake. A) HeLa cell (Scale 5 µm); B) Particles in cytoplasm (black arrows) (Scale 500 nm); C) Particles within vesicles (black arrow) (Scale 500 nm) (Inset 2X magnification of the region containing the particles, indicated by black arrows); D) Caveolae on the cell surface (black arrow) (Scale 500 nm) (Inset 2X magnification of the region containing the particles, indicated by black arrows); E) Nucleus (Scale 500 nm)

4.4.6 Uptake of BSA#@ RNP*_PME(2.5) nanoparticles by HeLa cells

Protein loaded nanoparticles BSA#@ RNP*_PME(2.5) showed a comparatively lower amount of uptake, the particle uptake was about half that of protein free nanoparticles. Also during the first hour only about 17% of the total uptake was observed (Figure 4.11). The particle uptake reached saturation after 4 hours. Confocal images clearly demonstrated that the protein molecules were successfully delivered into the cells. A control study involving BSA# without nanoparticles was performed and the study revealed that BSA# uptake did not take place in the absence of the nanoparticles. Further, it was clear from the confocal images that much of the BSA# remained co-localized with the particles (Figure 4.12). 3D distribution of BSA# and RNP*_PME(2.5) particles showed that as the particle exposure time increased from 1 hour to 6 hours, some protein release occurred, as evidenced by the presence of clusters of green spheres, however much of the BSA# remained in close proximity to the particles (Figure 4.13). Similar to the RNP*_PME(2.5) particles, BSA#@RNP*_PME(2.5) also showed clustering at initial time points (1 – 2 hours), however, as the exposure time increased, the particles spread more evenly around the cells.

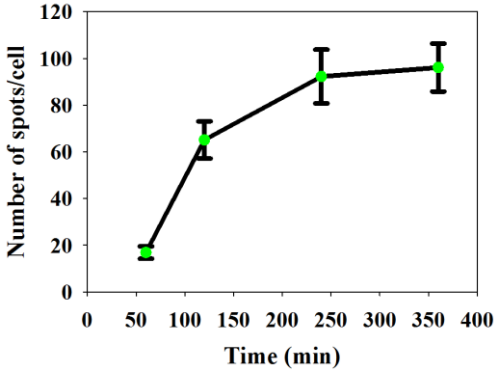

Figure 4.11: BSA#@ RNP*_PME(2.5) uptake versus time (n = 20 ± SEM)

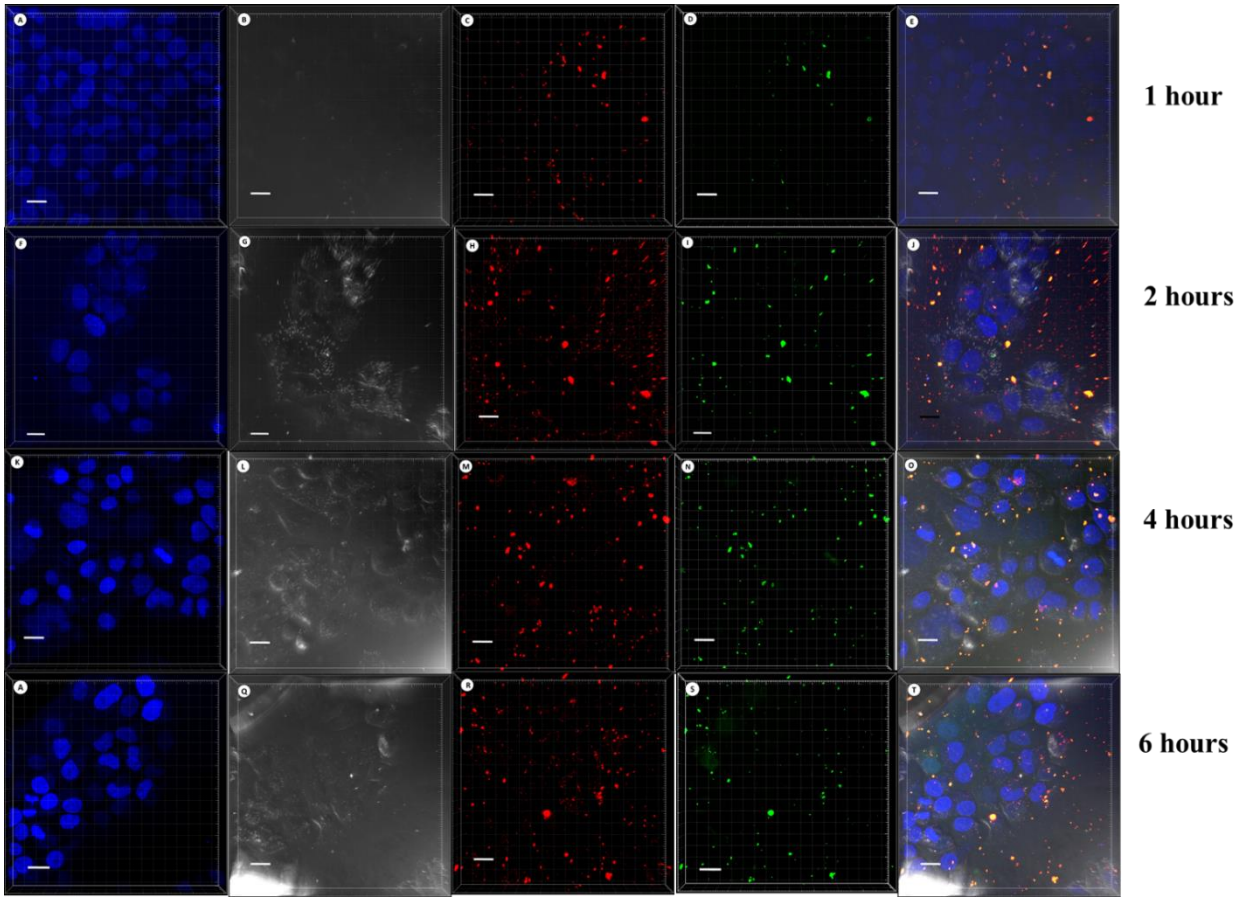

Figure 4.12: Time dependent uptake of BSA$^{\#}$@RNP*_PME(2.5)nanoparticles by HeLa cells (Scale 20 µm). The red spots indicate the presence of Rhodamine B isothiocyante functionalized nanoparticles RNP*_PME(2.5) and the presence of protein molecules was determined by identifying fluorescein isothiocyanate functionalized BSA, green spots.

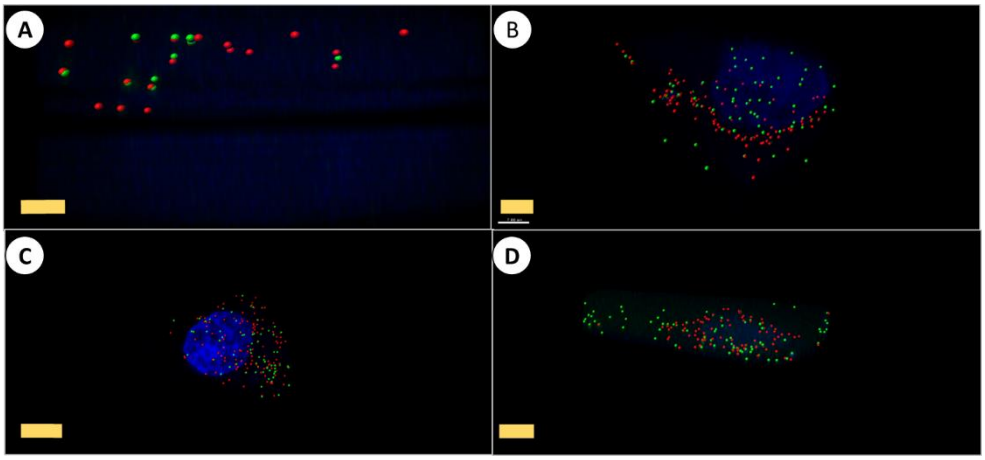

Figure 4.13 : Distribution of BSA$^{\#}$@RNP*_PME(2.5)nanoparticles in HeLa cells at different exposure times; A) 1 hour(Scale bar 5 µm); B) 2 hours (Scale bar 7 µm); C) 4 hours (Scale bar 10 µm) and D) 6 hours (Scale bar 5 µm)

Further analysis of the particle distribution was performed by TEM analysis. The vast majority of the particles were present in the cytoplasm. A few particles were observed to be localized within the mitochondria, demonstrating the ability of the particles to penetrate the mitochondrial cell membrane. In all cases, the particles were identified by their spherical morphology and from the difference in contrast from the surrounding cell organelles. Finally, the particles were observed to be localized within endosomes (Figure 4.14E), suggesting that the particles were taken up by receptor mediated uptake (Figure 4.14).

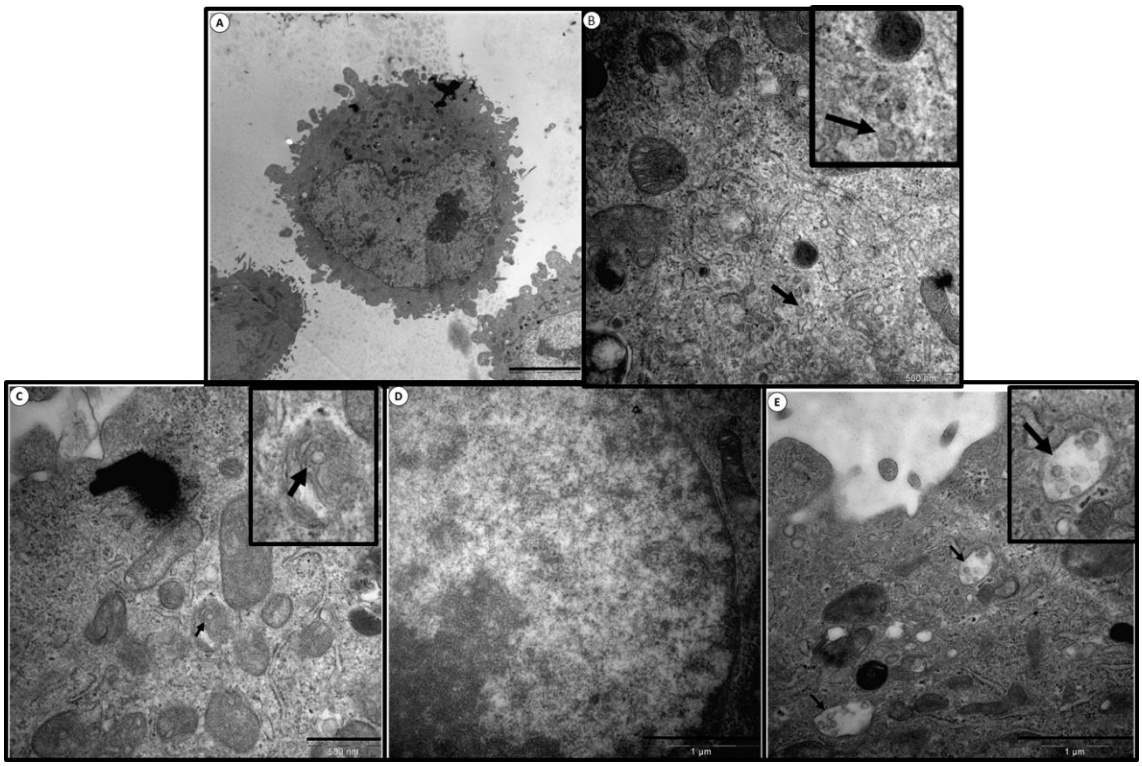

Figure 4.14: TEM images A) HeLa cell (Scale 5000 nm); B) Protein loaded nanoparticle BSA$^{\#}$@ RNP*_PME(2.5)localisation (black arrows) within the cytoplasm (Scale 1000 nm) (Inset 2X magnification of the region containing the particles, indicated by black arrows); C) Localization of nanoparticles within mitochondria (Scale 500 nm); D) Nucleus , note that particles were not observed (Scale 1000 nm) (Inset 2X magnification of the region containing the particles, indicated by black arrows); E) Particles within endosomes (indicated by black arrows) (Scale 1000 nm) (Inset 2X magnification of the region containing the particles, indicated by black arrows).

4.4.7 Effect of BSA# load on the particle uptake

BSA# load on the particles was varied from 111.1 to 166.7 to 223 mg/g and the effect of the loading on the particle uptake was studied. Lowest BSA# loading resulted in the smallest uptake levels. Particle uptake was nearly identical in the other two samples. (Figure 4.15) The samples were fixed after 6 hours. In all the cases, much of the BSA# was localized near the particles (Figure 4.16). 3D localization of the protein (green spheres) and particles (red spheres) showed that in samples with lower protein load 111.1 mg/g and 166.7 mg/g, protein molecules were in close proximity to the particles. At 223.0 mg/g the particles showed higher protein release (Figure 4.17).

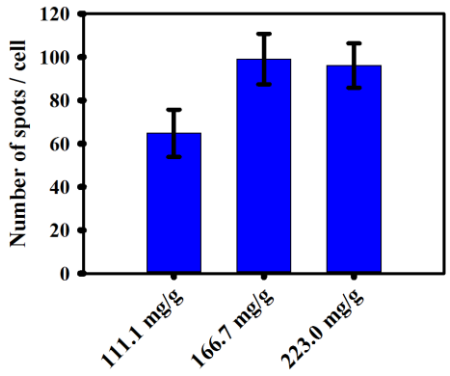

Figure 4.15: BSA#@ RNP*_PME(2.5) Particle uptake versus protein load. (n = 20 ± SEM.)

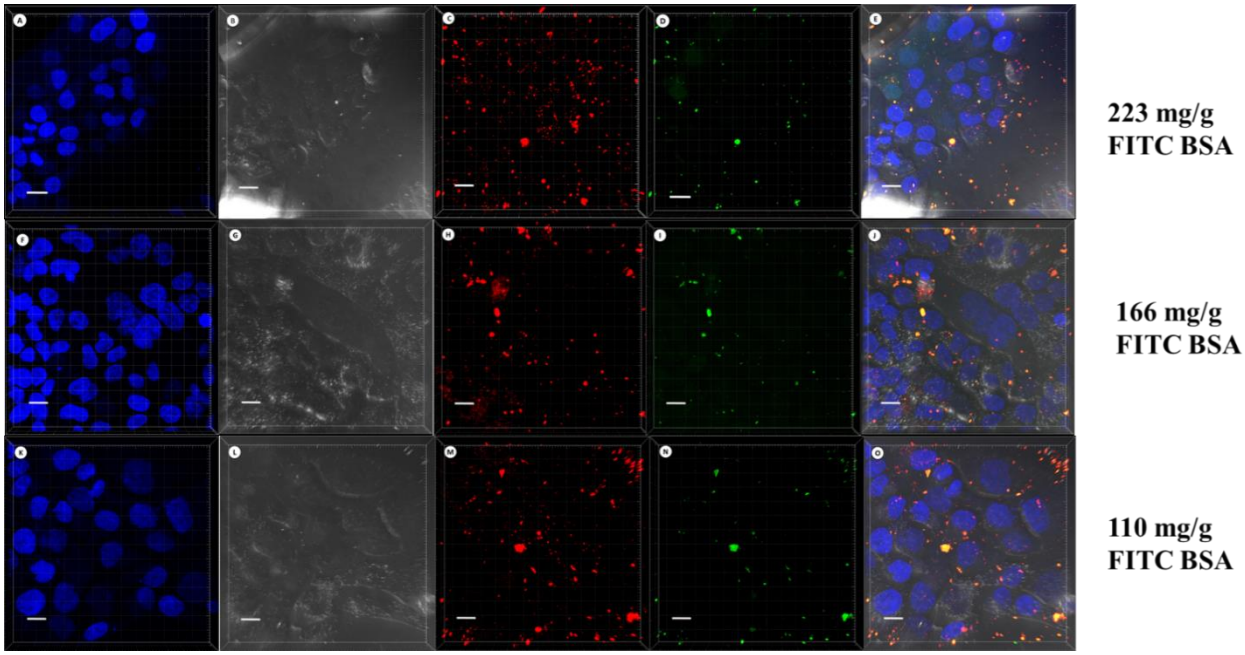

Figure 4.16: Effect of protein load in BSA#@ RNP*_PME(2.5) particles on particle uptake (Scale bar 20 µm). The red spots indicate the presence of Rhodamine B isothiocyanate functionalized nanoparticles RNP*_PME(2.5) and the presence of protein molecules was determined by identifying fluorescein isothiocyanate functionalized BSA, green spots.

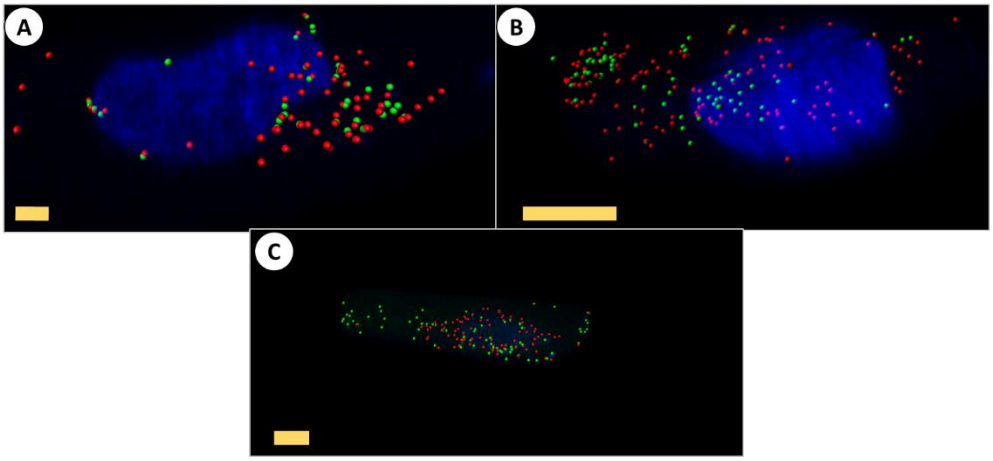

Figure 4.17: Distribution of BSA#@RNP*_PME(2.5)nanoparticles in HeLa cells at different protein load; A) 111.1 mg/g (Scale bar 5 µm); B) 166.7 mg/g (Scale bar 5 µm); C) 223.0 mg/g (Scale bar 10 µm)

4.4.8 Effect of prolonged incubation on the nanoparticle retention

In order to determine the fate of the particles following uptake, the RNP*_PME(2.5) and BSA#@ RNP*_PME(2.5) particle loaded cells were incubated in

particle free media for up to 3 hours. It was observed that protein loaded and unloaded particles demonstrated different properties.

Protein free RNP*_PME(2.5) particle numbers dropped significantly during the first hour of incubation in cell free media. Further incubation led to a small decrease in the particle numbers, which remained stable between 2.5 to 3 hours of incubation in particle free media (Figures 4.18 and 4.19). The observations were further validated by the 3D particle localization image. (Figure 4.20). TEM images of the HeLa cells from particle loaded cells following 3 hours of incubation in particle free media, showed very few particles and that all the particles were located in cytoplasm. Some of the particles were seen at the cell membrane, indicating that some of these particles were in the process of being exocytosed (Figure 4.21).

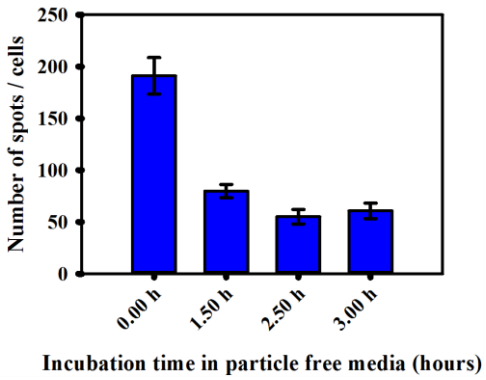

Figure 4.18: Effect of RNP*_PME(2.5) particle numbers on incubation in particle free media (n = 20 ± SEM)

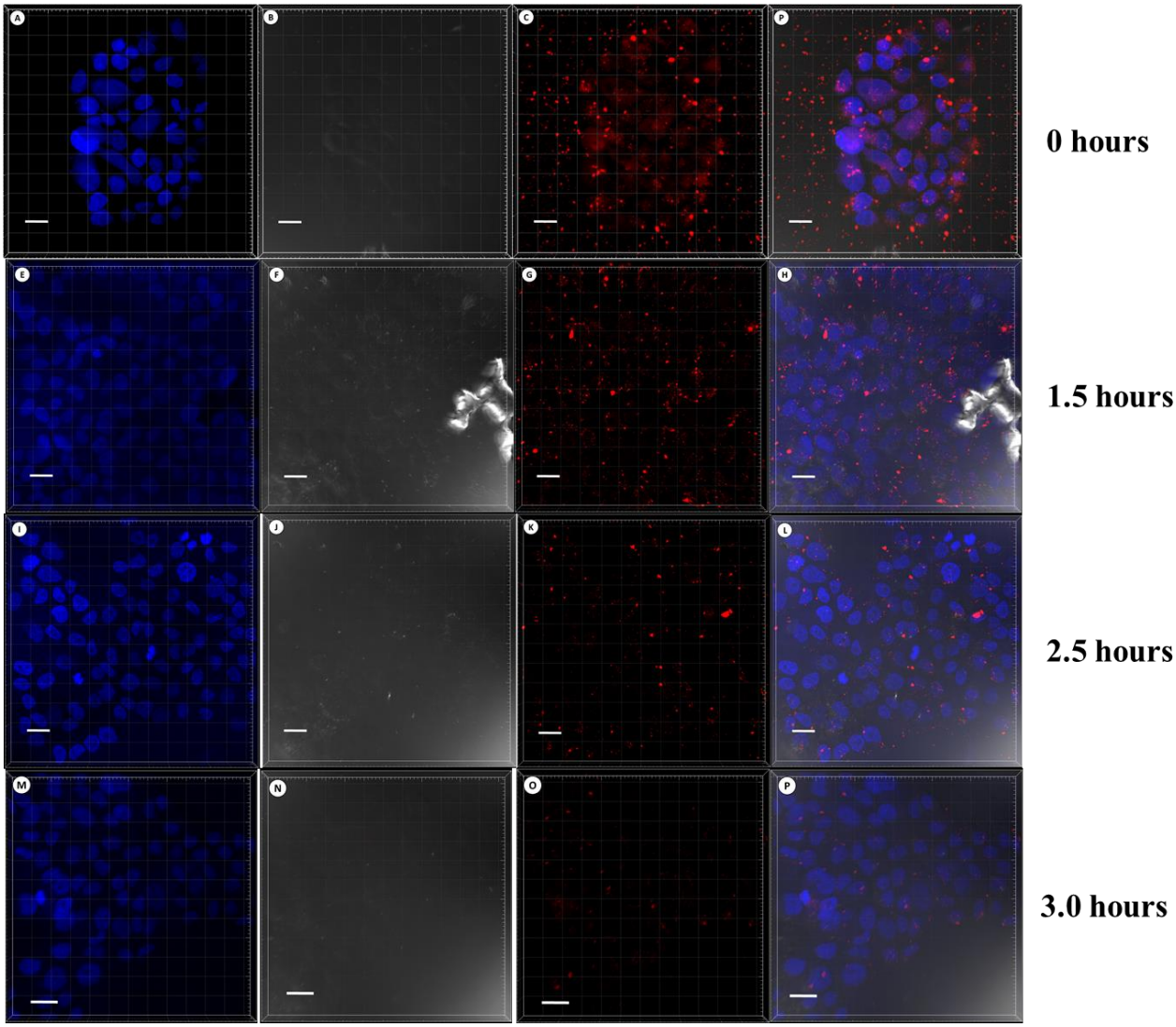

Figure 4.19: Effect of incubation in particle free media on RNP*_PME(2.5) particle loaded cells (Scale 20 µm). The red spots indicate the presence of Rhodamine B isothiocyanate functionalized nanoparticles RNP*_PME(2.5).

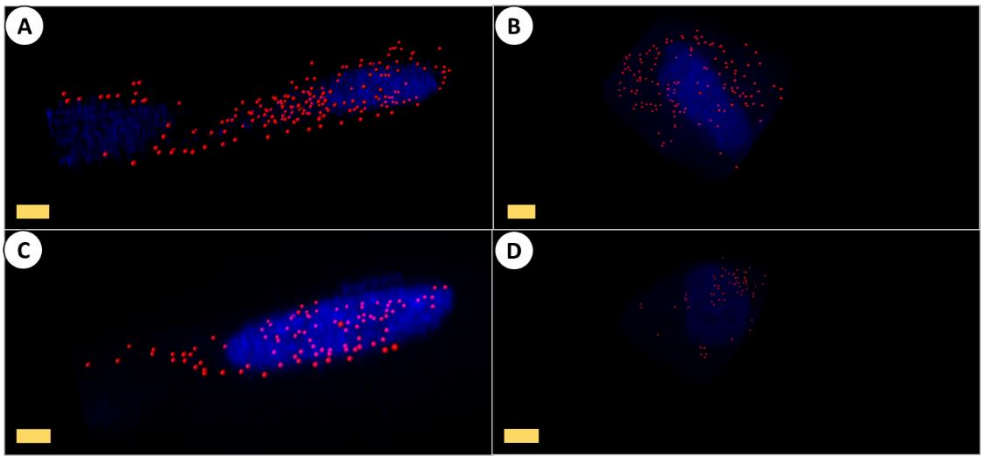

Figure 4.20: Distribution of RNP*_PME(2.5)nanoparticles in HeLa cells at different incubation times in particle free media; A) 0 hours (Scale bar 10 µm); B) 1.5 hours (Scale bar 10 µm); C) 2.5 hours (Scale bar 10 µm) and D) 3 hours (Scale bar 10 µm)

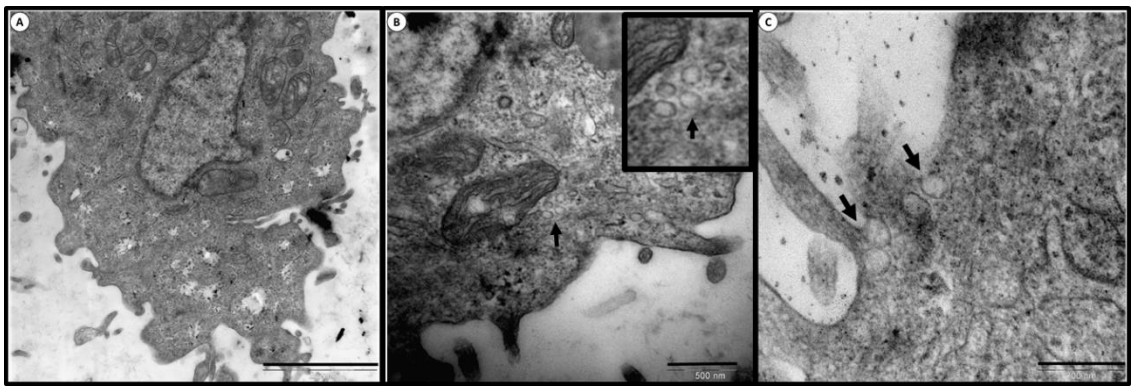

Figure 4.21: TEM images of RNP*_PME(2.5) particle loaded cells after 3 hours of incubation in cell free media. A) Complete HeLa cell (Scale 5000 nm); B) Localization of the particles in cytoplasm (Scale 500 nm) (Inset 2X magnification of the region containing the particles, indicated by black arrows); C) Particle exocytosis (indicated by black arrows) (Scale 200 nm)

BSA$^{\#}$ loaded nanoparticles BSA$^{\#}$@ RNP*_PME(2.5) exhibited significantly different properties. The particle numbers did not change upon incubation in particle free media (Figures 4.22 and 4.23). The 3D particle localization images (Figure 4.24) showed that while the particles and protein quantity remained the same there was a small increase in the number of BSA$^{\#}$ spheres (green spheres) that were not associated with the RNP*_PME(2.5) particles. TEM analysis of the cells loaded with BSA$^{\#}$@ RNP*_PME(2.5) particles were evenly distributed across the cell membrane, validating the observations from the confocal microscopy study. Furthermore the particles were not

found to be associated with any endosomes or lysosomes, suggesting that all the particles exhibited endosomal escape (Figure 4.25).

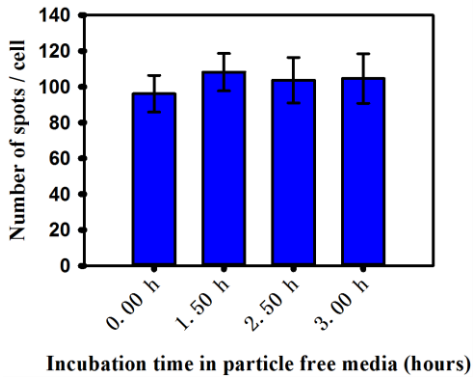

Figure 4.22: Effect of BSA#@RNP*_PME(2.5) particle numbers on incubation in cell free media (n = 20 ± SEM)

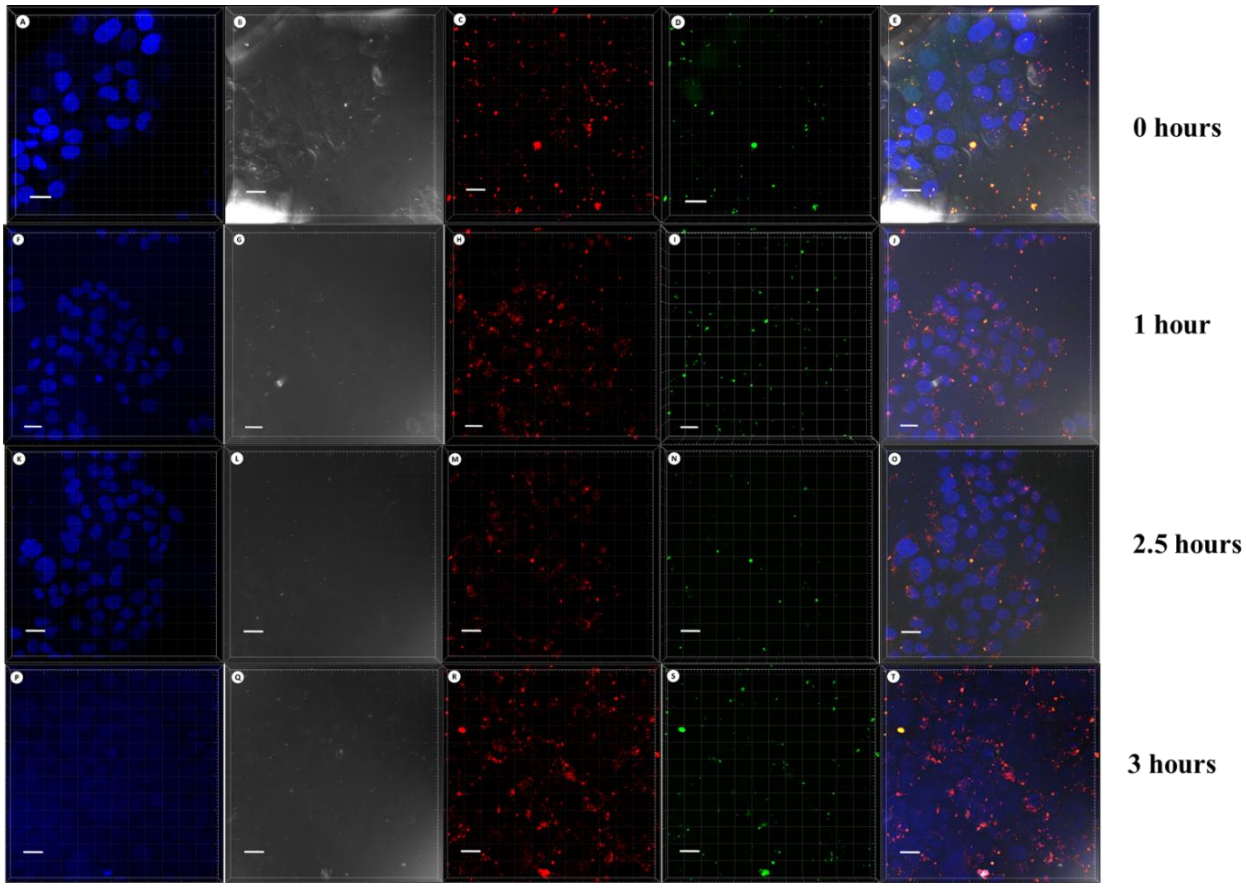

Figure 4.23: Effect of incubation in cell free media on BSA$^{\#}$@RNP*_PME(2.5) particle loaded cells (Scale 20 µm). The red spots indicate the presence of Rhodamine B isothiocyanate functionalized nanoparticles RNP*_PME(2.5) and the presence of protein molecules was determined by identifying fluorescein isothiocyanate functionalized BSA, green spots.

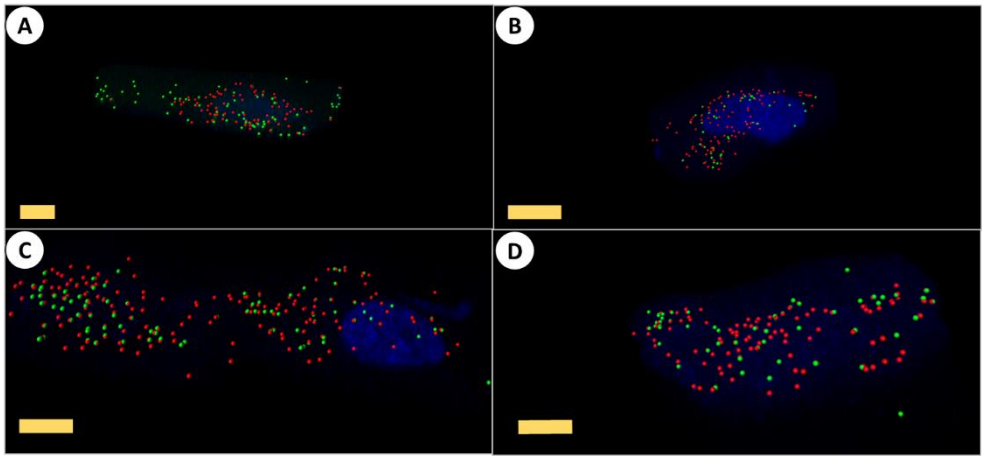

Figure 4.24: Distribution of BSA#@RNP*_PME(2.5) nanoparticles in HeLa cells at different incubation times in particle free media; A) 0 hours (Scale bar 5 µm); B) 1.5 hours (Scale bar 10 µm); C) 2.5 hours (Scale bar 10 µm) and D) 3 hours (Scale bar 10 µm)

.

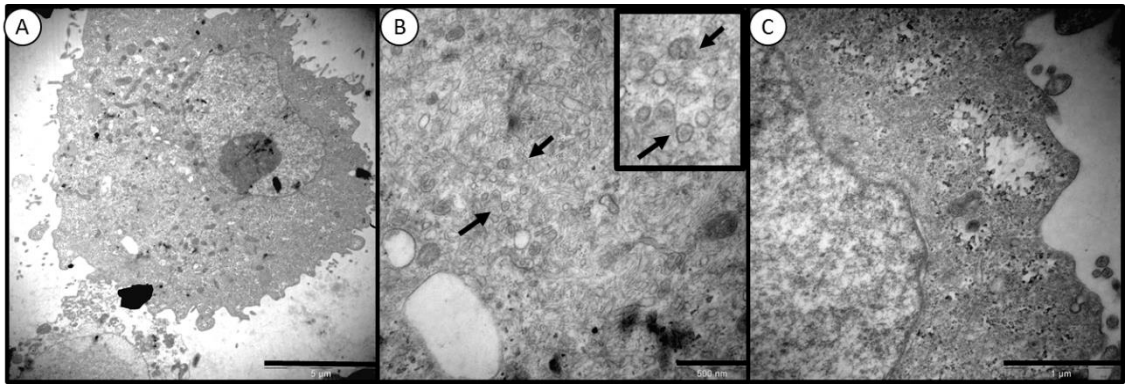

Figure 4.25: TEM images of BSA#@RNP*_PME(2.5) particle loaded cells after 3 hours of incubation in cell free media. A) Complete HeLa cell (Scale 5000 nm); B) Localization of the particles in cytoplasm (Scale 1000 nm) (Inset 2X magnification of the region containing the particles, indicated by black arrows); C) Nucleus, note the absence of particles (Scale 1000 nm)

4.4.9 Mechanism of particle uptake

The mechanism of particle uptake was studied by blocking specific nanoparticle uptake mechanisms. Clathrin receptors were blocked by treating cells with 450 mM sucrose, caveolar receptors were blocked using 5 µg/mL nystatin and folic acid receptors were blocked using 10 mM folic acid.

RNP*_PME(2.5) nanoparticles were taken up predominantly by caveolar receptors, as upon blocking the caveolar receptors, a reduction of over 70% in particle

uptake was observed , while blocking clathrin and folic acid receptors resulted in apparent 18% decrease and 32% increase in the particle uptake respectively (Figures 4.26 and 4.27). The statistical significance of the result was determined at p-value of 0.01 using Wilcoxon ranked sum test by comparing results obtained after 6 hours of incubation against particle uptake following receptor blocking. The study showed that blocking caveolar receptors using nystatin resulted in statistically significant change at p-value of 0.01 while blocking other receptors (clathrin and folic acid) did produce any statistically significant change. The observations were confirmed by the 3D particle localization images (Figure 4.28)

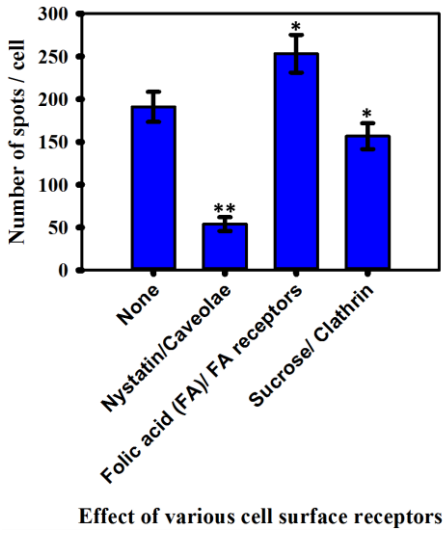

Figure 4.26: Receptor mediated uptake of RNP*_PME(2.5) particles (n = 20 ± SEM.). Statistical significance was measured at p-value of 0.01 using Wilcoxon ranked sum test. Statistical significance was determined by comparing against the uptake when surface receptors were not blocked as in Sample: None. Statistical significance is denoted by ** and non-significant results by *.

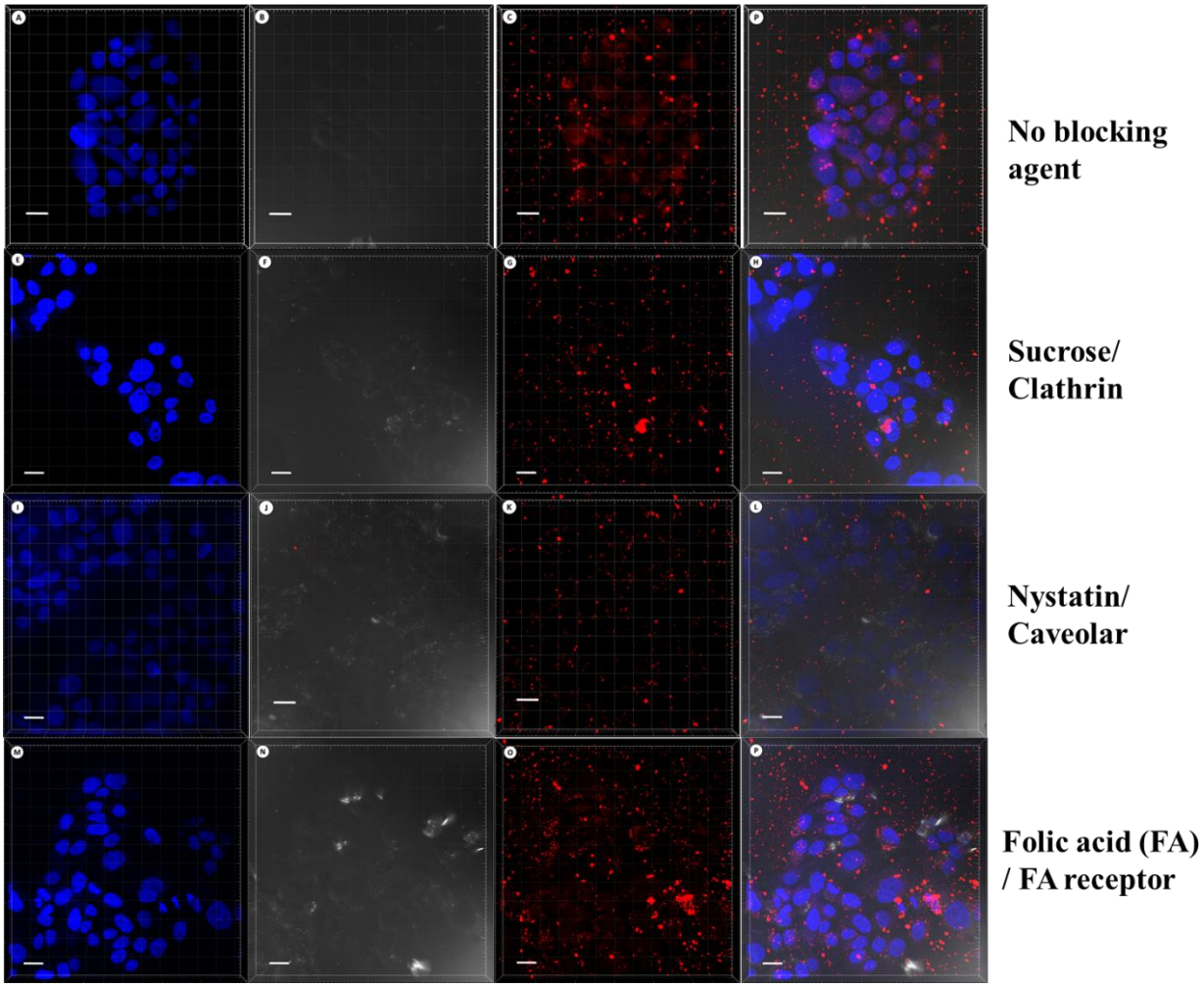

Figure 4.27: Confocal microscope images depicting the effects of blocking surface receptors on RNP*_PME(2.5) particle uptake. (Scale 20 µm). The red spots indicate the presence of Rhodamine B isothiocyanate functionalized nanoparticles RNP*_PME(2.5).

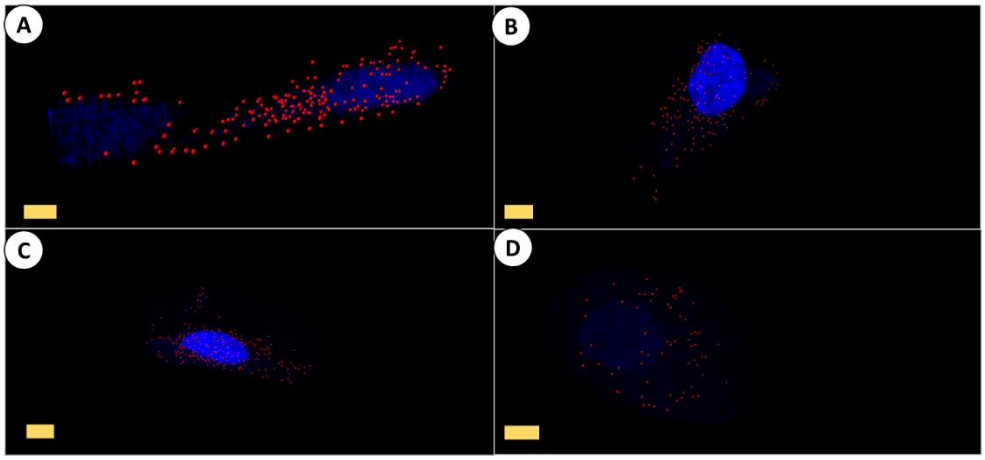

Figure 4.28: Distribution of RNP*_PME(2.5)nanoparticles in HeLa cells in presence of various cell surface receptor inhibitors; A) No inhibitor (Scale bar 10 µm); B) Clathrin (Sucrose) (Scale bar 10 µm); C) Folate receptor (Folic acid) (Scale bar 10 µm) and D) Caveolae (Nystatin) (Scale bar 10 µm)

BSA#@ RNP*_PME(2.5) particles were taken up predominantly by the folic acid receptor mediated pathway. Over 80% of the particle uptake was blocked, when the folic acid receptors were blocked while 24% of the particle uptake was blocked when caveolar receptors were blocked. Statistical significance of the result was determined at p-value of 0.01 using Wilcoxon ranked sum test by comparing results obtained after 6 hours of incubation against particle uptake following receptor blocking. The study showed that blocking folic acid receptors using folic acid resulted in statistically significant change at p-value of 0.01 while blocking other receptors (clathrin and caveolar) did produce any statistically significant change. (Figures 4.29 and 4.30). 3D localization images further confirm these observations (Figure 4.31).

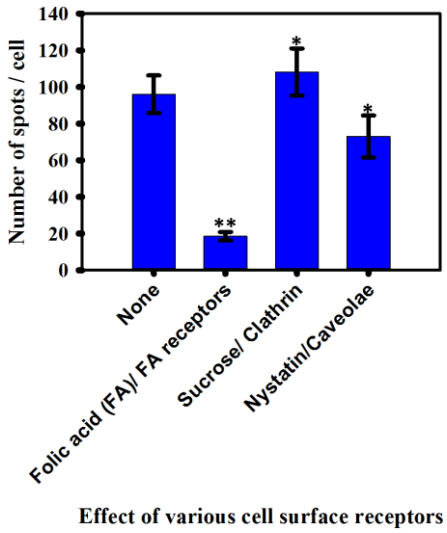

Figure 4.29: Receptor mediated uptake of BSA#@ RNP*_PME(2.5) particles (n = 20 ±Rel. std. dev.) Statistical significance was measured at p-value of 0.01 using Wilcoxon ranked sum test. Statistically significance was determined by comparing against the uptake when surface receptors were not blocked as in Sample: None. Statistical significance is denoted by ** and non-significant results by *.

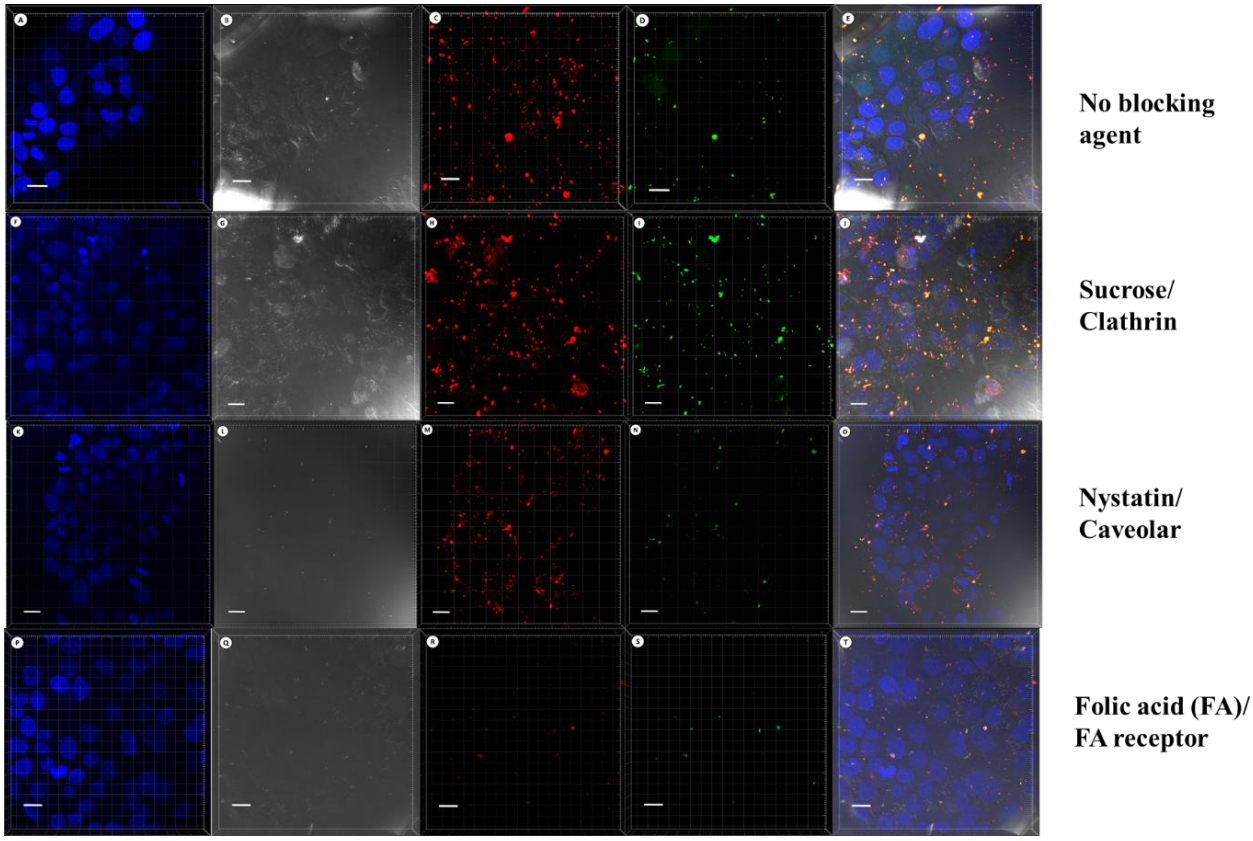

Figure 4.30: Confocal microscope images depicting the effects of blocking surface receptors on RNP*_PME(2.5) particle uptake. (Scale 20 µm). The red spots indicate the presence of Rhodamine B isothiocyanate functionalized nanoparticles RNP*_PME(2.5) and the presence of protein molecules was determined by identifying fluorescein isothiocyanate functionalized BSA, green spots.

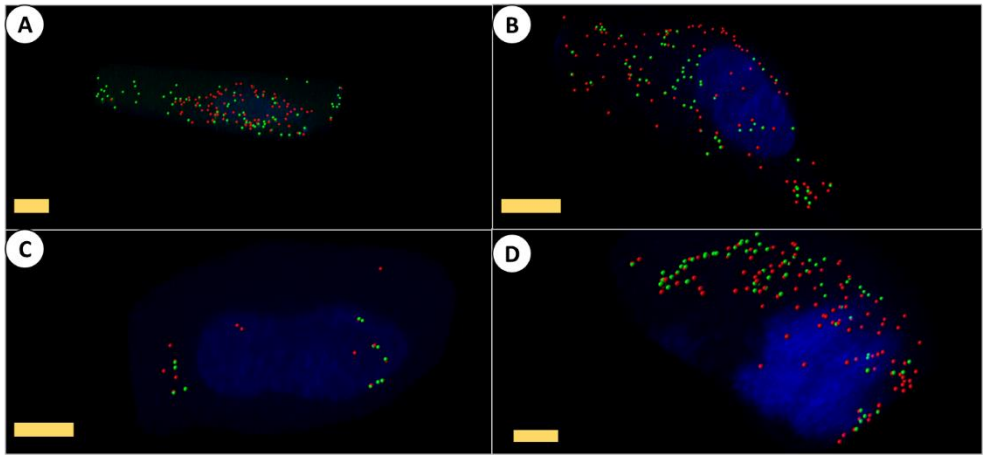

Figure 4.31: Distribution of BSA$^{\#}$@RNP*_PME(2.5) nanoparticles in HeLa cells at in presence of various cell surface receptor inhibitors; A) No inhibitor (Scale bar 10 µm); B) Clathrin (Sucrose) (Scale bar 10 µm); C) Folate receptor (Folic acid) (Scale bar 10 µm) and D) Caveolae (Nystatin) (Scale bar 10 µm)

4.5 Discussion

The applications of RNP_PME(2.5) nanoparticles for immobilization and intracellular delivery of FITC labelled BSA was studied. The aim of these experiments was to demonstrate the ability of the particles to deliver large protein molecules across the cell membrane. The pore size of the RNP*_PME(2.5) was 11.6 nm and was therefore considered suitable to entrap BSA (molecular dimensions 5 x 7 x 7 nm^3). Also BSA (molecular weight 66 kDa) is twice the size of cytochrome c, which was used in two previous studies, and was therefore considered a suitable candidate to test the ability of the particles as potential protein delivery agents.

An adsorption study was performed to determine the total loading of $BSA^{\#}$ on RNP*_PME(2.5) particles and the maximum loading obtained was 240.13 ± 5.62 mg/g. A lower $BSA^{\#}$ load of 223 mg/g was chosen for the drug delivery applications to exclude the possibility of free $BSA^{\#}$ in the solution. DLS was used to measure the hydrodynamic radii of the particles before and after loading. The measurements were performed in DMEM media. The studies revealed that the RNP*_PME(2.5) particles displayed aggregation in the media, evidenced by the observation that the hydrodynamic radius increased and the particle size distribution broadened. The particle aggregation could have resulted from the increased ionic strength of the media. The protein loaded particles $BSA^{\#}$@ RNP*_PME(2.5), however, did not show an increase in the hydrodynamic radius or a broadening of the particle size distribution. SEM analysis of protein immobilized particles revealed a smoothened particle surface (Figure 3.7) indicating the presence of protein molecules on the surface of the particles. These surface immobilized protein molecules could have played the role of steric stabilizing agents, which could have provided protection against aggregation in the cell culture media. Neither dispersion, however displayed any visible precipitate formation even after a few hours of exposure.

The integrity of the BSA# structure before and after immobilization was studied using CD. The study revealed that neither FITC attachment nor particle uptake resulted in changes to the protein structure at pH 7.40 (Figure 4.5).

Cell uptake and viability studies were performed on HeLa cell line. HeLa cell lines are cervical cancer cell lines and have been demonstrated as excellent systems to study nanoparticle-cell interactions. The cell viability study following particle uptake was performed using the MTT assay.[33] The study revealed that the neither particles nor BSA# showed any cytotoxicity. The RNP*_PME(2.5) particles were tested for concentration dependent cytotoxicity and were non-toxic up to the concentration of 0.2 mg/mL. This value was twice that of the previously published reports on MSNs.[37] The result indicates high levels of biocompatibility, which most likely benefits from the presence of a phosphonate functional group on the particle surface. BSA#@RNP*_PME(2.5) particles were tested for the cytotoxic effects by varying the protein load on the particles, while keeping the particle concentration fixed at 0.1 mg/mL. BSA# load ranging from 47 mg/g to 223 mg/g was used. Statistically significant differences in cell viability were not observed in any of these cases. These results conclusively demonstrate the high level of biocompatibility of these nano materials.

Nanoparticle uptake by the cells was analysed by confocal microscopy and the spots package on Imaris software. The package allows the visualization of spherical objects throughout the image stack based on the intensity of the point it represents.[38] This method was used previously to quantitatively estimate the fluorescent nanoparticle uptake.[39] A fixed nanoparticle concentration of 0.1 mg/mL was used for the study. The study revealed that the protein free RNP*_PME(2.5) nanoparticles showed a progressive and time dependent uptake and reached saturation after 6h of nanoparticle exposure. Previous studies involving silica nanoparticles required between 16 to 24 h of exposure

to facilitate uptake so the studies here showed a dramatic improvement in the time required for uptake.[29] The vast majority (~ 50% of the uptake occurred within the first hour (Figure 4.7). The protein loaded nanoparticles BSA$^{\#}$@RNP*_PME(2.5) showed a similar progressive trend in particle uptake, however the rate of particle uptake was lower (Figure 4.11). The final particle uptake was nearly half that of the RNP*_PME(2.5) particles suggesting that protein immobilization lowered the extent of particle uptake.

The mechanism of the particle uptake was analysed by blocking clathrin, caveolar and folic acid receptors. Previous studies involving the MSNs revealed that these are the dominant pathways involved in nanoparticle uptake.[24] Other pathways such as phagocytosis and macro-pinocytosis were not considered as they are predominantly involved in the uptake of medium sized (> 500 nm) particles and small molecule uptake respectively.[40] It was observed that RNP*_PME(2.5) particles showed caveolar receptor mediated uptake from confocal microscope analysis of the cells obtained from particle uptake experiments (Figure 4.26). Caveolar pathway is a non-destructive nanoparticle endocytosis pathway. Caveolar uptake involves caveolae, which are 50 to 100 nm invaginations in the cell membrane. They consist of lipid rafts, which are made of lipids such as cholesterol and the protein caveolin. Caveolin is a small (21 kDa) protein, which associates with lipids to form lipid rafts. Unlike the clathrin mediated nanoparticle uptake, caveolar endocytosis does not involve the lysosomes and therefore does not result in biomolecule degradation (the final particle destination is golgi apparatus) (Scheme 3).Further direct evidence was obtained from TEM analysis of cell sections (Figure 4.10 D), where the image showed the particle uptake by coated 80 nm pits, which are most likely caveolar receptors.[41] Additionally, vesicles containing particles (Figure 4.10 C) were observed, further strengthening the case for receptor mediated uptake.

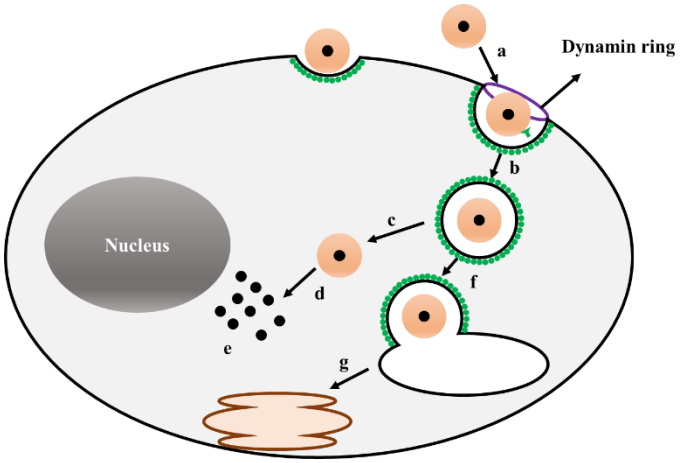

Scheme 3: Caveolar uptake, Various pathways a protein carrier might follow upon cell entry; a) protein carrier uptake through caveolar receptors, b) encapsulation in early endosome coated with caveolin, c) endosomal escape and carrier release, d) controlled release of encapsulated protein, e) protein action inside the cell, f) conversion of early endosomes to late endosomes, g) transfer to golgi apparatus.

Electron microscope analysis of the HeLa cells incubated with the nanoparticles RNP*_PME(2.5) showed that the particles were located in the cytoplasm (Figures 4.10 B and 4.21). This strongly indicates that the particles displayed endosomal escape. Previous reports noted that negatively charged nanoparticles display more rapid endosomal escape.[22, 41]

Protein loaded nanoparticles (BSA$^{\#}$@RNP*_PME(2.5) displayed folic acid receptor mediated uptake (Scheme 4), determined from confocal microscope analysis of the cells obtained from particle uptake experiments (Figure 4.29). Folic acid receptors are over expressed on many cancer cells and are one of the most important targets for various drugs.[42] HeLa cells display folic acid receptor α on their surface.[43] Folic acid receptors have been found to be located on the caveolae,[43] so it can therefore be surmised that the change in the particle uptake pathway does not represent a significantly different receptor mediated uptake All the previous studies that involved targeting these receptors required functionalization of the particle surfaces with folic acid groups.[44] In the current study folic acid receptor mediated uptake was observed despite the absence of folic acid

functionalization on the particles. TEM analysis of the HeLa cells following BSA#@RNP*_PME(2.5) particle uptake showed that some of the particles were present in the endosomes (Figure 4.14). The remaining particles were observed in the cytoplasm. This indicates that the particles displayed endosomal escape.

Wosikowski *et al*. demonstrated the uptake of Methotrexate (MTX) by KB cells.[45] KB cell lines are cancer cells and they express folate receptor alpha (FR-α) similar to HeLa cells.[41] MTX is an anti-folate drug, however FR-α have low affinity for this drug and is therefore not taken up by KB cells.[46] Wosikowski *et al*. demonstrated that conjugation of MTX to human serum albumin (HSA) increased the drug uptake by these cells, additionally, MTX-HSA conjugates were taken up by folate receptor mediated uptake.[45] In the above study, BSA (which has high degree of similarity to HSA[47]) loaded nanoparticles were taken up by folate receptor mediated pathway. It is therefore suggested that this protein-nanoparticle conjugate stimulates the folate receptor and leads to particle uptake.

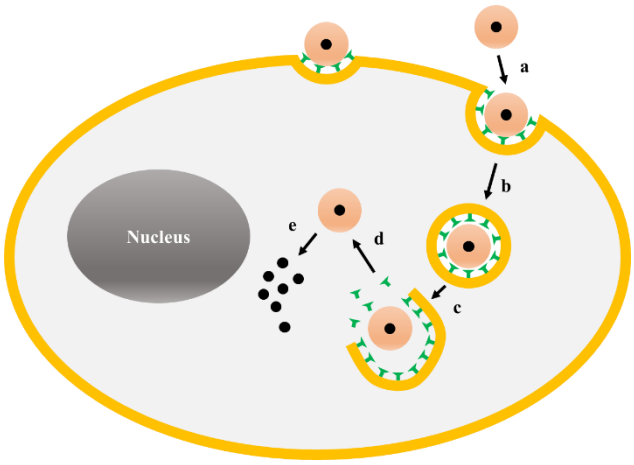

Scheme 4: Folic acid receptor mediated uptake a) folic acid receptor coating, b) encapsulation within endosomes, c) endosomal escape, d) controlled release of encapsulated protein, e) protein action inside the cell

Following the above experiments, which demonstrated particle uptake by the cells further experiments looked at the behaviour of the endocytosed particles over time. Thus

the media containing the particles was removed from the cultures and particle-free media was added to the cells and incubated for different time periods. RNP*_PME(2.5) nanoparticles numbers showed a steady drop during this time period. Three hours of incubation in the particle free media resulted in a near complete depletion of the number of nanoparticles observed. The result suggests that the particles were exocytosed from the cells. This observation was confirmed by TEM analysis. The BSA$^{\#}$@RNP*_PME(2.5) nanoparticles on the other hand, did not show any depletion in numbers. The particle were however, evenly distributed across the cell membrane, suggesting complete endosomal escape.[29] TEM analysis of the cells showed that the particles were not associated with any cell membrane and were evenly distributed across the cell membrane, confirming the observation by confocal microscopy. The vast majority of the BSA molecules, continued to remain associated with the particles, suggesting that the protein loaded particles showed slow release of the adsorbed protein molecules (Figure 4.12).

4.6 Conclusion

Nanoparticle mediated intracellular protein (BSA$^{\#}$) delivery was achieved by RNPPME(2.5) nanoparticles. The protein loaded particles were successfully used to deliver protein molecules across the cell membranes and the labelled protein entry into the cells was confirmed by confocal microscopy. . The particles demonstrated the ability to carry significantly large quantities of proteins, compared to the previously published reports.[48] Broadly, the study investigated four specific parameters. 1) cytotoxicity of the particles; 2) time dependent uptake; 3) fate of the particles loaded in cells incubated in fresh particle free media; 4) mechanism of particle uptake.

Cytotoxic assessment of the particles ($BSA^{\#}$ loaded and unloaded) was made using MTT assay. Concentration dependent cytotoxicity and protein load dependent cytotoxicity were assessed for protein free RNP*_PME(2.5) and loaded $BSA^{\#}$@RNP*_PME(2.5) particles respectively. The particles were found to be non-toxic during 24 hours of exposure to the cells. Following this, the time dependent uptake was studied. Confocal microscope images of HeLa cells with $BSA^{\#}$ loaded particles showed that there was strong co-localization between RNP*_PME(2.5) and $BSA^{\#}$. The result indicated that during the time of the experiment, the protein molecules remained localized on the particles. Protein load dependent particle uptake was also studied. Particles with 166.7 and 223 mg/g $BSA^{\#}$ were taken up in similar numbers, while the particles with 111.1 mg/g $BSA^{\#}$ were taken up in smaller numbers.

Particle exocytosis was studied by incubating the cells in particle free media. Strong reduction in the numbers of unloaded particles was observed just after incubation for one hour. The particle numbers remained relatively stable for the next two hours. TEM images of the HeLa cells containing RNP*_PME(2.5) particles showed exocytosis of the particles. The $BSA^{\#}$ loaded particles on the other hand were evenly distributed in the cell membrane and the numbers of these particles did not show any reduction due to incubation in particle free media. TEM analysis of both the samples described above also showed that all the particles were present in the cytosol, indicating that the particles showed endosomal escape.

Finally, the mechanism of particle uptake was studied. Three receptor mediated uptake pathways were studied. 1) clathrin; 2) caveolar; 3) folic acid. The protein free RNP*_PME(2.5) particles were taken up predominantly by caveolar pathway, as demonstrated by the significant reduction in particle numbers due to blocking of the corresponding receptors. Blocking folic acid receptors was found to strongly reduce the

uptake of BSA$^{\#}$ loaded nanoparticles BSA$^{\#}$@ RNP*_PME(2.5). The results presented above demonstrate novel properties of folic acid receptors; the roles of these receptors in nanoparticle entry regulation and in the uptake of protein loaded particles were previously unknown. The results presented here have potential applications in the areas of targeted drug delivery, since folic acid receptors are over expressed on cancer cells.

4.7 References

1. A. Angelova, B. Angelov, R. Mutafchieva, S. Lesieur and P. Couvreur, *Acc. Chem. Res*., 2011, **44**, 147–156.

2. Z. Gu, A. Biswas, M. Zhao ab and Yi Tang, *Chem. Soc. Rev.*,2011, **40**, 3638-3655.

3. P. Svenningsson, E. Westman, C. Ballard and D. Aarsland, *Lancet Neurol.*, 2012, **11**, 697-707.

4. A. Silva-Machado, S. Perrier and J. C. Bourdon, *Semin. Cancer Biol.*, 2010, **20**, 57-62.

5. T. Vermonden, R. Censi and W. E. Hennink, *Chem. Rev*., 2012, **112**, 2853–2888.

6. V. Torchilin, *Drug Discov. Today*, 2008, **5**, e95-e103.

7. L. N. Patel, J. L. Zaro and W. C. Shen, *Pharm. Res*., 2007, **24**, 1977–1992.

8. S. R. Schwarze, K. A. Hruska and S. F. Dowdy, *Trends Cell Biol.*, 2000, **10**, 290-295.

9. I. Walev, S. C. Bhakdi, F. Hoffmann, N. Djonder, N. Valeva, K. Aktories and S. Bhakdi, *Proc. Natl. Acad. Sci. USA*, 2001, **98**, 3185-3190.

10. G. P. Francesco, *PEGylated Protein Drugs: Basic Science and Clinical Applications*, Birkhäuser Basel, 2009, vol. 1

11. J. Futami and H. Yamada, *Curr. Pharm. Biotechnol.*, 2008, **9**, 180–184.

12. H. Murata, M. Sakaguchi, J. Futami, M. Kitazoe, T. Maeda, H. Doura, M. Kosaka, H. Tada, M. Seno, N. Huh and H. Yamada, *Biochemistry*, 2006, **45**, 6124–6132

13. C. A. Lackey, O. W. Press, A. S. Hoffman and P. S. Stayton, *Bioconjugate Chem.*, 2002, **13**, 996–1001

14. Y. Lee, T. Ishii, H. Cabral, H. J. Kim, J. H. Seo, N. Nishiyama, H. Oshima, K. Osada and K. Kataoka, *Angew. Chem., Int. Ed.*, 2009, **48**, 5309–5312

15. S. H. Kim, J. H. Jeong, C. O. Joe and T. G. Park, *J. Controlled Release*, 2005, **103**, 625–634

16. T. Akagi, X. Wang, T. Uto, M. Baba and M. Akashi, *Biomaterials*, 2007, **28**, 3427–3436

17. L. Y. Chou, K. Ming and W. C. Chan, *Chem. Soc. Rev.*, 2011, **40**, 233–245

18. R. J. Debs, L. P. Freedman, S. Edmunds, K. L. Gaensler, N. Duzgunes and K. R. Yamamoto, *J. Biol. Chem.*, 1990, **265**, 10189–10192

19. O. Zelphati, Y. Wang, S. Kitada, J. C. Reed, P. L. Felgner and J. Corbeil, *J. Biol. Chem.*, 2001, **276**, 35103–35110

20. M. Yokoyama, *J. Exp. Clin. Med.*, 2011, 1-8.

21. M. Mufamadi, V. Pillay, Y. E. Choonara, L. C. Du Toit, G. Modi, D. Naidoo and V. M.K. Ndescendo, *J. Drug Deliv.*, 2011, Article ID 939851, 19 pages.

22. J. Wadia and S. F. Dowdy, *Curr. Opin. Biotech.*, 2002, **13**, 52-56

23. Y. Gao, Y. Chen, X. Ji, X. He, Q. Yin, Z. Zhang, J Shi, and Y. Li, *ACS Nano*, 2011, **5**, 9788–9798.

24. I. Slowing, B. Trewyn, V. S. Y. Lin, *J. Am. Chem. Soc*., 2006, **128**, 14792–14793

25. J. F. Diaz and K. J. Balkus Jr., *J. Mol. Catal. B: Enzym*., 1996, **2**, 115-126.

26. K. T. Mody, D. Mahony, A. S. Cavallaro, F. Stahr, S. Z. Qiao, T. J. Mahony and N. Mitter, *Int. J. Pharm.*, 2014, **465**, 325-332.

27. H. H. Yang, S. Q. Zhang, X. L.Chen, Z. X. Zhuang, J. G. Xu, and X. R. Wang, *Anal. Chem*., 2004, **76**, 1316-1321.

28. R. K. Sharma, S. Das and A. Maitra, *J. Colloid Interface Sci*., 2005, **284**, 358-361.

29. I. I. Slowing, B. G. Trewyn and V. S. Y. Lin, *J. Am. Chem. Soc***.,** 2007, **129**, 8845-8849.

30. S. W. Song, K. Hidajat and S. Kawi, *Chem. Commun*., 2007, 4396–4398.

31. S. Y. Chen, Y. T. Chen, J. J. Lee and S. Cheng, *J. Mater. Chem.*, 2011,**21**, 5693-5703

32. M. M. Bradford, *Anal. Biochem.*, 1976, **72** , 1 -2, 248- 254.

33. W. Li, C. Chen, C. Ye, T. Wei, Y. Zhao, T. Lao, Z. Chen, H. Meng, Y. Gao, H. Yuan, G. Xing, F. Zhao, Z. Chai, X. Zhang, F. Yang, D. Han, X. Tang and Y. Zhang, *Nanotechnology*, 2008, **19**, 145101-145113.

34. K. Nagashima, J. Zheng, D. Parmiter, A. K. Patri, *Methods Mol. Biol.*, 2011, **697**, 83-91.

35. F. Lu, S.-H. Wu, Y. Hung, C. –Y. Mou, *Small*, 2009, **5**, 12, 1408- 1413.

36. Y. Zou, D. L. Broughton, K. L. Bicker, P. R. Thompson and J. J. Lavigne, *ChemBioChem*, 2007, **8**, 2048-2051.

37. J. S. Chang, K. L. Chang, D. F. Hwang and Z. L. Kong, *Environ. Sci. Technol.*, 2007, **41**, 2064-2068.

38. IMARIS 4.1 operating instructions. 1.9th ed. Zürich, Switzerland: Bitplane AG; 2004.

39. M. S. Cartiera, K. M. Johnson, V. Rajendran, M. J. Caplan and W. M. Saltzman, *Biomaterials*, 2009, **30**, 2790-2798

40. N. Oh and J. H. Park, *Int. J. Nanomed.*, 2014, **9**, 51-63

41. C. H. J. Choi, L. Hao, S. P. Narayan, E. Auyeung and C. A. Mirkin, *Proc. Natl. Acad. Sci. USA*, 2013, **110**, 7625-7630.

42. J. Panyam, W. Z. Zhou, S. Prabha, S. K. Sahoo and V. Labhasetwar, *FASEB J.* , 2002, **16**, 1217-1226.

43. L. Kelemen, *Int. J. Cancer*, 2006, **119**, 243-250.

44. G. L. Zwicke, G. A. Mansoori and C. J. Jeffery, *Nano Rev.*, 2012, **3**, 1-11.

45. K. Wosikowski, E. Biedermann, B. Rattel, N. Breiter, P. Jank, R. Löser, G. Jansen and G. J. Peters, *Clin. Cancer Res.*, 2003, **9**, 1917-1926.

46. S. Rinjboutt, G. Jansen, G. Posthuma, J. B. Hynes, J. H. Schornagel and G. J. Strous, *J. Cell Biol.*, 1996, **132**, 35-47.

47. A. Michnik, K. Michalik, A. Kluczewska and Z. Drzazga, *J. Therm. Calorim*, 2006, **84**, 113-117.

48. R. J. Lee, S. Wang and P. S. Low, *Biochim. Biophys. Acta*, 1996, **1312**, 237-242.

49. H. Ayame, N. Morimoto and K. Akiyoshi, *Bioconjugate Chem.*, 2008, **19**, 882–890.

Chapter 5

Chapter 5: Chemical and Biological catalytic activity of RNP_PME(2.5) *:C.rugosa* lipase@RNP_PME formation and use; RNP_PME catalytic conversion of glucose and fructose to platform chemical precursor HMF.

5.1 Summary

Applications of RNP_PME(2.5) nanoparticles in the fields of catalysis and enzyme immobilization (specifically *C. rugosa* Lipase enzyme subsequently referred to as enzyme) were explored. RNP_PME(2.5) nanoparticles acted as excellent Brönsted acid catalysts to convert fructose to 5-(Hydroxymethyl)furfural (HMF). Yields of 87% were obtained using 10 wt% fructose. The catalyst demonstrated excellent recyclability. Large pore nanoparticles were also used to immobilize lipase on the particles. Following immobilization, an increase in the maximum velocity and Michaelis constant of the enzyme was observed. The particles also afforded protection against denaturation.

5.2 Introduction

5.2.1 Heterogeneous catalysts for the synthesis of HMF from sugars

Currently petrochemicals are the source for the vast majority of chemicals and energy. However, diminishing petrochemical reserves and pollution caused during the production and use of petrochemicals resulted in the search for cleaner and renewable sources for platform chemicals and energy.[1] Biomass, especially in the form of carbohydrates is the most widely available carbon source on the planet and is considered an attractive source of new platform chemicals.[1] Carbohydrates contain carbon, hydrogen and oxygen atoms. In order to be used as platform chemicals or energy source it is important to reduce the number of oxygen atoms. Three strategies have evolved to achieve this aim. The elimination of small molecules such as carbon dioxide,

formaldehyde or formic acid reduces the number of oxygen atoms, however it also eliminates vital carbon atoms. Hydrogenation, preserves the total number of carbon atoms, however this method has limited application since only polyols can be produced by this method. Finally, dehydration reactions have been used to eliminate water molecules from the carbohydrate molecules. This method has been used to synthesize a variety of platform chemicals such as HMF (Scheme 1), furfural, levulenic acid etc.[2]

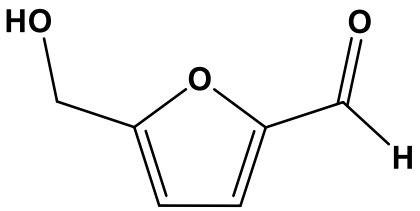

Scheme 5.1: HMF

HMF is an important platform chemical. It is naturally produced in carbohydrate rich foods such as honey and is considered as an indicator of food deterioration.[2] However, HMF is also a very important platform chemical. It has been used to synthesize a wide variety of commercially important compounds. Structures of these HMF derivatives are presented in Scheme 2. HMF was first synthesized by Düll and Keirmeyer in 1895, by heating sugars in presence of oxalic acid under pressure.[3]

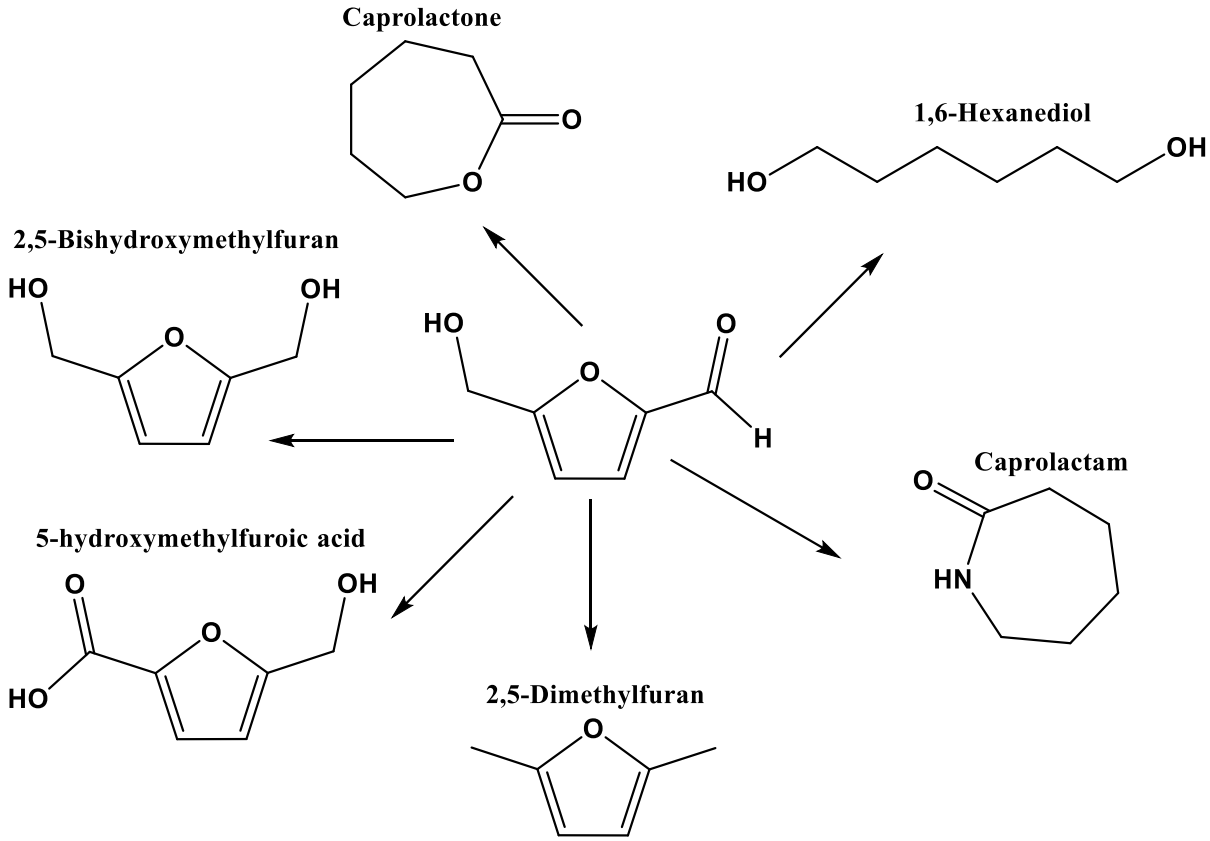

Scheme 5.2: HMF derivatives

Two general mechanisms were proposed to explain the formation of HMF under aqueous conditions. The acyclic pathway (Scheme 3), where the first step involved the formation of linear 1,2-enediol, by the Lobry deBruyn-Alberda van Ekenstein (LBAE) transformation. 1,2-enediol undergoes two further β-dehydrations and a ring closure to form HMF.[4] The cyclic pathway (Scheme 4) starts from cyclic ketofuranose, which is expected to undergo dehydration of the hemiacetal at C_2 to form carbenium cation, which then undergoes two consecutive β-dehydrations to form HMF.[5] Conclusive experimental evidence to support either mechanism has not been established. Studies have also shown that the choice of carbohydrates strongly affected the yield of HMF. Use of fructose resulted in higher yields compared to *glucose* as the starting material.[6]

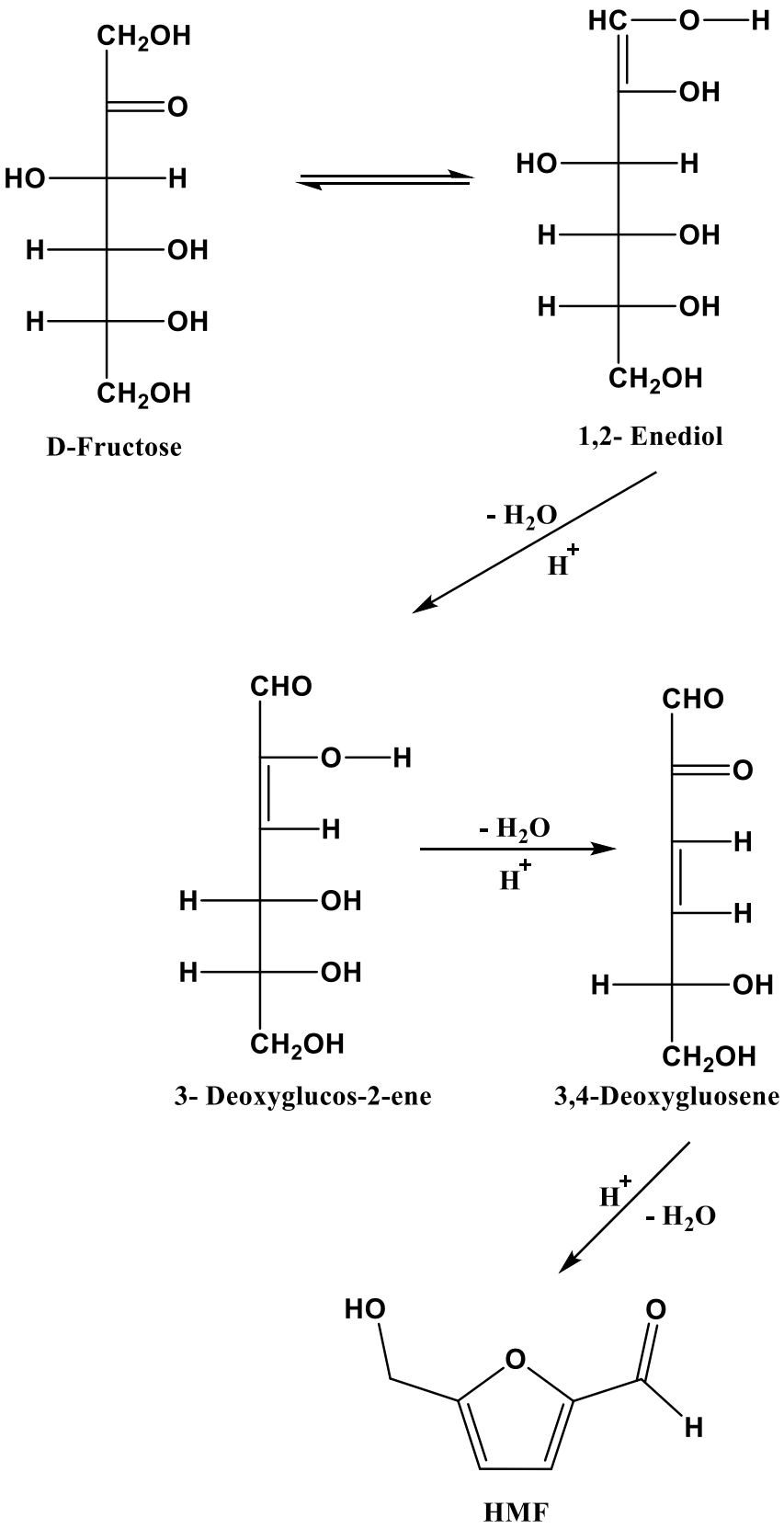

Scheme 5.3: Acyclic pathway for HMF synthesis

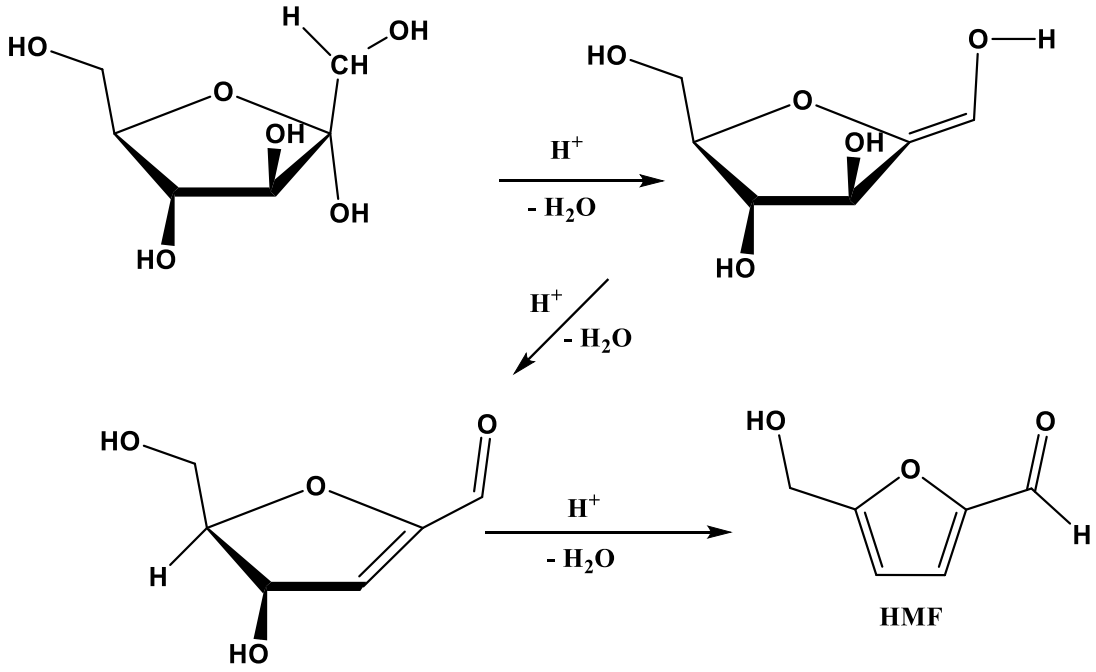

Scheme 5.4: Cyclic pathway for the synthesis of HMF

Synthesis of HMF in high yields remains a technical challenge. Under aqueous conditions, HMF produced from carbohydrates is rapidly converted to a variety of by products such as formic acid, levulenic acid or alternatively the sugars are converted to insoluble polymers called humins.[2] The challenge therefore is to improve the selectivity and isolated yield of HMF. Dumesic *et al.* developed a biphasic system designed to take advantage of the differences in the solubility characteristics of HMF and the by-products.[7] HMF is soluble in both aqueous and organic solvents (such as methyl isobutyl ketone (MIBK)), while the starting material glucose and the by-products such as formic acid are water soluble. In order to efficiently separate HMF from the aqueous phase Dumesic *et al*. used MIBK : 2-butanol (7:3 ratio). 2-butanol increased the solubility of HMF in the organic phase. However only modest yields between 40 to 60% were obtained using this method, when fructose was used as starting material.[7] Other groups have used DMSO as the solvent. In these reactions DMSO acted both as the solvent and as a catalyst.[8] However, the isolation of HMF from DMSO is an energy intensive process and is expected result in a significant loss of the product due to carbonization when carried out

on an industrial scale.[7] Other strategies for synthesis included using ionic liquids and Lewis acid catalysts such as $CrCl_3$[9] and $AlCl_3$.[10] The use of ionic liquids resulted in excellent yields.[11] However, due to the high cost of ionic liquids, the process would only lend itself to laboratory scale synthesis. The use of $CrCl_2$ and $CrCl_3$ produced good yields of HMF, especially when used in combination with ionic liquids[9] or solvents such as dimethyl acetamide (DMA).[12] In addition to the disadvantages mentioned above, the toxicity of the chromium salts severely limit the application of this process. Finally, the use of $AlCl_3$ resulted in moderate yields (~ 60%), however stoichiometric amounts (50%) of catalyst were used in the reaction.[10]

In order to overcome these problems, heterogeneous catalysts such as Amberlyst-13 were used in the synthesis of HMF.[7] These catalysts are more efficient, robust, easily separated and do not produce toxic by-products.[13] However, only moderate HMF yields were obtained using heterogeneous catalyst systems. Heterogeneous catalysts, especially zeolites, have been widely used in the petrochemical industry. Zeolites have a robust chemical structure and have been demonstrated to withstand extreme temperatures.[14] Various zeolites were used to convert sugars (glucose and fructose) to HMF with moderate yields.[15] The main challenge in the use of zeolites as catalysts resulted from the microporosity of these materials (pore size around 0.8 nm).[16] Previous studies on zeolites demonstrated that the materials exhibited diffusion limitation, which arose due to the small pore size of these materials. This caused inefficient removal of the product molecules resulting in deactivation of the catalyst.[17] Mesoporous bulk silica materials have been used to overcome this problem.[17] These materials have tunable pore size and have a robust structure. Moderate HMF yields were obtained using sulphonic acid functionalized mesoporous silcas.[18] Despite the moderate yields, organically functionalized SBA-15 silicas were used to develop flow based reactor systems for HMF

synthesis, highlighting the potential of heterogeneous catalysts.[19] Mesoporous silica nanoparticles have been demonstrated to have higher mass transfer co-efficient, therefore these particles could potentially be used as better catalysts.[20] Several studies involving MSNs showed little or no improvement over bulk materials.[21] Therefore there is a need to develop better and more efficient catalysts for HMF synthesis.

5.2.2 Lipase immobilization

Lipases are one of the most industrially important enzymes. Lipases can perform esterification at the oil-water interface and are classified as triacylester hydrolases EC 3.1.1.3 ((*EC numbers are used to classify enzymes based on the reactions they catalyse. Lipases belong to a class of enzymes known as hydrolases, which catalyse hydrolysis of a chemical bond. EC 3.1.1 classify the enzymatic reaction as hydrolysis of ester bonds*).[22] Unlike other enzymes lipases do not have substrate specificity and can catalyse a variety of reactions such as esterification, de-esterification, transesterification, acylation and can be used to perform enantiomeric separation of organic compounds.[23] Due to their excellent properties, lipases are used for a variety of applications ranging from organic synthesis to cheese making.[24] However, difficulty in recycling and reusing the enzymes have prevented applications in the area of large scale chemical synthesis.[25]

Immobilization of lipases on various surfaces has been demonstrated to improve catalytic efficiency. Immobilization of enzymes on solid surfaces typically limits conformational changes and affords protection.[26] Three dominant strategies have been used so far to immobilize lipase. The first strategy involved physical immobilization on mesoporous silica materials, such as SBA-15 or MCM-41.[27] Immobilization on mesoporous silica surfaces protected the enzymes from degradation. However, enzyme leaching was observed when unfunctionalized silica was used.[28] The second strategy involved chemical conjugation to nanoparticle surfaces and this method has been

extensively used with polymer or polymer coated nanoparticles.[25] This method helped overcome the problem of protein leaching.[28] Polymeric materials have low recyclability, which limits the applications of these systems.[29] However, the recyclability of the materials was improved when the robust materials such as carbon nanotubes[30] or mesoporous silica[31] were used. The final strategy involved encapsulation of lipases inside silica shells. This method resulted in good enzyme encapsulation,[32] especially when histidine tagged lipases were used.[33] Until recently, mesoporous silica nanoparticles have not been used to encapsulate lipases. Mesoporous silica nanoparticles have higher mass transfer co-efficient compared to bulk silicas[20] and could therefore act as good encapsulation substrates. The dimensions of lipase molecules are 5x4.2x3.3 nm^3. Previous studies involving SBA-15 silicas demonstrated that nanomaterials with pore diameter of around 15 nm are best suited for lipase immobilization.[34] The lack of studies detailing lipase encapsulation in mesoporous silica nanoparticles could be explained by the fact that very few reports have been published detailing the synthesis of nanoparticles with that pore diameter.

5.3 Experimental

Materials: RNP_PME(2.5) was synthesized using the methods described in Chapter 2. Lipase from *C. rugosa* (CRL), type VII, 4-nitrophenyl acetate, 4-nitrophenol (≥ 99%), methyl isobutyl ketone (≥ 98.5%), 2-butanol (99%), BSA (bovine serum albumin), sodium dihydrogen phosphate were purchased from Sigma Aldrich and were used without any further purification; fructose and dibasic sodium phosphate was purchased from BDH chemicals; NaOH pellets, ethanol, acetonitrile (99%) and HCl (35% w/w) was purchased from VWR and used without further purification. The particle synthesis and buffer preparation were carried out in deionized water dispensed from an 18 mΩ Millipore system supplied by Elba UK.

5.3.1 HMF synthesis

Fructose (100 mg, 0.55 mmol) was dissolved in deionized water (0.9 g) and RNP_PME(2.5) (15 mg) was added to this solution. An organic phase (4 g) containing MIBK and 2-butanol in 7:3 ratio was added to the reaction vessel to obtain a biphasic mixture. The biphasic mixture was sonicated using an ultrasonic probe in pulsed mode. The amplitude of the probe was set to 65%. Ultrasonic waves were applied with a 45 second pulse and 15 second pause sequence. The total sonication time was 5 minutes. It was found that the reproducible results were obtained only when the probe was properly centred in the reaction vessel. After sonication the mixture was allowed to settle for 15 minutes, at which point it separated into water-in-oil (upper) and oil-in-water (lower) phases. The reaction mixture was heated to 180 °C, while stirring at 600 rpm for 3 h. After the 3 hours the reaction was allowed to cool and the emulsion was broken by centrifuging the reaction vessel at 1000 rpm for 1 minute and the organic layer was separated and the solvent removed by using a rotary evaporator. The product was weighed and characterized by ^{1}H NMR.

Catalyst recyclability: After completion of the reaction, the reaction mixture was cooled without stirring and the emulsion was broken by adding a small amount of diethyl ether and the organic phase (top layer) removed. Following the organic layer removal, another batch of fructose (0.1g, 0.55 mmol) and organic phase (4 g, MIBK and 2-butanol in 7:3 ratio) was added and the process repeated. In this manner five catalytic cycles were assessed. In each case pure HMF (by NMR) was obtained from the organic phase. The experiment was performed in duplicate.

Effect of fructose concentration: The same process was repeated with different concentrations of fructose (from 10 to 50 wt%), while keeping the weight of the catalyst constant (15 mg).

Kinetic study: The kinetics of HMF production was assessed. Reactions were stopped after 5, 15, 30 and 60 minutes. For each time point, the upper (organic) phase was collected and the weight of HMF obtained was determined by solvent removal.

5.3.2 Reaction characterization

Optical microscopy: oil-in-water and water-in-oil emulsion mixtures were prepared as described above using 10 wt% of fructose in the aqueous phase. One drop of each emulsion was placed on a clean glass slide and observed using an optical microscope at 20X and 50X magnification. Images were collected and processed using ImagePro Express software.

Cryo-Scanning Electron Microscopy (Cryo-SEM): Cryo-SEM was used to image the emulsions generated during HMF synthesis. The analysis was carried out on Quanta FEG 450 SEM, equipped with Gatan ALTO 2500 cryotransfer for SEM. Sample preparation involved the following steps:

Instrument setup: Prior to sample preparation, the cryo stage was inserted into the SEM and the system was flushed with nitrogen gas and cooled using liquid nitrogen.

Sample preparation: One drop (~ 100 µL) of emulsion (oil in water (O/W) and water in oil (W/O) was placed on an aluminium stub and the sample was rapidly frozen by dipping in nitrogen slush for 5 minutes. The sample was then transferred to a vacuum pod and transferred into the preparation chamber of the SEM and chamber pressure was set to 8 bar. Following this, the sample temperature was raised to – 90 ± 3 °C and the sample was kept at this temperature for 2 minutes to sublimate ice. The sample temperature was then decreased to -130 °C.

Sample coating and imaging: When the sample temperature reached -130 °C, the chamber was flushed with ultra-pure argon gas (99.999 vol%) and the sample was coated with platinum. Following this, the sample was inserted into the microscope. The samples were imaged at 10 and 5 kV voltage for O/W and W/O emulsions respectively and the spot size for both samples was 5 nm.

Catalyst stability NMR study: The stability of the catalyst was determined by measuring the total phosphonate loading on the particles at different stages of the reaction. The reactions were set up based on the procedure described above. The reactions were stopped after different time periods (between 5 minutes and 1 hour). A blank reaction was performed for 3 hours without using any fructose to study the effect of the reaction conditions on the particles. Following this, the aqueous phases were freeze dried (for 30 hours) to obtain dry particles. These particles were then dissolved in 400 µL NaOD/D_2O and centrifuged to remove any undissolved impurities. 300 µL of the supernatant and 100 µL of internal standard solution (potassium dihydrogen phosphate[35] in D_2O) were added to an NMR tube.

5.3.3 CRL immobilization

CRL was supplied as a crude mixture, containing two isoforms of lipase[36] and a variety of biomolecules of non-enzymatic nature with specifications of 700 U/mg (U = µmol/ min). In this work the CRL loading was quantified by Bradford assay extrapolated from a BSA calibration curve (Appendix 4) and enzyme activity was measured from the

conversion of the substrate (4-nitrophenyl acetate) to product (4-nitrophenol) (Appendix 4).

Preparation of CRL solution: 3 g of C. rugosa lipase was added to 30 mL of sodium phosphate buffer (PB) (25 mM), pH adjusted to 5.00 by adding 1 M HCl, at 4 °C. After 16 hours of gentle stirring, the suspension was centrifuged at 14000 rpm for 25 minutes to separate the insoluble products. The clear brown solution thus obtained was stored at 4 °C.

Measurement of CRL concentration: Protein concentration was determined using Bradford assay[37] and the calibration curve obtained using BSA stock solution (0.1 mg/mL) (Appendix 4).

CRL adsorption study: Nanoparticle dispersions (1 mg/mL) of RNP_PME(2.5), in PB (25 mM) at pH 4.99 were prepared by sonication for 30 min. Different concentrations (0.06 – 2 mg mL^{-1}) of Lipase in PB (pH 4.99) were prepared. Mixtures containing 1 mL enzyme solution and 1 mL of nanoparticle dispersion were gently agitated and allowed to stand for 45 minutes at 20 °C. Next these enzyme-protein dispersions were centrifuged at 14000 rpm (10 min) and the particles and supernatant collected and the latter analysed by Bradford assay. Measurements were performed in triplicate

CRL load vs Time study: Nanoparticle dispersions RNP_PME(2.5) (2 mg mL^{-1}) were prepared by sonicating the particles in PB (25 mM, pH 4.99). Samples of this dispersion (1 mL) were added to lipase solutions (1 mL of 2 mg/mL), gently mixed and allowed to stand for different time periods. Then the enzyme-protein dispersion was centrifuged at 14000 rpm (15 min) and the particles and supernatant collected and analyzed by Bradford assay. Measurements were performed in duplicate

Enzyme catalysis: A 100 mM stock solution of the enzyme substrate 4-nitrophenyl acetate (4-NPA) in acetonitrile was prepared. Lipase stock solution of 0.03 mg mL^{-1} (determined by Bradford assay) was prepared in 25 mM PBS (pH 7.0). 0.3 mL of the substrate solution was mixed with 2.7 mL of the enzyme solution and the reaction was followed by UV-Vis spectroscopy, by monitoring the peak absorbance at 400 nm (corresponding to 4-nitrophenol). The reaction was carried out in a shaker at 250 rpm and the temperature was set at 25 °C. In order to perform enzyme kinetics study, the substrate concentration was varied from 1-100 mM. Each measurement was repeated 8 times. The reaction velocity (q) was calculated by determining the absorbance of nitophenol/minute and this was plotted against substrate concentration [S] in mM units.

Denaturation study: Urea is a protein denaturant and the effect of this on the reaction was studied by treating the reaction mixture described in the enzyme catalysis section with varying amounts of urea (from 1 to 4 M). The formation of 4-nitrophenol was followed spectroscopically by measuring the absorbance of the solution at 400 nm. Measurements were performed in triplicate.

5.4 Results

5.4.1 Nanoparticle characterization

SEM analysis revealed that the particles, RNP_PME(2.5) employed in this study, had, as previously, a spherical shape and raspberry texture. The particles were monodisperse with particle size ranging from 70 to 90 nm (Figure 5.1). Surface area and the pore size of the particles were determined using nitrogen adsorption porosimetry (Figure 5.2). The surface area of the particles was 724 m^2/g the particles displayed large pore diameter of 17.8 nm. A summary of the morphology of the particles is given in Table 5.1

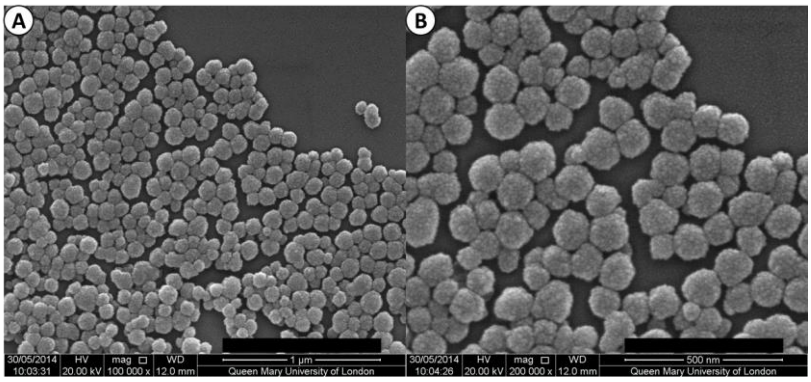

Figure 5.1: SEM images of RNP_PME(2.5) nanoparticles. Scale bar A) 1000 nm; B) 500 nm

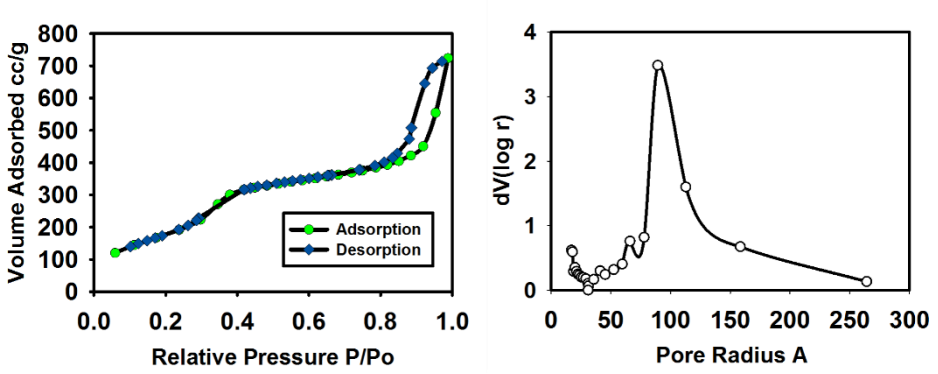

Figure 5.2 Nitrogen adsorption isotherm of RNP_PME(2.5) nanoparticles

Table 5.1 Morphological properties of RNP_PME(2.5) nanoparticles

Property	**RNP_PME(2.5)**
Particle shape	Spherical
Particle size distribution	70 -90 nm
Surface area	724 m^2/g
Pore volume	0.732 mL/g
Pore size	17.86 nm

5.4.2 HMF synthesis

Pickering emulsion formation

RNP_PME(2.5) nanoparticles were added to the biphasic mixture of aqueous fructose solution and the organic phase (MIBK:2-butanol in 7:3 volume ratio) and sonicated using an ultrasonic probe. Sonication resulted in the formation of a homogenous white emulsion, which slowly separated into two phases, the bottom phase was milky white oil in water (O/W) emulsion. This phase was visually identified, by shaking the reaction tube, to be more viscous than the original fructose solution. The second phase was the water in oil (W/O) phase. This layer had a cloudy appearance.

Optical microscopy was used to characterize the emulsions. One drop from each emulsion was placed on a clean microscope slide. The oil-in-water showed a large number of droplets. The size of the droplets varied between 2 to 20 µm. The droplets had a distorted spherical shape. Interestingly, aggregation between the droplets in the form of Ostwald ripening was not observed, suggesting that the emulsion was stable under the observation conditions (Figure 5.3). The water-in oil emulsion had smaller, more uniform sized droplets. The average droplet size was around 2 µm (Figure 5.4) and there were fewer droplets in this phase compared to the oil-in-water layer.

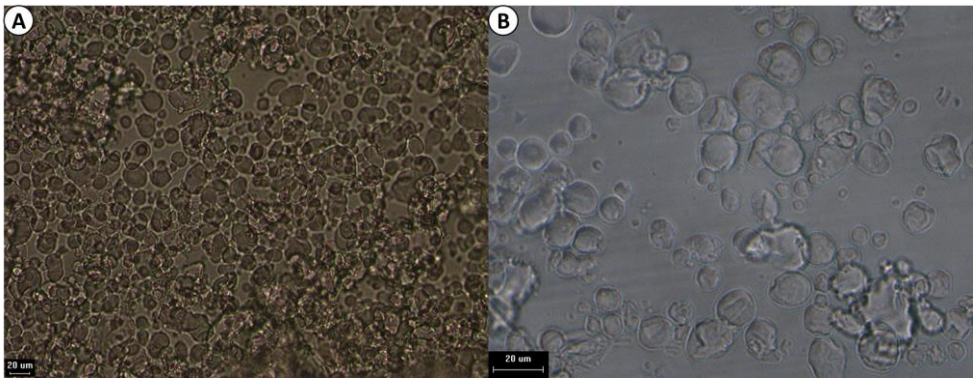

Figure 5.3: Optical microscope images of oil-in-water emulsion A) At 20X magnification (Scale bar 50 µm) and B) At 50X magnification (Scale bar 20 µm)

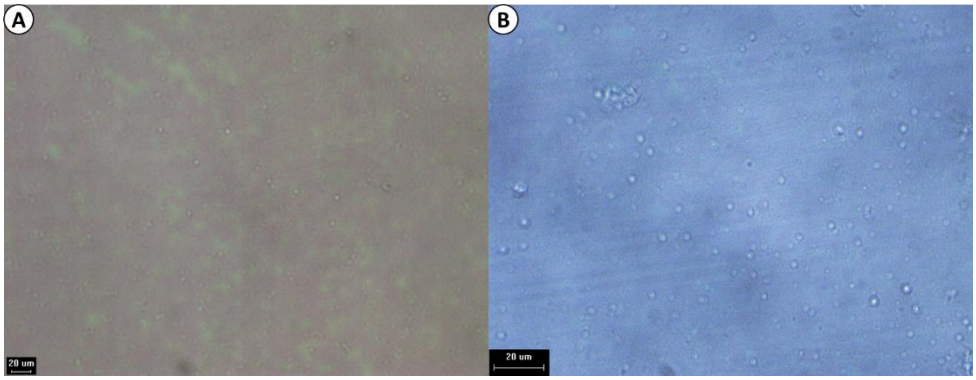

Figure 5.4: Optical microscope images of water-in-oil emulsion A) At 20X magnification (Scale bar 50 µm) and B) At 50X magnification (Scale bar 20 µm)

Cryo-SEM imaging

The Pickering emulsions were further imaged by cryo-SEM imaging. The technique allowed direct imaging of the emulsion droplets. The images, revealed that the droplets were covered by nanoparticles. The droplets from the aqueous phase (Figure 5.5) had a sea urchin like surface texture. The cryo-SEM images further revealed the presence of smaller particles (~ 1 µm in diameter, Figure 5.5), which were not observed using optical microscopy, due to lower resolution of the optical microscope. The particles were found to be localized on the surface of the droplets in irregularly shaped aggregates. However, images revealed that the particles displayed high interconnectivity, suggesting network formation. The images conclusively established the presence of Pickering emulsion (Figure 5.6).

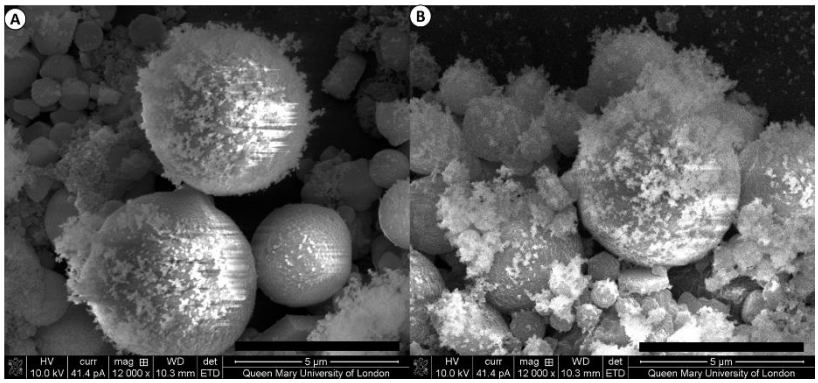

Figure 5.5: Cryo-SEM image of O/W emulsion (Scale bar figures A and B - 5000 nm)

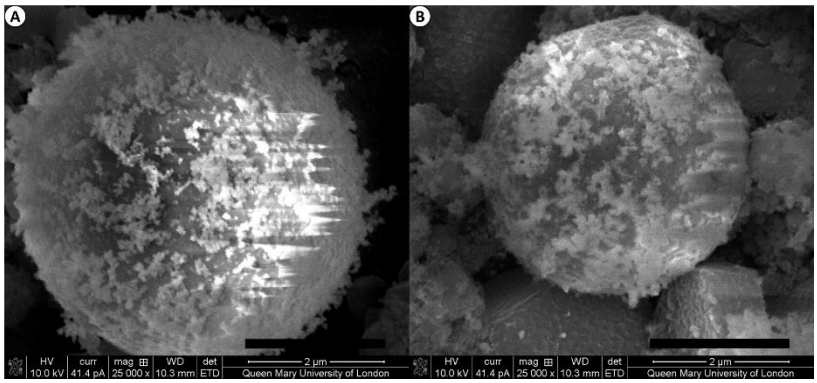

Figure 5.6: High magnification Cryo-SEM image of O/W emulsion (Scale bar figures A and B - 2000 nm)

The droplets observed in the organic phase had irregular morphology, as observed in the optical images and fewer nanoparticle stabilized water droplets were observed in the organic phase. (Figure 5.7). The irregular morphology was probably due to the collapse of the emulsion, following the sublimation step during sample preparation. Particles were observed on the irregularly shaped structures. The particles, however showed lower level of interconnectivity.

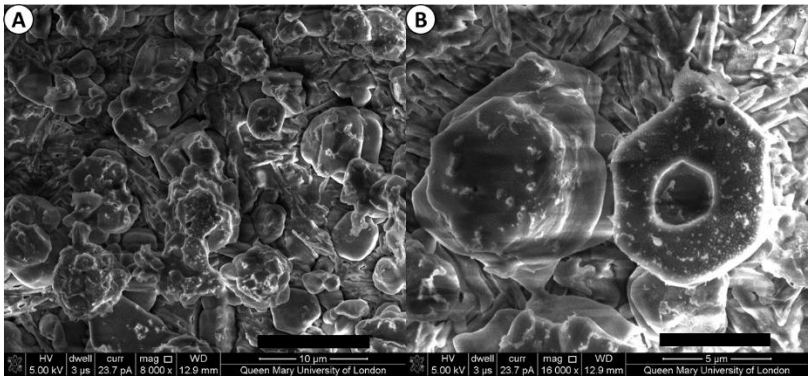

Figure 5.7: Cryo-SEM image of W/O emulsion (Scale bars, A – 10 µm and B – 5 µm)

5.4.3 HMF synthesis and catalyst recyclability:

HMF was synthesized using RNP_PME(2.5) nanoparticles as acid catalysts and fructose was used as the starting material (Scheme 5.4). The reaction was carried out in a thick glass sealed tube at 180 °C for 3 hours. As the reaction progressed both O/W and W/O layers underwent colour change. The W/O layer changed from cloudy to dark brown. The aqueous phase changed to dark orange from the initial milky white. In order to break the emulsion, the vial was centrifuged at 1000 rpm for 1 minute after it cooled to room temperature. The organic layer was then separated and the solvent was removed under vacuum. The final product yield of 87.36 ± 0.83 % was obtained.

In order to demonstrate the reusability of the catalyst a catalyst recycle study was carried out. Cycle 0 represented the first reaction, the catalyst was then subsequently recycled 4 times. After each reaction, the reaction was stopped and the organic layer was separated as described above. Following this, fructose and fresh organic layer were added to the reaction tube and sonicated and the reaction was carried out as described above. The results (Figure 5.8) showed that the isolated yield was constant, suggesting that the catalyst was highly efficient and recyclable with TON (turnover number) of 61.7

moles/mol of acid per gram of catalyst (on the basis of 2.5 mmol phosphonate /gram on the nanoparticles) after 5 cycles.

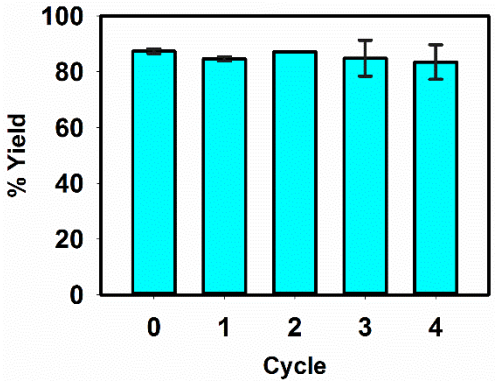

Figure 5.8: Catalyst recycle study (n= 2 ± std. dev.)

5.4.4 Effect of fructose concentration

The effects of fructose concentration on overall yield was studied. Different concentrations of fructose ranging from 10 wt% to 50 wt% were used. The reaction conditions were those described above and the isolated yields of HMF were calculated using the methods described above. The isolated yield of HMF decreased slightly from 87.36 % at 10 wt% to 79.97% at 50 wt% fructose concentration (Figure 5.9).

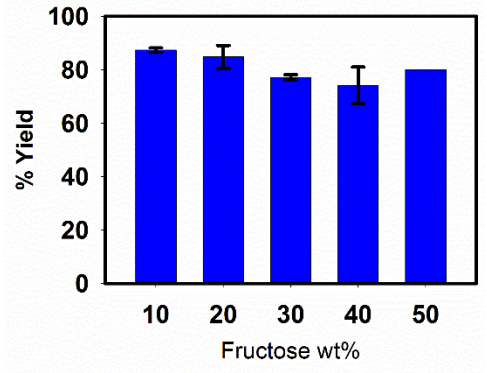

Figure 5.9: Effect of Fructose concentration on HMF yield (n= 2 ± std. dev.)

5.4.5 Kinetics profile of HMF formation

The kinetics of HMF formation were studied by stopping the reaction employing 10 wt% fructose at various time points during the first hour of the reaction. Isolated yield for each sample was calculated by collecting HMF from the organic phase. Figure 5.10 shows the variation of HMF isolated yield with time. A turnover frequency of 6.40 mol $h^{-1}g^{-1}$ was determined.

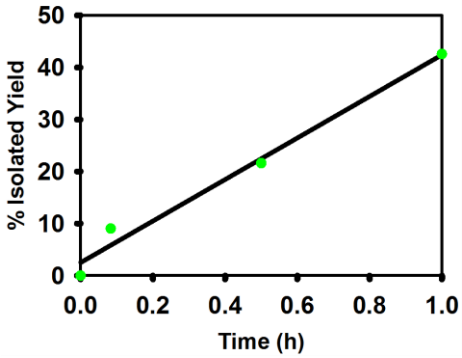

Figure 5.10: HMF yield versus time

5.4.6 Catalyst stability study

As the reaction progressed, the catalyst underwent chemical change. The catalyst at the start of the reaction was composed of phosphonate monoester, as the reaction progressed the phosphonate ester group was gradually converted to the acid group (Scheme 5). The conversion was tracked using ^{31}P NMR. Figure 5.11 shows the percentage of phosphonate monoester that was converted to phosphonate diacid. ^{31}P NMR spectra showing the conversion of phosphonate monoester to phosphonate diacid are shown in Figure 5.12 and 5.13.

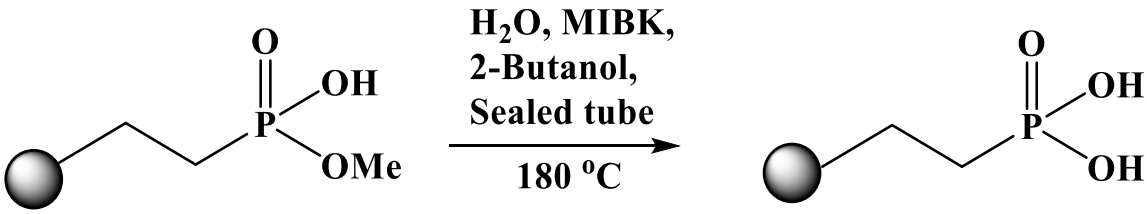

Scheme 5.5: Conversion of phosphonate monoester particles to phosphonic acid particles under the reaction conditions

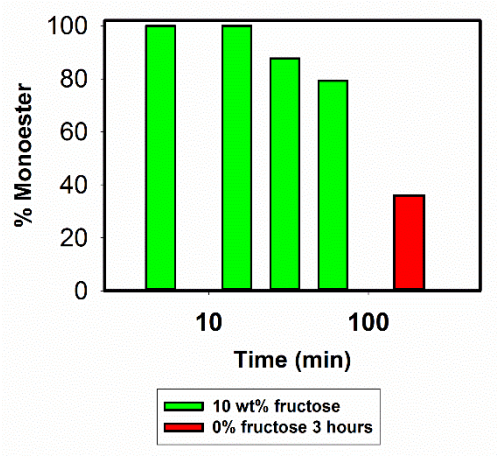

Figure 5.11: Relative change in the monoester concentration during the course of the reaction

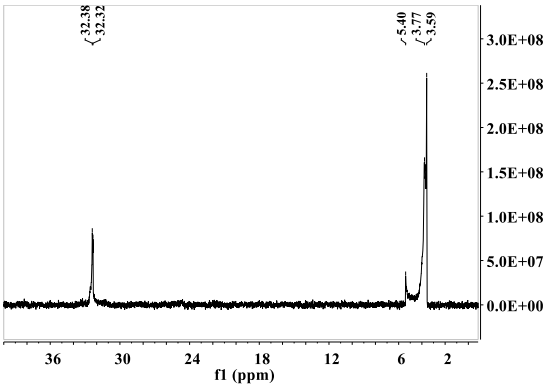

Figure 5.12: ^{31}P NMR spectra of the particles dissolved in $NaOD/D_2O$ showing phosphonate monester peak at δ_{31P} 32.3 ppm

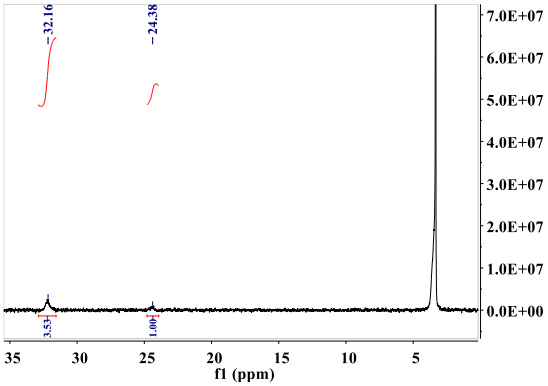

Figure 5.13: ^{31}P NMR spectra of the particles dissolved in NaOD/D_2O showing phosphonate monester (sodium salt) peak at δ_{31P} 32.2 ppm and phosphonate diacid (sodium salt) at 24.38

5.4.7 Immobilization of *C. rugosa* lipase (CRL)

Lipase load versus time

Time dependent adsorption of lipase was performed. The particles adsorbed a large amount of lipase immediately upon exposure to lipase. Some of the adsorbed lipase was then released back into the solution and it was re-adsorbed at a slower rate (Figure 5.14).

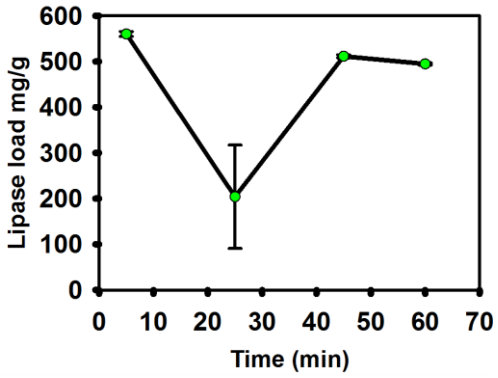

Figure 5.14: Lipase adsorption versus time (n= 2 ± std. dev.)

5.4.8 Adsorption of lipase on nanoparticles

A lipase adsorption study was performed on 1 mg/mL nanoparticle dispersions. The particles adsorbed a large quantity of lipase from solution. The final protein load on the particles was 586.6 ± 28.0 mg/g. (Figure 5.15).

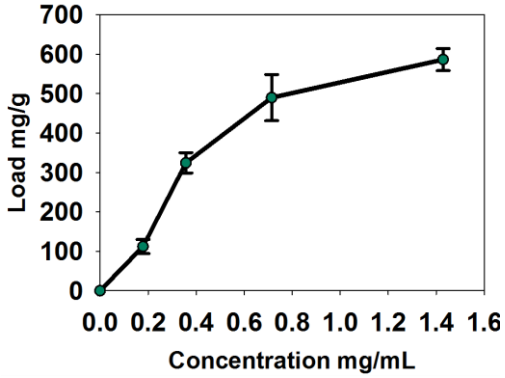

Figure 5.15: *C. rugosa* lipase uptake versus concentration study (n= 3 ± std. dev.)

5.4.9 Dynamic Light Scattering of lipase@RNP(2.5)

The hydrodynamic radius of the RNP_PME(2.5) an lipase@RNP_PME(2.5) nanoparticles was measured in sodium phosphate buffer at pH 5.0. Lipase@ RNP_PME(2.5) particle size was measured 30 minutes after loading. The RNP_PME(2.5) nanoparticles had a monodisperse size distribution of 196.86 ± 2.75 nm (n=3), upon loading lipase the hydrodynamic radius increased to 624.10 ± 8.00 nm (n =3) (Figure 5.16)

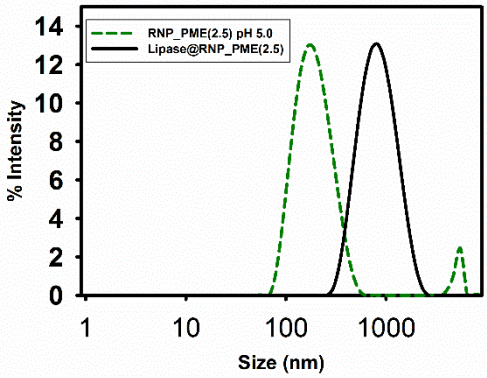

Figure 5.16: Hydrodynamic radius of nanoparticles.

5.4.10 Michaelis Menten kinetics

The effect of immobilization on the enzyme kinetics of lipase was studied by measuring Michaelis Menten kinetics (Equation 1) of the immobilized enzyme. The study

was performed by measuring the rate of hydrolysis of esterase substrate 4-nitrophenyl acetate. The study showed that there was no difference between the catalytic ability of the immobilized and free lipase (Figure 5.17). The q_m (maximum velocity, condition during which the enzyme is working at full capacity) values were 33.19 ± 8.76, 15.31 ± 4.31 U/mg (U = µmol/ min) respectively and the K_m (Michaelis constant, the substrate concentration at which the enzyme is working at half the maximum velocity or ½(q_m)) values were 0.027 ± 0.004 and 0.007 ± 0.002 mM respectively. The q_m and K_m values were obtained from Lineweaver-Burke plots (Equation 2) (Figure 5.18). The values were found to be statistically significant at $p < 0.01$ using student's T- test (Two tailed).

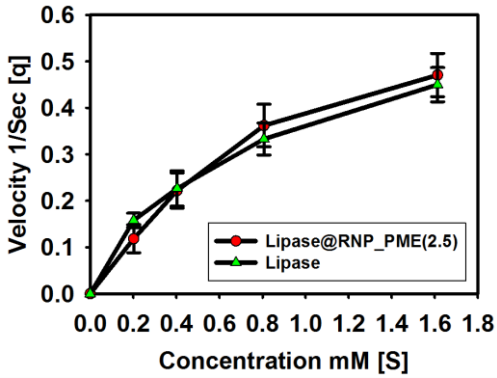

Figure 5.17: Rate of catalysis (q) versus substrate concentration (S) (n= 8 ± std. dev.)

$$q = \frac{q_m[S]}{K_m + [S]}$$

Equation 1: Michaelis- Menten equation

$$\frac{1}{q} = \frac{K_m}{q_m}\left(\frac{1}{[S]}\right) + \frac{1}{q_m}$$

Equation 2: Equation for Linewaver Burke plot

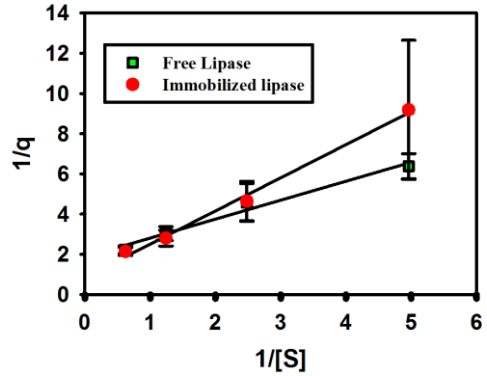

Figure 5.18: Lineweaver-Burke plot of free and immobilized lipase

5.4.11 Effect of urea

Urea is a protein denaturant, the effect of urea on the activity of the enzyme was studied. Upon addition of urea there was a strong reduction in the activity of free lipase. At 1M concentration, the relative activity of lipase dropped down to 39.1 ± 20.9 % and at 4M concentration, the activity dropped to 26.5 ± 20.5 %. Lipase@RNP_PME(2.5) sample did not show severe denaturation in presence of urea. It retained 89.2 ± 6.8 % of its original activity at 1M urea concentration and 59.9 ± 7.7 % of its original activity at 4M urea concentration (Figure 5.19). Statistical analysis was performed on the relative changes in the lipase activity on the enzyme before and after immobilization on nanoparticles. Statistical analysis was performed using paired t-test on the immobilized and free lipase. The study revealed that the increase was statistically significant at $p < 0.01$.

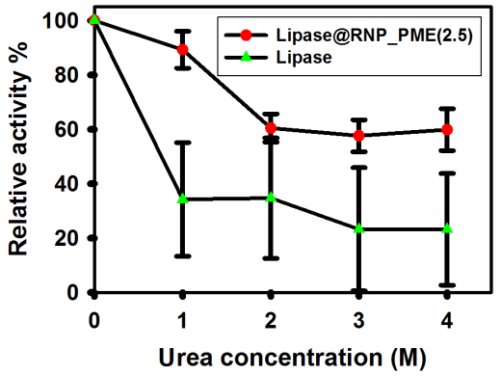

Figure 5.19: Effect of urea on enzyme activity (n = 3 ± Std. dev.)

5.5. Discussion

5.5.1 HMF synthesis

Platform chemicals that are sourced from renewable resources are of great importance to the future of the chemical industry. Biomass is the most abundant source of carbon and is an ideal platform for producing various industrially relevant compounds. One such compound is HMF. It holds great potential as it can be converted into a variety of chemicals with applications ranging from energy (2,5-dimethyl-furan) to polymers (2,5-furan-dicarboxylic acid).[2] The most commonly used method for synthesizing HMF involves acid treatment of sugars such as fructose, which undergo acid catalysed dehydration to form HMF. However, HMF undergoes acid catalysed degradation to a variety of by products such as formic acid, levulenic acid and insoluble polymers called humins.[7]

Pioneering work by Dumesic *et al*.[7] demonstrated that efficient separation of HMF can be achieved by using biphasic reaction systems. These systems take advantage of the differences in solubilities of HMF and the by-products. HMF is soluble in both water and a variety of water immiscible organic solvents such as MIBK, chloroform, ethyl acetate etc.[7] The isolated reaction yield was found to increase using phase transfer agents such as 2-butanol. Here, we used MIBK: 2-butanol as the organic solvent (HMF extraction) system, while the reaction was carried out in water. Phosphonic acid based catalysts are mildly acidic and have been previously used by the Sullivan group to perform various Brönsted acid catalysed reactions (Appendix 5). RNP_PME(2.5) particles were chosen to explore the potential of nanoparticle systems in catalysing HMF synthesis. Nanoparticles have been shown to have excellent material transfer co-efficient[20] and would therefore function as excellent catalysts. RNP_PME(2.5) nanoparticles employed in this work

displayed unique features such as large pore size (17.8 nm), high surface area (724 m^2/g) and good organic loading (2.5 mmol/g), this suggested that these particles could potentially be used for catalytic applications.

Nanoparticles have been demonstrated to stabilize emulsions and these particle stabilized emulsions are known as Pickering emulsions.[38] These emulsions, have excellent mass transfer properties and have demonstrated a variety of interesting properties such as controlled release and selective uptake. Due to these properties, Pickering emulsions have been used for drug delivery applications.[39, 40] Recent reports demonstrated the potential catalytic applications of these systems. Leclercq *et al*. used polymetalate nanoparticles for oxidation reactions.[41] Wu *et al*. used these emulsions to entrap enzymes and perform enzymatic catalysis.[42] However, Brönsted acid catalysed reactions have not been demonstrated using this system so far. In order to prepare Pickering emulsion stabilized by RNP_PME(2.5) particles, the organic phase containing MIBK:2-butanol and aqueous phase containing the nanoparticles and fructose were sonicated using an ultrasonic probe. The aim was to homogenize the system and form a water in oil emulsion. However, following sonication a dual emulsion system formed consisting of oil in water phase and a water in oil phase (Scheme 5.6). Inspection by optical microscopy revealed that the majority of the particles remained in the O/W phase. Few emulsion droplets were observed in the W/O phase. This was probably due to the hydrophilic nature of the phosphonate group. Previous studies on silica nanoparticle stabilized emulsions revealed that hydrophilic silica nanoparticles resulted in the formation of O/W emulsions.[43] The above results are in accordance with the published results. The small amount of W/O emulsion could have resulted from interactions with the hydrophobic interactions between the methoxy group on the phosphonate and the organic solvent.

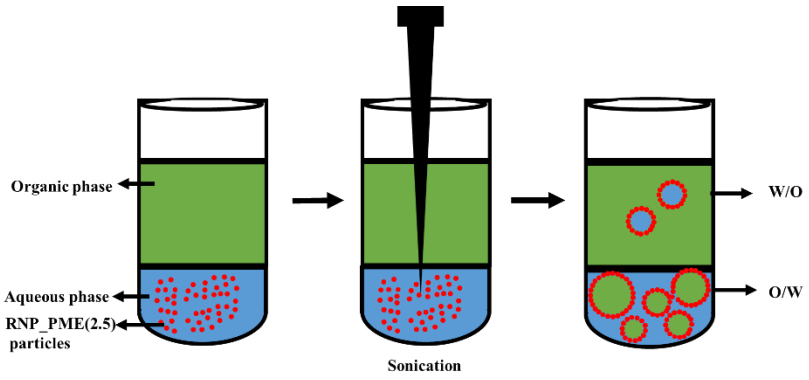

Scheme 5.6: Preparation of emulsions

Cryo-SEM studies of O/W emulsion revealed that the particles formed a network on the droplet surface (Figures 5.5 and 5.6). This could have played a role in stabilizing the particles. The gaps within the network could have helped facilitate the partition of HMF. Additionally, the particles retained their surface charge even in the presence of fructose (zeta potential = -27 mV), this could have further stabilized the emulsions. These results explain the stability of the emulsions despite the observed polydispersity in the droplet sizes (sizes between 2 to 20 µm). However, the emulsions were sensitive to centrifugation and were easily broken by gently centrifuging the reaction tubes at 1000 rpm. This helped efficiently recover most of the HMF produced during the reaction. RNP_PME(2.5) nanoparticle catalysed reaction resulted in an isolated HMF yield of 87.36 ± 0.83 %. This value was significantly higher than those reported from mineral acid[7] and heterogeneous (modified silica)[15,19] acid catalysed reactions that were carried out under similar biphasic reaction conditions. Only the reactions carried out in high boiling point solvents such as DMSO and ionic liquids gave yields greater than 90%.[8,11,12] However, extraction of HMF from DMSO on an industrial scale was demonstrated to be an energy intensive process and was expected to result in a significant loss of product.[7] Ionic liquids are expensive and therefore these methods do not lend themselves to commercial production of HMF. Aqueous synthesis provides an inexpensive platform for

HMF synthesis. In order to develop a commercially viable HMF production process, it is important to carry out the reaction at concentrations greater than 30 wt% of fructose.[7] Examples of such reactions have not been demonstrated in ionic liquid or DMSO based systems. Under aqueous conditions reactions carried out at 50 wt% fructose gave modest yields using mineral acid catalysts.[7] However, using RNP_PME(2.5) nanoparticle system yields up to 80% were obtained at 50 wt% fructose (Figure 5.9).

The reaction was carried out at 180 °C and the pressure in the reaction tube was over 10 bar. During the reaction, convection was observed. Following these observations, the mechanism of HMF transfer to the organic phase was postulated as follows. In the O/W phase fructose was present in the continuous water phase (since fructose is insoluble in the organic solvent phase) which was converted to HMF by the particles present on the oil droplet surface (Scheme 5.7). HMF was then rapidly partitioned into the oil droplet due to enhanced transport properties of emulsions. The droplet was then transported across the tube to the W/O phase where exchange of HMF occurred due to convection. Thus, gradually over the course of the reaction, HMF accumulated in the organic phase. This could have helped in the efficient exchange of HMF and therefore in the high yield observed.

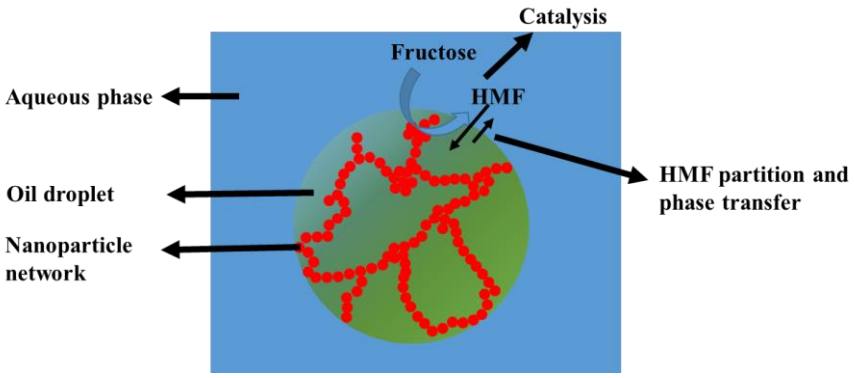

Scheme 5.7: HMF synthesis and phase transfer

Additionally, the particles also demonstrated excellent recyclability (Figure 5.8), which was probably a consequence of the robust silica framework.[44] The turnover frequency of the reaction was 6.40 $mol^{-1}h^{-1}g^{-1}$, which was significantly higher than found for solid acid resin based systems such as Amberlyst-15.[45] The results presented above can be explained by using two unique features of this system. First, RNP_PME(2.5) nanoparticles have a unique architecture consisting of large pore size, high surface area and high phosphonate loading. High surface area and large pore size enable better mass exchange and therefore improve the rate of catalysis.[20,46] The phosphonate group ~P(O)OMe(OH) is a mild acid group. The vast majority of the reports involving solid acid catalysed synthesis of HMF used strong acids such as sulphonic acids.[18] These acids promote HMF degradation and therefore result in loss of catalytic yield.[47] Finally, the reaction was carried out in a Pickering emulsion like system (Figures 5.3 and 5.4). Pickering emulsions are emulsions stabilized by particles.[48] Here, the emulsion was stabilized by RNP_PME(2.5) nanoparticles. The particles acted both as emulsion stabilizers and catalysts. Emulsions have been demonstrated as excellent systems for catalysis.[49] These results suggested that this nanoparticle based system has potential to be used as a catalyst in industrial HMF production.

5.5.2 Lipase catalysis

Lipase is an industrially relevant enzyme because it can catalyse a wide range of reactions. However, it has been demonstrated to undergo denaturation and has also been shown to exhibit poor recyclability.[25] Immobilization of enzymes has been demonstrated to enhance the enzyme activity and also offer protection from denaturation.[26] Chemical conjugation of lipases to nanoparticle surfaces is the current preferred strategy, however this method leads to lower loadings of the enzymes. Physical adsorption of lipases on

organofunctionalized mesoporous silica materials helped improve the catalytic properties of the enzyme and also protected the enzyme from degradation.[26] However, bulk silica materials have been shown to exhibit lower mass transport.[20] In order to improve the catalytic potential of these dispersed nanoparticle materials systems we used large pore RNP_PME(2.5) particles to adsorb lipase. Lipase uptake by the particles was measured using Bradford assay. Bradford reagent consists of the dye Coomassie Brilliant Blue G-250. The dye undergoes colour change depending on pH and upon binding the protein molecules (Scheme 8). In freshly prepared reagent the dye has red colour due to the presence of phosphoric acid. The measurement was performed in the presence a small amount of NaOH (1 M), which results in neutral , green coloured dye. Finally, the dye interacts with the cationic amino acids (arginine and lysine) on the protein molecules and forms the blue colour.[50] A calibration curve was obtained using BSA as it was known to give excellent colour response[50] and was found to produce similar response as lipase.[51] The particles as expected demonstrated very high protein load (586.5 mg/g) (Figure 5.15) and also showed rapid enzyme uptake (45 minutes for complete uptake) (Figure 5.14). This is a significant improvement over previous studies.[31,34]

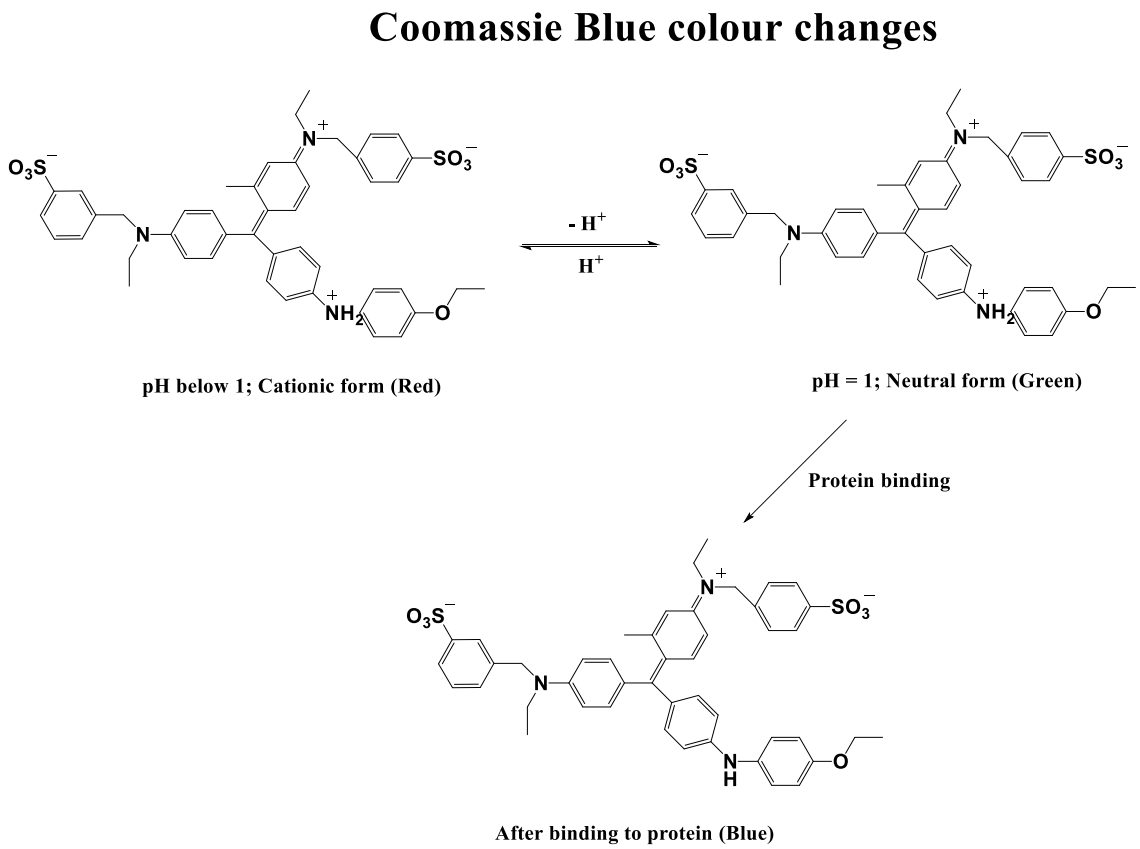

Scheme 5.8: Coomassie blue colour changes

The effects of the particles on the enzyme lipase was determined by measuring the Michaelis-Menten kinetics. Michaelis-Menten kinetics are an excellent tool for modelling enzymatic reactions. Michaelis- Menten equation provides a relationship between the rate of enzyme catalysis (q) and the substrate concentration [S]. Information about the interactions between enzyme and substrate can be obtained by determining the maximum velocity of the reaction q_m and the Michaelis constant K_m. q_m represents the maximum rate achieved by the system and K_m represents the substrate concentration at which the rate of the reaction is half of q_m. In addition to this, K_m also helps determine the interactions between the substrate and the enzyme. Higher K_m values represent lower affinity between the enzyme and the substrate and vice versa. [52]

In this study, immobilization of lipase on the particles resulted in the doubling of q_m and an increase of about 4 times in the K_m values. The increase in the K_m values

suggest that the immobilized enzyme has reduced affinity towards the substrate. This could have been caused by the phosphonate ester group on the particles. Carboxylate esters have been demonstrated as potent lipase inhibitors. Due to similarity in the structure of phosphonate esters and carboxylate esters, the functional group on the particles could have acted as competitive inhibitor to the lipase.[53] Further evidence for the competitive inhibition was obtained from the Lineweaver-Burke plot (Figure 5.18). The plots for free and immobilized lipases show trends that are similar to those observed during competitive inhibition.[52] However, contrary to many of the previous studies, the q_m value of the immobilized enzyme lipase@RNP_PME(2.5) also increased. The result suggested that despite the competitive inhibition, there was no distortion of the transition state which resulted in an increase in the maximum velocity (q_m).[54]

The ability of the particles to protect enzymes from denaturing agent urea was also studied. Urea is a non-specific protein denaturing agent. Interactions between urea and proteins have been shown to reduce hydrophobic effect and increase the solvation of the hydrophobic protein residues.[55] Free lipase showed a strong reduction in the protein activity in presence of urea. Immobilization of lipase protected the enzyme from denaturation. The immobilized enzyme retained 59.9 ± 7.7 % of its initial activity, while the free enzyme retained only 26.5 ± 20.5 %, in presence of 4 M urea (Figure 5.19). The free enzyme sample displayed high standard deviation of 20.5%, this could be due to the nature of the commercially sold crude enzyme extract. Commercially sold *C. rugosa* lipase extract has been demonstrated to contain at least three isoforms of lipase[56], these isoforms differ in their activity and selectivity, which could account for the large standard deviation.[56] Immobilization of crude lipase extract on the RNP_PME(2.5) particles could have resulted in selective immobilization of highly active isoforms, which resulted in a low variation in the results. The problem could be addressed by increasing the number of

repeats of the experiment to reduce the experimental error. The differences in the lipase activity in presence of urea between the free and immobilized lipase samples was most likely due to the immobilization of the lipase molecules inside the mesopores of the particles, which reduces the degree of freedom of the enzyme molecules and thus reduces the protein unfolding.[34]

5.6 Conclusions

A high yielding system for Brönsted acid catalysed conversion of fructose to HMF has been achieved using RNP_PME(2.5) nanoparticle system. HMF yields up to 87% were obtained using 10 wt% fructose. Similar yields were only achieved using high boiling point solvents such as DMSO or using ionic liquid based systems. Both these strategies have been previously demonstrated as unviable for industrial production of HMF. RNP_PME(2.5) nanoparticle based system demonstrated excellent recyclability and HMF yields showed almost no reduction after 5 catalytic cycles. The particles also demonstrated strong ability in catalysing fructose to HMF at high fructose concentrations.

Lipase was immobilized on RNP_PME(2.5) nanoparticles. The enzyme-particle conjugates exhibited similar activity to the free lipase suggesting that the enzyme structure remained unchanged post-immobilization. The particles exhibited very high enzyme load, 58 wt%, which is higher than in most of the published reports. In addition to this, enzyme uptake took place in under an hour, another improvement over previous reports. Finally, immobilization of the protein on the particle surface helped reduce the effect of the denaturant urea on the protein structure. The immobilized enzyme retained 59.9 ± 7.7 % of its original activity compared to the free enzyme which retained only 26.5 ± 20.5 % of its original activity. The RNP_PME(2.5) nanoparticle system, thus represents an excellent catalysis and enzyme immobilization system.

5.7 References

1. B. Kamm, *Angew. Chem. Int. Edit.*, 2007, **46**, 5056- 5058.
2. R.-Jan van Putten, J. C. van der Waal, E. de Jong, C. B. Rasrendra, H. J. Heeres, and J. G. de Vries, *Chem. Rev.*, 2013, **113**, 1499-1597.
3. /a) G. Düll, *Chem.-Ztg.*, 1895, **19**, 216. b) J. Kiermayer, *Chem.-Ztg.*, 1895, **19**, 1003.
4. M. S. Feather, J. F. Harris, *Adv. Carbohydr. Chem.*, 1973, **28**, 161.
5. F. H. Newth, *Adv. Carbohydr. Chem.*, 1951, **6**, 83.
6. B. F. M. Kuster, *Starch/*Staerke, 1990, **42**, 314.
7. Y. Román-Leshkov, J. N. Chheda, J. A. Dumesic, *Science*, 2006, **312**, 1933.
8. H. Kimura, M. Nakahara, N. Matubayasi, *J. Phys. Chem. A* , 2011, **115**, 14013.
9. L. Hu, Y. Sun, L. Lin, *Ind. Eng. Chem. Res.*, 2012, **51**, 1099–1104.
10. S. De, S. Dutta and B. Saha, *Green Chem*., 2011, **13**, 2859- 2868.
11. T. Stahlberg, W. Fu, J. M. Woodley and A. Riisager, *ChemSusChem*, 2011, **4**, 451-458.
12. J. B. Binder and R. T. Raines, *J. Am. Chem. Soc.*, 2009, **131**,1979–1985.
13. M J. Climent , A. Corma and S. Iborra, *Green Chem.*, 2011, **13**, 340-349..
14. W. Vermeiren and J.-P. Gilson, *Top. Catal.*, 2009, **52**, 1131-1161.
15. E. Nikolla, Y. Roman-Leshkov, M. Moliner and M. E. Davis, *ACS Catal*. 2011, **1**, 408–410
16. F.-Shou Xiao, L. Wang, C. Yin, K. Lin, Y. Di, J. Li, R. Xu, D. Sheng Su, R. Schlgl, T. Yokoi and T. Tatsum, *Angew. Chem.*, 2006, **118**, 3162 -3165.
17. K. Wilson, J. H. Clark, *Pure Appl. Chem.*, 2000, **72**, 1313-1319.

18. A. J. Crisci, M. H. Tucker, M.-Yung Lee, S. Gyu Jang, J. A. Dumesic and Susannah L. Scott, *ACS Catal*., 2011, **1**, 719–728.

19. M. H. Tucker, A. J. Crisci, B. N. Wigington, N. Phadke, R. Alamillo, J. Zhang, S. L. Scott and J. A. Dumesic, *ACS Catal*. 2012, **2**, 1865−1876.

20. H. Zhu, B. H. Shanks and T. J. Heindel, *Ind. Eng. Chem. Res.*, 2008, **47**, 7881–7887.

21. W.-Huei Peng, Y.-Ying Lee, C. Wu and K. C.-W. Wu, *J. Mater. Chem*., 2012, **22**, 23181- 23185.

22. Y. Yücela, C. Demira, N. Dizgeb and B. Keskinler, *Biomass Bioenerg.*, 2011, **35**, 1496-1501.

23. R. D. Schmid and R. Verger, *Angew. Chem. Int. Edit.*, 1998, **37**, 1608-1633.

24. A. Bassegoda, S. Cesarini and P. Diaz, *Comput. Struct. Biotechnol. J.*, 2012, **2**, 1-21.

25. C.-Hung Kuo, Y.-Chuan Liu, C.-Ming J. Chang, J.-Hwa Chen, C. Chang and C.-Jen Shieh, *Carbohydrate Polymers*, 2012, **87**, 2538–2545.

26. M. Il Kim, H. Ok Ham, S.-Dae Oh, H. Gyu Park , H. Nam Chang and S.-Ho Choi, *J. Mol. Catal. B: Enzym.*, 2006, **39**, 62-68.

27. S. Gao, Y. Wang , X. Diao, G. Luo and Y. Dai, *Bioresource Technol.*, 2010, **101**, 3830-3837.

28. M. Hartmann and X. Kostrov, *Chem. Soc. Rev*., 2013, **42**, 6277—6289.

29. T. G. Terentyeva, A. Matras, W. Van Rossom, J. P. Hill, Q. Ji and K. Ariga, *J. Mater. Chem. B*, 2013, **1**, 3248–3256.

30. T. Raghavendra, U. Vahora, A. R. Shah and D. Madamwar, *Biotechnol Progr*., 2014, DOI: 10.1002/btpr.1929

31. M. V. Kahraman, G. Bayramoglu, N. Kayaman-Apohan and A. Güngör, *Food Chem*., 2007, **1041**, 1385–1392.

32. V. Dandavate, H. Keharia and D. Madamwar, *Process Biochem.*, 2009, **44**, 349-352.

33. E. Woo , K. M. Ponvel , I.-S. Ahn and C.-Ha Lee, *J. Mater. Chem.*,2010, **20**, 1511-1515.

34. S. Gao, Y. Wang, X. Diao, G. Luo and Y. Dai, *Bioresour Technol.*, 2010, **101**, 3830-3837.

35. S. R. Walker, H. Cumming and E. J. Parker, *Org. Biomol. Chem.*, 2009, **7**, 3031-3035.

36. C. Lopez, N. P. Guerra and M. L. Rúa, *Biotechnol. Lett.* , 2000, **22**, 1291-1294.

37. M. M. Bradford, *Anal. Biochem*., 1976, **72** , 1 -2, 248- 254.

38. R. Aveyard, B. P. Binks and J. H. Clint, *Adv. Colloid Interfac.*, 2003, 546, 100-102.

39. T. Chen, A. J. Colver and S. A. F. Bon, *Adv. Mater*, 2007, **19**, 2286-2289.

40. A. D. Dinsmore, M. F. Hsu, M. G. Nicolaides, M. Marquez, A. R. Bausch, D. A. Weitz, *Science*, 2002, **298**, 1006-1008.

41. L. Leclerq, A. Mouret, A. Proust, V. Schmidtt, A. Bauduin, J. M. Aubry and V. N. Rataj, *Chem- Eur. J.*, 2012, **18**, 14352-14358.

42. C. Wu, S. Bai, M. B. Ansorge- Schumacher and D. Wang, *Adv. Mater*, 2011, **23**, 5694-5699.

43. B. P. Binks and C. P. Whitby, *Colloid Surface A*, 2005, **253**, 105-115.

44. L. Chen, J. Hu, Z. Qi, Y. Fang and R. Richards, *Ind. Eng. Chem. Res*. 2011, **50**, 13642–13649.

45. K. Shimizua and A. Satsuma, *Energy Environ. Sci*., 2011, **4**, 3140–3153.

46. W.-H. Peng, Y.-Y. Lee, C. Wu and K. C.-W. Wu, *J. Mater. Chem.*, 2012, **22**, 23181–23185.

47. A. J. Crisci • M. H. Tucker, J. A. Dumesic and S. L. Scott, *Top Catal.*, 2010, **53**, 1185–1192.

48. Z. Du, M. P. Bilbao-Montoya, B. P. Binks, E. Dickinson, R. Ettelaie and B. S. Murray, *Langmuir* 2003, **19**, 3106-3108.

49. K. Larson-Smith and D. C. Pozzo, *Langmuir*, 2012, **28**, 11725−11732.

50. http://www.bio-rad.com/webroot/web/pdf/lsr/literature/4110065A.pdf

51. F. Bellazza, A. Cipiciani, U. Costantino and M. E. Negozio, *Langmuir*, 2002, **18**, 8737-8742.

52. J. M. Berg, J. L. Tymoczko and L. Stryer, *Biochemistry*, MacMillan Education, 7th Ed., 2012.

53. M. L. M. Mannesse, J. W. P. Boots, R. Dijkman, A. T. Slotboom, H. T. W. N. van der Hijden, M. R. Egmond, H. T. Verheij and G. R. de Haas, *Biochim. Biophys. Acta*, 1995, 1259, 56-64.

54. A. Fersht, *Structure and Mechanism in Protein Science: Guide to Enzyme Catalysis and Protein Folding*, W.H.Freeman & Co Ltd, 3rd Ed. 1999.

55. B. Bennion and V. Daggett, *Proc. Natl. Acad. Sci. USA*, 2003, **100**, 5142-5147.

56. C. C. Akoh, G.-C. Lee and J.-F. Shaw, *Lipids*, 2004, **39**, 513-526.

Chapter 6

Chapter 6: Future work

The aim of the work in this thesis was to synthesize phosphonate functionalized silica nanoparticles and to explore their potential for drug delivery applications. The phosphonate functionalization gave the particles interesting properties such as high pore size, raspberry texture and excellent dispersion stability. Additionally, the particles were able to adsorb large quantities of BSA and successfully deliver FITC functionalized BSA across cell membranes of HeLa cells. The protein loaded particles displayed endosomal escape and the particles remained in the cells after endosomal escape. All these results suggest excellent biomedical potential for the particles, notably in the area of cell marker research and targeted drug delivery.

Cell markers are very important in cancer research and diagnostics.[1] They are used to identify cancer cells in biopsies.[2] Nanoparticle based cell markers have been used for labelling[3] and for *in vivo* tracking of the labelled cells.[4] BSA loaded particles displayed folic acid mediated uptake. This pathway was found in many different types of cancers and is therefore considered an excellent target for identifying cancer cells.[5] Future work in this area would involve the study of the fate of the particles following prolonged incubation (3 to 4 generations) of the particles in various cancer cells expressing folic acid receptors (KB, HeLa, CHO cells etc.). Additionally, in vivo uptake of the particles could be studied using a mouse model and the particle localization identified using 2–photon microscopy.

The second area of focus is targeted drug delivery. As mentioned previously, the particles displayed uptake by the folic acid pathway, which is present in many types of cancer.[5] BSA loaded particles could be potentially conjugated to various drugs and these drug loaded protein particle conjugates could be used for drug delivery applications.

Various hydrophobic anti–cancer drugs such as doxorubicin bind to BSA via hydrophobic interactions.[6] Previous studies performed in animal models suggested that such conjugation could be useful to address problems such as multi–drug resistant cancer.[7] The drug loaded protein–particle conjugates could be used to achieve targeted drug delivery. The initial studies would involve using HeLa cells as the model cell line and the cytotoxicity of the drug loaded protein–particle conjugates versus time measured by Alamar blue assay. Following this, animal studies would have to be used to determine *in vivo* efficiency.

The thesis also explored the use of the phosphonic acid functionalised particle dispersions as catalysts. The observation of Pickering emulsion formation and very efficient catalytic conversion of a tough substrate system is a promising start that can be exploited for systems requiring mild acid catalysis. The system also clearly holds promise as a host for enzymes with multiple application possibilities.

Finally in terms of modified silica nanoparticle development the phosphonate modifier has clearly played several important roles in determining the formation and properties of the wide pore nanoparticles described in this work. It is of course possible that these roles could be covered by judicious choices of conditions with other modifiers. However while chemistry is key, the mechanical conditions employed for each action are also a very important consideration when it comes to gaining more precise control over the properties of these fascinating materials and this is an aspect that requires much further investigation.

6.1 References

1. R. K. Ambasta, A. Sharma and P. Kumar, *Vasc. Cell*, 2011, **3**, 26–34.

2. A. A. Ghazani, S. McDermott, M. Pectasides, M. Sebas, M. Mino–Kenudson, H. Lee, R. Weissleder and C. R. Castro, *Nanomedicine*, 2013, **9**, 1009–1017.

3. M. Lewin, N. Carlesso, C–H. Tung, X–W. Tang, D. Cory, D. T. Schadden and R. Weissleder, *Nat. Biotechnol.*, 2000, **18**, 410–414.

4. Y–S. Lin, C–P. Tsai, H–Y. Huang, C–T. Kuo, Y. Hung, D–M. Huang, Y–C. Chen and C–Y. Mou, *Chem. Mater.*, 2005, **17**, 4570–4573.

5. Y. Yu and P. S. Low, *Adv. Drug Deliv. Rev.*, 2012, **64**, 342–352.

6. D. Agudelo, P. Bourassa, J. Bruneau, G. Bérubé, E. Asselin and H. A. Tajmir–Riahi, *PLOS One*, 2012, **7**, e43814–e43826.

7. K. Ohkawa, T. Hatano, K. Yamada, K. Joh, K. Takada, Y. Tsukada and M. Matsuda, *Cancer Res.*, 1993, **53**, 4238–4242.

Appendix 1

Appendix 1

Appendix for Chapter 2

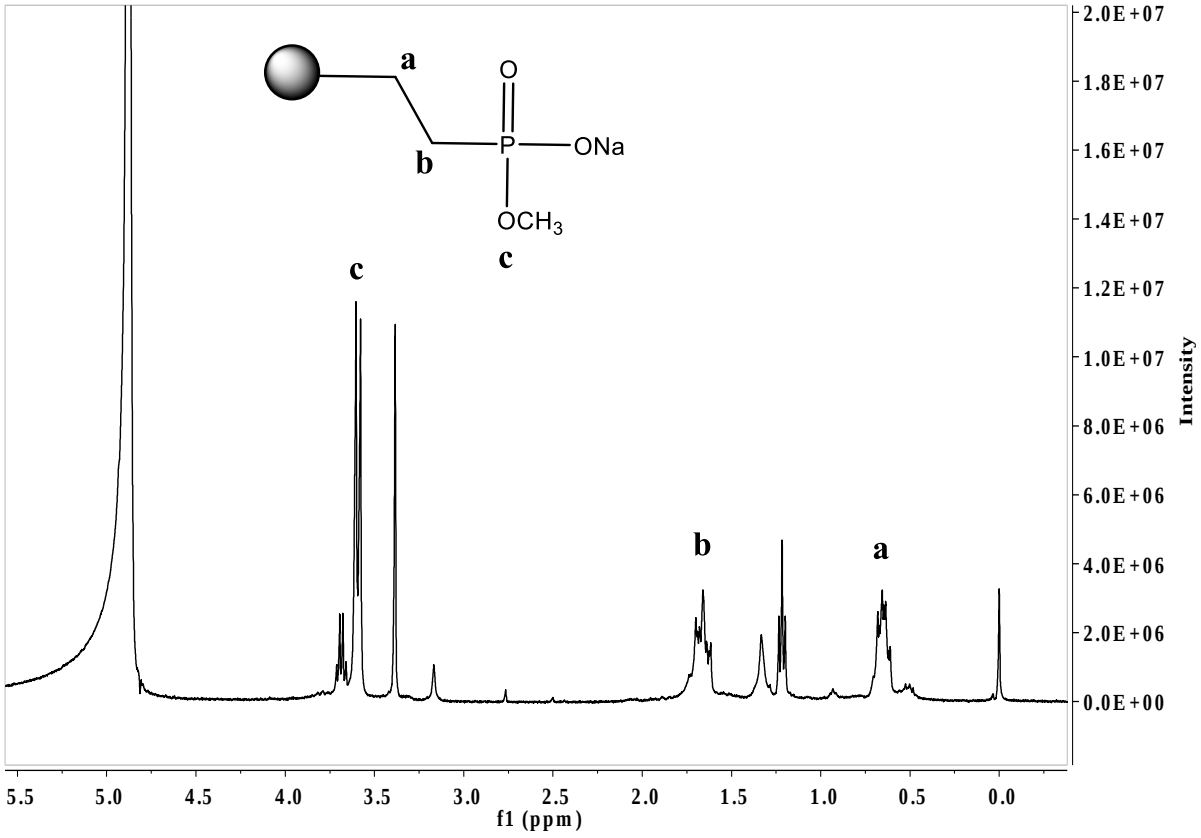

Figure 1: ^{1}H NMR spectrum of RNP_PME(2.5) nanoparticles in $NaOD/D_2O$

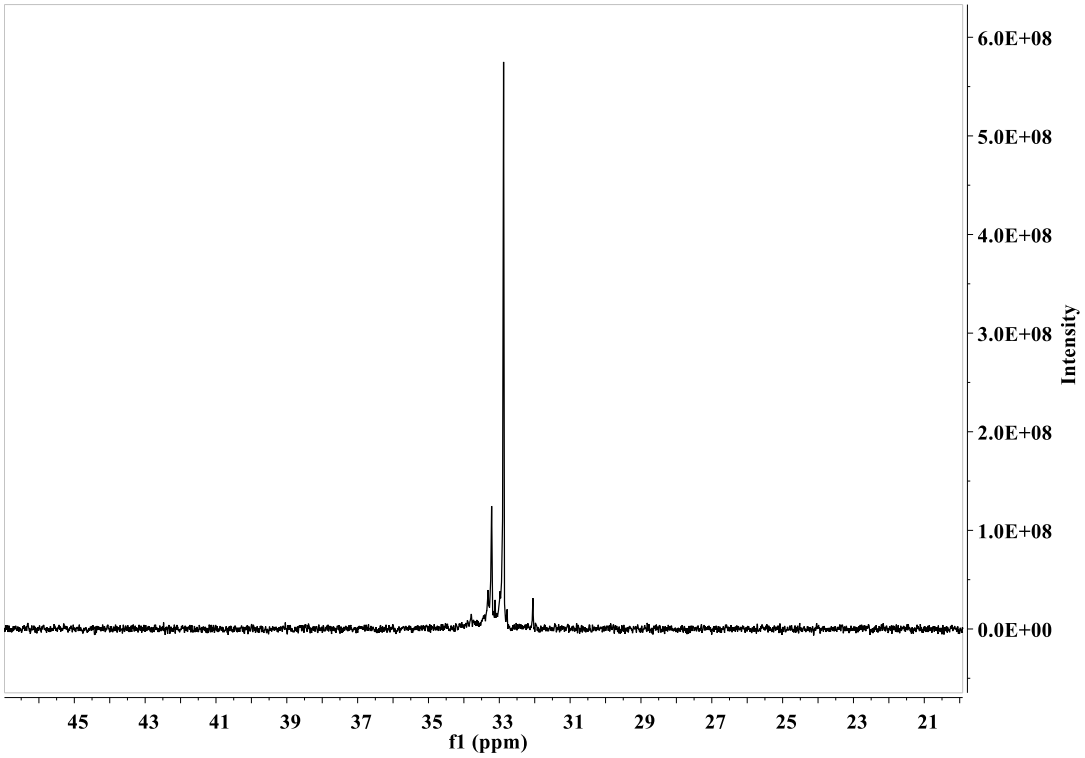

Figure 2: ^{31}P NMR spectrum of RNP_PME(2.5) nanoparticles in NaOD/D_2O

^{29}Si NMR spectra– Deconvolution

1.

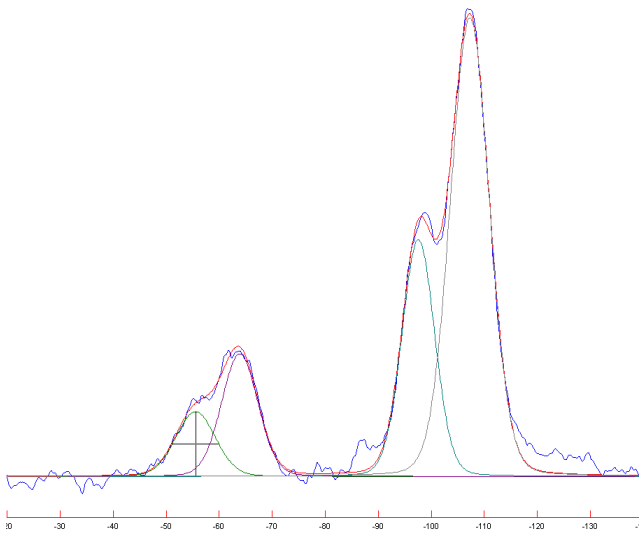

RNP_PME(2.5)

2. 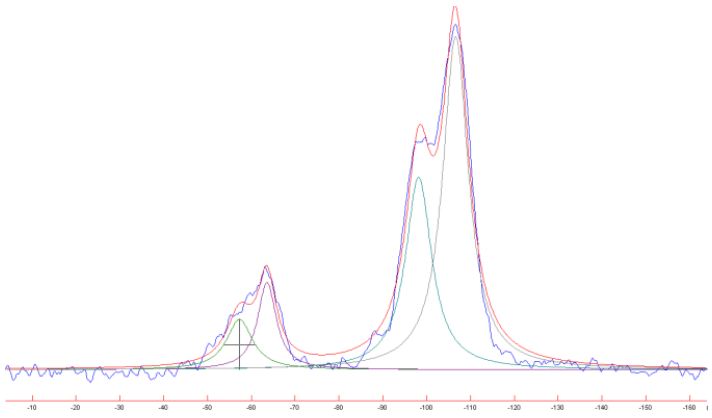

NP_PEE(2.1)

3. 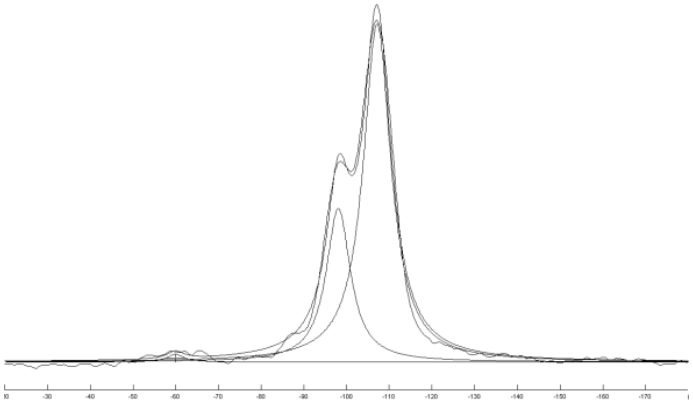

NP_PME(0.2)

4. 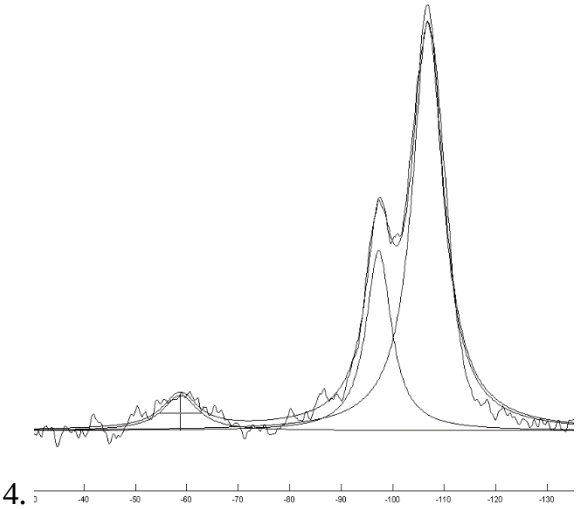

NP_PME(1.0)

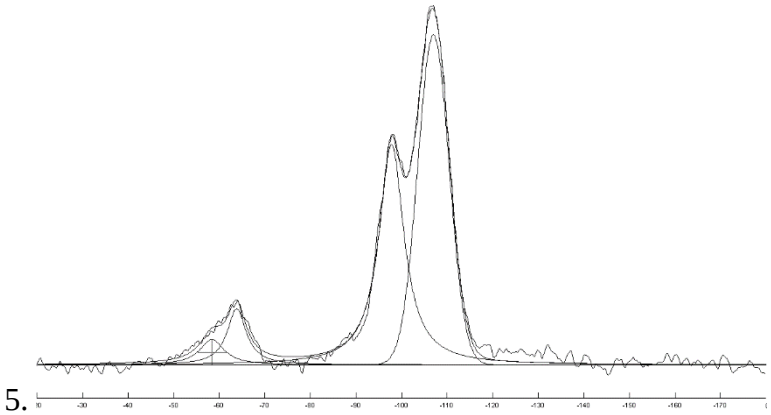

5.

CP_PME(1.6)

Zetapotential measurement :

Zetapotential measurements were performed on a Malvern Zetasizer Nano ZS instrument equipped with a 633 nm laser. For analysis 2 mg/mL particle dispersion in a disposable capillary cuvette was prepared by sonication for (15 min) in water. 3 measurements were performed for each sample.

Appendix 2

Appendix 2

Appendix for chapter 3

Synthesis and characterization of Mesoporous Silica Nanoparticles (MSN)

MSNs were synthesized according to a previously published report.[1] To 480 mL of deionized water, NaOH (2 M, 3.5 mL) and CTAB (1 g) were added and stirred at 1000 rpm. The temperature of the reaction mixture was raised to 80 °C and once all the surfactant was dissolved and the temperature settled, TEOS (5 mL) was added dropwise to the reaction vessel. About 2 minutes later, the reaction mixture turned cloudy and white precipitate began to settle at the bottom of the flask. The reaction was carried out for 2 hours. After 2 hours the white precipitate was filtered off and dried under ambient conditions. The white solid (2.5 g) was then suspended in acidified ethanol (35 mL of ethanol and 2 mL of 35 % HCl) and refluxed overnight to remove the surfactant. The surfactant free particles were filtered and washed with ethanol and deionized water and dried under vacuum. The particles (1 g) were characterized by FTIR, SEM, TEM and nitrogen adsorption porosimetry.

Results

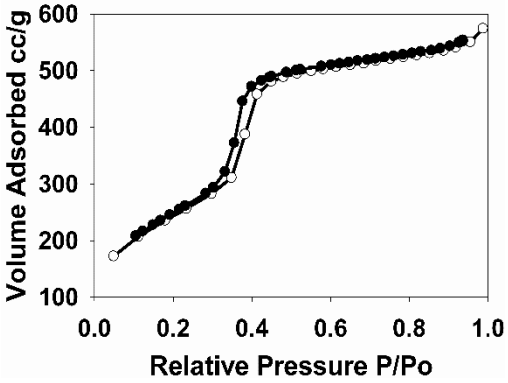

Figure 1: Nitrogen sorption isotherm of mesoporous silica nanoparticles

Reference:

1. I. I. Slowing, B. G. Trewyn and V. S. Y. Lin, *J. Am. Chem. Soc*., 2007, **129**, 8845-8849.

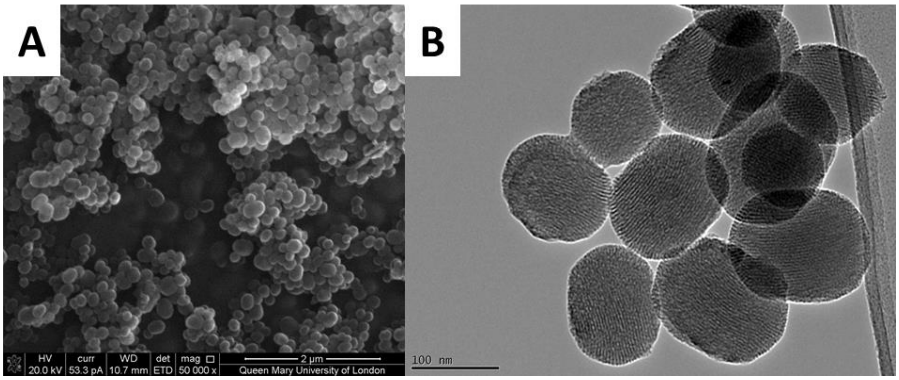

Figure 2: SEM (Figure A, Scale 2000 nm) and TEM (Figure B, Scale 100 nm) of meosporous silica nanoparticles.

BSA Calibration curve

BSA stock solution was prepared by dissolving BSA in PBS (concentration of 2 mg/mL). The stock solution was then serially diluted to produce concentrations between 0.125 to 2 mg/mL (Figure 3). The absorbance at 280 nm was recorded on UV-Vis spectrophotometer (Figure 4).

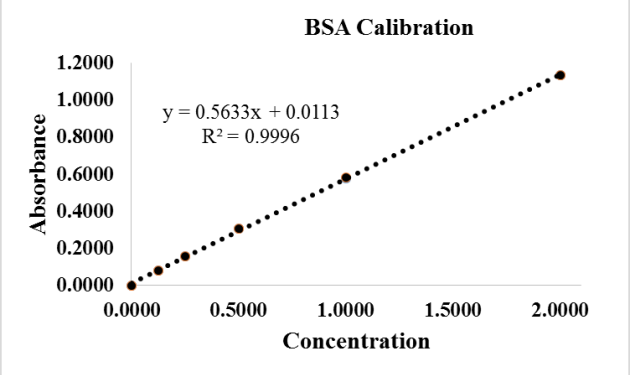

Figure 3: BSA calibration curve in PBS

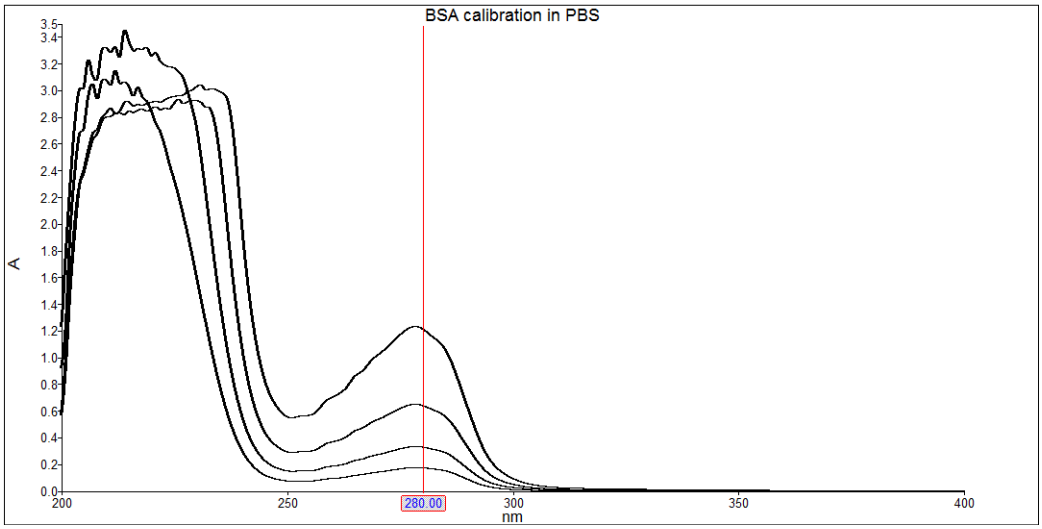

Figure 4: BSA UV-Vis adsorption spectra

3. Linearized Langmuir plots (Figure 5) were obtained using the data from figure 3.1, the data was fitted according to the following equation:

$$\frac{C(e)}{Q(e)} = \frac{1}{Q_m K_L} + \frac{C(e)}{Q(m)}$$

Where, C(e) stands for equilibrium concentration (mg/mL) ; Q(e) stands for the amount of protein adsorbed at equilibrium (mg/g); K_L is the Langmuir constant and Q(m) is the maximum protein load.

C(e) was calculated using the following formula:

$$C(e) = C(0) - \frac{Q(e) \times M}{V}$$

Where C(0) is the initial protein concentration (mg/mL); M is the weight of the particles (g) and V is the total volume (mL)

Figure 5: Linearized Langmuir plots of BSA adsorption on the nanoparticles.

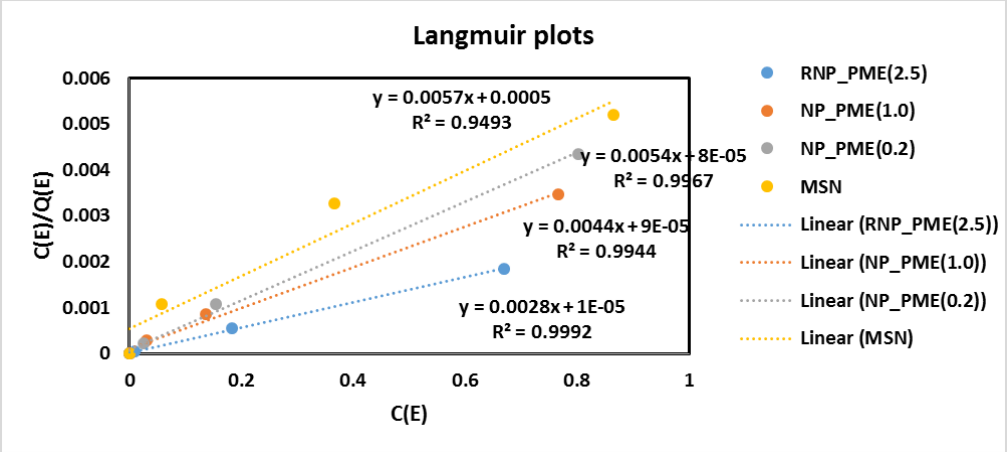

Figure 6: K_d (distribution co-efficient) vs C(0) (Initial concentration plots). The distribution co-efficient was used to determine the affinity between the nanoparticles and protein molecules. Higher the K_d the stronger the affinity. K_d value decreases with concentration since the particle surface gets coated by the protein molecules and there are fewer sites available to adsorb.

$$K_d = \frac{\big(C(0) - C(e)\big)V}{C(0)M}$$

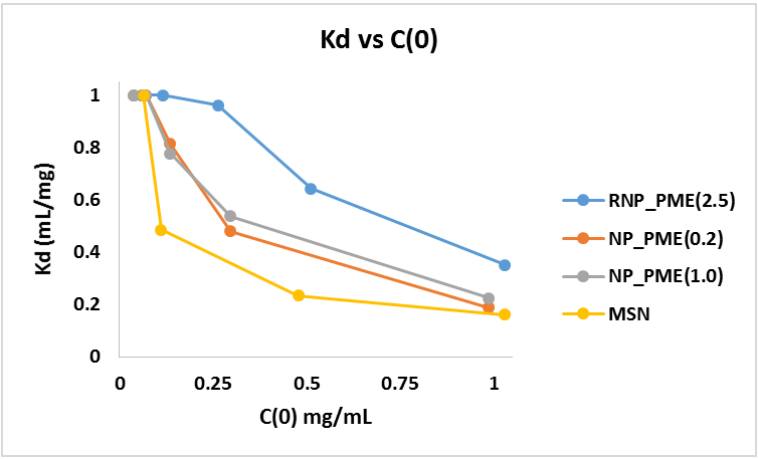

Appendix 3

Appendix 3

Appendix for Chapter 4

1. BSA Bradford assay calibration curve (Figure 1)

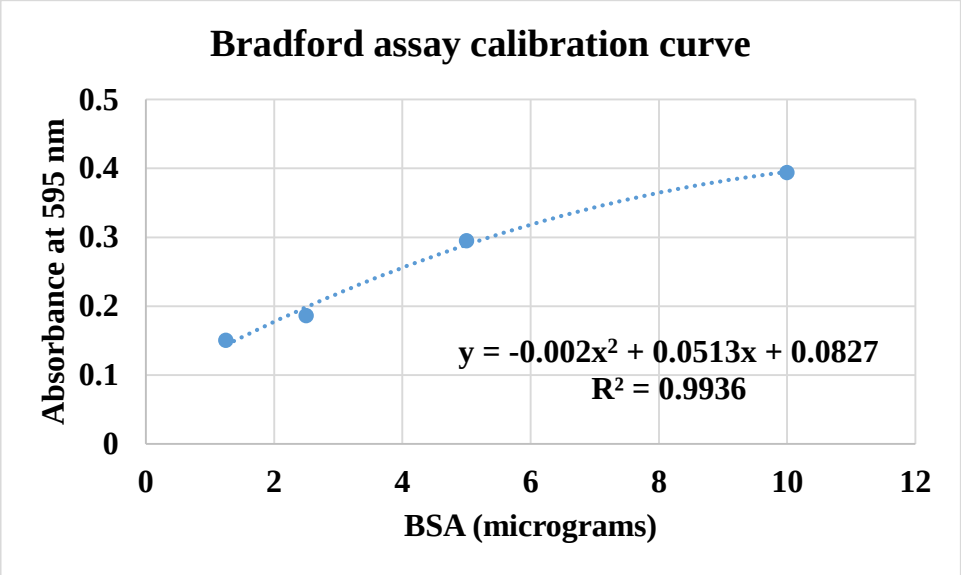

2. UV-Vis Spectrum of FITC_BSA or BSA[#] (Figure 2)

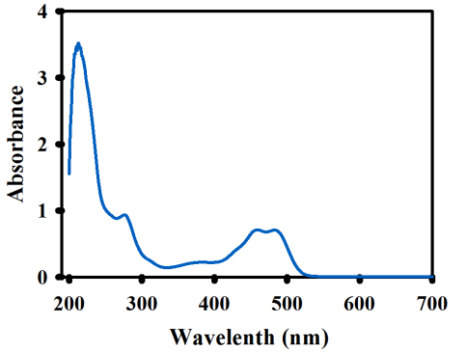

3. MTT cell viability study using BSA# (n = 3 ± Std. dev.) (Figure 3)

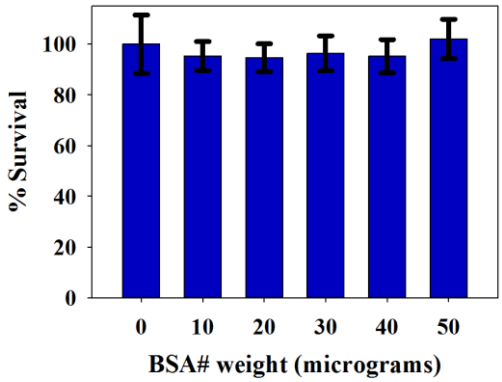

Figure 3: MTT cell viability study using BSA#

4. Spots Analysis using Imaris:

Spots package in Imaris is used to model point like structures in the image. This package was used to represent particles distributed inside the cells as spheres and the total number of spots per cell data was used to identify patterns of nanoparticle uptake. In this section a brief overview of the method used to detect particles is described.

1. 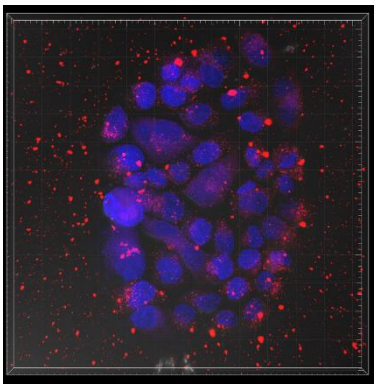

Figure 4: Confocal image

2. 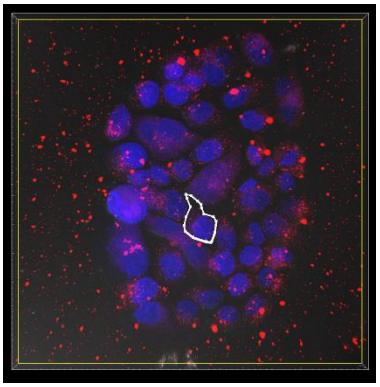

Figure 5: Contour (using surface function) is drawn around individual cells in each image in the stack. (Every confocal microscope image is a collection of around 20 to 30 individual images)

3. 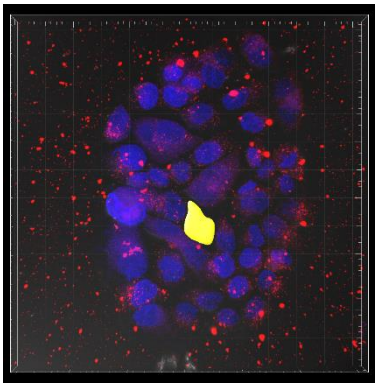

Figure 6: Using the surface function in Imaris, a surface (yellow object in the image) is created. A surface is an artificial solid object created to visualize the region of interest. Following the creation of the surface, channel of choice (red for the RNP*_PME(2.5) particles) is selected.

4. 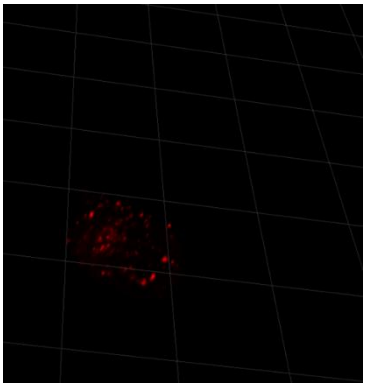

Figure 7: Using the surface function a new channel, which exclusively identifies the particles in the region of interest is created.

5. 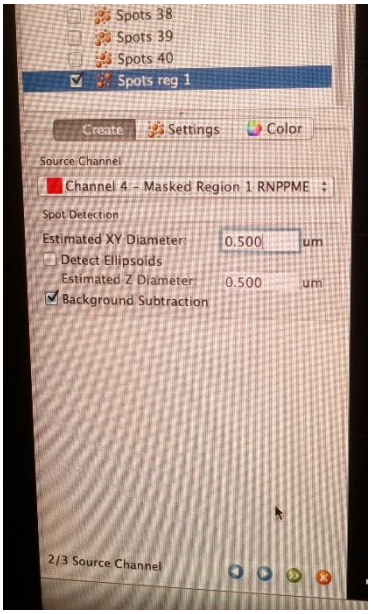

Figure 8: The spots function is used to identify point-objects and represent them as spheres. First, the region of interest is identified and the size of the spots in micrometres is given.

6. 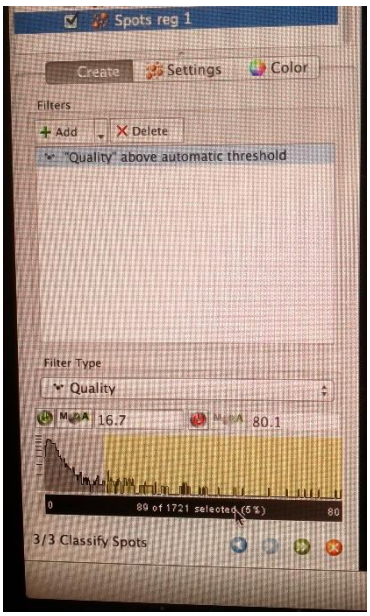

Figure 9: The detection threshold is then manually adjusted to correct the errors in automatic spots detection.

7. 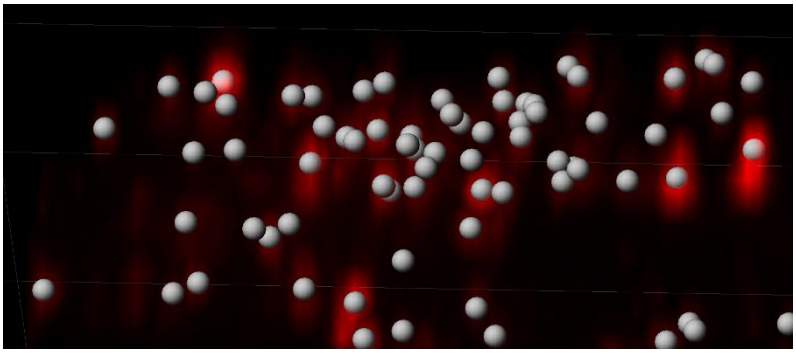

Figure 10: After a suitable threshold value is determined (the value varies from one region to another.) the spots function creates spots (white spheres) in the region of interest.

Appendix 4

Appendix 4

Appendix for chapter 5

1. Bradford assay calibration using BSA

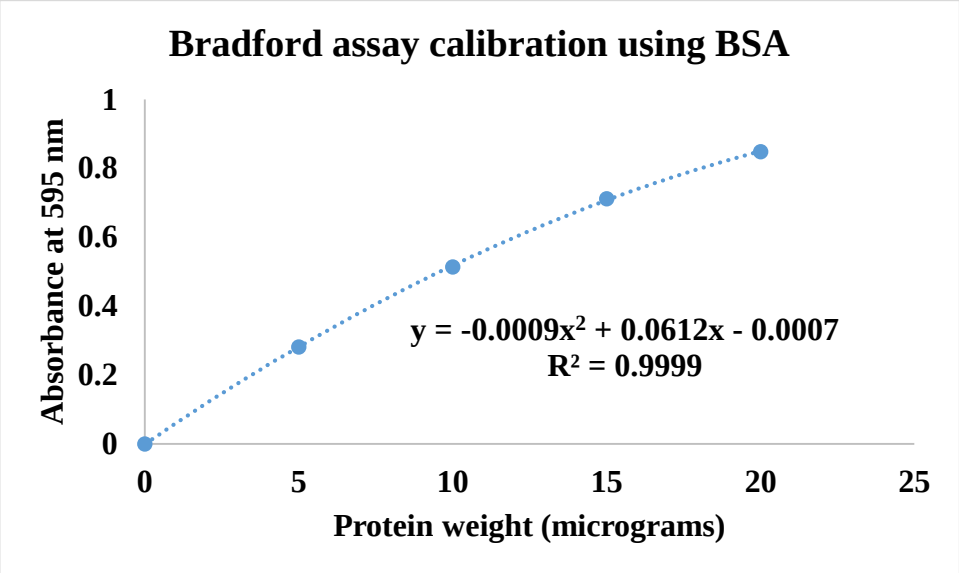

2. Calibration 4-nitrophenol in phosphate buffer (pH 7)

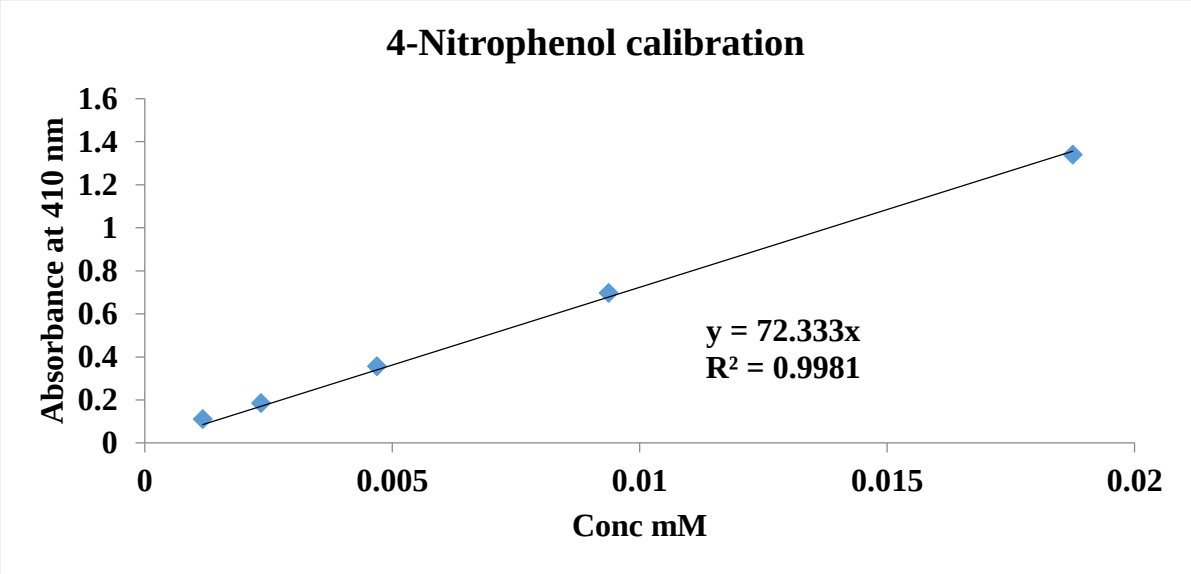

Appendix 5

Published paper

Title: “New phosphonic acid polysilsesquioxane mild solid acid catalysts”

Reference: M. Sebah, S. P. Maddala, P. Haycock, A. Sullivan, H. Toms, J. Wilson, *J. Mol. Catal. A* , 2013, **374- 375**, 59- 65.

Journal of Molecular Catalysis A: Chemical 374–375 (2013) 59–65

Contents lists available at SciVerse ScienceDirect

Journal of Molecular Catalysis A: Chemical

journal homepage: www.elsevier.com/locate/molcata

New phosphonic acid polysilsesquioxane mild solid acid catalysts

Majda Sebah [1], Sai P. Maddala [1], Peter Haycock, Alice Sullivan *, Harold Toms, John Wilson

School of Biological and Chemical Sciences, Queen Mary University of London, Mile End Road, London E1 4NS, UK

ARTICLE INFO

Article history:
Received 6 November 2012
Received in revised form 18 March 2013
Accepted 21 March 2013
Available online xxx

Keywords:
Polysilsesquioxane
Solid acid catalyst
Phosphonic acid
Transesterification
5-Hydroxymethylfurfural

ABSTRACT

A simple easily scalable one-pot route to new phosphonic acid polysilsesquioxanes, PAPSQ, $[(O_{3/2}SiCH_2R)_x(O_{3/2}SiCHR(CH_2)_2SiO_{3/2})_y]_n$ where $R = CH_2PO_3H_2$, is described in this paper. Nuclear magnetic resonance (NMR), electron microscopy (SEM), thermogravimetric analysis, nitrogen sorption porosimetry, phosphorus and available acid analysis were used to characterise the new PAPSQ materials. The materials were shown to be very efficient and recyclable mild solid acid catalysts for organic transformations including those relevant to biomass conversion such as esterification, transesterification and dehydration of fructose to the important intermediate 5-hydroxymethylfurfural.

1. Introduction

Molecular cages, resins, glasses and ordered mesoporous solids derived from precursor organotrialkoxysilanes such as $RSi(OMe)_3$ or the bridged type precursors $(MeO)_3SiRSi(OMe)_3$ are polysilsesquioxanes, PSQ, and are represented as $[RSiO_{3/2}]_n$ or $[O_{3/2}SiRSiO_{3/2}]_n$ in the fully condensed forms. The organic groups R are important in determining the properties and applications PSQ display. Polysilsesquioxane, PSQ, materials, $[RSiO_{3/2}]_n$ or $[O_{3/2}SiRSiO_{3/2}]_n$ where R is a functional organic group are of great current interest with potential application areas in energy materials, drug delivery systems and as separation media [1–6]. The organic–inorganic hybrid composition provides excellent thermal stability and built-in chemical functionality makes these materials ideal candidates for heterogeneous catalysis applications. New PSQ materials and their catalytic applications are frequently reported [7–13] but the translation of this research to industrial application is apparently limited by the complexity of synthesis and cost [7,8]. PSQs with phosphonic acid functional groups are a relatively little explored class. Compared to stronger Brønsted acid functions such as sulfonic acid, phosphonic acid is relatively mild and consequently may be less prone to promotion of side reactions. We report here on new phosphonic acid functionalised PSQs which are readily synthesised on a large scale, along with studies that demonstrate their use as solid Brønsted acid heterogeneous catalysts.

2. Experimental

Solvents and reagents used were purchased from Aldrich. Proton, carbon and phosphorus NMR spectra of PAPSQ materials dispersed in $NaOD/D_2O$ were recorded on Bruker AMX 400 or 600 MHz instruments. Solid state spectra were obtained using a Bruker AMX 600 MHz instrument: ^{29}Si HPDec MAS, frequency 119.2 MHz, spinning speed 12 kHz; 1 min recycle delay, with 2 μs ~45° pulse; ^{31}P CP MAS; frequency 242.9 MHz, spinning speed 12 kHz, 1 ms contact time, 1.5 s delay, 90° pulse for 2.0 μs. SEM was recorded on a JEOL 6300F scanning electron microscope and TGA on a TA Q500 ramped at 10 °C/min under nitrogen. Nitrogen adsorption–desorption was recorded on a Qantachrome Nova porosimeter. Phosphorus elemental analysis was obtained from Medac Ltd.

2.1. *Preparation PAPSQa and PAPSQb* $[(O_{3/2}SiCH_2R)_{1.5}(O_{3/2}SiCHR(CH_2)_2SiO_{3/2})]_n$ $R = CH_2PO(OH)_2$

To dimethyl phosphite (37.2 g, 31 mL, 0.338 mol) was added vinyltrimethoxysilane (33 mL, 0.215 mol) and the mixture heated with stirring at 110 °C for 2 h. Di-*tert*-butyl peroxide (1 drop) was added every 15 min for 2 h after which no vinyl resonances could be detected by ^1H NMR. The excess dimethyl phosphite was removed under reduced pressure and the residual colourless liquid containing, **1**, dimethylphosphonatoethyltrimethoxysilane and **2**, 2,4-*bis*(trimethoxysilyl)-1-dimethylphosphonato butane in ratio 1.5:1 (^{31}P NMR ($CDCl_3$) **1** 35.68(s) **2** 35.48(s)) was treated further.

* Corresponding author.
E-mail address: a.c.sullivan@qmul.ac.uk (A. Sullivan).
[1] Joint first authors.

1381-1169/$ – see front matter © 2013 Elsevier B.V. All rights reserved.
http://dx.doi.org/10.1016/j.molcata.2013.03.021

2.1.1. PAPSQa

HCl (160 mL of 5 M) was added to 20 g of the colourless liquid (from Section 2.1) and then stirred under reflux for 5 h. On cooling to room temperature the white solid was filtered and washed extensively with distilled water and methanol. The solid was dried under reduced pressure at 120 °C for 4 h to afford a white powder **PAPSQa** (10.9 g, 89.7%). Surface area: 65 $m^2\ g^{-1}$, ^{29}Si MAS δ_{Si}: −63 (br s) deconvoluted peaks at −53, −58, −63. ^{31}P CPMAS NMR δ_P 33 ($PO(OH)_2$, 90%) 24 (Si—OH–O=P$(OH)_2$, 10%). Found *P* 4.96 mmol g^{-1}.

2.1.1.1. Accessible acid measurement. In a typical measurement to determine the phosphonic acid first proton exchange capacity, a sample of PAPSQa 0.2040 g was shaken in 50 mL of 0.5 M sodium formate solution for 60 h. The formic acid produced was titrated with 20 mM NaOH. Accessible acid in PAPSQa: 3.3 mmol g^{-1}.

*2.1.1.2. NMR **PAPSQa** dispersed in (NaOD/D_2O).* PAPSQa was dispersed in NaOD/D_2O wherein the phosphonate is fully ionised while Si-C bonds remain intact. This is a convenient way to confirm presence of components (1) and (2) (see below)

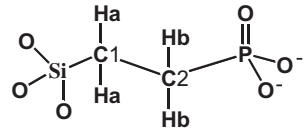

(1)

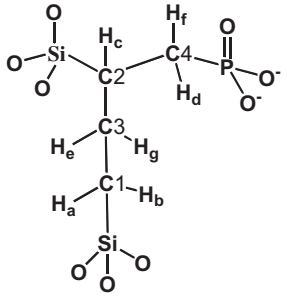

(2)

δ_P (PAPSQa) 26.8 (s, *P* (1)), 25.6 (s, *P* (2)) intensity ratio 1.5:1. δ_H (1) 0.65 (Ha, m, 2H), 1.36 (Hb, m, 2H); δ_C (1) 7.6 (C1), 22.6 (d, C2) (Assignments confirmed by HSQC [14]), δ_H (2) 0.53 (m, Hb, J(b,a),15.27 Hz, J(b,e), 3.43 Hz, J(b,g), 8.73 Hz), 0.73 (m, Ha, J(a,b), 15.27 Hz, J(a,e), 10.45 Hz, J(a,g), 4.2 Hz), 0.99 (m, Hc, J(c,d), 5.22 Hz, J(c,e), 9.76 Hz, J(c,f), 9.32 Hz, J(c,g), 4.27 Hz, J(c,P), 14.10 Hz), 1.27 (m, Hd, J(d,f), 14.90 Hz, J(d,P), 17.62 Hz), 1.55 (m, He, J(e,g), 13.48 Hz), 1.63(m, Hf, J(f,P), 16.2 Hz), 1.89 (m, Hg, J(e,g), 13.48 Hz), δ_C (2) 11.6 (C1), 21.1 (C2), 26.6 (C3), 31.0 (d, C4) (Assignments confirmed by HSQC [14]).

Note: the NUMERIT [15] simulated and experimentally observed ^{1}H NMR spectrum features of the complex seven proton spin system in component (2) are shown in Supplementary Information Fig. A.

Supplementary data associated with this article can be found, in the online version, at http://dx.doi.org/10.1016/j.molcata.2013.03.021.

2.1.2. PAPSQb

To 6.0 g of the mixture of **1** and **2** mole ratio 1.5:1 (from Section 2.1) was added aqueous hydrochloric acid (1 M, 15 mL) and methanol (180 mL). The resultant solution was placed in a polypropylene plastic bottle and warmed to 90 °C for 16 h. The formed glass was ground to a powder. To this powder, hydrochloric acid (5 M, 50 mL) was added slowly and the resultant mixture was stirred under reflux for 12 h. On cooling to room temperature the solid was filtered and then washed extensively with distilled water, methanol and diethyl ether. The solid was then dried at 120 °C for 4 h to yield a white powder PAPSQb (2.9 g, 79%).

Surface area: 80 $m^2\ g^{-1}$, ^{31}P NMR (NaOD/D_2O) δ_P: 25.2, 26.3 ratio 1:1.5; ^{31}P CPMAS NMR δ_P 32.2 (br s), ^{29}Si MAS δ_{Si}: −63 (br s) deconvoluted peaks at −58, −64, found *P* 5.1 mmol g^{-1} Accessible acid by titration 3.3 mmol g^{-1}.

2.2. Catalysis

Quantity of catalyst used (mol%) was based on the available acid determined by titration. Percentage conversions were determined by ^{1}H NMR spectroscopy or isolated products. Turnover numbers are based on three cycles in each case. Blank reactions were performed in the absence of catalyst. The catalyst was recycled either after filtration and washing or after removal of the product solution and addition of fresh reagent and solvent. Leaching was assessed by interrupting the reaction (ketalisation, esterification and transesterification) at partial conversion (1 h), separating the liquid phase from the catalyst using a 0.2 μm filter and measuring conversion again at the specified reaction time. No evidence of leaching was detected. The ketalisation, esterification and transesterification experiments were also run using the equivalent quantity of phosphoric acid as catalyst.

2.2.1. Protection of ketones (ketalisation)

A mixture of acetophenone (4.8 g, 40.0 mmol, 4.7 mL), ethane-1,2-diol (6.7 g, 107.6 mmol, 6.0 mL) catalyst (30 mg, 0.25 mol%) in toluene (30 mL) was refluxed 10 h using a Dean-Stark apparatus. The reaction was followed by TLC. The reaction mixture was cooled to room temperature, the catalyst filtered off and washed with ether (20 mL). The ketal product 2-methyl-2-phenyl-1,3-dioxolane was obtained as a white solid from the filtrate after washing with water (3 × 20 mL) and drying over magnesium sulfate.

^{1}H NMR ($CDCl_3$): δ_H: 1.67 (s, 3H), 3.78 (t, 2H), 4.02 (t, 2H), 7.25–7.56 (m, $5H_{arom}$).

2.2.2. Esterification of oleic acid

Oleic acid (1 g, 3.54 mmol), catalyst (20 mg, 1.9 mol%) and ethanol (6 mL) were combined and the reaction mixture was refluxed for 8 h then heated to 90 °C for 2 h using an air condenser. The evaporated solvent was replaced with dry ethanol and the mixture heated a further 2 h using an air condenser. Ether (30 mL) was added to the cooled mixture and the catalyst was filtered off, washed with diethyl ether and retained for recycling. The organic solvents were removed from the filtrate. Conversion to the ethyl oleate was determined by integration of the total alkene proton signal at δ_H 5.33 (m, 2H) against the ester methylene signal at δ_H 4.11 (q, 2H, O$CH_2$$CH_3$).

2.2.3. Transesterification of ethyl oleate

Ethyl oleate (1.55 g, 5 mmol), catalyst (50 mg, 3.3 mol%) and pentanol (10 mL) were refluxed for 12 h. The reaction was followed by TLC. On cooling, ether (30 mL) was added and the catalyst was filtered off. The organic solvents were removed. Conversion was determined by integration of the alkene proton signals at δ_H 5.35 and the ester methylene signal at δ_H 4.13 (t, 2H, O$CH_2$$(CH_2)_3CH_3$).

2.2.4. HMF synthesis

Fructose (206 mg, 1.14 mmol) was dissolved in deionized water (1.8 g) and PAPSQa (209 mg) was added to this solution. An organic phase (2 g) containing MIBK and 2-butanol in 7:3 ratio was added to the reaction vessel to obtain a biphasic mixture. The reaction mixture was heated to 130 °C, while stirring at 600–700 rpm for 12 h. The reaction mixture was then cooled to 90 °C without stirring,

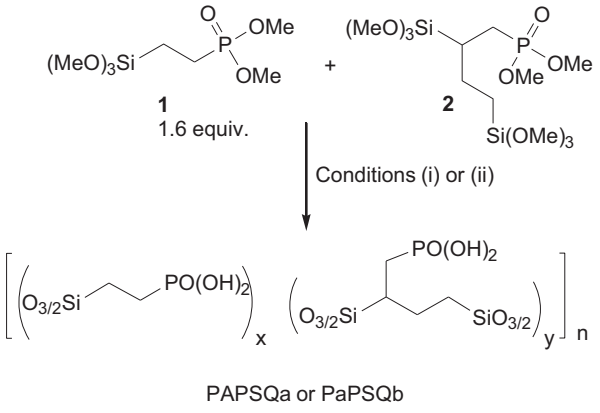

Scheme 1. Conditions: (i) direct hydrolysis with 5 M HCl gives PAPSQa $x/y = 1.5$; or (ii) sol-gel process **1** and **2** (MeOH, aqueous HCl) and hydrolysis of xerogel with 5 M HCl gives PAPSQb $x/y = 1.5$.

the organic phase (top layer) removed, another batch of fructose (200 mg) and organic phase added and the process repeated. In this manner three catalytic cycles were assessed. In each case pure HMF (by NMR) was obtained from the removed organic phase. The isolated yields of HMF from the organic layers based on D-fructose taken in each cycle were 51, 57 and 57%.

Repeating this process with PAPSQb (203 mg) and fructose (204 mg) in three catalytic cycles afforded HMF product yields of 59, 72 and 73%.

2.2.5. Comparative catalytic activity for ketalisation, esterification and transesterification

The reactions as described above in Section 2.2.1, Section 2.2.2, and Section 2.2.3 and identical ones employing phosphoric acid as catalyst at the same mol% phosphorus were sampled at regular intervals up to 5 h and the % conversion evaluated.

2.2.6. Comparative catalytic activity for ketalisation

A mixture of acetophenone (4.8 g, 40.0 mmol, 4.7 mL), ethane-1,2-diol (6.7 g, 107.6 mmol, 6.0 mL) and catalysts PAPSQa, PAPSQb or phosphoric acid, adjusted to give 0.2 mol% acid, was refluxed as in Section 2.2.1 and samples taken for analysis at regular intervals.

3. Results and discussion

3.1. Synthesis

The objective of this work was to explore simple routes for the synthesis of new phosphonic acid functionalised polysilsesquioxanes, PAPSQ and to investigate the solid acid catalytic activity of these materials. We have previously reported on the microporous PAPSQ material $[_{3/2}OSiCH_2CH(PO(OH)_2)CH_2CH_2SiO_{3/2}]_n$ which has an in-framework phosphonic acid group [16]. The precursor for this material required the tedious synthesis of 1,4-bis(triethoxysilyl)but-2-ene and subsequent radical addition of $HPO(OEt)_2$ to the *ene* fragment making this a relatively long and costly method. Others have reported [17] on the 2-component PAPSQ system $[(O_{3/2}SiCH_2CH_2(PO(OH)_2))_x(O_{3/2}Si(CH_2)_2SiO_{3/2})_y]_n$ obtained by co-hydrolysis and condensation of the precursors $[(EtO)_3SiCH_2CH_2PO(OEt)_2]$ and $[(MeO)_3Si(CH_2)_2Si(OMe)_3]$.

New phosphonic acid polysilsesquioxanes, PAPSQ, $[(O_{3/2}SiCH_2\mathbf{R})_x(O_{3/2}SiCH\mathbf{R}(CH_2)_2SiO_{3/2})_y]_n$ where $\mathbf{R} = CH_2PO_3H_2$, were synthesised starting from the *mono* and *bis*-trialkoxysilylalkylphosphonate esters (Scheme 1). The known phosphonate ester compounds, **1,** dimethylphosphonatoethyl trimethoxysilane [18] and **2,** 2,4-*bis*(trimethoxysilyl)-1-dimethylphosphonatobutane [19], were formed in this work as a two-component mixture in a simple radical addition reaction between dimethylphosphite and vinyltrimethoxysilane in the presence of di-*tert*-butylperoxide. Both compounds were produced even when excess dimethylphosphite was employed. For dimethylphosphite:vinyltrimethoxysilane 1.6:1, compounds **1** and **2** were formed in 1.5:1 ratio as evidenced by the relative integration of ^{31}P NMR resonances at δ 35.68 for **1** and δ 35.48 for **2**. The percentage of **2** in the mixture may be increased by increasing the proportion of vinyltrimethoxysilane in the reaction. For example, at dimethylphosphite:vinyltrimethoxysilane ratio of 0.5 the ratio of **1**–**2** formed was 0.9:1. This simple reaction allowed for easy one-pot formation of precursors to bridged polysilsesquioxane materials PAPSQ with very high phosphonic acid loading. In contrast the multi-step routes to $[_{3/2}OSiCH_2CH(PO(OH)_2)CH_2CH_2SiO_{3/2}]_n$ and $[(O_{3/2}SiCH_2CH_2(PO(OH)_2))_x(O_{3/2}Si(CH_2)_2SiO_{3/2})_y]_n$ mean that these are significantly more demanding to synthesise.

The phosphonate ester mixture was converted to two-component amorphous phosphonic acid polysilsesquioxane materials, PAPSQ. This was achieved either by a one-pot hydrolytic co-polycondensation of the mixture of **1** and **2**, using 5 M HCl to give directly the phosphonic acid polysilsesquioxane designated PAPSQa or by sol-gel processing to an isolated intermediate ethylphosphonate ester xerogel followed by hydrolysis of the crushed xerogel with 5 M HCl to give the material PAPSQb (see Scheme 1). The materials obtained were washed extensively with distilled water, methanol and diethyl ether. Of the two routes, the one pot direct hydrolysis route had the advantage of avoiding any need to form, isolate and grind an intermediate ethylphosphonate ester xerogel $[(O_{3/2}SiCH_2\mathbf{R})_x(O_{3/2}SiCH\mathbf{R}(CH_2)_2SiO_{3/2})_y]_n$ where $\mathbf{R} = CH_2PO(OEt)_2$. It avoided the need for large quantities of methanol and facilitated the synthesis of much larger batches of material in ~10 h compared to ~30 h. In addition the direct hydrolysis route also afforded a 10% higher overall yield of product.

3.2. NMR features

Materials PAPSQa and PAPSQb had similar NMR spectroscopic features. The ratio x/y of phosphorus components in the PAPSQs shown in Scheme 1 was determined from the ^{31}P NMR of materials dispersed in $NaOD/D_2O$ solution (Fig. 1). The ^{31}P CPMAS NMR of the solid PAPSQ appeared as broad peaks around δ 33 ppm (Fig. 1). A small peak was also present at δ 24 ppm indicative of some Si—OH–O=P(OH)$_2$ interaction [20,21].

When the materials were dispersed in $NaOD/D_2O$ the ^{31}P resonances of the two fully ionized phosphonic acid components were clearly distinguished and shifted to higher field compared to the phosphonic acid (Fig. 1(b) and (f)). Under these conditions the bulk material Si—O—Si framework was sufficiently hydrolysed to facilitate dissolution while Si—C bonds remained intact and this was a convenient way to observe the different phosphorus containing components. Solid state ^{29}Si NMR on PAPSQa and PAPSQb gave broad resonances centred at δ −63 ppm, Fig. 1(c) and (g) which after deconvolution, Fig. 1(d) and (h) were found to have the silicon environments in (PAPSQa)PAPSQb T^1(12.7%)0%,T^2(27.8%)49.8%, and T^3(59.5%)50.2%, with overall condensation (82%)83% respectively. T^n denotes the number of Si—O—Si bonds at the trifunctional silicon.

The silicon–carbon–phosphorus skeletons of the two phosphorus components in PAPSQa were observed in the ^1H and ^{13}C NMR spectra of a sample dispersed in $NaOD/D_2O$ (see experimental). Spectral assignments of the different proton environments in dispersed PAPSQa were made after simulation using HSQC (Hetero Single Quantum Coherence) [14] and NUMERIT [15] experiments (see supplementary information Fig. A).

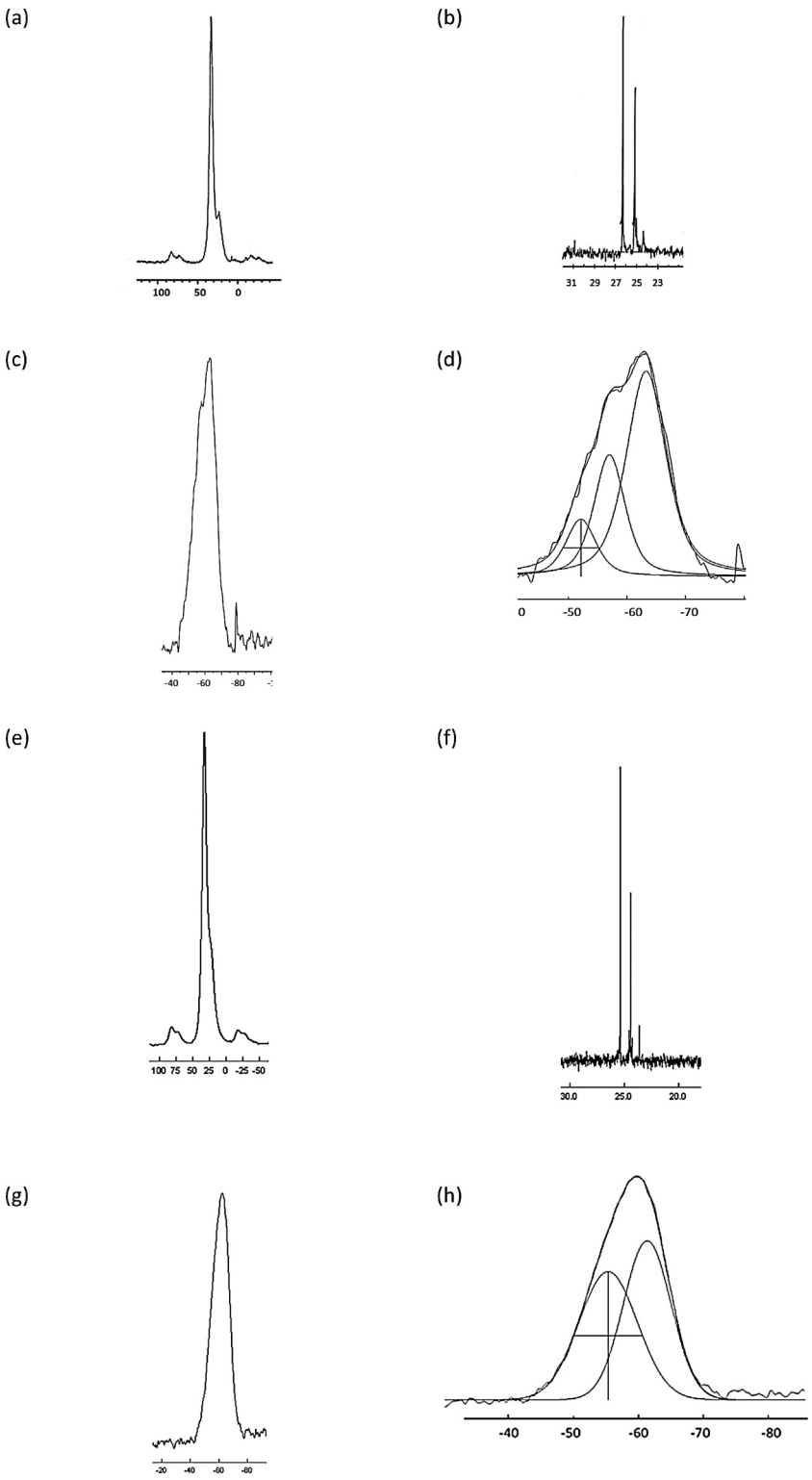

Fig. 1. ^{31}P CPMAS NMR (a) PAPSQa (e) PAPSQb ^{31}P NMR in NaOD/D_2O (b) PAPSQa (f) PAPSQb ^{29}Si MAS NMR (c) PAPSQa (g) PAPSQb and Deconvoluted ^{29}Si MAS NMR (d) PAPSQa (h) PAPSQb.

3.3. Texture

The as synthesised PAPSQa and PAPSQb were ground to fine powders. The ground powders were non porous and had surface areas and pore volumes of 65 m^2/g, 0.09 cm^3/g (PAPSQa) and 200 m^2/g, 0 cm^3/g PAPSQb. A fused nanoparticle surface texture was seen for both materials as shown in Fig. 2 where PAPSQb displays a finer texture.

3.4. Thermal properties

The TGA profiles of as-formed PAPSQa and PAPSQb materials pre-dried at 120 °C were recorded under nitrogen and are shown in Fig. 3. Weight loss from PAPSQa(PAPSQb) of 1.3%(5%) due to retained solvent or water was observed below 150 °C. Further gradual weight loss ~8%(5%) was observed between 150 and 475 °C. This may reflect further condensation of silanol. The weight loss

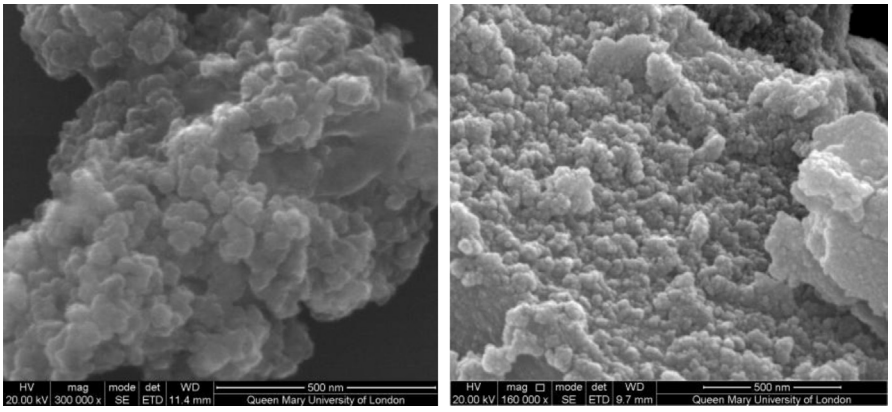

Fig. 2. SEM of (a) PAPSQa (b) PAPSQb.

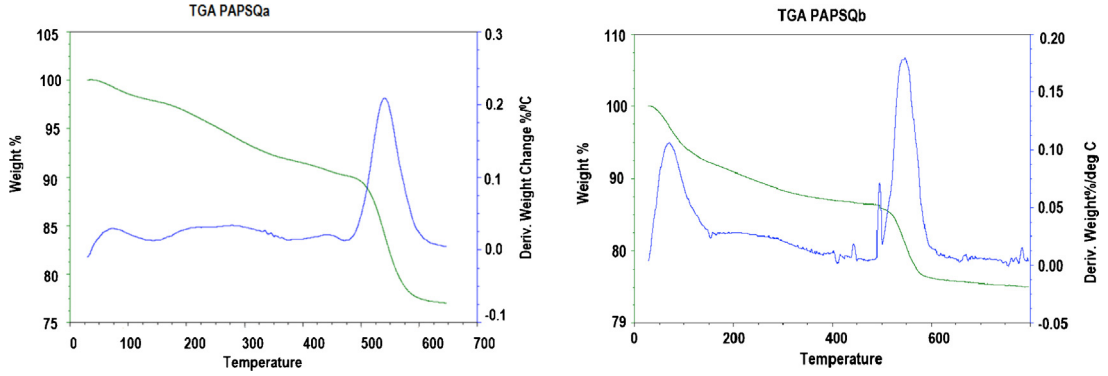

Fig. 3. TGA of (a) PAPSQa (b) PAPSQb.

12%(10%) above 475 °C could represent condensation due to P—O—P bond formation and/or elimination of small hydrocarbon fragments. Overall weight loss at 600 °C was less than 23% in both cases.

3.5. Catalytic studies

To assess stability and activity the PAPSQ materials were initially assessed as catalysts in organic transformations including protection of ketones and esterification/transesterification of acids and esters respectively. This was followed by a more complex transformation involving dehydration of fructose where there are several potential products. All results are summarised in the Table 1.

The % conversions (92–98%) for ketalisation of acetophenone (Scheme 2) measured after 10–12 h from catalysts PAPSQa and PAPSQb were high.

Both catalysts were easily separated from reaction media by filtration and were recycled further without loss of activity. To achieve a comparison between the catalysts PAPSQa, PAPSQb and a homogeneous analogue, the initial progress of reaction was followed for the ketalisation of acetophenone using the solid acids and phosphoric acid under identical conditions and with 0.2 mol% of the acid in each case. The results (Fig. 4) showed steady rates of conversion in all three cases with 94% conversion for PAPSQa after 4.5 h, while phosphoric acid had 85% and PAPSQb 73% conversion in the same time period. The apparent differences in conversion profiles for the solid acids may in part be due to minor differences in mechanical mixing during the process (powder PAPSQb was considerably finer than powder PAPSQa which affected its distribution

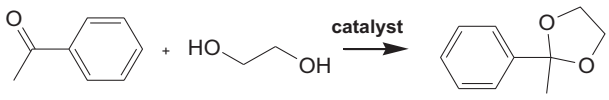

Scheme 2. Ketalisation of acetophenone.

Table 1
PAPSQ solid acid catalytic data.

Entry	Catalyst	(%) Conversion or yield[e] for cycles 1,2,3 (TON)[f]
1[a]	PAPSQa	97,97,97 (1175)
2[a]	PAPSQb	98,97,97 (1175)
3[a]	Phosphoric acid	90
4[b]	PAPSQa	97,95,97 (154)
5[b]	PAPSQb	96,99,99 (154)
6[b]	Phosphoric acid	50
7[c]	PAPSQa	92,93,93 (84)
8[c]	PAPSQb	92,92,92 (84)
9[c]	Phosphoric acid	93
7[d]	PAPSQa	51, 57, 57 (2.7)
8[d]	PAPSQb	59, 72, 73 (3.5)

[a] Ketalisation of acetophenone. Conditions: 40 mmol acetophenone and ethane-1,2-diol (6 mL) in toluene (30 mL) and 30 mg phosphonic acid 0.25 mol% based on titrated acid (or 0.25 mol% phosphoric acid). Blank reactions (no catalyst) gave zero conversion.

[b] Esterification of oleic acid. Conditions: 3.5 mmol oleic acid, 20 mg catalyst corresponding to phosphonic acid, 1.9 mol% based on titrated acid (or 1.9 mol% phosphoric acid); ethanol (6 mL), at 90 °C for 12 h.

[c] Transesterification ethyloleate conditions: 5 mmol ethyl oleate, 50 mg catalyst corresponding to phosphonic acid 3.3 mol% based on titrated acid and pentanol (10 mL); refluxed 12 h.

[d] 10 wt% aqueous fructose in 1:1 w/w aqueous/organic phases (organic phase 7:3 MIBK:2-butanol) and 1:1 w/w fructose and PAPSQa.

[e] Conversion determined by NMR for entries 1–6 and yield of HMF isolated from organic phase only and confirmed by NMR for entry 7 and 8.

[f] TON = mole product mol^{-1} available acid after the 3 cycles.

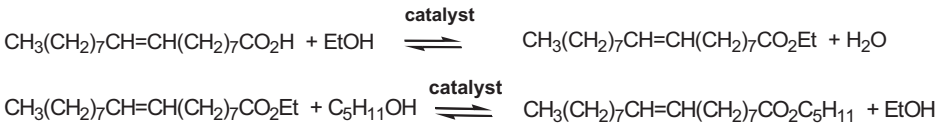

Scheme 3. Esterification of oleic acid and transesterification of ethyloleate.

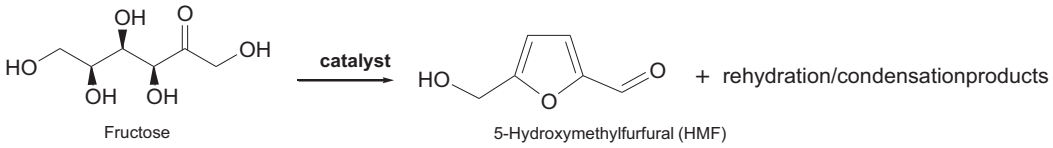

Scheme 4. Dehydration of fructose to HMF.

in this two phase toluene–ethanediol mixture). The PAPSQa profile indicates a slightly faster rate of conversion compared to the homogeneous phosphoric acid catalyst in this reaction.

Both catalysts PAPSQa and PAPSQb gave high conversions for esterification of oleic acid and trans-esterification of ethyl to pentyl oleate (Scheme 3).

These experiments showed that the solid catalysts could be recycled and continued to be active after several runs when held at temperatures in the range 90 °C (ketalisation) to 140 °C (transesterification). Turnover numbers (TON) which reflect the mol% of available acid used (see Table 1) were calculated for the specific conditions employed in each case but it should be noted that experiments to optimise these were only carried out for the ketalisation transformation where the conversion continued to be high as the mol% catalyst was reduced to 0.25 mol% resulting in TON of 1175 mol ketal mol^{-1} available acid after three cycles without loss of activity. With an equivalent quantity of phosphoric acid as catalyst and the timescales employed, the conversions were found to be much lower for the esterification and comparable for transesterification reactions. This was considered reasonable since the transesterification reaction was carried out at higher temperatures and water was not a by-product. Compared to organic transformations catalysed by sulfonic acid supported on silica or polysilsesquioxane [8,22–27], reports on catalysis using corresponding phosphonic acid systems are scant. Sulfonic acid has the advantage of significantly greater acid strength with pKa = −1 compared to di-protic phosphonic acid with pKa values typically ∼2.3–2.9 and 7.7–9 for the first and second ionizations [28]. A milder acid catalyst might however sometimes be preferable particularly where a number of products can be formed and selectivity for a particular product is required. In this context there is great interest in the conversion of fructose to 5-hydroxymethylfurfural, HMF, where rehydration and condensation by-products are a complicating factor in the synthesis (Scheme 4).

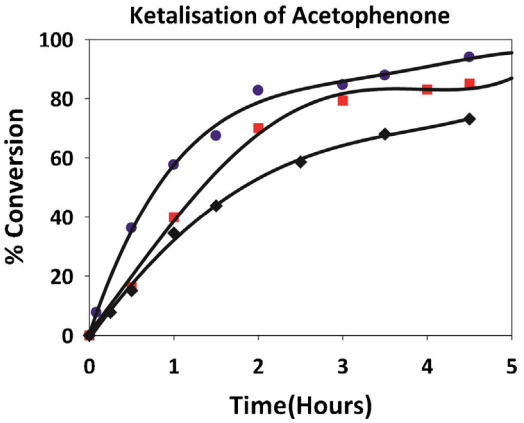

Fig. 4. Reaction profiles for ketalisation of acetophenone with PAPSQa (●), PAPSQb (♦) and phosphoric acid (■) Conditions: 40 mmol acetophenone and ethane-1,2-diol (6 mL) in toluene (30 mL); catalyst at 0.2 mol% *P* in each case.

HMF is an important intermediate for 2,5-disubstituted furans such as the dicarboxylic acid derivative which has been suggested as an alternative for terephthalic acid and hence a source of biomass derived polymers. The industrial use of HMF is limited by high production costs [29,30]. Some efficient biphasic catalytic systems were recently reported. Dumesic et al. published in-depth studies employing mineral acids including phosphoric acid, the sulfonic acid polystyrene ion-exchange resin catalysts PK-216 and Amberlyst 70 and various silica supported sulfonic acids in biphasic media [31]. We followed conditions reported by Dumesic for a sulfonic acid resin catalyst, consisting of 10 wt% aqueous fructose in 1:1 w/w aqueous/organic phases (organic phase 7:3 MIBK:2-butanol) and 1:1 w/w fructose and catalyst. The reaction with PAPSQa or PAPSQb as catalyst was run at several temperatures up to 130 °C where the highest yield of HMF was isolated. Three cycles were incorporated in the present experiment wherein between cycles the organic MIBK-2-butanol phase (upper layer) containing the product HMF was separated and fresh fructose and organic phase added to the residual hot aqueous phase containing the catalyst. Our analysis was based on isolated HMF from the organic phase only and thus represents the minimum yield since the HMF formed is distributed between aqueous and organic layers. This analysis allowed us to determine whether a constant flow of HMF would result with addition of fresh substrate and organic phase. Rehydration or condensation reaction by-products if formed remain in the aqueous layer. The HMF isolated yields increased after the first cycle for both PAPSQa and PAPSQb catalysts. Thus while leaving the aqueous phase and catalyst unperturbed except for the addition of fresh fructose, the catalysts remained active and the yield of HMF increased during the three cycles of HMF production. Both solid acids resided completely in the aqueous phase of the two-phase mixture and dispersed well in this phase in the stirred mixture. The surface area of catalyst PAPSQb being roughly three times that of PAPSQa may account for the higher 5-HMF yield from PAPSQb. For the identical biphasic system employing the sulfonic acid ion-exchange resin catalyst PK-216, at 90 °C for 8–16 h, or phosphoric acid at 90 °C -180 °C for 8 min the HPLC determined yields of HMF from the organic phase after a single cycle were 23 and 28% respectively [30]. Catalyst stability due to leaching of functional groups was identified as an issue for some silica supported sulphonic acid catalysts when employed in a continuous flow reactor for HMF production [32] but hybrid sulfonic acid catalysts had greater stability in this respect.

4. Conclusion

New phosphonic acid polysilsesquioxane materials, PAPSQs, were readily formed from an easily prepared two-component precursor mixture. Direct hydrolysis of the precursor mixture afforded a simple and fast route to the target material (PAPSQa) that avoids isolating the intermediate phosphonate ester modified material which is an inevitable step of the alternative sol-gel route (to PAPSQb). The mildly acidic glassy particulate materials PAPSQa and PAPSQb displayed effective solid Brønsted acid catalytic activity. Ketalisation proceeded at a faster rate for PAPSQa than with dissolved phosphoric acid or PAPSQb as catalyst. PAPSQs hold much promise as catalysts for transformations that would benefit from a mild acid catalyst such as those where more than one product is routinely formed. In this context the solid acids were used to demonstrate a constant flow of the important intermediate 5-hydroxymethylfurfural, HMF, as the substrate fructose and organic solvent were replenished in this important example of a biomass conversion reaction.

Overall phosphonic acid polysilsesquioxane PAPSQa is a new low cost easy to synthesise organic-inorganic hybrid with good thermal stability and viable catalytic applications can be envisaged for this material. In future work different compositional variations including metal derivatives will be investigated.

Acknowledgements

MS thanks EPSRC and SM thanks Queen Mary University of London, for Ph.D. studentship funding.

References

[1] L.-C. Hu, K.J. Shea, Chem. Soc. Rev. 40 (2011) 688–695.
[2] N. Mizoshita, T. Tani, S. Inagaki, Chem. Soc. Rev. 40 (2011) 789–800.
[3] A. Mehdi, C. Reye, R. Corriu, Chem. Soc. Rev. 40 (2011) 563–574.
[4] F. Hofmann, M. Cornelius, J. Morell, M. Fröba, Angew. Chem. Int. Ed. 45 (2006) 3216–3251.
[5] B. Hatton, K. Landskron, W. Whitnall, D. Perovic, G.A. Ozin, Acc. Chem. Res. 38 (2005) 305–312.
[6] H.S. Sankaraiah, J.M. Lee, J.H. Kim, S.W. Choi, Macromolecules 41 (2008) 6195–6204.
[7] A. Zamboulis, M. Moitra, J.J.E. Moreau, X. Cattoen, M. Wong Chi Man, J. Mater. Chem. 20 (2010) 9322–9338.
[8] Q.H. Yang, J. Liu, L. Zhang, C. Li, J. Mater. Chem. 19 (2009) 1945–1955.
[9] C.M. Kang, J.L. Huang, W.H. He, F. Zhang, J. Organomet. Chem. 695 (2010) 120–127.
[10] J.L. Huang, F.X. Zhu, W.H. He, F. Zhang, W. Wang, H.X. Li, J. Am. Chem. Soc. 132 (2010) 1492–1493.
[11] X.S. Yang, J.L. Huang, F.X. Zhu, H.X. Li, Acta Chim. Sinica 68 (2010) 217–221.
[12] A. Kuschel, S. Polarz, J. Am. Chem. Soc. 132 (2010) 6558–6565.
[13] A.C. Coelho, S.S. Balula, S.M. Bruno, J.C. Alonso, N. Bion, P. Ferreira, M. Pillinger, A.A. Valente, J. Rocha, I.S. Goncalves, Adv. Synth. Catal. 353 (2010) 1759–1769.
[14] D. Massiot, F. Fayon, M. Capron, I. King, S. Le Calvé, B. Alonso, J.-O. Durand, B. Bujoli, Z. Gan, G. Hoatson, Magn. Reson. Chem. 40 (2002) 70–76.
[15] Kirk Marat, NUMARIT – A spin simulation/iteration package for the X32, University of Manitoba.
[16] M. Jurado-Gonzalez, D. Li Ou, B. Ormsby, A.C. Sullivan, J.R.H. Wilson, Chem. Commun. (2001) 67–68.
[17] Q. Yang, J. Yang, J. Liu, Y. Li, C. Li, Chem. Mater. 17 (2005) 3019–3024.
[18] M.G. Voronkov, V.A. Pestunovich, N.F. Chernov, A.I. Albanov, E.F. Belogolova, L.V. Klyba, A.E. Pestunovich, Russ. J. Gen. Chem. (Zh. Obshch. Khim.) 76 (2006) 1554–1561.
[19] O.N. Dolgov, M.G. Voronkov, Russ. J. Gen. Chem. (Zh. Obshch. Khim.) 40 (1970) 1660.
[20] A. Aliev, B. Ormsby, D. Li Ou, A.C. Sullivan, J. Mater. Chem. 10 (2000) 2758.
[21] M. Jurado-Gonzalez, D. Li Ou, A.C. Sullivan, J.R. Wilson, J. Mater. Chem. 12 (2002) 3605–3609.
[22] M.P. Kapoor, Y. Kasama, M. Yanagi, T. Yokoyama, S. Inagaki, T. Shimada, H. Nanbu, L.R. Juneja, Micropor. Mesopor. Mater. 101 (2007) 231.
[23] K. Nakajima, D. Lu, I. Tomita, S. Inagaki, M. Hara, S. Hayashi, K. Domen, J.N. Kondo, Adv. Mater. 17 (2005) 1839.
[24] C.M. Li, J. Liu, L. Zhang, J. Yang, Q.H. Yang, Micropor. Mesopor. Mater. 113 (2008) 333.
[25] D. Dube, M. Rat, F. Beland, S. Kaliaguine, Micropor. Mesopor. Mater. 111 (2008) 596.
[26] A. Bugrayev, N. Al-Haq, R.A. Okopie, A. Qazi, M. Suggate, A. Sullivan, J. Wilson, J. Mol. Catal. A Chem. 280 (2008) 96–101.
[27] G. Morales, G. Athens, B.F. Chmelka, R. van Grieken, J.A. Melero, J. Catal. 254 (2008) 205.
[28] L.D. Quin, A Guide to Organophosphorus Chemistry, Wiley, Canada, 2000 (Chapter 5), p. 133.
[29] K. Shimizu, A. Satsuma, Environ. Sci. 4 (2011) 3140–3153.
[30] Y. Roman-Leshkov, J.N. Chheda, J.A. Dumesic, Science 312 (2006) 933–937.
[31] A.J. Crisci, M.H. Tucker, M.-Y. Lee, S.G. Jang, J.A. Dumesic, S.L. Scott, ACS Catal. 1 (2011) 719–728.
[32] M.H. Tucker, A.J. Crisci, B.N. Wigington, N. Phadke, R. Alamillo, J. Zhang, S.L. Scott, J.A. Dumesic, ACS Catal. 2 (2012) 1865–1876.